NASA Conference Publication 3337

Pt.
N95-33535

Space Electrochemical Research and Technology

Proceedings of a conference held at
NASA Lewis Research Center
Cleveland, Ohio
May 1–3, 1995

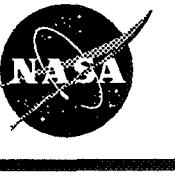

Trade names or manufacturers' names are used in this report for identification only. This usage does not constitute an official endorsement, either expressed or implied, by the National Aeronautics and Space Administration.

NASA Conference Publication 3337

Space Electrochemical Research and Technology

Proceedings of a conference
held at and sponsored by the NASA Lewis Research Center
Cleveland, Ohio
May 1–3, 1995

National Aeronautics and
Space Administration

Office of Management

**Scientific and Technical
Information Program**

1996

Page intentionally left blank

TABLE OF CONTENTS

Advanced Secondary Batteries

Development of a Micro-Fiber Nickel Electrode for Nickel-Hydrogen Cell
Doris L. Britton, NASA Lewis Research Center 3

High Performance Nickel Electrodes for Space Power Applications
Prosper K. Adanuvor, Johnnie A. Pearson, Brian Miller, and Bruce Tatarchuk, Auburn University; and Doris L. Britton, NASA Lewis Research Center 11

Bending Properties of Nickel Electrodes for Nickel-Hydrogen Batteries
Brad A. Lerch and Richard M. Wilson, NASA Lewis Research Center; Dennis Keller, Real World Quality Systems, Inc.; and Ralph Corner, NYMA, Inc. 23

Effect of KOH Concentration and Anions on the Performance of a Ni-H_2 Battery Positive Plate
Hari Vaidyanathan and Kathleen Robbins, COMSAT Laboratories, and Gopalakrishna M. Rao, NASA Goddard Space Flight Center 41

Advanced Dependent Pressure Vessel (DPV) Nickel-Hydrogen Spacecraft Cell and Battery Design
Dwaine K. Coates, R. Doug Wright, and Ron S. Repplinger, Eagle-Picher Industries, Inc. 53

Electrolyte Management Considerations in Modern Nickel Hydrogen and Nickel Cadmium Cell and Battery Designs
Lawrence H. Thaller and Albert H. Zimmerman, The Aerospace Corporation 61

Fuel Cells

A Novel Unitized Regenerative Proton Exchange Membrane Fuel Cell
O.J. Murphy, A.J. Cisar, A. Gonzalez-Martin, C.E. Salinas, and S.F. Simpson, Lynntech, Inc. 83

Fuel Cell Systems for First Lunar Outpost—Reactant Storage Options
P.A. Nelson, Argonne National Laboratory 101

The TMI Regenerable Solid Oxide Fuel Cell
Thomas L. Cable, Robert C. Ruhl, and Michael Petrik, Technology Management, Inc. 109

Engineering Development Program of a Closed Aluminum-Oxygen Semi-Cell System for an Unmanned Underwater Vehicle—An Update
Dane W. Gregg and Susan E. Hall, Loral Defense Systems—Akron 119

Advanced Concepts

SPE OBOGS: On-Board Oxygen Generating System
James F. McElroy and William F. Smith, United Technologies Corporation 133

Hermetically Sealed Aluminum Electrolytic Capacitor
Robert S. Alwitt and Yanming Liu, Boundary Technologies, Inc., and William Elias, BACE Technologies 147

SOL-GEL Technology and Advanced Electrochemical Energy Storage Materials
Chung-tse Chu and Haixing Zheng, Chemat Technology, Inc. 163

Development of Electrochemical Supercapacitors for EMA Applications
John A. Kosek, Thomas Dunning, and Anthony B. LaConti, Giner, Inc. 179

High Energy Density Electrolytic Capacitor
David A. Evans, Evans Company 189

Advanced Secondary Batteries

Page intentionally left blank

51-44
008839

DEVELOPMENT OF A MICRO-FIBER NICKEL ELECTRODE FOR NICKEL-HYDROGEN CELL

Doris L. Britton
NASA Lewis Research Center
Cleveland, Ohio

256898
8P.

ABSTRACT

Development of a high specific energy battery is one of the objectives of the lightweight nickel-hydrogen ($Ni-H_2$) program at the NASA Lewis Research Center. The approach has been to improve the nickel electrode by continuing combined in-house and contract efforts to develop a more efficient and lighter weight electrode for the nickel-hydrogen cell. Small fiber diameter nickel plaques are used as conductive supports for the nickel hydroxide active material. These plaques are commercial products and have an advantage of increased surface area available for the deposition of active material. Initial tests include activation and capacity measurements at different discharge levels followed by half-cell cycle testing at 80 percent depth-of-discharge in a low-Earth-orbit regime. The electrodes that pass the initial tests are life cycle-tested in a boiler plate nickel-hydrogen cell before flightweight designs are built and tested.

INTRODUCTION

The nickel electrode is the most critical as well as the heaviest component of nickel-based battery systems such as nickel-hydrogen and nickel-cadmium. These systems are used in aerospace, military, and commercial applications. Because of its relatively high specific energy and excellent cycling capability, the $Ni-H_2$ battery is used extensively in aerospace system. For the past several years, NASA Lewis Research Center has been developing the $Ni-H_2$ cell. The overall objective of the program is to improve the components, design, and operating characteristics of the cell. In certain aerospace applications, such as space station, space satellites and space telescope, the weight and size of the components are of extreme importance. It is, therefore, essential to reduce the weight of these components as much as possible. Table 1 shows the weight distribution of a typical 50 AH $Ni-H_2$ cells. The nickel electrode accounts for 38% of the cell weight.

The heavy-sintered nickel powder plaque has been the substrate of choice for many years to support the electrochemically active material in these nickel-based batteries. The nickel powder plaque accounts for a considerable portion of the weight of the electrodes. Because of this shortcoming, NASA Lewis took the initiative of originating an active program to improve the electrode weight by the use of lightweight plaques. As a result, NASA Lewis is the leader in the lightweight nickel electrode development program.

Earlier electrodes made from porous lightweight plaques had a common feature of exhibiting low initial utilization (1). The use of nickel fiber materials with a small fiber diameter has been shown to reduce this problem. One advantage of using small nickel fibers is the significant increase in the surface area available for deposition of the active material as well as an increase in the electrochemical accessibility to the active material. Superior performance of the small diameter nickel fiber electrode has been demonstrated.

EXPERIMENTAL PROCEDURES

Nickel Fiber Plaques and Electrodes

The nickel electrode consisted of a porous metal substrate, called a plaque, whose pores are partially filled with an electrochemically active material. The variables involved in the plaque design include material type, plaque thickness, porosity (a void fraction), and pore size.

The state-of-the-art (SOA) aerospace nickel electrodes use a sintered and porous nickel powder as the electrode substrate. The sintered plaques are made by either the dry powder (loose powder) process or the wet slurry process. The dry powder process consists of adding loose nickel powder into a nickel grid at elevated temperature (800 to 1000°C) in a reducing atmosphere. In the case of the wet slurry process, a viscous aqueous solution of a binder is added to the loose nickel powder to make a nickel slurry solution. The slurry is added into a nickel grid and sintered at elevated temperature (800 to 1000°C) in a reducing atmosphere. The binder, used in the slurry process, is decomposed in the sintering furnace. Sintering is the process through which a loose mass of nickel particles is transformed into a coherent body without reaching a melting point (2). These sintered nickel powder plaques are very strong and dimensionally stable, but have the disadvantage of being heavy. The weight of nickel-based batteries would be improved by the use of lightweight nickel fiber plaque.

The recent availability of new small fiber nickel materials has made possibly the fabrication of lightweight nickel plaques. Since the sintered nickel powder plaques make up a large portion of the weight of the nickel electrodes, the use of these newly available nickel fiber plaques should decrease the weight significantly. Three nickel fiber plaques used in this development program were developed by Memtec America Corporation (called Memtec), by Ribbon Technology Corporation (called Ribtec) and by Auburn University. These new materials enabled plaques to be made with reduced pore sizes as well as increased surface area, conductivity, strength, and porosity.

The lightweight nickel fibers from Memtec are produced by a proprietary wire drawing and fabric formation technique (3). These fibers have a smaller fiber diameter, smaller pore sizes than the heavy-sintered nickel powder plaque. The Memtec nickel fibers can be prepared with a variety of fiber diameters, thickness, and porosities. Fiber diameters are generally from eight to 15 μm with porosities ranging from 90 to 95% and thicknesses of up to 2 mm. Substrates have been produced in nickel and Hastelloy.

Previously, Ribtec developed a high volume process for producing fine nickel fibers by further processing coarse fiber made directly from its patented molten metal technology. Ribtec micrometal fibers are available in sintered or unsintered mats with thicknesses of up to 3 mm,

porosities of up to 95% and fiber diameter of 20 μm or less.

NASA Lewis also has a grant with Auburn University in Alabama to develop high surface area, low weight composite nickel fiber electrodes (4). The sintered fiber mats were produced using small nickel fibers and cellulose fibers. The nickel fibers have diameters of approximately 2 μm and are 2 to 3 mm in length. The cellulose fibers are 20 to 30 μm in diameter and 100-1000 μm in length.

As mentioned earlier, porosity and thickness are two important variables involved in the evaluation of the nickel plaques. These variables affect the specific energy, performance, and cycle life of the Ni-H_2 cell. One advantage of the lightweight fiber plaques over the SOA heavy-sintered plaque is that the lightweight fiber plaques can easily be manufactured with larger porosities than the SOA plaques. Lightweight plaques are commercially available in porosities up to 98% while commercial SOA sintered plaques are available in porosities of 80 to 85%. The specific energy of a Ni-H_2 cell will increase by replacing the SOA sintered nickel electrode with the highly porous lightweight nickel fiber electrode. For example, the specific energy of a 50 AH Ni-H_2 cells, as shown in figure 1, increases from 88 WH/kg to 100 WH/kg by replacing the nickel electrode made from an 80% porous SOA plaque with the lightweight nickel electrode made from a 98% porous fiber plaque, with the same thickness (1.5 mm) and loading level (1.8 g/cm^3 void volume). The specific energy of the Ni-H_2 cell improves as the values of the variables increase.

In addition, use of thicker nickel electrodes will reduce the required number of electrodes and separators thereby reducing total cell weight. The thicker the plaque, the greater the amount of active material that can be deposited and thus, the greater the initial capacity per unit area and the lower the electrode weight. Highly porous and thick fiber plaques are attractive potential candidates for some lightweight nickel electrodes.

Electrochemical Impregnation

Plaques evaluated from Memtec and Ribtec come in different porosities, thicknesses, and fiber diameters. The plaques are electrochemically impregnated in an aqueous bath at various periods of time and current densities (5). The impregnated plaques are formed by charging and discharging for 20 min at approximately the 3C rate. The formation process serves to remove impurities, which are chiefly nitrates, carried over from the impregnation bath.

The theoretical capacity is calculated from the weight of the active material in the electrode and the electrochemical equivalent of 0.289 AH/g of active material. The active material weight is calculated from the weight gained after the impregnation and formation procedures. The complete procedure for the electrochemical impregnation used in this program is discussed in reference 6.

Electrode Evaluation Testings

The electrodes are life-cycle tested using a low-Earth-orbit regime at 80-percent depth of

discharge (DOD). The percent utilization of the electrode is calculated by using the ratio of the measured capacity to the theoretical calculated capacity. Failure of the electrode is defined as the point where the discharge voltage degrades to -0.2 V against the Hg/HgO reference electrode during the 35-min discharge. Performance testings of the electrode at different discharge rates are conducted before and after the life cycle test.

After the end of life, the cell is disassembled and the components are visually inspected. After a thorough rinsing and drying, the nickel electrode is weighed and the thickness measured.

EXPERIMENTAL RESULTS

Examples of electrochemical impregnation and cycle test results of nickel fiber electrodes are shown in table 2. Active material loading levels of up to 1.8 g/cm^3 void volume were attained during the electrochemical impregnation process. As mentioned before, earlier lightweight nickel fiber electrodes made from a larger nickel fiber diameter (25 μm) have a common feature of exhibiting a low initial utilization which gradually increases with cycling. This shortcoming is not found in nickel electrodes made from smaller diameter nickel fibers (20 μm and less), as can be seen in table 2, with initial utilization in the range of 93 to 108%. Maximum utilization values of more than 100% were readily attainable (percent utilization of more than 100% can be attained since the valence change of the nickel ions during charge and discharge can be greater than one and the percent utilization values in this report are calculated based on a nickel ion valence change of one). More than 800, 2000, and 3000 cycles were reached before reaching the end of life for the Memtec, Auburn, and Ribtec nickel electrodes.

Expansion of the nickel fiber electrode is one of the factors that could affect the performance of the electrode. The thickness of the nickel fiber plaques increased by as much as 25% during impregnation. Additional thickness growth of 30 to 50% occurred after cycling these electrodes as shown in table 2. These expansions, both during impregnation and cycling, are larger than observed in the heavy-sintered SOA nickel electrodes. Our program is designed to address this problem.

The pore size distribution of the uncycled and cycled Memtec and Ribtec nickel electrodes are shown in figures 2 and 3. Cycling of both electrodes increased the total pore volume which is mainly due to the expansion of the electrodes. There is a twofold increase in the volume of the Memtec electrode after it cycled (figure 2). In the case of the Ribtec electrode, as shown in figure 3, the uncycled and cycled electrodes show their respective highest peak at 3 μm and 9 μm with respective incremental volume of 0.024 and 0.027 cm^3/g.

CONCLUSIONS

Improving performance and cycle life as well as increasing the specific energy of the Ni-H_2 system is the main thrust of the technology program at NASA Lewis. One of the ways of achieving these goals is by developing lightweight nickel electrodes.

Initial problems associated with lightweight plaques, such as low loading levels and low initial utilization, have been solved by the use of small diameter nickel fibers. The use of these nickel fibers would result in a significant increase in the surface area available for deposition of active material without a significant reduction in void volume. Superior performance of these nickel fiber electrodes has been demonstrated.

The issue of expansion during impregnation and cycling, resulting in premature electrode failure, needs to be investigated. Heavily loaded (2.0 g/cm^3 void volume) and thicker (1.5 mm) nickel fiber electrodes are currently being evaluated in-house.

REFERENCES

1. "Performance of Lightweight Nickel Electrodes," Britton, D.L., Proceedings of the 33rd International Power Sources Symposium, Cherry Hill, NJ, June 1988, NASA TM 100958.

2. "Alkaline Storage Batteries," Falk, S.U., et al., sponsored by the *Electrochemical Society, Inc.*, copyright 1969 by John Wiley & Sons, Inc., pp. 115-123.

3. "High Energy Density Micro-Fiber Based Nickel Electrode," Coates, D.K., et.al, Proceedings of the 12th International Rechargeable Battery Symposium, Deerfield Beach, Fl, March 1995.

4. "High Surface Area, Low Weight Composite Nickel Fiber Electrodes," Johnson, B.A., et.al., Proceedings of the Space Electrochemical Research and Technology, NASA, Cleveland, OH, April 1993.

5. "Lightweight Fibrous Nickel Electrodes for Nickel-Hydrogen Batteries," Britton, D.L., Fourth Annual Battery Conference on Applications and Advances, Long Beach, CA, 1989, NASA TM 101997.

6. "Progress in the Development of Lightweight Nickel Electrode for Aerospace Applications," Britton, D.L., Proceedings of the Third International Rechargeable Battery Seminar, Deerfield Beach, Fl, 1992, NASA TM 105591.

Table 1. Weight Distribution of a 50 AH Ni-H_2 Cell Using SOA Nickel Electrode.

Components	Weight, g	%
Nickel electrode	513	38
Hydrogen electrode	76	6
Separator	47	4
Electrolyte	206	15
Pressure Vessel	249	19
Miscellaneous	245	18
Total Cell Weight	1336	100

Table 2. Electrochemical Impregnation and Cycle Life Data of the Nickel Fiber Electrodes.

Electrode	Loading Level (g/cm^3)	Init. Util (%)	Max. Util. (%)	Cycles	Expansion (%)	mAh/g
Memtec	1.7	98	103	813	55	189
Ribtec	1.8	108	109	3721	46	198
Auburn	1.8	93	122	2091	30	195

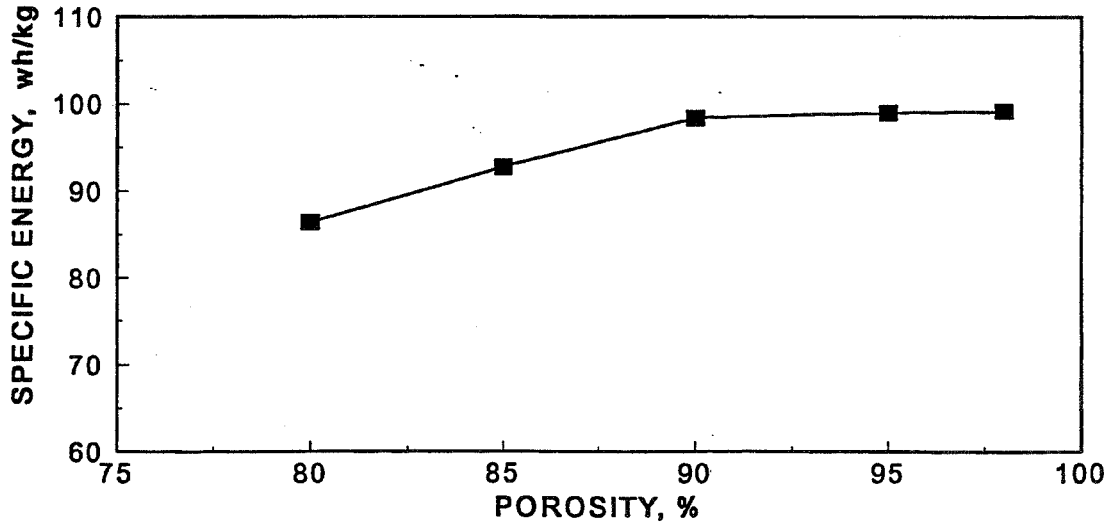

Figure 1. Effect of porosity in a 50 AH Ni-H_2 cell (1.8 g/cm^3 void volume loading level, 1.5 mm thick, 100% utilization).

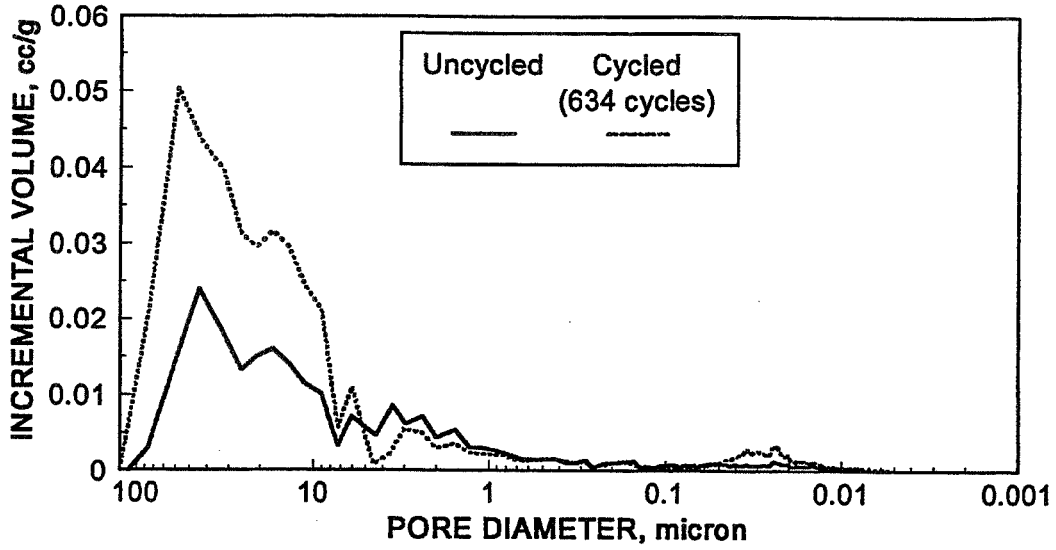

Figure 2. Pore size distribution curves of the uncycled and cycled Memtec nickel fiber electrode.

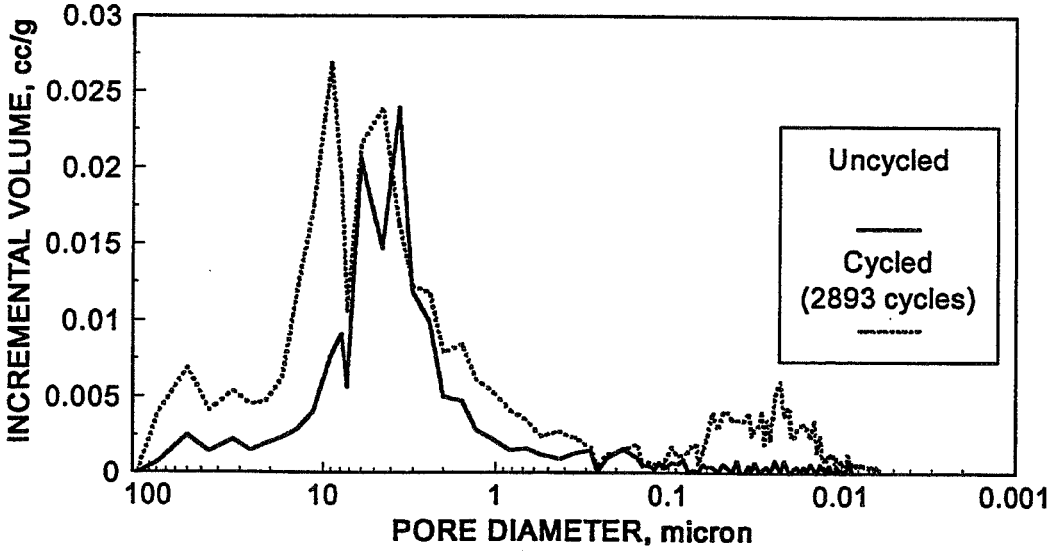

Figure 3. Pore size distribution curves of the uncycled and cycled Ribtec nickel fiber electrode.

Page intentionally left blank

52-44
00880
10P.
2569021

HIGH PERFORMANCE NICKEL ELECTRODES FOR SPACE POWER APPLICATIONS

Prosper K. Adanuvor, Johnnie A. Pearson,
Brian Miller, and Bruce Tatarchuk
Auburn University
Auburn, Alabama

and

Doris L. Britton
NASA Lewis Research Center
Cleveland, Ohio

ABSTRACT

Performance characteristics such as efficiency, specific energy density and power density of nickel electrodes are generally limited by the electrode microstructure and the nature of the active material within the electrode matrix. Progress is being made in our laboratory in a collaborative effort with NASA-Lewis Research Center to develop lighter weight, mechanically stable and highly efficient nickel electrodes for aerospace applications. Our approach is based on an electrode microstructure fabricated from a mixture of nickel fibers as small as 2μm diameter and cellulose fibers. Performance data in flooded cell tests and cycle life data will be presented. Performance characteristics will be compared to other electrode microstructures such as the Fibrex Fiber mat and the Fibrex-Powder substrate. The flexibility of our electrode microstructure and the significant advantages it offers in terms of weight and performance will be demonstrated, in particular its ability to accept charge at high rates and to discharge at high rates.

INTRODUCTION

There is a growing demand in the aerospace industry for reliable nickel batteries with long cycle life and high performance characteristics, combined with a minimum weight and small dimensions. Since the nickel electrode in nickel batteries such as Ni-H_2 and Ni-Cd has been identified as the limiting electrode in terms of performance and weight (1-3), attempts to improve the performance of such battery systems have been focused predominantly on the positive nickel electrode. The major achievements in this endeavor in the past two decades include the development of alternative electrode microstructures such as the nickel foam, nickel plated graphite, nickel felt and fibrous substrates like the Fibrex (™ National Standard) fiber mat, and effective methods of loading and distributing the active material into the electrode matrix (4-9). These alternative microstructures possess the advantage of lower weight, higher porosities and have demonstrated significant performance improvement in several instances (3-4,10). However, work is still progress in an effort to improve the overall performance of these microstructures and it will be some time before they pose a serious threat to the dominance of the sintered powder plaque.

The demand for high performance nickel electrodes in batteries and in other specialized applications has led to the development of a novel type of composite nickel fiber microstructure (11-12) in our laboratory. This microstructure has shown great promise as a current collector matrix for the nickel hydroxide electrode. The main advantages it offers include: relative ease of fabrication using established paper-making techniques and environmentally benign ingredients, significantly lower mass compared to other microstructures because it can be fabricated from fibers as small as 1-2μm in diameter,

high porosities and high surface area. For example, our 2μm diameter nickel fiber composite electrode has a surface area that is an order of magnitude greater than a 20-30μm diameter Fibrex fiber mat electrode. Furthermore, because the fibers are sinter bonded together to form an interlocking net-work of metal fibers, our microstructure has sound structural and mechanical integrity as well as excellent electrical and heat transport characteristics. The flexibility of our electrode microstructure fabrication process makes it posssible to make collectors with adjustable physical properties such as void volume (porosity), thickness, surface area, weight, mechanical strength and electrical conductivity. Collectors with uniform properties can be readily fabricated just as well as collectors with graded or variable characteristics.

The next challenge has been how to introduce the nickel hydroxide active material into this microstructure in a manner that exploits its superior physical characteristics. This has been accomplished by electrochemical impregnation. By carefully controlling and monitoring the impregnation conditions such as temperature, pH, current density, and solution concentration, it has been possible to coat the interlocking network of metal fibers with thin uniform layer of active material. Uniform loadings up to about 2 g/cc void volume have been achieved without significant surface coating or clogging of the void spaces. This uniform loading procedure gives us the capability to design electrodes with properties tailored to a specified mission profile.

The key attributes of our composite fiber electrode are its open architecture which facilitates electrolyte accessibility, uniform distribution of active material on the fibers within the void volume, high surface area which translates to minimum thickness of active material on the fibers and therefore more effective utilization of active material, low heat and electrical resistivity, uniform current distribution along the interlocking network of conducting fibers, and lower weight. It is our contention that these attributes should translate into superior performance of this electrode microstructure.

To test this proposition, a comparative study with other electrode microstructures was conducted. The substrates studied were our nickel fiber composite electrode (henceforth referred to as Auburn composite electrode), the Fibrex fiber mat electrode, and the Fibrex-Powder mat (fiber:powder ratio 80:20) electrode. The study consisted of evaluating the efficiency and other performance characteristics such as power and energy density as a function of the electrode substrate. A parallel study was conducted at NASA-Lewis to evaluate the cycle life of the Auburn composite electrode. Some of these results will also be presented.

EXPERIMENTAL PROCEDURE

Electrode Fabrication

Nickel fibers approximately 2μm in diameter and 1-2mm in length (Memtec, Inc.) were blended with cellulose fibers 20-30μm in diameter to form a paper preform using a procedure described elsewhere (11-14). Circular discs ca. 19mm were cut from the paper preforms. A number of these discs were stacked on top of each other and a strip of nickel foil approximately 1mil x 2mm x 12mm in dimension was inserted in the middle of the stack to a depth of ca. 1-2mm to serve as the current collector tab. The stack was sandwiched between two quartz plates and sintered under a slight compression in a hydrogen reducing atmosphere at approximately 1050°C. Sintering gasifies the cellulose to create the void volume. Simultaneously, the nickel fibers weld together at points of contact to create an intimate interlocking network of conducting metal fibers. A collector matrix ca. 41mil thick and 93% porous was fabricated by

this process. A Fibrex and a Fibrex-Powder collector of approximately the same dimensions as the Auburn composite collector were also fabricated. The Fibrex electrode was made from Fibrex fiber mat consisting of nickel fibers approximately 25μm in diameter, and the Fibrex-Powder electrode was fabricated from a Fibrex powder mat consisting of fibers ca. 20μm in diameter.

All three collectors were impregnated under similar conditions. The composition of the impregnation bath was as follows: 2M $Ni(NO_3)_2.6H_2O$, 0.23M $Co(NO_3)_2.6H_2O$, and 0.10M $NaNO_2$. The initial pH of the bath was 4.0 and the impregnation temperature was maintained at 90°C. The collector to be impregnated was placed in the solution equidistant from two nickel counter electrodes, with the leads of the working and counter electrodes connected to a constant current power supply source. The impregnation was carried out under galvanostatic conditions at a current density of $10mA/cm^2$ per unit collector surface. All three electrodes were loaded to within $1.67\pm0.03g/cm^3$ of the void volume after the impregnation and formation cycles. The physical characteristics of the electrode substrates are presented in Table 1.

Electrode Evaluation Tests

Testing was carried out in a flooded cell consisting of a nickel oxide counter electrode and a Hg/HgO reference electrode. All measurements were carried out at room temperature (24°C) in a 26 wt% KOH solution. All electrodes were first conditioned before commencing performance testing. The conditioning process consisted of cycling the electrode by repeatedly charging and discharging at the C-rate to 20% overcharge and then to 100% depth of discharge. The C-rate for the conditioning cycles was based on the theoretical capacity of the electrode. The theoretical capacity was evaluated from the weight of active material in the electrode after the impregnation/formation process. The utilization during the process was determined by measuring the capacity after every 10 cycles and computing the ratio of the measured capacity to the theoretical capacity. The capacity measurements involved charging at the C/2 rate to 60% overcharge and discharging at the C/2 rate to -0.2V vs Hg/HgO reference electrode. The capacity at the end of the 60th cycle was taken as the standard capacity of the electrode. All subsequent measurements were based on the standard capacities.

Variable discharge measurements were carried out at C/10, C/4, C/2, C, 2C, 4C and 7.5C discharge rates. Charging for all variable discharge measurements was done at the C/2 rate to 40% overcharge. The capacity was determined by discharging at the specified discharge rate to -0.2V vs Hg/HgO reference. After a high discharge rate, a C/4 discharge was performed to ensure that the electrode was fully discharged. In a corresponding manner, measurement of electrode performance as a function of charge rate was conducted at the following charging rates: C/10, C/4, C/2, C, 2C, 4C and 7.5C, to 40% overcharge. By adjusting the charging time accordingly, the total charge input was maintained at 1.4C at each charge rate. The discharge capacities were evaluated by discharging at the C/2 rate to -0.2V vs Hg/HgO reference electrode. All measurements were conducted in duplicate and the averages were used to compute the discharge capacities, charge and discharge efficiencies, and energy and power densities. The average charge or discharge voltage required to evaluate the energy and power characteristics was computed by numerically integrating the area under the charge/discharge curves.

Cycle life testing of the Auburn composite electrode was conducted at NASA-Lewis on the basis of a testing protocol set up by Britton and described elsewhere (3). The results reported here are based on a 20mil thick, 90% porous Auburn composite electrode loaded to about 1.68g/cc void volume.

RESULTS AND DISCUSSION

Performance Evaluation

The results of studies carried out in our laboratory on the impregnation of the Auburn electrode microstructure established the following conditions for obtaining an optimum coating of active material on the fibers: moderate initial pH of impregnation bath, typically 3.5-4.5; high impregnation temperatures, preferably above 70°C; moderately high solution concentration normally about 2.0M $Ni(NO_3)_2.6H_2O$; and low impregnation current density, typically less than $20mA/cm^2$ per unit electrode surface but preferably around $10mA/cm^2$. It has been found that for higher loading levels, tapering off the current density or applying a graded current might reduce the likelihood of clogging of voids and surface deposition. The SEM micrograph in Fig.1 illustrates an ideal impregnation situation. The coating appears as a thin uniform layer on the fibers, without clogging of the void spaces. One of the fibers to the right hand edge was intentionally punctured in order to expose the bare fiber for comparison with the coated fibers. In contrast, the micrograph for the bare sintered but unimpregnated electrode is shown in Fig. 2. The intimate bonding of the fibers at the points of contact, the void space and the interlocking network of conducting fibers are clearly obvious.

Figure 3 is a plot of the utilization versus conditioning cycle. The Auburn composite shows the highest utilization. Also, it approaches its full utilization a lot faster than the Fibrex and the Fibrex-Powder electrodes. Cycle life testing of the Fibrex electrode by Britton (3) showed that it takes hundreds of cycles for the Fibrex to attain its full capacity. The slow utilization rate shown in Figure 3 appears in concert with this trend. The higher utilization of the Fibrex-Powder compared to the Fibrex indicates that addition of small diameter nickel particles to the larger diameter fibers enhances the the utilization and shortens the conditioning time. Figures 4 and 5 are the plots of the charge (Amp-H) and energy (Watts-H) efficiencies at various charging rates. The Auburn composite appears to accept charge better than the Fibrex electrodes, especially at the moderate to high charging rates. In terms of charging efficiency it appears that the best range for charging the fibrous electrode microstructure is between C/2 to 4C, which falls in the quick to fast charge range for the traditional sintered nickel powder electrode. It is apparent from these plots that at the lower charging rates not all the charge or energy input goes into converting the active material into electrochemically usable form. The situation seems to improve considerably at the intermediate charging rates and then drops off again at the higher charging rates. The major factor contributing to the decline in charging efficiency at the higher rates is the competing parasitic oxygen evolution reaction. Higher charging rates lead to higher average charging voltages; the higher voltage makes the oxygen evolution reaction more competitive and the net result is a reduction in the charging efficiency.

Figures 6 and 7 show the variation of specific energy and power density with discharge rate. Again the Auburn composite shows the best performance in terms of energy and power densities, in particular at the moderate to high discharge rates. Compared to the Fibrex electrode, the performance of the Fibrex-powder electrode is superior in terms of specific energy but inferior in terms of power density. The disparity in performance appears to be greater at the higher discharge rates. The capacity discharge curves indicated that at high rates of discharge, the Fibrex-Powder electrode discharged at a much lower voltage than the Fibrex electrode. On the other hand, the Fibrex-Powder electrode showed higher discharge capacities over nearly the whole range of discharge rates. This observation implies that the utilization of the active material is much more efficient in the Fibrex-Powder electrode than in the Fibrex. On the other hand, the conductivity appears to be much better for the Fibrex than for the Fibrex-

Powder. Furthermore, the addition of powder to the Fibrex to make the Fibrex-Powder electrode results in a bulkier electrode. These factors contribute to the differences observed in the energy and power densities for the two electrodes in question.

The excellent performance of the Auburn electrode may be attributed to the efficient utilization of the active material as well as to the superior characteristics of the electrode microstructure. For example, at the higher rates the average voltage for the Auburn electrode was typically less on charge and greater on discharge than the corresponding values for the Fibrex electrodes. This would indicate lower resistivity of the Auburn electrode in relation to the Fibrex electrodes. The more efficient utilization of the active material as well as the better charging and discharging characteristics of the Auburn electrode may be due to the thin layer of active material on the fibers and excellent conductivity of the matrix. Thinner coating translates into shorter transport distances for protons and electrons within the active material and consequently, to more effective utilization of the latter.

Cycle Life

The cycle life data for the Auburn electrode is shown in Fig. 8. This electrode took less than 50 cycles to attain 100% utilization, and about 500 cycles to reach its full utilization of 120%. However, catastrophic failure occurred after about 2000 cycles. A 30 mil thick and 85% porous Fibrex electrode cycled under similar conditions (3) took about 500 cycles to attain 100% utilization, 2000 cycles to reach full utilization and about 2000 more cycles before failure. Fig. 9 depicts the performance of the Auburn electrode at selected cycles in the cycle life profile. The initial utilization and the utilization after 413 cycles follow a similar trend that shows the electrode performing better at the higher discharge rates than at the lower rates. On the other hand, at cycle 2091 when the electrode had already failed, the performance at the lower discharge rates was far better than at the higher rates. What is significant is that at failure, the utilization did not suffer at the lower discharge rate but did so at the moderate to high discharge rates. Even at the high discharge rates, the utilization never fell below the value for the initial utilization at that point. This is in contrast to the case of the Fibrex where at failure the utilizations at the higher potentials fell far below the initial utilization values. This implies that at failure, the Auburn electrode like the Fibrex, retains its low discharge rate capacity but suffers a high discharge rate penalty, although to a lesser degree than the Fibrex.

CONCLUSION

The Auburn electrode displayed the best performance characteristics in terms of efficiency, power and energy density, particularly at high rates of charge or discharge. However, the cycle life of the Auburn electrode was only about half that reported for the Fibrex electrode (3). The performance of the Fibrex-Powder electrode was in general superior to that of the Fibrex electrode. This confirms that incorporating smaller diameter nickel particles or fibers into the matrix of the larger fibers can enhance the performance at the risk of increasing the weight of the electrode. The longer cycle life of the Fibrex electrode with the larger fibers and the excellent performance characteristics of the Auburn electrode with much smaller fibers indicate that it should be possible to combine the desirable qualities of smaller and larger diameter fibers to design an optimum nickel electrode for a specified mission profile. The flexibility and versatility of our electrode fabrication protocol should facilitate this process.

ACKNOWLEDGEMENT

This project was funded by NASA-Lewis Research Center, Electrochemical Technology Branch, Contract #NAS-NAG3-1154 under the auspices of the Auburn University Space Power Institute. The authors would like to acknowledge the contributions of Richard Ferro, Bradley Johnson, and Greg Swain to the initial phase of this project.

REFERENCES

1) W.R. Scott and D. W. Rusta, "Sealed Nickel-Cadmium Batteries Applications Manual", NASA Reference Publication #1052, (1979).

2) J. D. Dunlop and J. F. Stockel, *Proc. 15th IECEC Conference*, p. 1878, (1980).

3) D. L Britton in Nickel Hydroxide Electrodes, D. Corringan and A. Zimmerman, Ed., p. 234, Electrochemical Society, Inc. , Pennington, New Jersey (1990).

4) G. Crespy, R. Schmitt, M. Gutjahr and H. Saufferer, Power Sources 7, p. 219, Ed., J. Thompson, Academic Press (1979).

5) W. A. Ferrando and R. A. Satula, U.S. Patent # 4,215,190, (1980).

6) J. F. Joyce, U.S. Patent # 4,298,383, (1981).

7) S. L. Colucci, U.S. Patent # 4,312,670, (1982).

8) B. Bugnet and D. Doniat, *Proc. of the 31st Power Sources Symposium*, p. 171, Cherry Hill, New Jersey, (1984).

9) H. N Seiger and V. J. Puglisi, *Proc. of the 27th Power Sources Conference*, p. 115, (1976).

10) D. L. Britton, *Proc. of the 34th Power Sources Symposium*, p. 235, (1990).

11) B. Tatarchuk et al. U.S. Patent #5,080,963, Jan. 1992.

12) B. Tatarchuk et al. U.S. Patent # 5,102,745, April 1992.

13) D. Kohler, J. Zabasajja, A. Krishnagoplan, and B. Tatarchuk. *J. Electrochem. Soc.*, **137**, 136 (1990).

14) D. Kohler, J. Zabasajja, F. Rose, and B. Tatarchuk. *J. Electrochem. Soc.*, **137**, 1750 (1990).

Figure 1 - SEM micrograph of an impregnated nickel fiber composite electrode. Fiber diameter 2 μm.

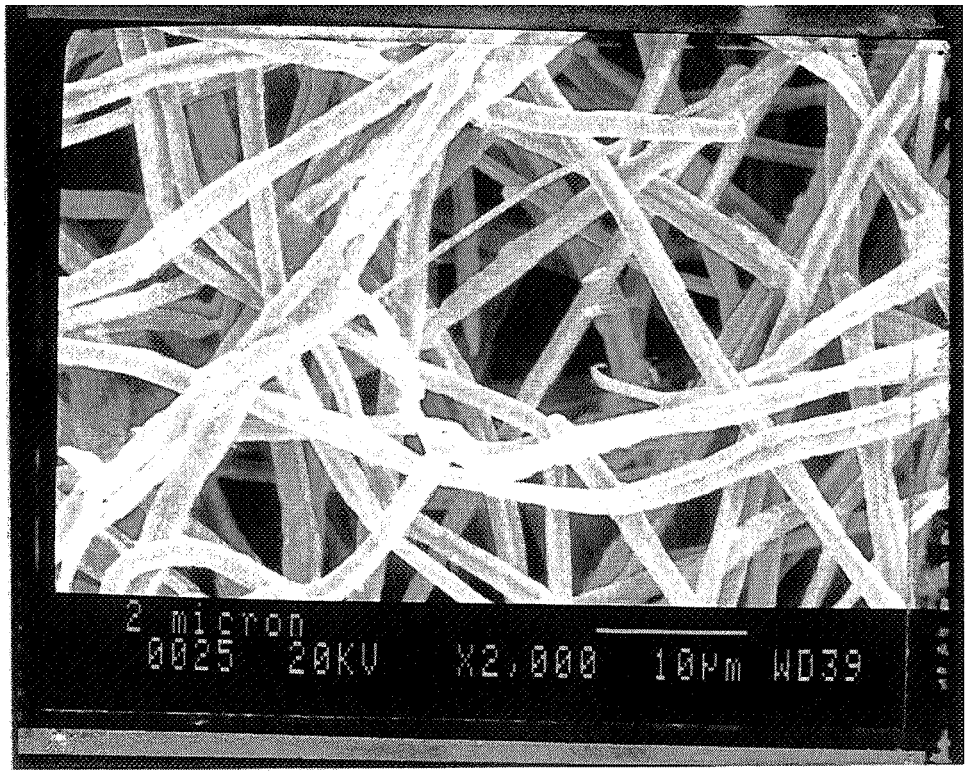

Figure 2 - SEM micrograph of unimpregnated nickel fiber composite electrode. Fiber diameter 2 μm

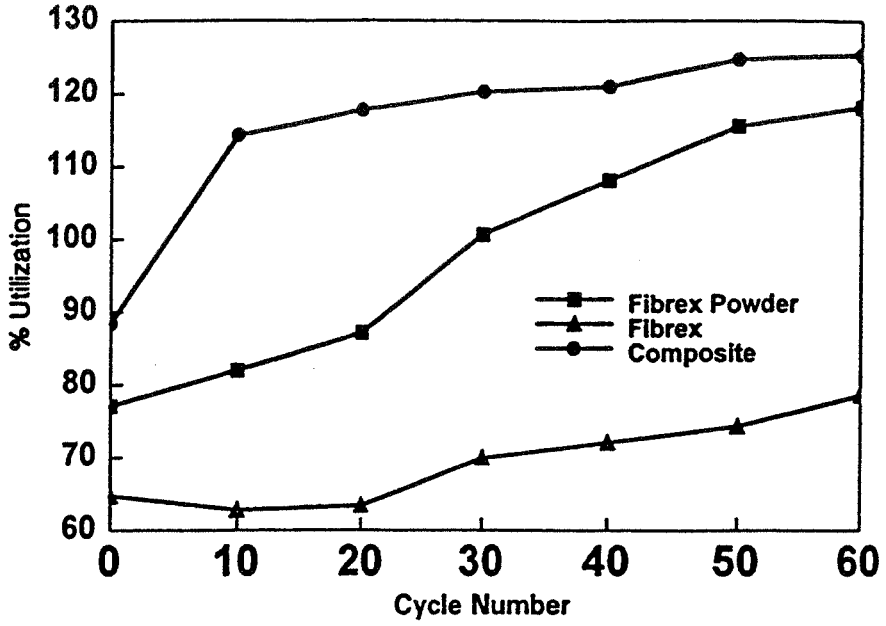

Fig. 3 - Conditioning Cycles for electrode microstructures

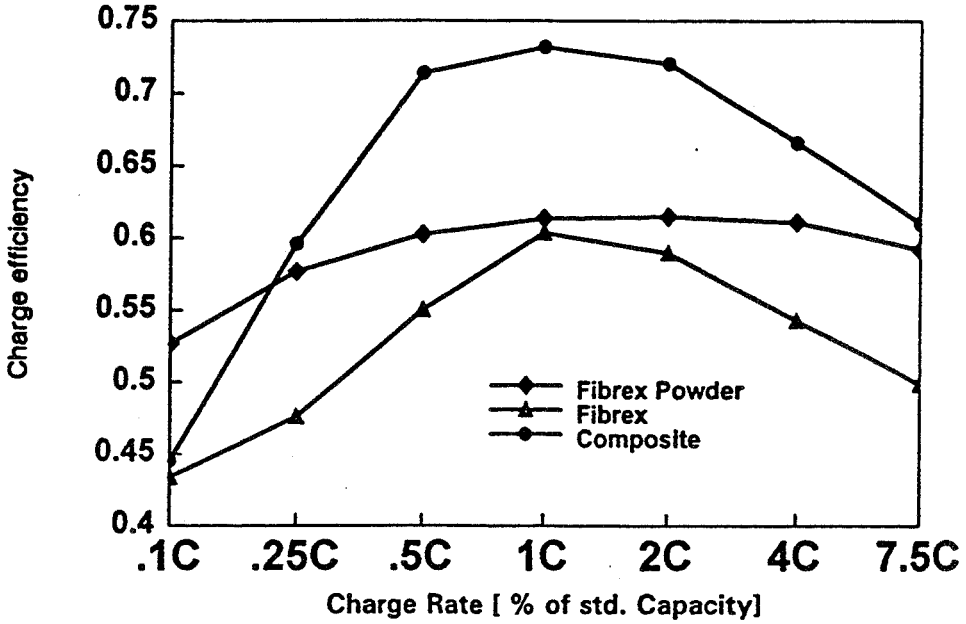

Fig. 4 - Charge (amp-hr.) Efficiency as a function of charge rate

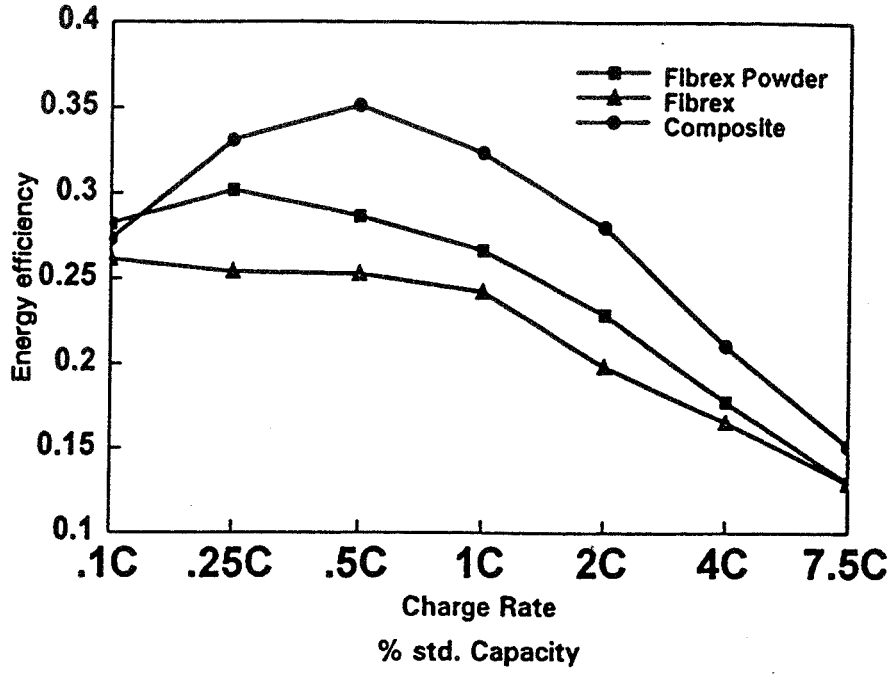

Fig. 5 - Energy (Watt-hr.) Efficiency as a function of charge rate.

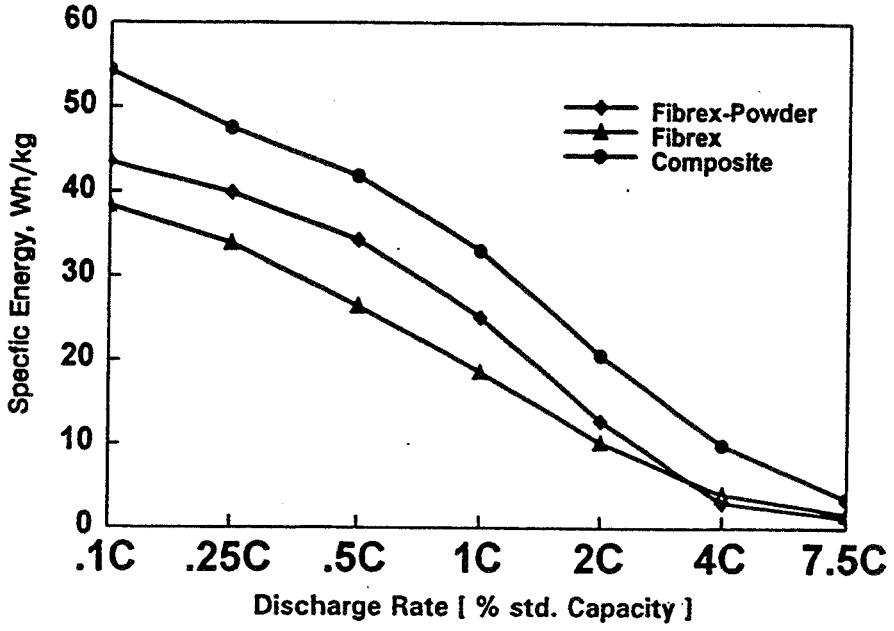

Fig. 6 Specific energy as a function discharge rate.

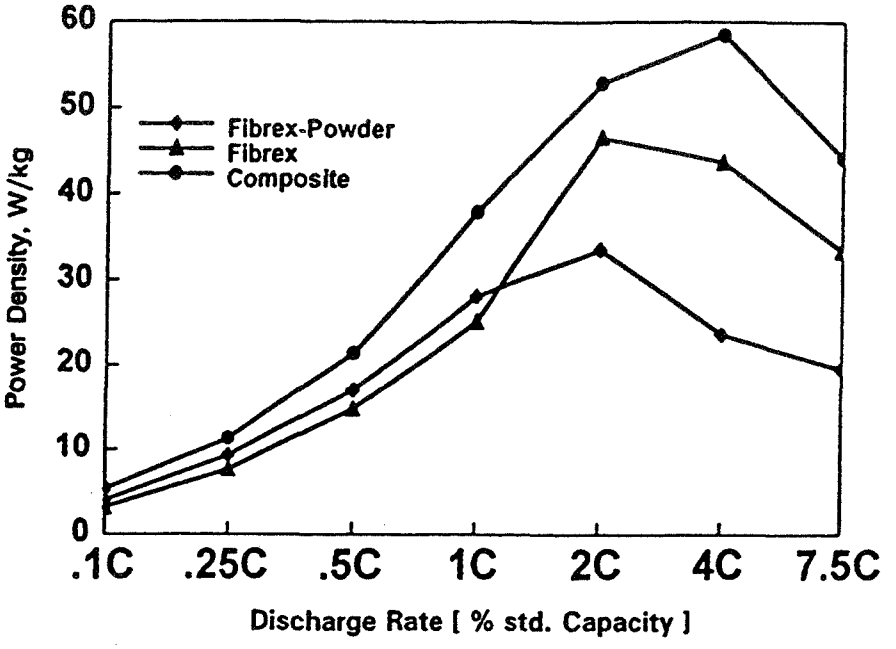

Fig. 7 Power Density as a function of discharge rate

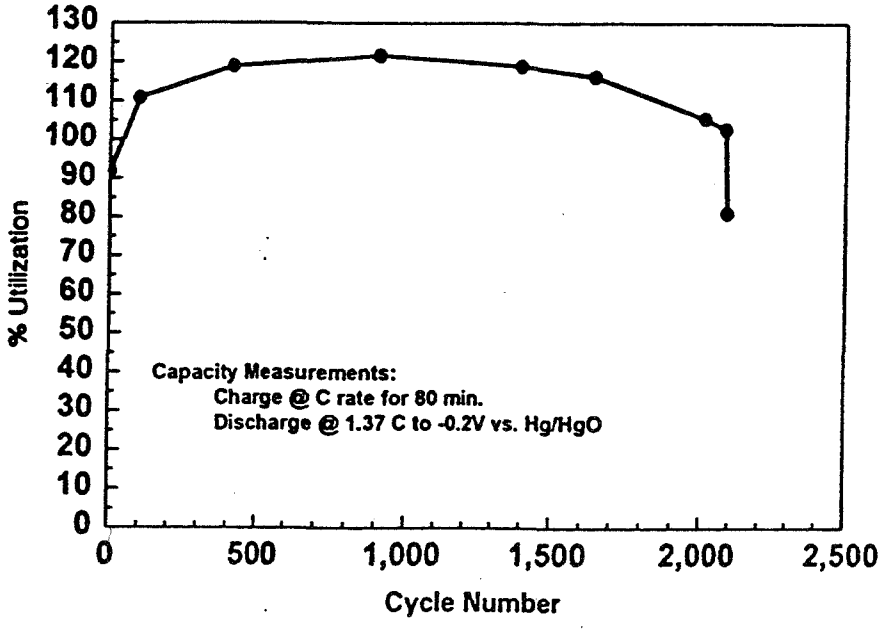

Fig 8 Life Cycle Testing of Composite Electrode

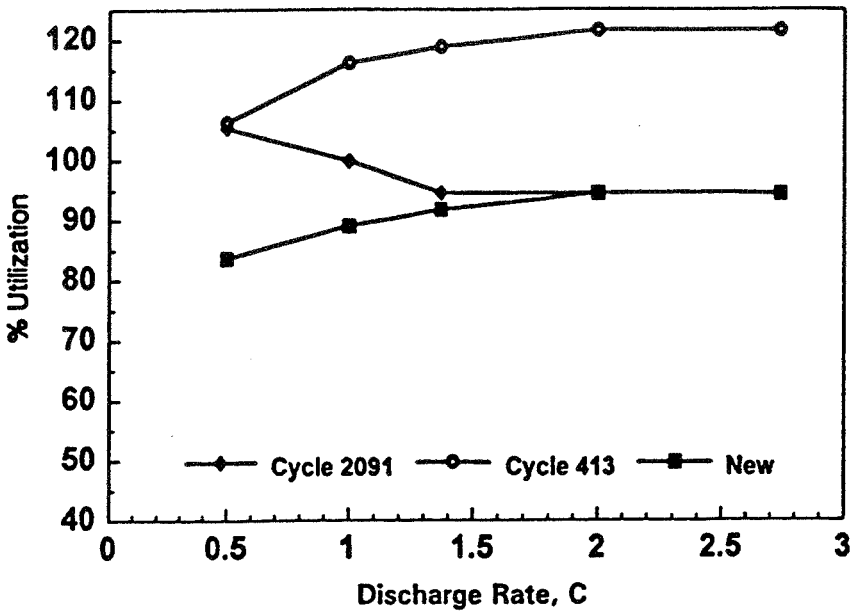

Fig. 9 Performance data of composite electrode at selected intervals during life cycle testing.

Page intentionally left blank

53-44
008541

BENDING PROPERTIES OF NICKEL ELECTRODES FOR NICKEL-HYDROGEN BATTERIES

Brad A. Lerch and Richard M. Wilson
NASA Lewis Research Center
Cleveland, Ohio

056908
18p.

Dennis Keller
Real World Quality Systems, Inc.
Rocky River, Ohio

and

Ralph Corner
NYMA, Inc.
Brook Park, Ohio

SUMMARY

Recent changes in manufacturing have resulted in nickel-hydrogen batteries that fail prematurely by electrical shorting. This failure is believed to be a result of a blistering problem in the nickel electrodes. In this study the bending properties of nickel electrodes are investigated in an attempt to correlate the bending properties of the electrode with its propensity to blister. Nickel electrodes from three different batches of material were tested in both the as-received and impregnated forms. The effects of specimen curvature and position within the electrode on the bending strength were studied, and within-electrode and batch-to-batch variations were addressed. Bend strength was found to increase with the amount of surface loading.

INTRODUCTION

Nickel-hydrogen batteries are used to store energy in satellites. Future plans are to use them in the International Space Station Alpha. The batteries consist of alternate nickel and hydrogen electrodes, gas screens, and a separator sandwiched around a central core in a pressure vessel container. The nickel electrodes, which are manufactured by sintering nickel powder onto a nickel-wire mesh, are porous structures (approximately 80-percent porosity), with a typical cross section as shown in figure 1. The sintered electrode is electrochemically impregnated with active nickel hydroxide ($Ni(OH)_2$). Recent changes in manufacturing have resulted in Ni electrodes that "blister" during service. After a blister forms, it subsequently spalls, sometimes reaching the hydrogen electrode and shorting the electrode stack. The blistering is believed to occur because the electrodes were sintered too long and a more continuous, fused layer of nickel (i.e., less porous) was formed near the surfaces of the electrodes. This layer restricts the $Ni(OH)_2$ from penetrating the full thickness of the electrode during impregnation, and thus, the $Ni(OH)_2$ is concentrated near the surface. This is called surface loading. Surface loading

can contribute to a number of undesirable events such as lowering the active material utilization and the ampere-hour capability; trapping the acidic impregnation solution in the electrode pores, which causes additional corrosion of the nickel-wire mesh support structure and thus further weakens the sinter; and generating oxygen at the nickel electrode during overcharging. In the latter case, as oxygen gas is generated within the electrode, surface loading is believed to prevent the gas from escaping. The gas pressure builds internally, pushing on the contiguous, surface-loaded layer until blistering occurs.

The surface-loaded layer, being more dense than the rest of the electrode, should be stronger than the more porous layers in a "good" electrode. A bend test, which concentrates the applied stresses in the surface layers, may be useful in differentiating between electrodes with and without surface loading. If bending strength, or some other mechanical property, could be correlated with surface loading, such a test could be used in quality control, allowing only electrodes with a minimum propensity to blister to be put into service. Bend tests may also be useful in monitoring electrode or batch uniformity, providing a quality control check on the manufacturing process. The study reported herein was meant to be a first-cut investigation into the bending properties of Ni electrodes and to provide a basis for follow-on studies.

MATERIAL

Three batches of Ni electrodes were supplied in both the as-sintered and impregnated forms. These batches represent electrodes (1) from a baseline design (batch B); (2) from an improved design (batch A); and (3) from an optimized manufacturing process that produced a more uniformly sintered product (batch C). Three electrodes per batch were tested. As-sintered electrodes were flat squares as shown in figure 2, parts (a) to (c). The impregnated electrodes were flat rounds (fig. 2(d)).

Specimens were taken from the electrodes as indicated in figure 2. The specimens were thin strips, nominally 7 mm wide by 70 mm long by 0.78 mm thick. A razor blade was used to cut the specimens from the electrodes, with the long axis of the specimen parallel to one set of wires in the Ni-wire mesh. Ten samples were sectioned from as-sintered electrode s/n 100 (serial number 100) of batch A. Usually, four specimens were sectioned from each of the other electrodes. The test matrix is shown in figure 3.

THREE-POINT BEND TESTS

Three-point bend tests were run according to ASTM Standard E855—"Bend Testing of Metallic Flat Materials for Spring Applications Involving Static Loading." It should be noted, however, that the specimen dimensions did not comply with the standard, but we were limited by the physical dimensions of the electrodes. Also, an existing three-point bend

fixture, which was used for the tests, possessed 4.7-mm-diameter rollers for the contact support points and load applicator rather than the knife edges recommended in the standard. A 40-mm span was employed in the bend tests; a schematic of the test fixture is shown in figure 4. Specimen deflection at midspan was inferred from machine crosshead displacement, with no correction for the stiffness of the load frame. We believed that no corrections were needed because the stiffness of the specimens was much less than that of the load frame. The bend tests were run at a constant crosshead displacement of 0.05 in./min. Load-displacement diagrams were plotted for each specimen, and the following data were calculated from these curves: elastic modulus E_b; displacement at maximum load δ_p; and bending strength σ_p. These quantities are indicated in a typical load-displacement diagram in figure 5. The elastic modulus was obtained by determining the slope of the straight portion of the curve (i.e., the initial load-displacement points) and using the following equation:

$$E_b = PL^3/4bh^3\delta \tag{1}$$

where

- P load increment
- L span length between supports (40 mm)
- b specimen width (nominally 7 mm)
- h specimen thickness (nominally 0.78 mm)
- δ deflection at midspan

The maximum bending strength was obtained as follows:

$$\sigma_p^1 = 1.5P_pL/bh^2 \tag{2}$$

where P_p is the maximum load.

Equation (2) is derived from plate theory; however, the specimens used in this study are better represented by beams. The maximum bending strength from beam theory is given by

$$\sigma_p^2 = 2P_pL/bh^2 \tag{3}$$

Equation (3) is not given in ASTM Standard E855.

Both the beam theory and plate theory values for maximum bending strength are listed in tables I and II, along with the elastic modulus and the displacement at maximum load. Since equations (2) and (3) differ only by a constant, we

arbitrarily decided to use the results from equation (2) in subsequent analyses. Only the absolute values, not the trends, were changed by using values from equation (3).

RESULTS

The two curves plotted in figure 6 show a large difference between the bending behavior of the as-sintered and impregnated electrodes. The as-sintered samples were significantly less stiff and were weaker than the impregnated samples. In addition, the impregnated samples reach their maximum strength at a lower displacement δ_p. The mean values of bending strength and initial modulus are summarized in table III.

Several analyses of variance were performed on the bending strengths (as calculated by eq.(2)) to investigate the effect of different factors and components on the variance. The following sections address these analyses.

Effect of Specimen Curvature

After the specimen was cut from the electrode, the specimen was left with a slight curvature along its length (similar to that shown in fig. 4). To check if the curvature had an effect on the bending strength, five specimens from electrode s/n 100 (batch A, as-sintered) were tested in the curve-up position, and the other five in the curve-down position. Statistical analysis indicated that there was no significant difference between the curve-up and curve-down configurations. For convenience, all of the remaining specimens in this study were tested in the curve-down position (as shown in fig. 4).

Effect of Specimen Position Within the Electrode

Hanging electrodes were impregnated in an electrolytic bath, the design of which made it possible for the bottom of the electrode to be more heavily impregnated than the top. Thus, a positional difference may have been manifested in the resulting bend strengths. To test this hypothesis, two specimens were taken from the top and two from the bottom of each electrode (fig. 2). The mean bending strengths are given on a per batch basis in table IV. Statistical analysis of the data showed no significant strength difference between the top and bottom of the as-sintered batch A electrodes. The other two batches (batches B and C), however, were found to have small, but statistically significant, differences in strength between the top and the bottom in the as-sintered condition: the bottom was stronger. The small differences in bend strength could be detected because of good test-to-test reproducibility (see $S_{specimen}$ in table IV). After impregnation, the bending strengths of specimens taken from the bottom of the electrodes were often higher than those taken from the top. However, there was no statistically significant strength difference between the top and bottom of the electrode for any of the three batches. The inability to detect statistically significant positional differences in the impregnated electrodes was due to the large increase in test-to-test variation (see $S_{specimen}$ in table IV).

Figure 7 is a micrograph taken from batch A impregnated electrode s/n 202. Figure 7(a) shows a specimen taken from the top of the electrode (bend specimen #21), and figure 7(b) shows one from the bottom of the electrode (bend specimen #23). There is a much more uniform distribution of $Ni(OH)_2$ in the top of the electrode (fig. 7(a)) compared to the bottom (fig. 7(b)), where the $Ni(OH)_2$ is concentrated near the electrode surfaces (i.e., surface loading). This concentration of $Ni(OH)_2$ is believed to have strengthened specimens taken from the bottom of the electrode, as evidenced by the higher bending strength of specimen #23 (16.9 MPa) compared to specimen #21 (14.5 MPa) in batch A. Surface loading in the micrographs is difficult to observe by the black and white images shown in figure 7. There have been two color imaging techniques developed to aid in the identification of the various phases within the electrode. These techniques are described in ref. 1. Color micrographs are also shown in ref. 1, but they could not be reproduced in this article.

Strength Variation

This section addresses the bending strength variation in the electrodes.

Variation level 1: Within electrode.—*Within* a given electrode, the 95-percent confidence variations about the mean were

As-sintered: $\pm$ 1.95 MPa

Impregnated: $\pm$ 6.30 MPa

These numbers include positional (i.e., top-to-bottom) and test-to-test variation.

Variation level 2: Within batch.—Significant electrode-to-electrode variation within a batch was discernible over and above the within-electrode variation. The within-batch 95-percent confidence variations about the mean were

As-sintered: $\pm$ 2.45 MPa

Impregnated: $\pm$ 7.99 MPa

These numbers include electrode-to-electrode, positional (i.e., top to bottom), and test-to-test variation. These values, therefore, represent the variation that can be expected by testing a random electrode in the future.

Differences in Mean Bending Strength Among Batches

At the 99.9-percent confidence level, statistical analysis showed significant differences among the mean bending strengths of the as-sintered electrodes in the batches (table III): from strongest to weakest they were batch B, batch C, and batch A. This difference, however, was moderated by impregnation. After impregnation, only batch B had a marginally

significant (90-percent confidence) strength increase over batch A, and batch C was not significantly different from either batch A or B. This moderation was due to the larger within-batch variation in the impregnated material.

DISCUSSION

Nickel electrodes were subjected to three-point bend tests in an effort to determine relative amounts of surface loading and the subsequent propensity of the electrodes to blister during service. Figure 7 shows that there is a relationship between the bending strength and the amount of surface loading: the more surface loading, the higher the bend strength. This figure also explains why batch A impregnated electrode s/n 202 had a lower strength (and stiffness[1]) than the other electrodes in this batch; that is, it had less surface loading. Therefore, bend tests can be used as a screening test for surface loading.

The amount of surface loading within the electrode varies (at least in batch A), as evidenced in figure 7. This is believed to be due to various factors in the electrolytic impregnation setup. Further investigation into the specific impregnation process is required to remedy the nonuniformity between the top and bottom of the electrodes. Although this difference is manifested in the mechanical properties, the effects of this nonuniformity on the electrical properties have not been determined.

The initial theory attributing surface loading to over-sintering and the formation of a continuous, fused layer of Ni powder on the surfaces does not appear to hold. In figure 1 the Ni powder appears to be distributed uniformly in both as-sintered and impregnated electrodes for all the batches. Furthermore, the Ni-powder particles are reasonably isolated from one another. Therefore, another explanation of the cause of surface loading is required. No connection has been proven in this study between the amount of surface loading and the propensity of the electrodes to blister. However, it should be pointed out that all of the batches showed surface loading, and all of the batches blistered when tested in the recirculating stack design.[2] This connection, if there is one, needs further study. It is interesting to note that the Ni-wire mesh is not wetted by the $Ni(OH)_2$, and this could play a role in the blistering process.

It has been industrial practice to bend test as-sintered electrodes for quality control purposes. This study has shown that the impregnation process results in a substantial change in both the mean bending strength (and stiffness) as well as the variability in strength. In addition, as shown by batch A, uniform as-sintered electrodes can develop nonuniformities (i.e.,

---

[1]Although stiffness was not thoroughly examined, it is believed to follow trends similar to the bend strength.

[2]In this design the positive and negative electrodes alternate position in the electrode stack (i.e., +/-/+/-).

increased within-electrode variation) during impregnation. Therefore, testing as-sintered electrodes is not recommended as a predictor of electrode behavior because the electrode properties change drastically after impregnation.

SUMMARY AND CONCLUSIONS

Three-point bend tests were performed on three differently processed batches of both as-sintered and impregnated electrodes. Our findings were as follows:

1. The impregnated electrodes were stiffer and stronger than the as-sintered electrodes.

2. In batches B and C, there were small, but statistically significant, differences in bend strength between specimens taken from the top and the bottom of the as-sintered electrodes. The large variation amongst the impregnated specimens statistically obscured any positional differences in bending strength.

3. Bend tests can be used to determine relative amounts of surface loading; the more surface loading, the higher the bend strength.

4. Bend testing of as-sintered electrodes is not recommended as a predictor of electrode behavior since the properties drastically changed after impregnation.

ACKNOWLEDGMENT

The authors thank Ralph Pawlik for his assistance with the experiments.

REFERENCE

1. B.A. Lerch, R.M. Wilson, D. Keller and R. Corner: Bending Properties of Nickel Electrodes for Nickel-Hydrogen Batteries. NASA TM–106756, January 1995.

TABLE I.—BEND TEST RESULTS OF AS-SINTERED SPACE STATION BATTERY ELECTRODES

Serial number	Specimen number	Displacement at maximum load, δ_p, mm	Elastic modulus, E_b, MPa	Maximum bending strength, MPa		Curvature	Figure
				Plate theory, σ_p^1, MPa	Beam theory, σ_p^2, MPa		
Batch A (84-percent porosity)							
100	1	3.34	1155	5.74	7.65	Down	2(a)
	2	4.02	1279	6.42	8.55	Up	
	3	3.51	1622	7.44	9.91	Down	
	4	5.29	1635	8.32	11.10	Up	
	5	2.58	1879	7.14	9.52	Down	
	6	3.60	1492	7.07	9.42	Up	
	7	3.55	1497	6.95	9.27	Down	
	8	4.02	1354	7.11	9.48	Up	
	9	3.30	1708	7.35	9.80	Down	
	10	3.81	1230	6.39	8.51	Up	
101	11	2.96	991	4.86	6.47	Down	2(c)
	12	3.47	1074	5.06	6.74		
	(12B)	3.30	1244	5.72	7.63		
	13	3.50	1141	5.51	7.35		
	14	2.88	1164	5.04	6.72		
102	21	3.38	1074	5.47	7.29		
	22	3.26	1115	5.38	7.17		
	(22B)	2.96	1139	5.23	6.97		
	23	2.88	1171	5.40	7.19		
	24	3.26	1202	5.80	7.74		
Batch B (81-percent porosity)							
110	1	3.47	2356	8.96	11.95	Down	2(b)
	2	3.13	2253	9.85	13.13		
	3	3.85	2565	9.90	13.19		
	4	3.09	2727	10.32	13.76		
111	11	2.03	2302	8.08	10.77		
	12	2.54	2705	9.47	12.61		
	13	3.13	3295	12.02	16.02		
	14	2.71	1917	10.32	13.75		
112	21	2.54	2529	9.40	12.53		
	22	3.00	2475	9.84	13.12		
	23	3.38	1968	9.56	12.75		
	24	(a)	(a)	10.64	14.19		
Batch C (optimized plaque; 81-percent porosity)							
120	1	3.64	1524	7.08	9.43	Down	2(c)
	2	3.64	1510	7.25	9.66		
	(2B)	3.51	1405	6.52	8.69		
	3	3.89	1577	7.79	10.39		
	4	3.93	1554	7.96	10.62		
121	11	3.30	1628	7.44	9.92		
	12	3.81	1759	7.87	10.49		
	13	4.53	1799	8.71	11.62		
	14	3.55	1583	7.90	10.53		
122	21	3.17	1839	7.59	10.12		
	22	2.41	1750	7.77	10.36		
	23	3.72	1826	8.44	11.25		
	24	4.36	2056	9.87	13.15		

[a]No data—recorder error.

TABLE II.—BEND TEST RESULTS OF IMPREGNATED SPACE STATION BATTERY ELECTRODES

Serial number	Specimen number	Displacement at maximum load, δ_p, mm	Elastic modulus, E_b, MPa	Maximum bending strength, MPa		Curvature	Figure
				Plate theory, σ_p^1, MPa	Beam theory, σ_p^2, MPa		
Batch A (84-percent porosity)							
200	1	0.97	7 772	17.15	22.86	Down	2(d)
	2	.93	8 535	19.76	26.35		
	3	1.14	9 448	22.12	29.49		
	4	1.10	12 165	25.35	33.80		
201	11	1.57	10 068	24.66	32.88		
	12	1.27	11 869	21.69	28.91		
	13	.85	13 096	20.47	27.29		
	14	.85	13 454	20.85	27.79		
202	21	1.48	5 470	14.53	19.37		
	22	1.57	5 153	14.71	19.61		
	23	1.31	6 252	16.88	22.50		
	24	1.52	7 985	17.18	22.91		
Batch B (81-percent porosity)							
210	1	1.86	6 998	21.36	28.47	Down	2(d)
	2	2.16	7 714	25.54	34.05		
	3	2.28	7 320	28.26	37.67		
	4	1.69	7 025	21.96	29.27		
211	11	1.99	6 975	22.30	29.73		
	12	1.86	9 180	23.84	31.78		
	13	1.95	8 869	25.98	34.64		
	14	1.86	7 509	23.98	31.98		
212	21	1.65	11 171	20.34	27.11		
	22	1.61	9 989	25.72	34.28		
	23	1.52	10 674	26.15	34.86		
	24	1.86	8 725	29.13	38.83		
Batch C (optimized plaque; 81-percent porosity)							
220	1	1.02	7 724	16.3	21.7	Down	2(d)
	2	1.44	11 533	22.3	29.7		
	3	——	9 999	——	——		
	4	5.84	9 779	22.9	30.5		
221	11	1.10	10 718	20.7	27.6		
	12	1.27	13 042	26.4	35.2		
	13	1.06	11 113	20.1	26.8		
	14	1.06	15 373	24.7	32.9		
222	21	——	——	20.4	27.2		
	22	1.23	10 351	19.3	25.6		
	23	1.57	9 461	22.2	29.6		
	24	1.27	8 026	18.7	25.0		

TABLE III.—MEAN VALUES OF BENDING STRENGTH AND MODULUS

	Mean bending strength, MPa	Mean elastic modulus, MPa
As-sintered electrodes		
Total	7.9	1 789
Batch A	5.9	1 253
Electrode 100	6.9	1 496
101	5.2	1 123
102	5.5	1 140
Batch B	9.9	2 422
Electrode 110	9.8	2 476
111	10.0	2 555
112	9.9	2 236
Batch C	7.9	1 692
Electrode 120	7.3	1 514
121	8.0	1 693
122	8.4	1 868
Inpregnated electrodes		
Total	21.8	9 469
Batch A	19.6	9 273
Electrode 200	21.1	9 480
201	21.9	12 122
202	15.8	6 216
Batch B	24.5	8 511
Electrode 210	24.3	7 265
211	24.0	8 133
212	25.3	10 134
Batch C	21.4	10 623
Electrode 220	21.1	9 759
221	23.0	12 562
222	20.2	9 547

TABLE IV.—MEAN BENDING STRENGTH AS A FUNCTION OF POSITION IN THE ELECTRODE

	Mean bending strength, MPa		
	Batch A	Batch B	Batch C
As-sintered			
Top	5.96	9.27	7.36
Bottom	6.38	10.46	8.45
[a]$S_{specimen}$	.48	.85	.49
Impregnated			
Top	18.75	23.18	20.90
Bottom	20.48	25.91	21.72
[a]$S_{specimen}$	1.48	2.65	2.81

[a]Standard deviation among repeat tests within a position.

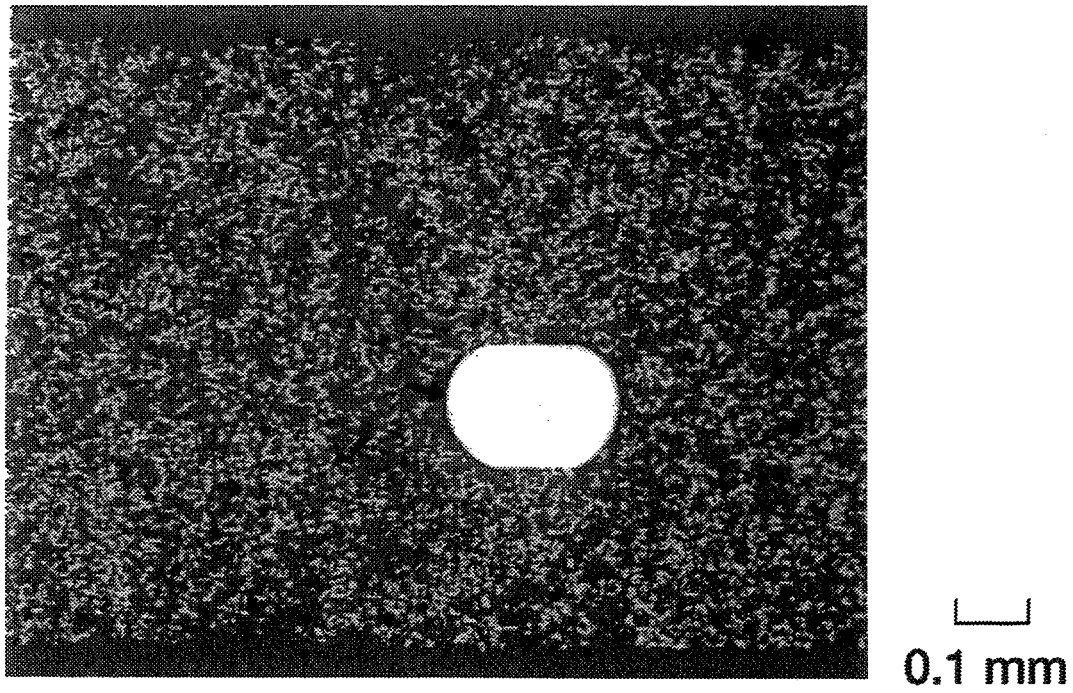

Figure 1.—Electrode cross-section (arrow indicates Ni-wire mesh), as-sintered

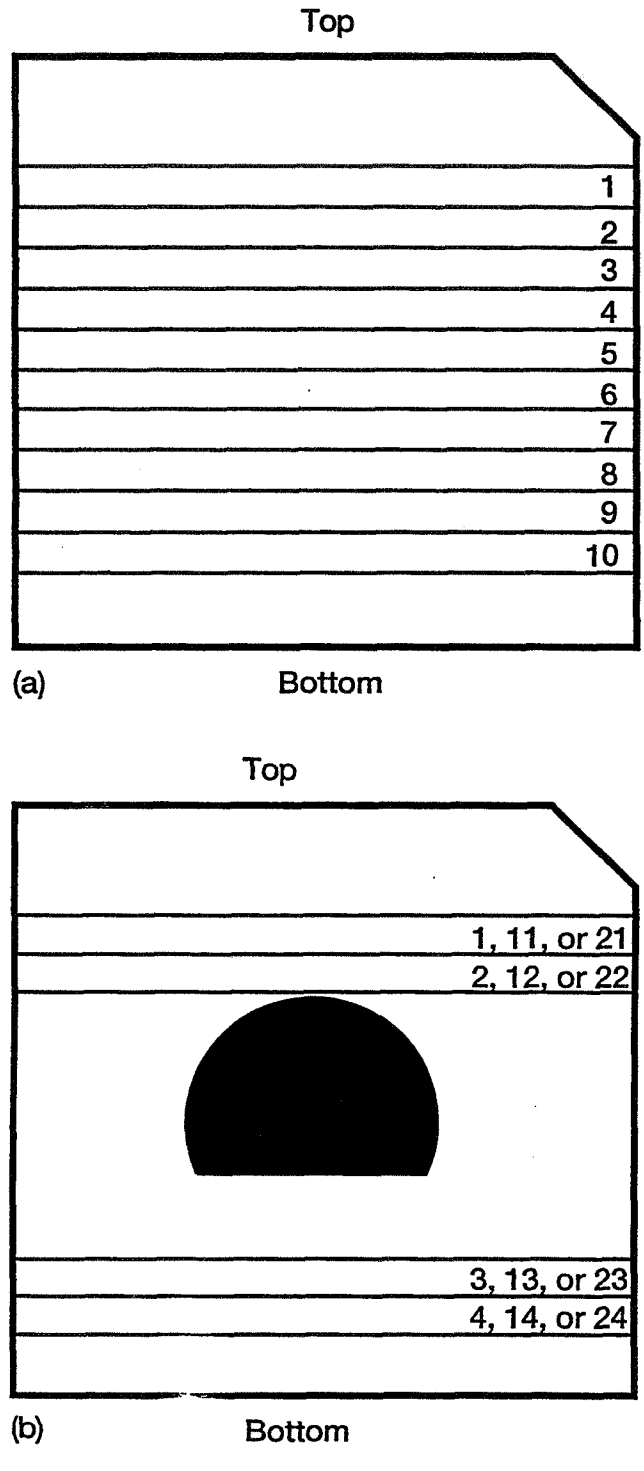

Figure 2.—Specimen location in electrodes. (a) to (c) As-sintered specimens. (d) Impregnated electrode specimens.

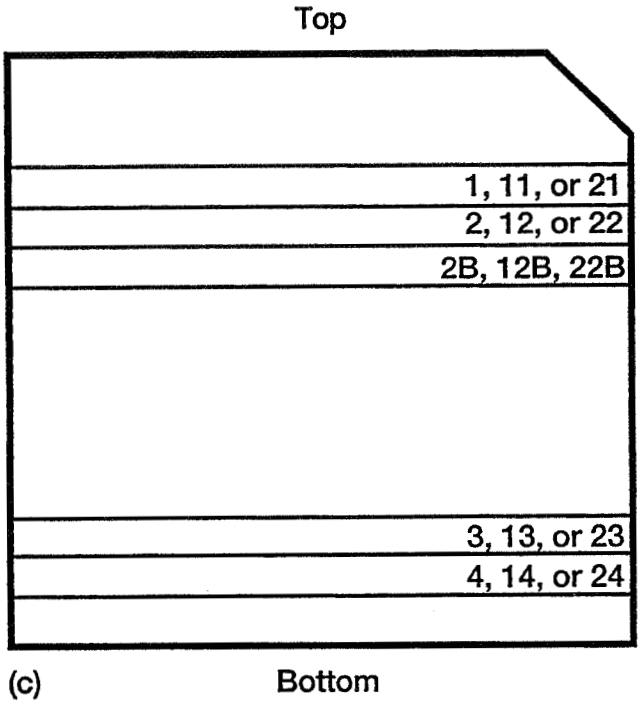

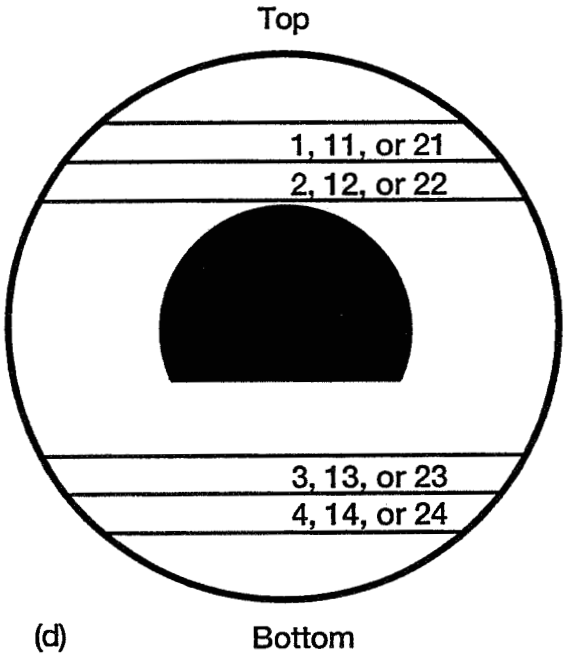

Figure 2.—Specimen location in electrodes. (a) to (c) As-sintered specimens. (d) Impregnated electrode specimens.

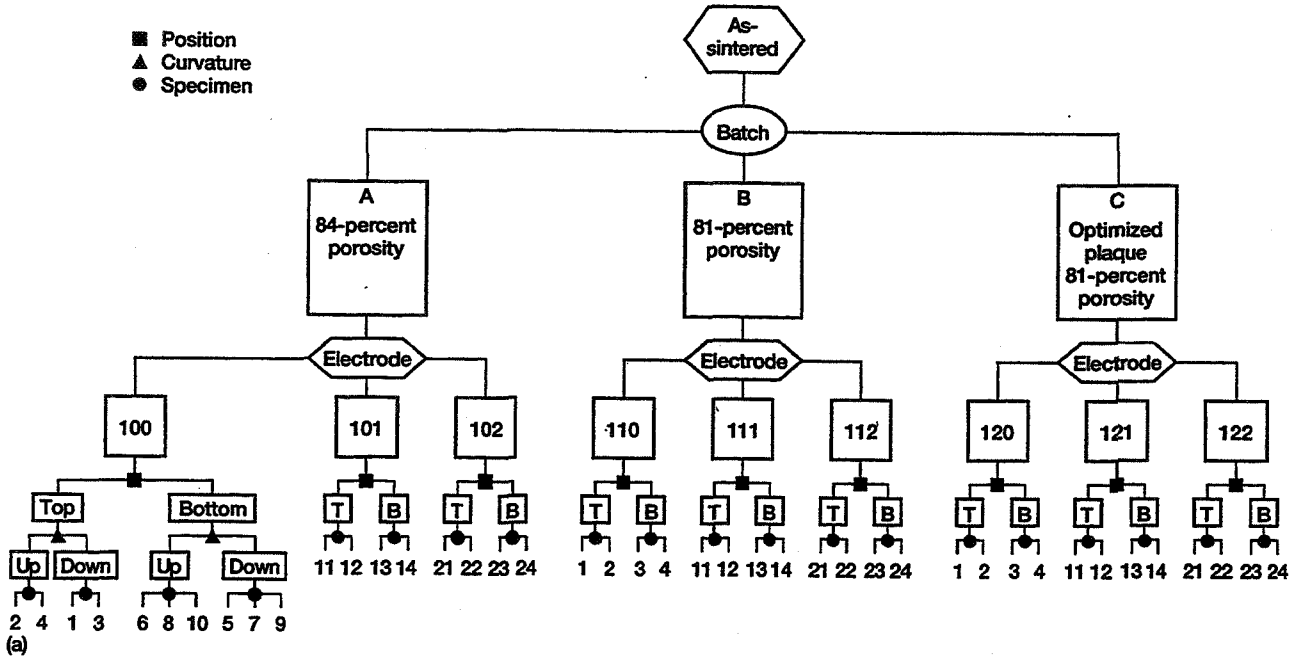

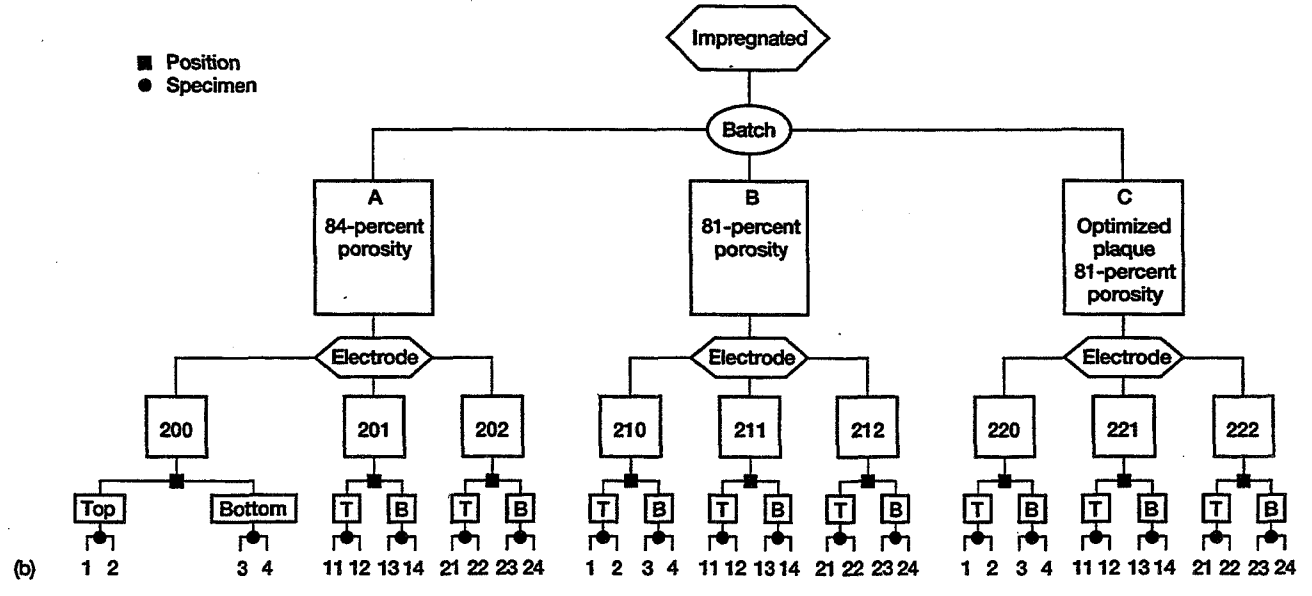

Figure 3.—Test matrix. (a) As-sintered electrodes. (b) Impregnated electrodes.

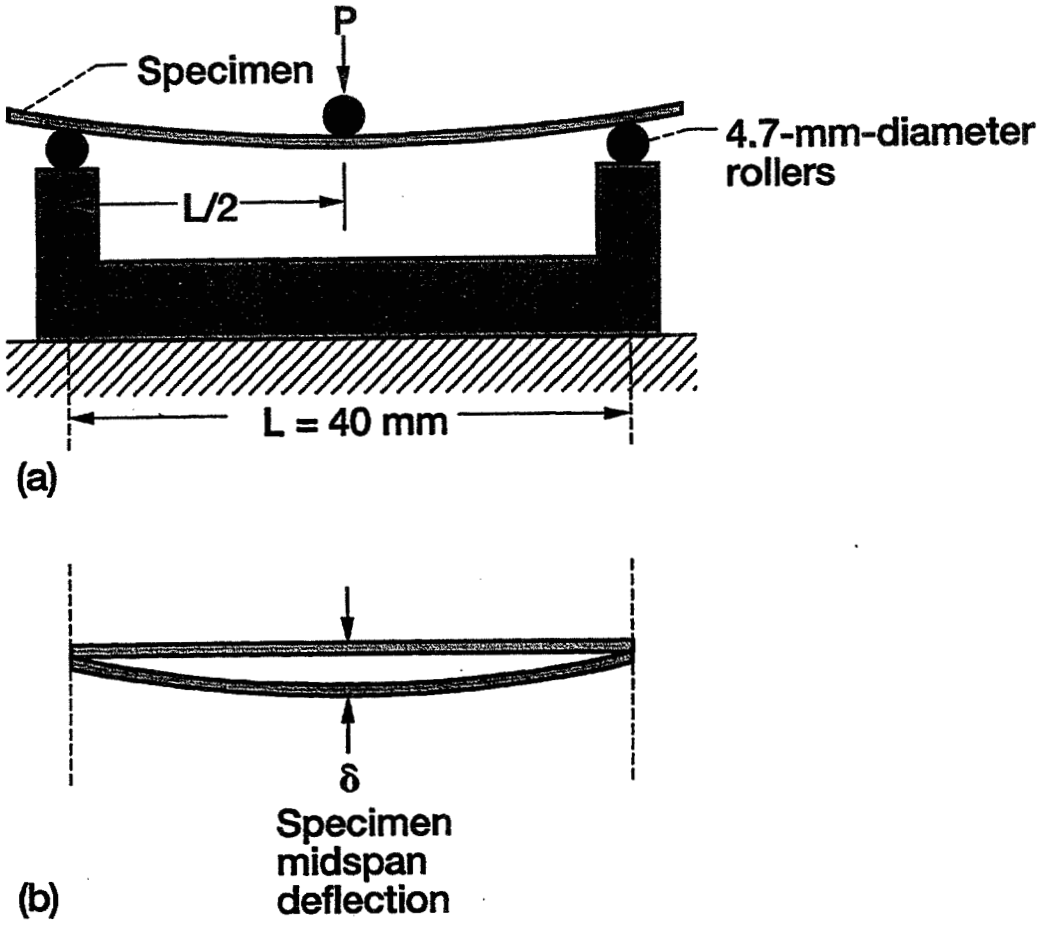

Figure 4.—Three-point bend fixture. (a) Schematic of fixture. (b) Specimen midspan deflection.

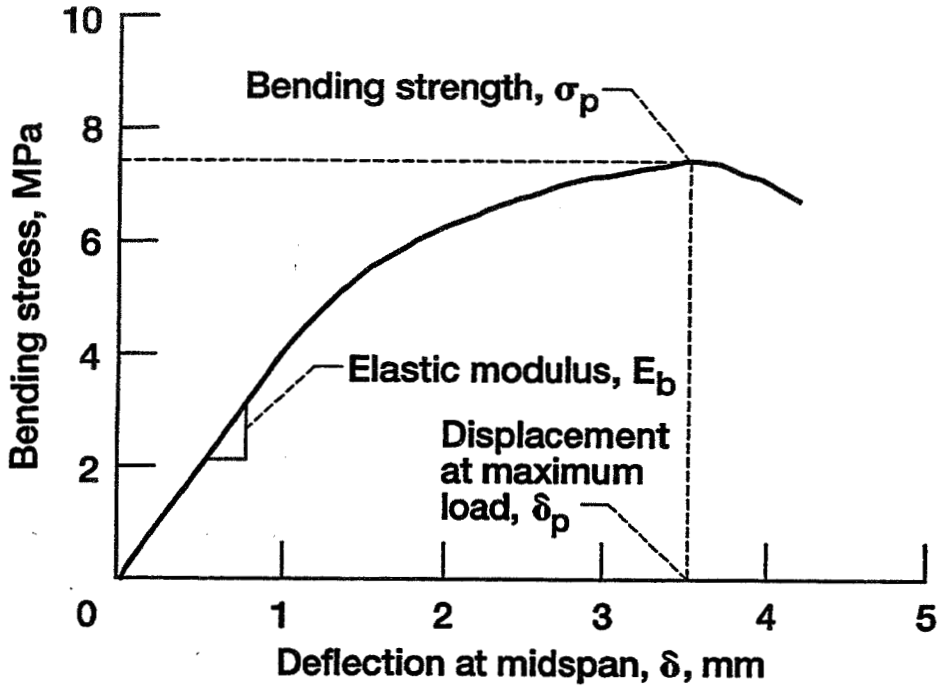

Figure 5.—Typical stress-displacement diagram showing critical measurements.

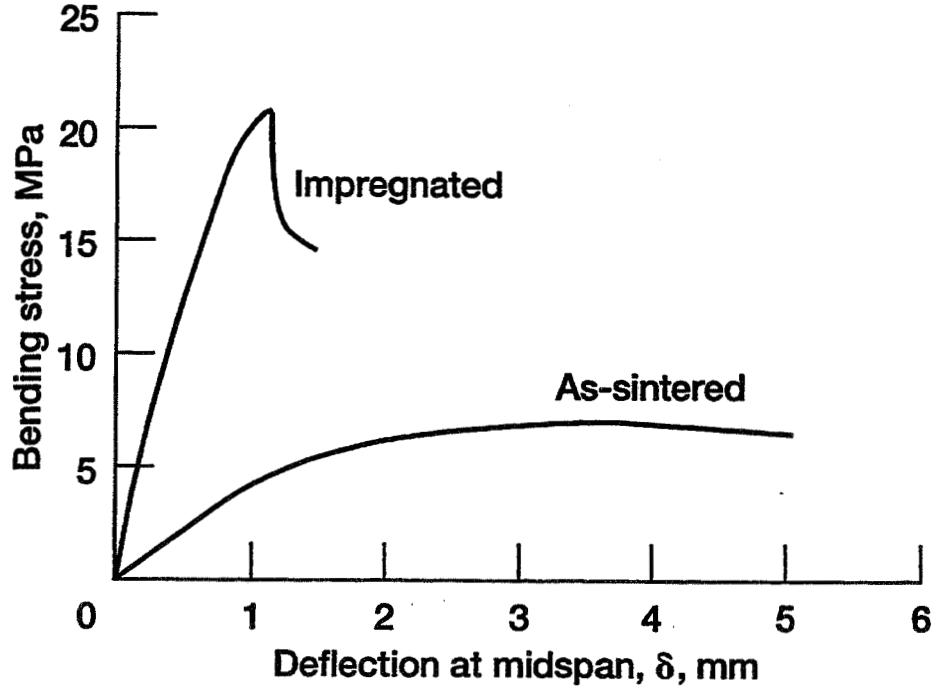

Figure 6.—Typical bending behavior of as-sintered and impregnated electrodes.

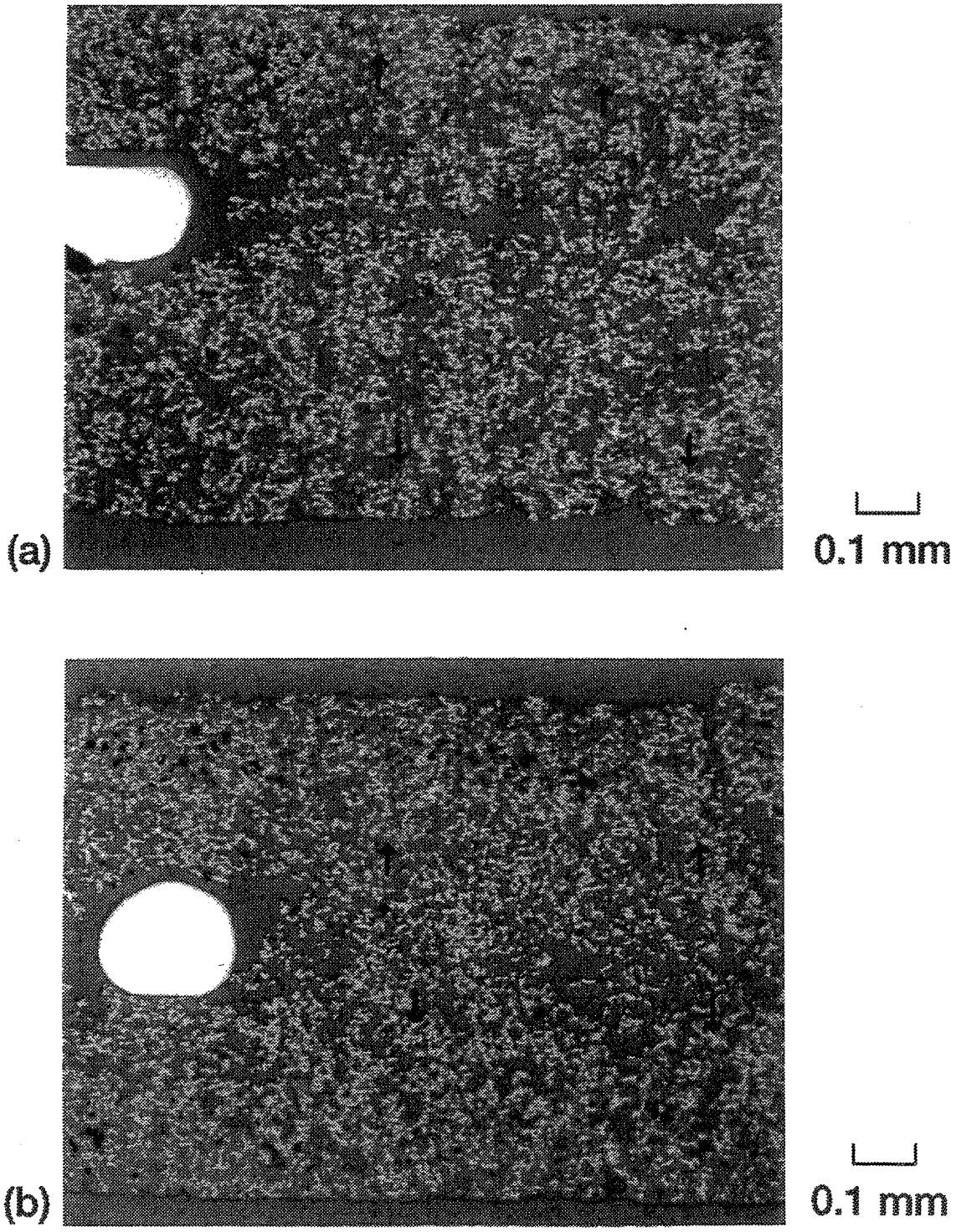

Figure 7.—Micrographs of batch A impregnated electrode s/n 202. Arrows indicate extent of $Ni(OH)_2$ surface loading. (a) Taken from top of electrode. (b) Taken from bottom of electrode.

54-44
008842

EFFECT OF KOH CONCENTRATION AND ANIONS ON THE PERFORMANCE OF A Ni-H_2 BATTERY POSITIVE PLATE

Hari Vaidyanathan and Kathleen Robbins
COMSAT Laboratories
Clarksburg, Maryland

and

Gopalakrishna M. Rao
NASA Goddard Space Flight Center
Greenbelt, Maryland

056911
12f

ABSTRACT

The capacity and voltage behavior of electrochemically impregnated sintered nickel positive plates was examined by galvanostatic charging and discharging in a flooded electrolyte cell. Three different concentrations of potassium hydroxide (KOH) (40%, 31%, and 26%) and 31% KOH containing dissolved nitrate, sulfate, or silicate were investigated. The end-of-charge voltage at C/10 charge and at 10°C showed the following order: 40% KOH > 31% KOH alone and in the presence of the anions > 26% KOH. The mid-discharge voltage at C/2 discharge was higher in 26% KOH, almost the same for 31% KOH with and without the added contaminants, and much lower for 40% KOH. The plate capacity was marginally affected by cycling in all cases except for 40% KOH, where the capacity declined after 1,000 cycles at 80% depth of discharge (DOD). At the end of cycling, all the plates tested experienced a weight loss, except in the case of 31% KOH, as a result of active material extrusion. Cyclic voltammetry of miniature electrodes in 31% KOH showed that the cathodic peak potentials are less polarized in the presence and absence of silicate at -5°C compared to 25°C, indicating a slightly higher voltage during discharge in a Ni-H_2 battery. Furthermore, the features of the current-potential profile were practically unchanged in the presence of silicate.

INTRODUCTION

The $Ni(OH)_2$/NiOOH cathode has been used in aerospace batteries for the past three decades, and its manufacture and performance features have been extensively discussed by several authors [1–5]. This cathode is the capacity- and life-limiting component in Ni-H_2 cells, and its reaction, molecular composition, and structure are very complex. The active material in the cathode has a theoretical energy of 0.279 Ah/g, and the charge transfer reaction occurs between +2 and +3.6 valency states. This positive plate yields a practical energy of 0.12 Ah/g in Ni-H_2 cells, and it endures more continuous charge/discharge cycles than any other cathode used in batteries. Several methods can be employed to fabricate this cathode; the use of cationic additives such as Co^{++}, Cd^{++} and Li^{+} is very common. The effects of additives and impurities have been examined by others, and generally the cationic types have been found to have beneficial effects [3], [6–7]. Among the anions, carbonate is believed to increase the ohmic resistance, sulfate is reported to increase corrosion of the sintered matrix, and silicate and nitrate are reported to decrease the capacity [8]. The current study is directed at the effects of hydroxyl, sulfate, silicate, and nitrate on the performance of the $Ni(OH)_2$ cathode.

DESCRIPTION OF THE TEST

The positive plates were of the sintered and electrochemical impregnated type, with a 0.9-mm thickness and a 50-cm^2 area. Two types of plates, differing only in the nature of the sintered plaque, were used for the study. The chemical composition of the positive plate is given in Table 1; all of the plates contained the cobalt hydoxide additive. The plates were tested individually by immersing them in a coolant-jacketed glass cell containing 800 ml of KOH. The counter electrode was a sheet of nickel, and the voltage was measured using a Hg/HgO reference electrode. First, the capacity of all 14 plates at 10°C was measured. Then, plates were repeatedly charged and discharged in a cycling regime consisting of charge for 28 min. and discharge for 17 min., with an overcharge of 5% and a depth of discharge of 80% at the rate of 32 cycles per day. The anionic additives were introduced immediately after the initial capacity determination. The sodium silicate level was 0.1% based on electrolyte weight, the potassium nitrate level was 0.5%, and the sodium sulfate level was 0.1%.

CAPACITY VARIATION

Figure 1 shows the capacities of the plates as a function of electrolyte composition. The capacity was highest in 40% KOH and lowest in 26% KOH, with the effect of nitrate, silicate, and sulfate being very minimum. The reason for the higher capacity in 40% KOH is the larger voltage window available for the plates during charge before predominant oxygen evolution sets in which increases the amount of oxidized species in the plates and/or higher proportions of Ni^{+4} in the charged state as a nickelate species. Figure 2 depicts the variation of capacity with cycling (1,000 cycles) for the plates. (For purposes of comparison, only plates using dry powder sintered plaque were included). The capacity actually increased to varying degrees for all the plates except that in 40% KOH. The increase in capacity may be due to the active material formation effect. The smaller increase in capacity for 26% KOH was unexpected. Several reasons can account for the capacity loss for the plates in 40% KOH such as swelling of the plate, loss of active material due to extrusion, and increase in ohmic resistance between the sinter and the active material.

Figure 3 shows the variation of capacity below 1 V (second plateau capacity) for the plates as a function of electrolyte composition. The plate tested in 40% KOH behaved differently than the rest, with significantly higher capacity at low voltage.

VOLTAGE CHARACTERISTICS

The end-of-charge voltage after 16 hrs of charge at C/10 varied as a function of electrolyte composition, as shown in Figure 4. The end-of-charge voltage was insensitive to the presence of sulfate. Silicate ions increased the voltage by 48 mV, and nitrate by 23 mV, compared to that obtained in 31% KOH. The largest effect was in 40% KOH, where the end-of-charge voltage increased by 78 mV, compared to that obtained in 31% KOH. High voltage during charge is undesirable since it promotes anodic corrosion of the sintered nickel skeleton. Because high end-of-charge voltage increases the voltage requirements for the charging source, it is disadvantageous for aerospace Ni-H_2 batteries.

Figure 4 plots the mid-discharge voltage obtained during discharge at C/2 as function of electrolyte composition. The presence of nitrate, silicate, and sulfate did not affect the voltage with respect to that obtained in 31% KOH. In the presence of 26% KOH, the voltage was 26 mV higher than that obtained in 31% KOH. In 40% KOH, the mid-discharge voltage was lower by 27 mV. This is a very interesting result. The reason for the higher voltage may be due to a slightly lower amount of K^+ ions incorporated in the lattice of the charged active material (NiOOH) in 26% KOH and/or an increased amount of H_2O molecules.

STRUCTURAL EFFECTS

In addition to being measured for weight and thickness, the plates were examined visually before and after cycling. The amount of extruded active material was determined by collecting and weighing the residue from the test

cell. The microrostructural features of the plates were determined by cross sectioning, followed by backscattered electron (BSE) image analysis using a procedure described in an earlier publication [9]. Visual examination of the plates at the end of cycling revealed several structural and mechanical imperfections such as blistering and warping. These are recorded in Table 2.

The increase in thickness of the plates as a result of cycling is recorded in Table 3. The expected increase in thickness at the end of 1,000 cycles is about 1%, which was obtained for the plates tested in 31% KOH with no additives. Except for 31% KOH, all other electrolyte compositions induced some noticeable imperfections irrespective of whether the plate was dry powder sinter or slurry sinter. The swelling was significantly higher in the presence of nitrate and in 40% KOH. Higher swelling in 26% KOH than in 31% KOH was observed in this test, and is in agreement with previous results for cycled positive plates in Ni-H_2 cells [10]. The reason for higher swelling in nitrate and 40% KOH is the higher corrosion of the sintered nickel in these electrolytes which weakens the sinter-to-sinter and sinter-to-substrate bonds.

Table 3 also records the active material weight loss in various electrolytes. The weight loss was significant in 40% KOH and in the electrolytes containing silicate. The reason for the higher weight loss in these electrolytes is the corrosion of the sintered nickel and the surface chemical effect which produces loosely held mossy structures.

Figure 5 shows the microstructure of plates cycled in 26% KOH and 40% KOH. The micrographs, which were taken at a magnification of 60, indicate that, in the case of the plate cycled in 40% KOH, the microstructure has undergone considerable change in the distribution of the active material across the plate thickness. The surface of the plate is becoming depleted of active material, macrovoids have developed, and the plate thickness has increased compared to the one for 26% KOH. On the other hand, the plate cycled in 26% KOH shows no evidence of any change in the microstructure. Figures 6 and 7 show the distribution curves for the active material void and sinter fractions which were deduced from the BSE images using the method described in Reference 9 which consisted of grey level histogram plotting for the plate cycled in 26% KOH and 40% KOH, respectively. The active material distribution is uniform across the thickness for the plate cycled in 26% KOH, and is very nonuniform for the plate cycled in 40% KOH. The calculated fill factor is only 63.1%, with a sigma of 14.4% for the active material in the 40% KOH plate. The results indicate considerable movement of active material in the plate structure if the plate is cycled in 40% KOH. Very stable conditions are indicated for the plate cycled in 26% KOH.

CYCLIC VOLTAMMETRY

The voltage profile of a miniature positive electrode (1 cm^2) was obtained by using cyclic voltammetry in 31% KOH. The potential of the positive plate was continuously changed using a triangle-wave generator and a potentiostat from -0.5 to 0.65 V (*vs* a Hg/HgO reference electrode) at a rate of 0.1 mV/s. Figure 8 shows two voltage profiles: Curve A corresponds to a plate in 31% KOH, and curve B to another plate in 31% KOH containing 0.1% sodium silicate. The plate exhibited two anodic peaks (Peak I and Peak II), an oxygen evolution maximum, and a cathodic peak (Peak III). The two anodic peaks can be correlated with the oxidation of two different types of nickel species. Only one cathodic peak indicates reduction to a single nickel species. The peak potentials are listed in Table 4. The voltage profile of the positive plate in the presence and absence of 0.1% (by weight) sodium silicate at -5°C and 25°C was obtained, and the peak potentials obtained are included in Table 4. The data indicate the following:

- The cathodic peak potentials are less polarized at -5°C (compared to 25°C) in the presence and absence of silicate, indicating a slightly higher voltage during discharge in a Ni-H_2 battery.

- The cathodic peak potentials are unaffected by the presence of silicate, indicating that the silicate does not influence the electrochemical reduction reaction.

- The anodic Peak I potential is unaffected by the presence of silicate and the Peak II potential is marginally affected at -5°C. These data indicate that silicate does not influence the electrochemical reaction.

- At 25°C, the anodic Peak I and Peak II potentials are lower in the presence of silicate. Absorption of silicate on the nickel hydroxide could explain the lowering of the peak potentials.

MECHANISM OF ANIONS

A number of studies have shown that when inorganic salts are introduced during processing of the electrode or in the cell electrolyte, cations such as Co^{+2}, Zn^{+2}, Cd^{+2}, K^{+} and Li^{+} are incorporated in the crystal lattice of $Ni(OH)_2$ which changes the lattice parameters [11]. The foreign cations are said to occupy the vacant sites to make up for the nickel deficit in the structure. On the other hand, anions are believed to be absorbed in between layers of $Ni(OH)_2$ [12]. Thus, the cationic additives alter the behavior of the nickel hydroxide by virtue of their ability to stabilize a higher valent nickel (Ni^{+4}), increase the ion transport by expanding the lattice, increase the degree of hydration by enlarging the interstitial spacing, and increase the conductivity by reducing the stoichiometry. The effect of anions is limited to the alteration of surface texture. The reaction most affected by this is electrocatalytic oxygen evolution on the charged active material NiOOH, since the O_2 evolution is very sensitive to surface conditions such as the structure of the double layer and absorbed species. This is the reason for the increase in the end-of-charge voltage for the positive electrode in the presence of anions. The effect of anions on surface conditions is also reflected in the adhesion of the active material which in turn affects the extent of swelling and a resultant loss of active material. For aerospace application, the role of aniomic impurities in the swelling of the electrode and spalling of the active material is of importance, since the processes are life-limiting. Therefore, minimizing anionic impurities is vital for long-life nickel electrodes.

CONCLUSIONS

The experimental results suggest the following conclusions:

1. An increase in KOH concentration (from 26% to 40%) significantly affects performance features such as capacity stability with cycling, end-of-charge voltage, and mid-discharge voltage more than trace amounts of nitrate, sulfate and silicate as impurities.

2. Trace amounts of nitrate increase plate swelling.

3. Trace amounts of silicate increase active material loss by extrusion.

4. The effect of anions like sulfate, silicate and nitrate are minor compared to that of cations like Co, Cd, and Zn. This is because cations are easily incorporated into the crystal lattice thus altering the lattice parameters. The anions influence the surface structure. This confirms the hypothesis of earlier work by other authors that in the charged state there is a predominance of nickelate species. The formation of nickelate can also account for the fractional valency of 3.6 for the charged species.

5. Although the positive plate electrochemistry appears to be tolerant to anionic impurities, such impurities are still undesirable from the standpoint of the mechanical strength and physical integrity which are required in batteries.

6. The effect of anions was the same whether the positive plate was based on slurry or dry powder sintered plaque.

7. BSE image analysis indicated that there is no movement of active material across the cross section of the plate in the case of 26% KOH.

REFERENCES

1. P. C. Milner and U. B. Thomas, "The Nickel Cadmium Cell," *Advances in Electrochemistry and Electrochemical Engineering*, Editor, C. W. Tobias, New York: Interscience, Vol. 5, p. 1.

2. J. L. Weinninger, Symposium on the Nickel Electrode, Fall Meeting 1981, The Electrochemical Society, Pennington, New Jersey, Vol. 82.4, *Proc.*, p. 1.

3. G. Halpert, Symposium on the Nickel Hydroxide Electrode, Fall Meeting 1989, The Electrochemical Society, Pennington, New Jersey, *Proc.*,Vol. 90-4, p. 3.

4. D. Picket, A. Powers, F. Montague, and G. Zelter, 29th Intersociety Energy Conversion Engineering Conference, Monterey, California, August 1994, AIAA, Washington, D.C., *Proc.*, Part 1, p. 69.

5. A. H. Zimmerman, Extended Abstracts, No. 59, Fall Meeting of the Electrochemical Society, Miami Beach, Florida, 1994, p. 96.

6. D. H. Fritts, Symposium on the Nickel Electrode, Fall Meeting 1981, The Electrochemical Society, Pennington, New Jersey, 1982, *Proc.*, Vol. 82.4, p.1.

7. L. Demourgues and C. Delimas, *J. Electrochem. Soc.*, 1994, Vol. 141, p. 713.

8. A. H. Zimmerman, "Mechanisms for Capacity Fading in the Ni-H_2 Cell and Their Effect in Cycle Life," Aerospace Corporation, El Segundo, California, Report No. ATR-93 (8363) -3, Nov. 1994.

9. H. Vaidyanathan, M. W. Earl, and T. D. Kirkendall, *J. Power Sources*, 1991, Vol. 36, p. 269.

10. H. S. Lim and J. J. Smithrick, 28th Intersociety Conversion Engineering Conference, American Chemical Society, Washington, D.C., 1993, *Proc.*,Vol. 1, p. 151.

11. B. C. Cornilsen, X. Shaw, and P. C. Loyselle, "Symposium on the Nickel Hydroxide Electrode, Fall Meeting 1989, The Electrochemical Society, Pennington, New Jersey, *Proc.*,Vol. 90-4, p. 82.

12. P. Delahaye - Vidal, F. Portemer, B. Blaudoin, K. Tekdia-Elhsissen, P. Genin, and M. Figlarz, Symposium on the Nickel Hydroxide Electrode, Fall Meeting 1989, The Electrochemical Society, Pennington, New Jersey, *Proc.*,Vol. 90-4, p. 44.

TABLE 1

Chemical Composition of the Positive Plate

ITEM	MASS. GRAM	PERCENT
Positive Plate	14.29	100
$Ni(OH)_2$	5.25	36.74
$Co(OH)_2$	0.51	3.57
Nickel Sintered Plate	8.45	59.13
Other (Water)	0.08	0.56

TABLE 2

Physical Changes Due to Cycling

ELECTRODE I-D	SINTER TYPE	WEIGHT WITH TAB (g)	ELECTROLYTE	CHANGE IN APPEARANCE AFTER 1,000 CYCLES
1A	Dry Powder	17.68	31% KOH	Small blisters only on top of the plate
23A	Dry Powder	18.13	30%	Small blisters on top of the plate
3A	Slurry	16.26	31%	Only two blisters
3A	Dry Powder	17.71	26%	Large blisters on top and bottom of the plate
21B	Dry Powder	17.72	26%	Many tiny blisters on top of the plate
7A	Dry Powder	17.39	40%	Warping
22A	Dry Powder	17.72	40%	Warping and cracking
13A	Slurry	16.41	40%	Blisters on both sides of the plate
4A	Dry Powder	17.73	31% KOH + KNO_3	Many blisters on top and bottomof the plate
9A	Slurry	16.46	31% KOH + KNO_3	Many blisters on bottom of the plate
15B	Dry Powder	18.03	31% KOH + Na_2SO_4	Slight warping, small blisters on bottom of the plate
6B	Slurry	15.84	31% KOH + Na_2SO_4	Blisters on both sides of the plate
14B	Dry Powder	18.08	31% KOH + Na_2SiO_3	Slight warping
11B	Slurry	16.29	31% KOH + Na_2SiO_3	Slight warping

TABLE 3

Swelling and Extrusion of Plate

ELECTROLYTE	SWELLING	WT. LOSS
31% KOH	1%	0.18%
26% KOH	4.90%	0.85%
40% KOH	12.36%	6.31%
31% KOH + Nitrate	8.90%	0.38%
31% KOH + Silicate	1.80%	1.90%
31% KOH + Sulfate	2.40%	0.75%

TABLE 4

Peak Potentials Obtained by Cyclic Voltammetry

TEMPERATURE	ELECTROLYTE	ANODIC PEAK I POTENTIAL (V)	ANODIC PEAK II POTENTIAL (V)	SWEEP REVERSAL O_2 EVOL. POTENTIAL (V)	CATHODIC PEAK POTENTIAL (V)
-5°C	31% KOH	0.481	0.574	0.64	0.275
	31% KOH + 0.1% Na_2SiO_3	0.482	0.570	0.64	0.272
25°C	31% KOH	0.495	0.544	0.64	0.262
	31% KOH + 0.1% Na_2SiO_3	0.474	0.529	0.64	0.264

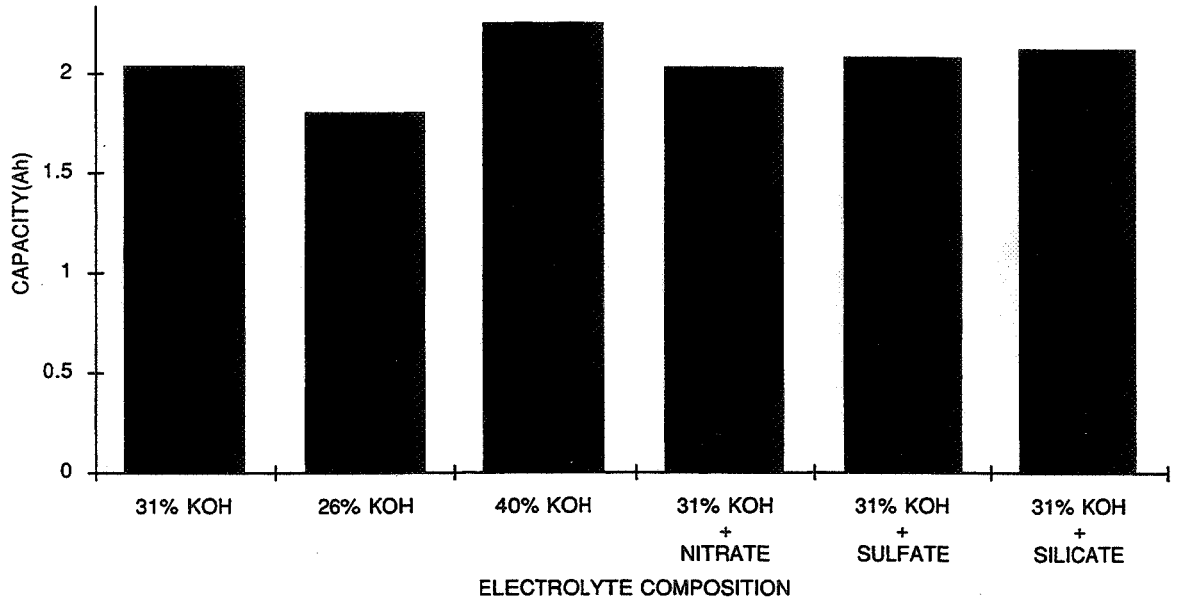

Fig. 1.—Initial capacity of plates.

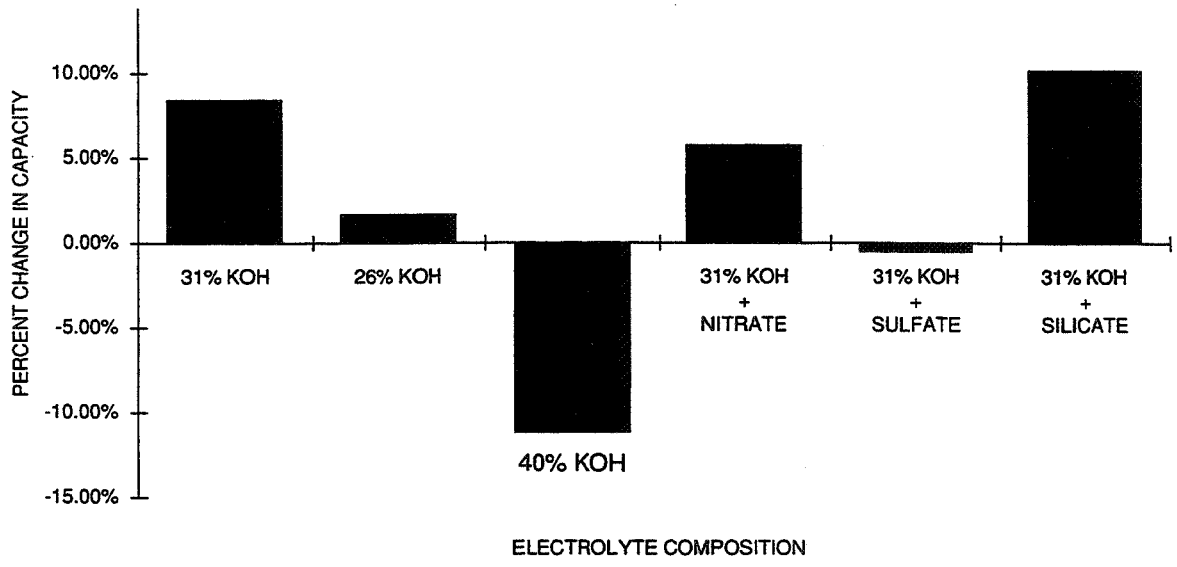

Fig. 2.—Variation capacity with cycling.

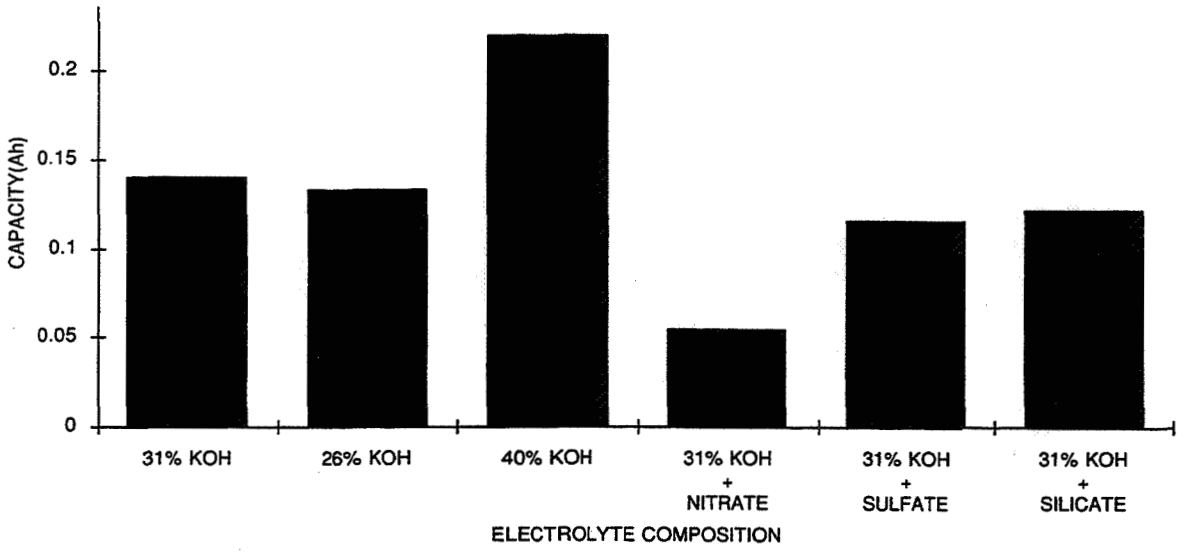

Fig. 3.—Low voltage capacity in plates.

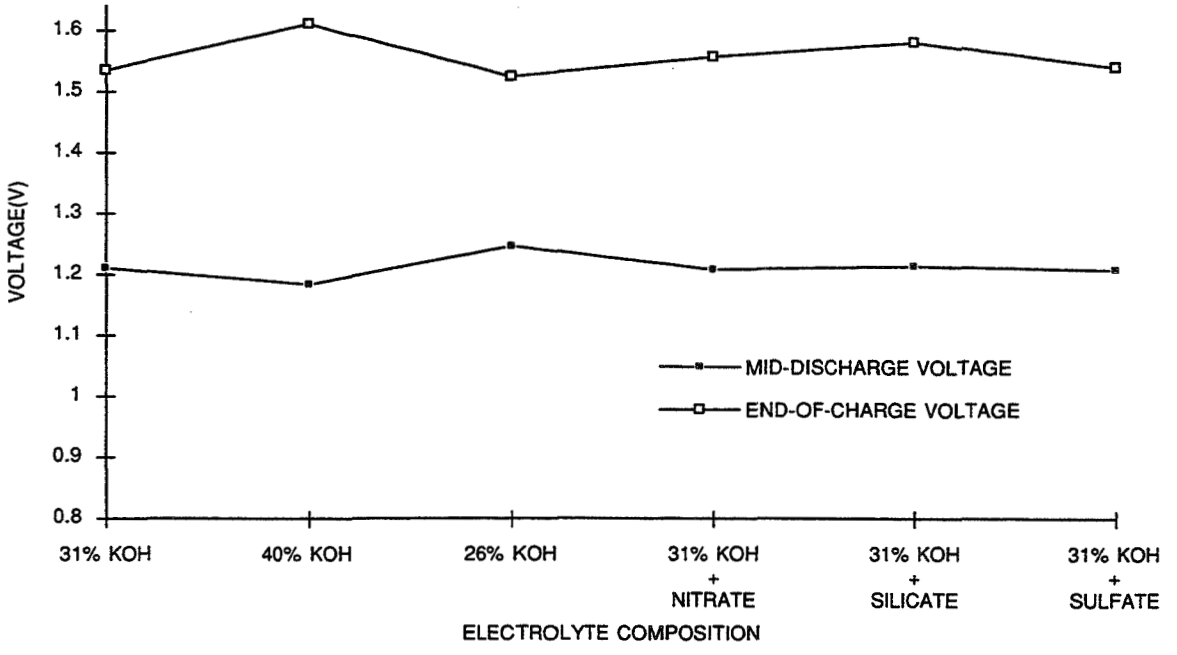

Fig. 4.—End-of-charge and mid-discharge voltages.

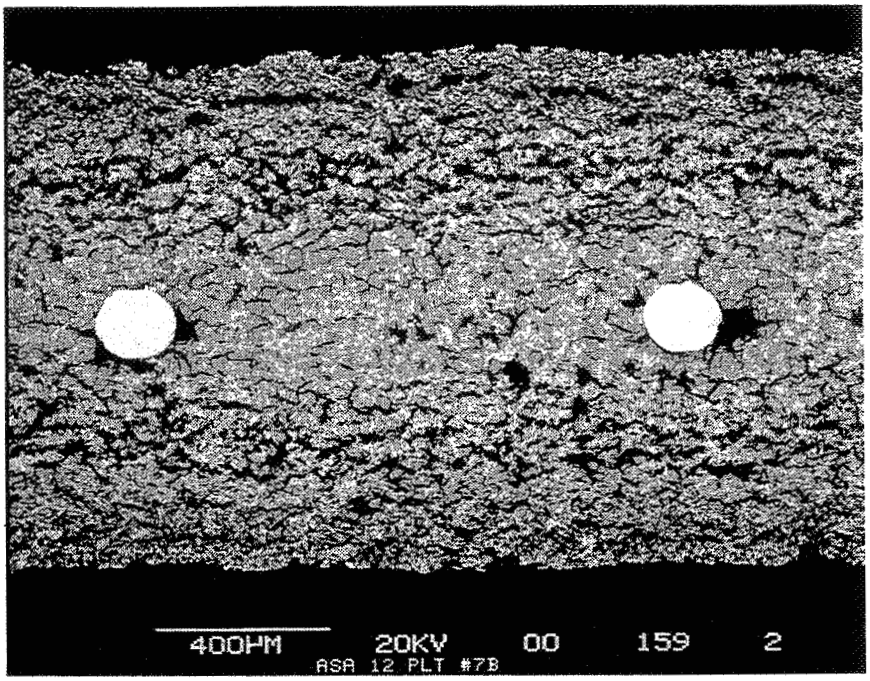

Fig. 5a.—BSE image of the cross section of the positive plate cycled in 40% KOH.

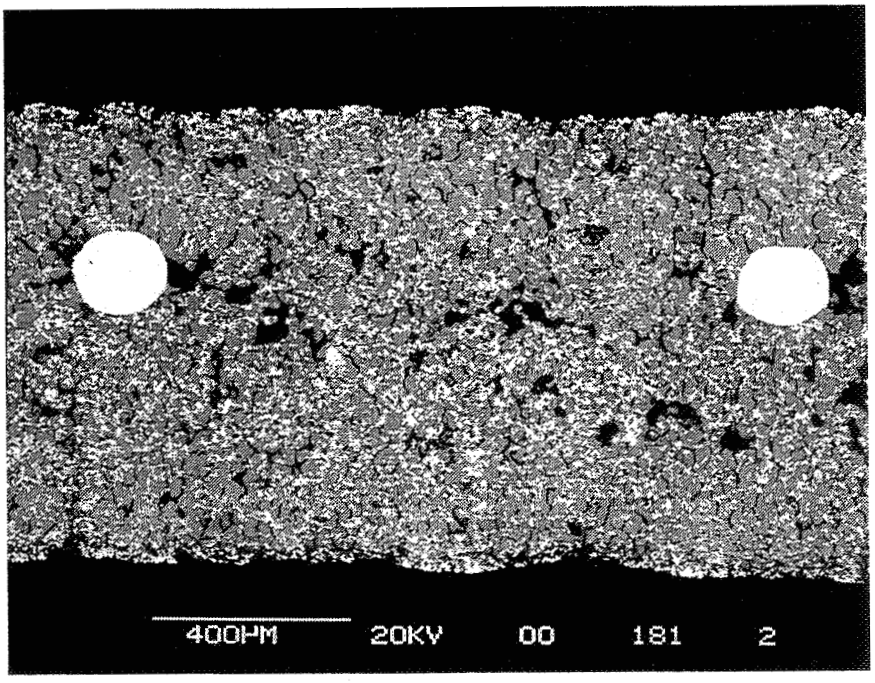

Fig. 5b.—BSE image of the cross section of the positive plate cycled in 26% KOH.

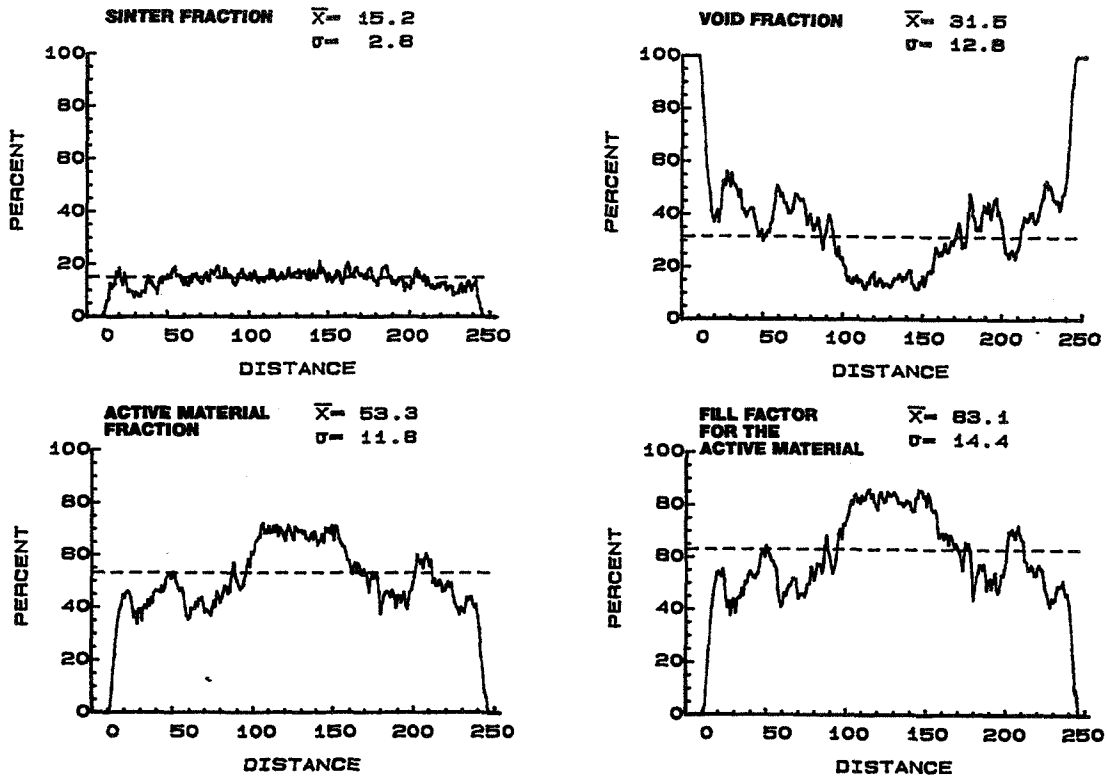

Fig. 6.—Distribution profiles obtained by BSE image analysis for the plate after 1,000 cycles in 40% KOH (x = average, σ = standard deviation, distance = plate thickness in arbitrary unit).

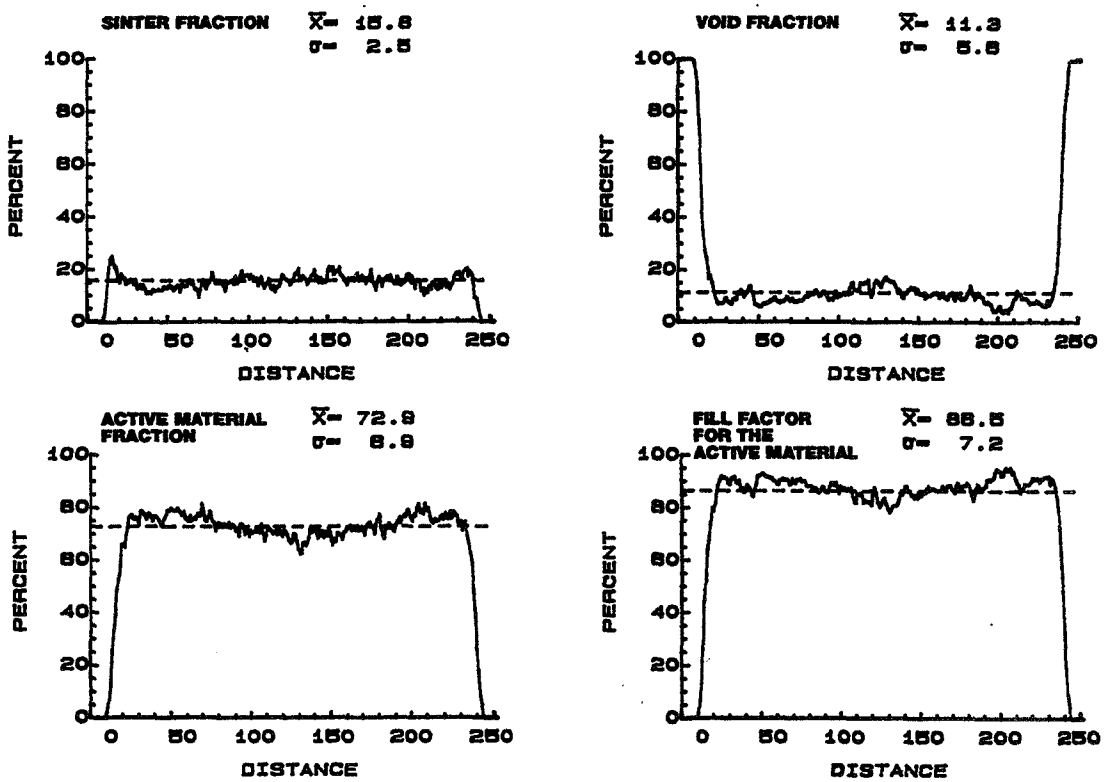

Fig. 7.—Distribution profiles obtained by BSE image analysis for the plate after 1,000 cycles in 26% KOH (x = average, σ = standard deviation, distance = plate thickness in arbitrary unit).

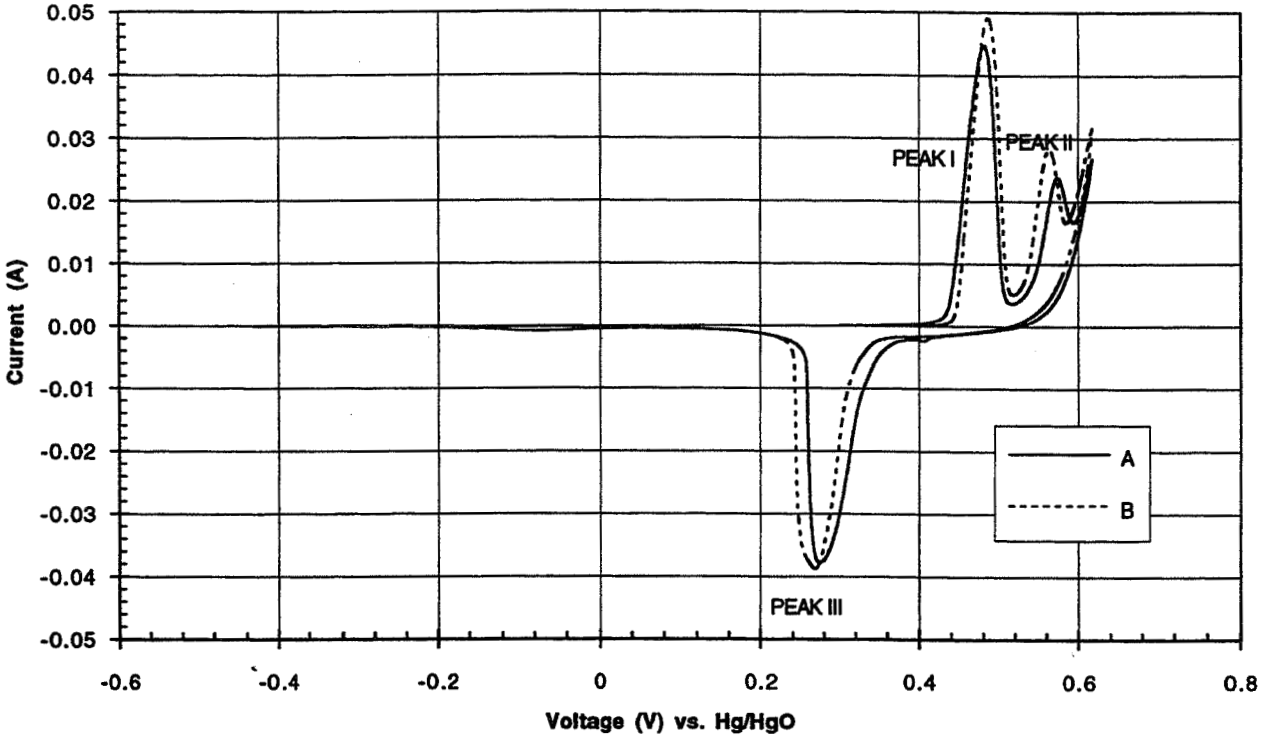

Fig. 8.—Cyclic voltammograms obtained for the positive plates. Curve "A" in 31% KOH and curve "B" in 31% KOH + silicate.

Page intentionally left blank

S5-44
008843
8P.

ADVANCED DEPENDENT PRESSURE VESSEL (DPV) NICKEL-HYDROGEN SPACECRAFT CELL AND BATTERY DESIGN

Dwaine K. Coates, R. Doug Wright, and
Ron S. Repplinger
Eagle-Picher Industries, Inc.
Joplin, Missouri

356916

ABSTRACT

The dependent pressure vessel (DPV) nickel-hydrogen (NiH_2) battery is being developed as a potential spacecraft battery design for both military and commercial satellites. Individual pressure vessel (IPV) NiH_2 batteries are currently flying on more than 70 earth-orbital satellites and have accumulated more than 140,000,000 cell-hours in actual spacecraft operation. The limitations of standard NiH_2 IPV flight battery technology are primarily related to the internal cell design and the battery packaging issues associated with grouping multiple cylindrical cells. The DPV cell design offers higher specific energy and reduced cost, while retaining the established IPV NiH_2 technology flight heritage and database. A design performance analysis will be presented at both the cell and battery level. The DPV is capable of delivering up to 76 Watt-hours per kilogram (Wh/kg) at the cell level and 70 Wh/kg at the full battery level. This represents a 40% increase in specific energy at the cell level and a 60% increase in specific energy at the battery level compared to current IPV NiH_2 technology.

INTRODUCTION

The NiH_2 battery has a number of unique features and advantages which are superior to other battery systems. The battery has virtually unlimited overcharge and overdischarge capability if the resultant heat from the oxygen/hydrogen gas recombination reaction is adequately removed. Since hydrogen gas is one of the battery reactants, the internal pressure in the battery provides a reliable measurement of battery state-of-charge. The internal pressure can be readily monitored remotely by a pressure transducer or strain gauge. The NiH_2 battery is also the most reliable aerospace battery system available. Batteries have completed more than 140,000,000 cell-hours in orbital spacecraft operation. NiH_2 batteries offer the longest cycle life of any battery system. Batteries on test have completed more than 100,000 charge/discharge cycles. Batteries have operated in geostationary-earth-orbit for more than 15 years. NiH_2 batteries have low internal impedance and excellent high rate discharge capability, pulse discharge capability and power density. The many advantages and features of the NiH_2 battery are the reason the system has been heavily developed for advanced critical applications such as earth-orbital spacecraft. Many of these same features and advantages are also equally desirable in terrestrial commercial battery applications.

Several distinct NiH_2 cell and battery designs are currently in production and under development for a wide variety of applications. These include traditional aerospace applications such as earth-orbital communications satellites as well as terrestrial uses such as telecommunications equipment, utility load leveling and remote location power systems. Traditional individual pressure vessel (IPV) NiH_2 technology has been supplemented by newer common pressure vessel (CPV) cell designs and other cell and battery designs such as the single pressure vessel (SPV) and low pressure (LPV) battery. The dependent pressure vessel (DPV) battery design is the next step in the continued development and evolution of the NiH_2 battery system.

DPV CELL DESIGN

Cell component level development work is aimed at improving cell level performance while reducing system cost. The nickel electrode is currently the limiting component in terms of cell performance and energy density. Work is directed at increasing the energy density of the electrode by increasing the ratio of active materials to inactive materials. Hydrogen electrodes currently provide excellent levels of performance, reliability and cycle life. Development

work is oriented towards reducing the cost of the catalytic materials used in electrode manufacture and reducing direct labor costs. Alternative separator materials are being identified and qualified in an effort to reduce system cost while maintaining current levels of performance and reliability. Cell mechanical design is oriented towards mass and volume efficiency and maximizing specific energy and energy density.

Cell Mechanical Design

A unique feature of the DPV cell design is the prismatic (rectangular) electrode stack. Although the standard NiH_2 cell design is a flat plate stack arrangement, the normal geometry is circular/cylindrical. A typical 90 millimeter (mm) diameter IPV cell design is shown in Figure 1. The prismatic electrode stack, as proposed in the DPV cell design, suggests an optimum geometry for the pressure vessel, which is also quite different than the standard NiH_2 cell design. The pressure vessel is circular and flat and contains a bracket which holds the electrode stack in place. The DPV cell/ electrode stacking concept is shown in Figure 2. This pressure vessel geometry is another unique feature of the DPV cell. The flat sides of the pressure vessel are intended to be supported by the battery endplates in the final assembly. The DPV cell is termed "dependent" because the cell geometry requires the cell to be externally supported in order to contain the hydrogen pressure developed inside the cell during charging. The cell pressure vessel is therefore dependent on the battery structure for mechanical support. Since the pressure vessel is not required to support the full internal cell pressure, the pressure vessel can be made with a thinner wall thickness and a corresponding weight savings. The rounded edge of the pressure vessel is designed to contain the full internal cell pressure. The rounded shape, over a relatively small radius, is very efficient for pressure containment with a minimum weight of pressure vessel material.

The pressure vessel is manufactured from stainless steel. It consists of two identical, seamless halves. A lip around the edge where the two halves meet assists in the laser weld which closes the cell girth and provides a hermetic seal. One of the pressure vessel halves is fitted with cell terminal bosses and a fill tube. The cell terminal uses an internal boss arrangement which provides the minimum external protuberance and minimizes the overall dimensions of the cell. The boss is then attached to the pressure vessel by a laser weld. The bosses are offset 15° from a central axis which passes through the fill tube. The terminal bosses and fill tube are offset 30° from the central axis of the girth weld as shown in the cell outline drawings in Figure 3 and 4.

The electrode stack consists of the electrochemically active part of the cell. It contains nickel electrodes and hydrogen electrodes interspersed with an absorbent separator material. A back-to-back stacking arrangement is used as shown in Figure 2. The back-to-back stacking arrangement provides that each nickel electrode is opposed by the catalyst side of a hydrogen electrode. This puts the hydrophobic sides of the two adjacent hydrogen electrodes facing towards each other. A gas spacer is inserted in order to facilitate hydrogen gas diffusion into and away from the hydrogen electrode during charge and discharge. A metal stacking bracket holds the electrode stack in place within the cell pressure vessel. The bracket is spot welded to one pressure vessel half prior to cell assembly. Separation material electrically insulates the electrode stack from the pressure vessel and the stacking bracket. The electrical tabs from the electrodes within the electrode stack emerge through a window in the stacking bracket. The lead bundles are stress relieved by introducing an "S" into the leads with respect to the flat plane through the girth weld of the cell. This prevents mechanical stress, such as launch vibration, from being transmitted into the electrode/tab connection. A side view of the DPV cell is shown in Figure 4.

DPV BATTERY DESIGN

The DPV cell is basically an IPV type design in that each pressure vessel contains only one cell, and therefore delivers only 1.25 VDC. Most applications require voltages which necessitate the connection of multiple cells in series. This is a simple straightforward concept, however it is a critical aspect of design for high reliability spacecraft applications. The cells must be packaged into batteries or battery modules which will meet the performance and reliability requirements of the spacecraft. This includes the mechanical, electrical and thermal design of the battery.

Mechanical Design

The mechanical design of the battery addresses primarily the physical aspects of packaging. The cells must be bound together into physically manageable units for handling and spacecraft integration. In fact, the mechanical design is primarily defined by how the battery must physically fit into the spacecraft. Standard practice for battery integration is to mount the battery to a baseplate which is not only the mechanical interface to the spacecraft but also the thermal interface as well. The dimensions of the baseplate are defined by the physical footprint of the battery, the space/volume available in the spacecraft structure and the thermal requirements of the battery/spacecraft interface. The spacecraft configuration must be considered in designing the battery and vice versa.

One of the advantages of the DPV cell design is that the mechanical battery assembly concept is much simpler than with standard cylindrical IPV cells. The DPV cells are designed to be sandwiched between two endplates, which defines the basic packaging concept for the battery design. It is simple, efficient, easily assembled and requires few parts. A multicell IPV NiH_2 battery requires additional parts, such as cell mounting sleeves, which mean additional weight and cost and additional handling and assembly work. The DPV battery packaging concept has an established heritage in the aerospace industry. The endplate/connecting rod battery design has been used with nickel-cadmium (NiCd) and silver-zinc (AgZn) cells for spacecraft applications for many years. Several battery assembly possibilities exist, which make overall DPV battery design modular and flexible. This makes the DPV battery adaptable for a variety of spacecraft designs. There is a significant advantage of the endplate battery design because the percentage of the total battery weight contributed by the battery packaging components is smaller than with the standard IPV battery. This results in a lower packaging factor in progressing from the cell design to the battery design. The battery packaging factor reflects the decrease in specific energy experienced between the cell level and the battery level due to additional battery components. The DPV battery minimizes battery level components.

The DPV battery assembly presents the cells in a single row sandwiched between two endplates. The endplates are tied together with stainless steel, threaded connecting rods. Mechanical support of the cells is provided by the endplates to support the internal hydrogen pressure developed during charging and prevent the flat sides of the cells from deforming. Another basic design is shown in Figure 5, where the cells are packaged into two rows, each containing an equal number of cells. An unequal number of cells could be accommodated by using a "dummy cell" spacer, however this would incur a small penalty by adding weight which doesn't contribute to energy storage. Wiring and connectors are omitted from the figure for clarity. The advantage of two rows of cells is that the overall battery is somewhat more compact. A typical 22 cell, 28 VDC, 50 ampere-hour battery, for example, would be approximately 22 centimeters (cm) in diameter (footprint) and approximately 85 cm in length for a single row of cells. For the same battery with two rows of cells, these dimensions would be approximately 41 cm wide and 47 cm long. The battery with two rows of cells provides a more nearly square package. A disadvantage is that the larger endplates contribute slightly more weight to the overall battery package. Therefore the single row battery will have slightly higher energy density, but the double row battery will typically be easier to integrate into a spacecraft.

Electrical Design

The electrical design includes aspects and components such as intercell connection, conductor IR voltage losses, the battery electrical interface, connectors, battery monitoring, charge controllers and battery electronics such as strain gauges, strain gauge amplifiers, heaters, heater controllers, cell bypass diodes, cell voltage monitoring, current monitoring, temperature monitoring and others, depending on the specific battery design, spacecraft design and interface requirements. The battery electrical interface includes integration into the spacecraft and interface with additional batteries or battery modules on the spacecraft. Communications satellites typically carry two non-redundant batteries. Having two separate batteries, rather than a single larger one, aids in balancing the battery mass in the spacecraft and also eases the thermal interface requirements. In contrast, some small satellites may contain only a few cells wired in series with no battery electronics. The batteries have to be adaptable to a wide range of spacecraft designs, power levels and electrical requirements.

The battery cells are series-connected in the battery, observing cell polarity. The positive terminal of one cell is connected to the negative terminal of the next, and so on. One end of the cell string will have a remaining positive terminal open and the other end will have an unused negative cell terminal. These cell terminals are connected to the

battery interface connector and provide the power connections to the spacecraft. Silver foil, nickel foil or spacecraft-rated wiring is used as the intercell connectors. It depends primarily on the length required between cell terminals and the allowable voltage losses. Batteries are generally designed to minimize the length of the intercell connection. This is done in IPV batteries by inverting every other cell such that the positive and negative cell terminals alternate at the top and bottom of the battery. This eliminates having to connect the top of one cell to the bottom of another. The DPV battery is even more efficient by aligning all of the cell terminals along a central axis running the length of the battery. Or in the case of the dual cell, side by side battery design, two rows of cell terminals along the length of the battery. Foil bus bar type intercell connectors are the most efficient method for very short connections such as in the DPV battery. Silver or nickel would be used based primarily on cost considerations. The exposed portion of the intercell connector between cell terminals can be insulated with space-rated materials, though this is not typically required. The intercell connector is mechanically connected to the cell terminal. Wire, or redundant wires, are generally used for the slightly longer connection between the two cell terminals and the battery connectors. The wire is mechanically connected to the cell terminals and soldered into the battery connector.

Strain gauge circuitry is a critical item. This component measures the microflex of the pressure vessel produced by internal pressure changes. A four bridge, active circuit is used. Two gauges are active and two gauges are null indicators. The strain gauge must be calibrated after installation on the specific cell on which it will be operated. This is done after the cell closure girth weld, but before electrolyte activation, by pressurizing the cell pressure vessel with helium gas. Since the strain gauge bridge is an active circuit, an excitation voltage must be provided through the battery electronics and interface. The output signal is small, so an amplification circuit is typically supplied on the battery to boost the signal to an adequate level for spacecraft telemetry. The strain gauge output signal provides a direct indication of the cell internal pressure, and therefore the cell state-of-charge. Strain gauges are typically included on three cells in the battery for comparison and redundancy purposes. Cell heaters are usually supplied in order to closely control the battery temperature during all phases of operation. Some batteries are supplied with on-board heater controller circuitry. Heat is removed by thermal fins which contact the battery baseplate/thermal radiator. Battery temperature is monitored using thermistors. Generally, three are mounted at different locations in the battery. This provides redundancy and a measure of temperature uniformity across the battery. Battery current sensing is provided by an on-board current sensing element, usually of the non-contact, inductive type. All battery monitoring information such as voltage, current, temperature and strain gauge output are supplied to the spacecraft telemetry system through the battery electrical interface connector.

Thermal Design

Temperature control is an important aspect of battery design and spacecraft integration. Cell heaters are typically supplied to help regulate cell temperature during orbital operation. The battery is also mounted to a baseplate to remove excess heat when required. The battery baseplate usually mounts directly to a bulkhead in the spacecraft and radiates excess battery heat into space. A considerable amount of thermal analysis, calorimetry testing and thermal modeling has been done with the NiH_2 system. Basically, the cell is endothermic during the bulk of charging until near the end-of-charge. At this point, as the cell goes into overcharge, oxygen gas is evolved at the nickel electrode. This oxygen gas is being generated in the presence of large excess of hydrogen gas and in the presence of a good catalyst (the hydrogen electrode). The reaction of hydrogen and oxygen gas is exothermic, so excess heat is generated by the cell which must be removed. The NiH_2 cell is capable of accepting extreme amounts of overcharge if this heat is removed. Even so, the cell temperature begins to rise near full state-of-charge and provides an indication, along with the pressure, that full charge has been achieved.

In an IPV battery each cell is mounted in a thermal sleeve which serves as a heat sink to conduct excess heat from the cell into the battery baseplate. This is fairly efficient thermally, but the sleeve adds weight and cost to the battery. The approach to thermal design in the DPV battery is more direct and cost and weight efficient. A thin thermal shim is inserted between each pair of adjacent cells so that each cell has a thermal shim contacting both flat sides of the pressure vessel. The shim is made from aluminum, which is a very thermally conductive material. The shim is electrically insulated from, and thermally coupled to, the metal pressure vessel by a thin layer of electrically insulating but thermally conductive material. The material is space-rated and is currently used for the same purpose in IPV batteries. Each shim has a flange which contacts the battery baseplate. This provides a direct thermal path from the cell pressure

vessel into the baseplate, which acts as a heatsink. The baseplate would either contact a thermal radiator in the spacecraft or would act as a radiator itself. A thermal shim directly contacts the large flat surface of the pressure vessel on both sides of each cell. This provides a large cross-sectional area through which heat can be removed from the internal electrode stack. The electrode stack has a large thermal cross-section with respect to the pressure vessel because the stack directly contacts the flat pressure vessel wall. In the IPV cell in Figure 1, the electrode stack is perpendicular to the cylindrical pressure vessel wall with no direct contact between the electrode stack and the pressure vessel. Heat can only be rejected by the electrode stack across a narrow hydrogen gap between the electrode stack and the pressure vessel wall. The DPV provides a more direct thermal path for heat rejection by the cell.

DESIGN PERFORMANCE ANALYSIS

DPV Design Performance Parameters

Some important differences exist between the IPV and DPV cell designs, especially the inherent cost advantage of the DPV cell. The standard IPV cell uses an Inconel alloy pressure vessel and the cell closure girth weld is done using an electron beam welder. The DPV cell pressure vessel is stainless steel and uses a laser weld closure. The DPV design uses an advanced polymeric separator material as opposed to zirconium-oxide cloth, which is a significant cost reduction. The DPV cell also uses a new design hydrogen electrode which greatly reduces the catalyst loading, and therefore the cost, of the electrode and the cell. Alternative hydrogen electrode substrate material and lower cost gas diffusion membrane material also provides additional cost reduction. The lower cost, improved specific energy fiber nickel electrode is also baselined for the DPV design. This nickel electrode provides higher specific energy and ultimately lower cost. The baseline design also calls for using 26% aqueous potassium hydroxide as the electrolyte, instead of the standard 31%. This provides some benefit in increasing the cycle life of the nickel electrode. The DPV uses a prismatic electrode stack which is much more efficient than the standard cylindrical electrode stack. Rectangular cell components produce less waste when cut to size from the stock material, which is also rectangular. The nickel electrode stock, separator material and gas diffusion membrane are all produced in a roll with a fixed width. Die-punching circular components for the IPV cylindrical electrode stack leaves a significant amount of material which is unusable. This scrap must be added to the overall cost of the cell.

In Table 1, the overall performance parameters are compared for a state-of-the-art, high energy density IPV cell design and the DPV cell. The IPV cell is a standard 90 mm diameter design (76 Ah) and yields the highest energy density currently available in a high reliability, long cycle life NiH_2 cell. The DPV cell is listed in two design configurations. The first uses current design aerospace sintered nickel electrodes and the second is based on advanced fiber nickel electrode technology. Since the nickel electrodes account for about 40% of the total cell weight, any improvement in the nickel electrode will have a significant effect on cell level specific energy. The 76 Ah IPV cell delivers 53.1 Whkg-1 and 52.2 Whl-1. This is a fully qualified cell design which has completed many successful hours in spaceflight operation. The DPV cell design (70 Ah), using the same nickel electrodes as the 76 Ah cell, delivers 61.2 Whkg-1 and 73.5 Whl-1. The improvement in specific energy results primarily from the increased design simplicity of the DPV cell and a reduced internal parts count. The prismatic electrode stack in the DPV cell has a larger cross-section than the electrodes in the 90 mm IPV cell. This results in a reduced number of electrodes, and associated components, required to deliver the same capacity.

The second DPV cell uses an advanced fiber-based nickel electrode. This nickel electrode has approximately 25% higher specific energy than the standard sintered nickel powder aerospace electrode. All of the other design aspects of the cell are the same as the other DPV cell. The increase in the specific energy of the nickel electrode results in an increase of the cell capacity to 85 Ah with a slightly lower overall cell weight. The cell specific energy increases to 76.2 Whkg-1 and the energy density increases to 89.3 Whl-1. With more capacity in the same cell volume, this cell design will operate at a higher pressure and would require a slightly heavier pressure vessel. This cell design results in a substantial increase in performance compared to a state-of-the-art IPV cell. However, the fiber-based nickel electrode which enables this performance increase has not yet been spaceflight qualified. Testing and qualification of the fiber nickel electrode is an important issue which is currently being addressed.

Table 2 is a comparison of performance parameters for the IPV and DPV designs at the full battery level. Each battery contains 22 cells for an output voltage of 28 VDC. A current production 45 Ah IPV battery is used for the baseline design for comparison purposes. The DPV is compared in two configurations. One design uses the current sintered aerospace nickel electrode and the second design uses the advanced fiber-based nickel electrode. The current IPV battery yields 42.0 Whkg-1 and 28.7 Whl-1. This is substantially lower than the IPV cell. This reflects the inefficiency which results in packaging the IPV cell into a battery. The specific energy of the IPV cell is 53.1 Whkg-1 and the specific energy of the IPV battery is 42.0 Whkg-1. This corresponds to a packaging factor of 1.26, i.e. a reduction in specific energy of 26% occurs in transitioning from the cell to the battery. By comparison, the DPV cell has a packaging factor of about 1.10, in transitioning to the full battery design. The DPV cell delivers 61.2 Whkg-1 and the battery yields 56.6 Whkg-1 for the lower energy version. The DPV cell yields 76.2 Whkg-1 and the battery delivers 70.4 Whkg-1 for the advanced high energy version (fiber nickel electrodes). In other words, a larger percentage of the total battery weight is the weight of the cells, rather than battery packaging components. All of the energy storage is provided by the cells. The battery packaging components add mass but not energy storage, so specific energy is decreased from the cell level. The DPV design inherently requires less battery packaging mass and therefore maximizes the battery specific energy. Similar significant improvements are observed in the volumetric efficiency (energy density) of the cell and battery.

CONCLUSIONS

The nickel-hydrogen electrochemical energy storage system provides the best reliability, performance and cycle life available in an aerospace qualified battery system. The dependent pressure vessel cell design provides an important advance in this critical aerospace battery technology. The DPV cell and battery design is in the preliminary stages of full spaceflight qualification. The technology will provide a substantial improvement in the mass and volume performance of the NiH_2 battery system. An advanced DPV design delivers 76.2 $Whkg^{-1}$ at the cell level and 70.4 $Whkg^{-1}$ at the full battery level. This represents a 43% increase in specific energy at the cell level and a 67% increase at the battery level, compared to standard IPV flight technology. Volumetric energy density is increased by 70% at the cell level and 100% at the battery level, in comparing the DPV design with the established IPV cell and battery design. Testing and qualification is still required to fully qualify the DPV design for spaceflight applications.

	IPV[1] Cell	DPV[2] Cell	DPV[3] Cell
Capacity (Ah)	76.0	70.0	85.0
Voltage (V)	1.25	1.25	1.25
Diameter (cm)	8.9	19.7	19.7
Length (cm)	29.2	-	-
Thickness (cm)	-	3.9	3.9
Mass (g)	1790	1430	1395
Specific Energy (Wh/Kg)	53.1	61.2	76.2
Energy Density (Wh/l)	52.2	73.5	89.3

1. Current flight cell
2. Projected - Based on current aerospace nickel electrode
3. Projected - Based on advanced microfiber nickel electrode

Table 1. Performance Comparison of the Advanced DPV Cell Compared to the IPV Cell

	IPV[1] Battery	DPV[2] Battery	DPV[3] Battery
Capacity (Ah)	45.0	70.0	85.0
Voltage (V)	28.0	28.0	28.0
Length (cm)	63.2	47.0	47.0
Width (cm)	36.3	40.6	40.6
Height (cm)	19.2	21.6	21.6
Mass (kg)	30.0	34.6	33.8
Specific Energy (Wh/Kg)	42.0	56.6	70.4
Energy Density (Wh/l)	28.7	47.5	57.7

1. Current flight battery
2. Projected - Based on current aerospace nickel electrode
3. Projected - Based on advanced microfiber nickel electrode

Table 2. Performance Comparison of the DPV Spacecraft Battery Compared to the Standard IPV Battery

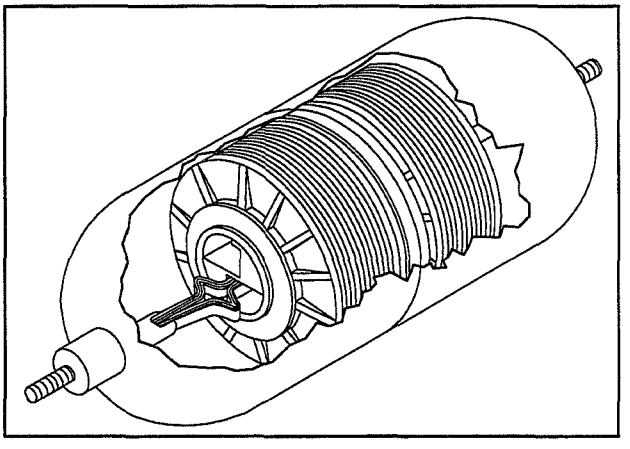

Figure 1. Typical Dual-Stack Individual Pressure Vessel (IPV) Ni-H_2 Spacecraft Battery Cell Design

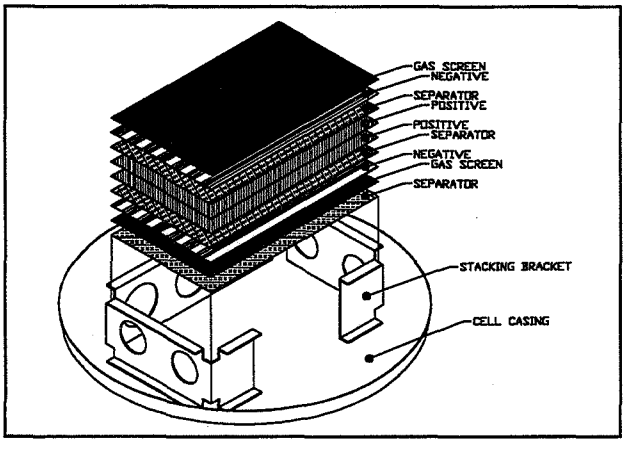

Figure 2. Dependent Pressure Vessel (DPV) Cell Internal Electrode Stack Construction Showing Arrangement of Cell Components

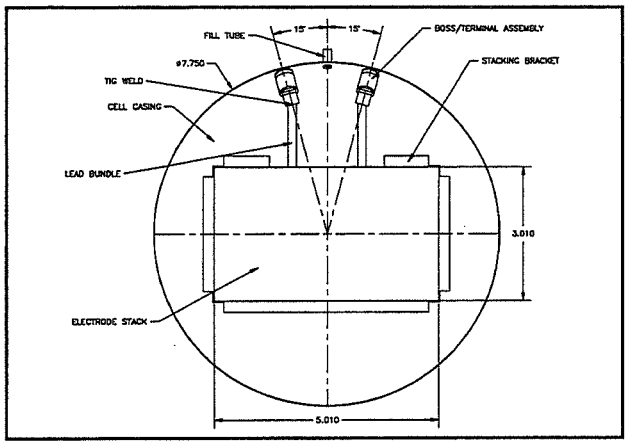

Figure 3. Dependent Pressure Vessel (DPV) Battery Cell Mechanical Design Showing Overall Cell Dimensions

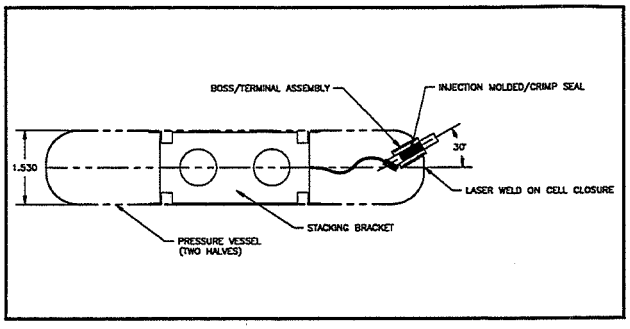

Figure 4. Dependent Pressure Vessel (DPV) Cell Side View with Cell Terminal Design Detail

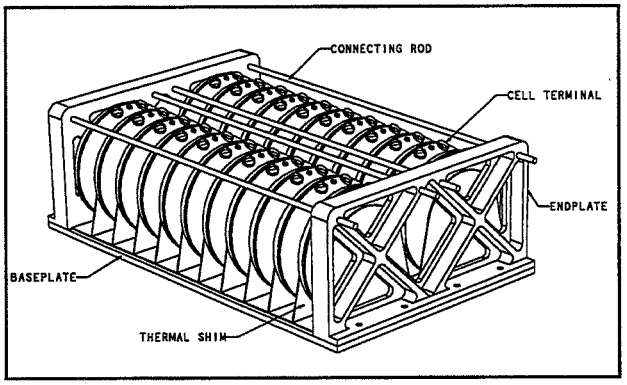

Figure 5. Compact DPV Spacecraft Battery Design Using Two Rows of Cells. The Battery Contains 22 Individual Ni-H_2 Cells for an Output Voltage of 28.0 VDC.

56-44
088444

ELECTROLYTE MANAGEMENT CONSIDERATIONS IN MODERN NICKEL HYDROGEN AND NICKEL CADMIUM CELL AND BATTERY DESIGNS

Lawrence H. Thaller and Albert H. Zimmerman
The Aerospace Corporation
El Segundo, California

056900
20 p.

ABSTRACT

In the early 1980s, the battery group at the NASA Lewis Research Center (LeRC) reviewed the design issues associated with nickel hydrogen cells for low-Earth orbit applications. In 1984, these issues included gas management, liquid management, plate expansion, and the recombination of oxygen during overcharge. The design effort by that group followed principles set forth in an earlier LeRC paper that introduced the topic of pore size engineering. Also in 1984, the beneficial effect of lower electrolyte concentrations on cycle life was verified by Hughes Aircraft as part of a LeRC-funded study. Subsequent life cycle tests of these concepts have been carried out that essentially have verified all of this earlier work. During the past decade, some of the mysteries involved in the active material of the nickel electrode have been resolved by careful research done at several laboratories.

While attention has been paid to understanding and modeling abnormal nickel hydrogen cell behaviors, not enough attention has been paid to the potassium ion content in these cells, and more recently, in batteries. Examining the potassium ion content of different portions of the cell or battery is a convenient way of following the conductivity, mass transport properties, and electrolyte volume in each of the cell or battery portions under consideration. Several of the consequences of solvent and solute changes within fuel cells have been well known for some time. However, only recently have these consequences been applied to nickel hydrogen and nickel cadmium cell designs. As a result of these studies, several unusual cell performance signatures can now be satisfactorily explained in terms of movement of the solvent and solute components in the electrolyte.

This paper will review three general areas where the potassium ion content can impact the performance and life of nickel hydrogen and nickel cadmium cells. Sample calculations of the concentration or volume changes that can take place within operating cells will be presented. With the aid of an accurate model of an operating cell or battery, the impact of changes of potassium ion content within a potential cell design can be estimated. All three of these areas are directly related to the volume tolerance and pore size engineering aspects of the components used in the cell or battery design. The three areas follow.

1. The gamma phase uptake of potassium ion can result in a lowering of the electrolyte concentration. This leads to a higher electrolyte resistance as well as electrolyte diffusional limitations on the discharge rate. This phenomenon also impacts the response of the cell to a reconditioning cycle.

2. The transport of water vapor from a warmer to a cooler portion of the cell or battery under the driving force of a vapor pressure gradient has already impacted cells when water vapor condenses on a colder cell wall. This paper will explore the convective and diffusive movement of gases saturated with water vapor from a warmer plate pack to a cooler one, both with and without liquid communication.

3. The impact of low-level shunt currents in multicell configurations results in the net movement of potassium hydroxide from one part of the battery to another. This movement impacts the electrolyte volume/vapor pressure relationships within the cell or battery.

INTRODUCTION

During the development of the fuel cell technology that is now used on board the Space Shuttle, the concepts of optimum volume and volume tolerance became quantitative characteristics that were assigned to different cell designs. A previous paper details the general principles of pore size engineering as applicable to alkaline cells and batteries.[1] Briefly, optimum volume denotes the volume of electrolyte at which a particular fuel cell design has its highest performance. Volume tolerance refers to the amount of change in electrolyte volume that can take place within a cell that still leaves it operating in an acceptable manner. Alkaline fuel cells are designed to be filled with a designated amount of electrolyte, which is to remain within each cell. This situation is similar to that of nickel hydrogen or nickel cadmium cells. With the increased interest in more than one cell within a single container, some nickel hydrogen devices are even more closely related to alkaline fuel cells from an electrolyte management point of view. The volume tolerance and optimum volume characteristics of battery cell designs are generally not highlighted even though they are present.

Over the past two decades, there has been a gradual increase in the availability of data bases developed during the life cycle testing of different cell designs. From the scatter in the longevity seen in these cycling tests, and from the results of examining internal components after disappointing cycling performances, it can be safely concluded that inappropriate cell designs or components were used to produce some of these cells. If the instances of poor quality plate and improperly prepared asbestos are eliminated, there still exists a number of reported and unreported cases of disappointing life cycle tests that can be assumed to result from inappropriate cell or battery design.

Earlier NASA reports addressed design considerations for nickel hydrogen cells.[2,3] These considerations emphasized the management of gas movement, electrolyte volume changes, internal heat generation, and expansion of the positive plates over the life of a cell. The beneficial effects of using lower concentrations of KOH were also noted. This paper will review several other phenomena that were not included in these earlier publications. The impacts of these other phenomena, based on volume tolerance considerations, will also be outlined. Where available, appropriate literature citations will be referenced. Sample calculations will review the techniques used to estimate the changes in electrolyte volumes that result from these phenomena. The modeling studies currently in place and under development within The Aerospace Corporation will be described, as well as how these models can be used to explore the design features of candidate cell configurations, as they may be affected by volume tolerance considerations.

PHENOMENA IMPACTING ELECTROLYTE QUANTITY AND CONCENTRATION

Potassium Uptake by Nickel Electrode

The operation of the nickel hydroxide electrode in alkaline battery cells has been known for years to involve a number of electrochemical and chemical reactions. These reactions allow the nickel-containing active materials in this electrode to cycle between several solid-state compounds (phases). One of these phases, generally labeled as γ-NiOOH, has been found by a number of researchers to absorb

potassium from a KOH electrolyte solution as it forms.[4,5] The quantity of potassium absorbed per mole of nickel atoms has been found to be between 0.25 and 0.33 mole. The simplest measure of this potassium uptake is illustrated by measurements of weight increase in nickel electrodes, as indicated in Figure 1.[6] These basic measurements indicate material being absorbed from solution to the extent of 0.30 to 0.32 mole KOH per nickel atom. It is assumed that the solid phase has a limiting nickel oxidation state of 3.67, an assumption that is consistent with thin film electrode capacity studies. This stoichiometry suggests the compound, $Ni_3O_6H{\cdot}KOH$, as a more accurate representation of γ-nickel oxyhydroxide. The formation of γ-phase in an operating battery cell will therefore involve the uptake of 0.33 potassium hydroxide units per nickel atom. As the KOH is withdrawn from the electrolyte, there is a reduction in its conductivity, diffusional limiting current, and volume.

Movement of Water Vapor Under the Influence of a Temperature Gradient

When a temperature difference is present within a cell or battery, water vapor may be transported from one part of the cell to another in order to maintain conditions of constant vapor pressure (isopiestic) within the device. The condensation of water vapor onto a cold surface from the humid air within a room is an illustration of maintaining isopiestic conditions. This situation has been experienced within operating nickel hydrogen cells to the extent that performance was adversely affected and cycling had to be interrupted. The paper by Earl et al. covers the example of a volume tolerance problem that was introduced by a temperature gradient from the plate pack to the lower cell dome.[7] Another example of volume tolerance problems are found in a paper that mentions that early performance problems were rectified by opening the cells and submitting them to a reactivation procedure.[8]

Redistribution of Potassium Hydroxide as a Consequence of Shunt Currents

A third situation possibly present in multicell devices starts with a shunt current caused by an inadvertent electrolyte film bridging from one cell to another. Besides causing an electrical inefficiency, this process slowly results in the net movement of solute from one cell to the next as dictated by the transference numbers of the individual ions. This situation did arise in one fuel cell, which will be described in more detail in a later section.[9]

VOLUME TOLERANCE CHARACTERISTICS OF BATTERY CELLS

Volume tolerance characteristics will only be treated in generalities because of the extensive nature of the topic. Briefly, the pore size character of the components is fixed by the physical properties of the electrodes. It is only the pore character of the separator and the compression of the components within the cell that can be selected by the designer. Alkaline fuel cells incorporate a separate electrolyte reservoir plate that accommodates changes in electrolyte volume without affecting the electrolyte quantities within the separator or electrodes. This is accomplished by proper selection of the pore size of this cell component. The reservoir, by virtue of its rather open pore structure relative to the separator and the wetable portions of the gas electrodes, maintains the proper amount of electrolyte in the electrode and separator portions of the cell. In battery cells, electrolyte changes over the course of a charge-discharge cycle as well as with time must be considered. The separator is generally used as the reservoir. There is an increasing degree of coarse pore character from asbestos to zircar to pellon, which permits more electrolyte to be stored. With zircar, care must be taken not to completely fill the large pores, since in the past, this has resulted in early failures due to excessive popping damage to the hydrogen electrode. As reported by Fuhr, overly wet zircar cells, when laid on their side, had problems during life cycle testing.[10] It was suggested that the excess electrolyte formed a pool along the bottom of the cell and as

the oxygen bubbles built up behind the electrolyte-filled separator, there were occasional large pops due to the energetic recombination of oxygen with the hydrogen on the hydrogen electrode.

An accurate cell component model incorporating the pore size distribution of the individual cell components would be very helpful in exploring the volume tolerance aspects of candidate nickel cadmium and nickel hydrogen cell designs.

SAMPLE CALCULATIONS

The following sections will describe a number of examples where changes in electrolyte volume and concentration can take place within an electrode, a plate pair, or a plate pack. These changes can result from a variety of driving forces that are present in ground-based or on-orbit conditions. Temperature control and thermal gradients are very important to the maintenance of proper electrolyte distribution within a cell or battery. Also, the volume tolerance characteristics of these cells or batteries, although possibly less well understood, often make the difference between good cell performance and cell failure. In each of the following examples, the driving forces tending to disrupt the distribution of electrolyte will be described. If there are any forces that would tend to restore proper electrolyte distribution, they will also be noted. The steps involved in estimating the steady-state conditions within the cell or battery as a consequence of these disruptive forces will then be outlined. The solutions will be given in terms of the ratio of the final volume to the initial volume (V/V_o).

Effects Related to Potassium Uptake by Nickel Electrodes

In this section, various conditions of operation that are common to nickel hydrogen battery cells are considered that can influence the performance as related to potassium uptake by the active material. While the same general issues are important in nickel cadmium cells, the nickel hydrogen cell environment results in more rapid potassium uptake, largely due to the more efficient nickel electrodes typically used and the reactions of hydrogen gas within the nickel electrode.[11] Clearly, any performance problems related to potassium uptake will strongly depend on the dynamics of electrolyte movement within the cell stack, as well as the temperature of the cell and many other variables. Here, we give an overview of how some of the major operating and design variables relate to potassium uptake.

A fully integrated model of the nickel hydrogen battery cell has been developed, as described in references 12-14. This model includes all electrochemical and physical processes that are known to occur in nickel hydrogen battery cells, as well as realistic three-dimensional sintered substrate structures within the nickel electrodes. When simulating nickel hydrogen cell performance during many cycles, it was discovered that gradual conversion of the charged β-NiOOH to the γ-phase occurred. While this conversion resulted in an increase in total stored capacity, it seemed to degrade discharge voltage performance under some conditions. This degradation resulted from an overall reduction in the concentration of the electrolyte as potassium was absorbed into the γ-phase during operation. The problems in cell performance resulted from two effects. First, the diminished electrolyte volume associated with the lower electrolyte concentration tended to starve the separator for electrolyte, thus increasing cell impedance. Second, at low KOH concentrations, the hydrogen electrode could become starved for hydroxide ions at high discharge rates, thus developing a large concentration polarization and forcing the cell to a very low discharge voltage. It was assumed in all these simulations that the γ-phase discharged to an α-phase that retained the potassium until it dissolved and recrystallized as β-$Ni(OH)_2$ via an Ostwald ripening process.

Discharge rate is a significant factor in the potassium ion issue since this is what depletes the hydroxide at the negative electrode. Figure 2 exhibits the electrolyte concentration profiles found between positive and negative electrodes at different discharge rates, along with the resulting discharge voltage profiles. We use a C/2 discharge rate as a standard for performance comparisons, because this is a typical operational discharge rate for nickel hydrogen battery cells. Typically, if KOH concentration drops below about 10% in the cell, it is impossible for the normal cell transport processes to maintain adequate electrolyte in the separator and negative electrode. Clearly, it is necessary to have adequate quantity and concentration of KOH electrolyte in the cell if this condition is to be avoided. Figure 3 indicates the depletion in concentration as γ-phase forms with different starting volumes of electrolyte. Figure 4 indicates the situation where a relatively dry cell that worked very well with 38% KOH would experience real performance problems with 31% KOH, or where a cell with 26% KOH would not work as well as with 31% KOH. Clearly, the selection of amount and concentration of KOH is an issue that needs to be traded off against the increased cycle life that is possible with lower electrolyte concentrations. By including sufficient KOH volume in the cell (held within appropriate reservoirs), it is also possible to realize the high cycle life capabilities of lower KOH concentration, while maintaining good performance for situations where significant γ-phase is formed.

The results indicated in Figure 4 suggest a reason for the generally puzzling observation that cycle life for nickel hydrogen cells improves as KOH concentration decreases down to 26%, but that cycle life decreases almost catastrophically if the KOH concentration drops much below 26%.[15] With sufficient electrolyte, or with alternative charge and discharge test profiles, it should be possible to operate cells containing well below 26% electrolyte. Thus, the optimum electrolyte concentration within any cell is determined by cell design and operation, as well as by electrolyte volume and the expansion of the nickel electrodes during cycle life operation.

It is clear that the effects of potassium uptake in the nickel electrode depend on the rate and extent of formation of γ-phase active material. The rate of γ-phase formation depends on the structure of the nickel electrode, cobalt additives, overcharge time and rate, temperature and thermal gradients, open-circuit stand, and the cell cycling profile. Our nickel hydrogen cell model has been utilized here to indicate how the rate of γ-phase formation depends on these variables. Applying this general modeling approach to the evaluation of the performance of the nickel hydrogen cell, it is possible to identify and develop designs that will perform reliably and with margin over a wide range of conditions.

The application of extended amounts of overcharge, particularly at higher rates, has long been known to build up significant quantities of γ-phase, while decreasing the KOH concentration as this phase forms. Since extended overcharge itself is generally regarded as stressful to the cell components, this condition is typically avoided in operational cells. However, since the γ-phase discharges at a lower voltage than does the β-phase, repetitive cycles with even small amounts of overcharge can build up large amounts of γ-phase. Figure 5 exhibits the discharge performance for cells that have experienced differing amounts of overcharge, and which contain about 3.0 g of 31% KOH/Ah of capacity. Figure 5 clearly indicates a marked drop in discharge voltage as the amount of overcharge and the quantity of γ-phase increases. As seen in the figure, greater capacity does not always guarantee better battery performance. Figure 6 indicates the effect of extended cycling on performance. As the nickel hydrogen cell is cycled repetitively to a given depth of discharge (DOD), the amount of γ-phase present increases and finally approaches the quantity of material that is not repetitively cycled. This effect provides the 30-40 mV memory effect that is commonly seen in nickel electrodes that have not been recently reconditioned. As indicated in Figure 6, these changes can result in a significant drop in end-of-discharge voltage, as well as a characteristic depressed discharge voltage during the final discharge of cell capacity.

Cell temperature is very important to the rate of formation of γ-phase, since this rate is dictated by the potential that the cell can reach before oxygen evolution commences at a high rate. At low temperatures (0°C), γ-phase forms very rapidly, while at higher temperatures (20 °C), large amounts of γ-phase are difficult to form by simple overcharge of the cell. Figure 7 indicates the effects of temperature on the C/2 discharge voltage signatures for a typical nickel hydrogen cell with about 3.0 g of 31% KOH/Ah. Depressed discharge voltage clearly is much more of a problem at the lower temperatures.

In a nickel hydrogen cell, the catalytic reactions of the hydrogen gas with the metallic nickel in the nickel electrode initiate conversion of β-phase to γ-phase during open-circuit stand. This conversion can lead to an unusual distribution of active material phases, which is impossible to achieve through normal charge/discharge operation, as indicated in Figure 8. These reaction and conversion processes are one major reason why large amounts of residual capacity can be completely isolated by the layers of discharged material formed during extended open-circuit stand. These processes can also fully convert the stored charge in a nickel hydrogen cell into the γ-phase, which, as indicated in Figure 9, will give a quite depressed discharge voltage signature if insufficient electrolyte is present in the cell.

Cell design is critical to whether the formation of γ-phase constitutes a long-term performance problem. Thermal designs that produce large thermal gradients between the top and bottom of a cell (particularly in dual stack cells) can give depressed discharge voltages only during portions of the discharge. In nickel cadmium cells, these thermal design issues are not as significant as in most nickel hydrogen cell designs, simply because each nickel electrode has a negative electrode on each side. The equivalent nickel hydrogen cell design (generally termed the dual anode cell) should be able to operate at much higher currents without significant voltage depression, simply because it allows twice the diffusional flux between positives and negatives. It is also important that the electrolyte concentration and volume guidelines discussed here be satisfied in each cell contained within a large multicell common pressure vessel (CPV) (single pressure vessel [SPV]). The designs used for SPV systems must also be robust enough to tolerate the changes in electrolyte distributions and any water vapor or oxygen transport between cells that can occur over life.

As discussed previously, nickel cadmium cells are also subject to losses in discharge voltage when significant quantities of γ-phase are formed, generally after extended shallow DOD cycling at low temperatures (below 10°C). These losses are expected to occur primarily when KOH volume falls below about 3 g/Ah, a correlation that has been previously made in nickel cadmium life tests. Reconditioning either a nickel cadmium or a nickel hydrogen cell will discharge all the γ-phase material, and at least temporarily will allow performance to return to normal. Since γ-phase can form predominantly in localized regions of cells in response to thermal gradients, it can result in high stress and accelerated degradation in these regions of the cell. Regular reconditioning provides a mechanism for eliminating this form of accelerated degradation as well as maintaining and monitoring performance in both nickel cadmium and nickel hydrogen cells. The mechanisms discussed here clearly suggest that regular reconditioning is most critical in battery cells that contain relatively low volumes of electrolyte. Cells containing over 4.0 g KOH/Ah are not as likely to realize major benefits from regular reconditioning, unless they are subjected to large thermal gradients.

Effects Caused by Temperature Differences

Single Plate Pack with a Cold Dome - Without Wall Wick. - The driving force for water vapor movement is the difference in vapor pressure between the electrolyte in the plate pack and water at the cold, lower dome. There are no restoring forces in ground testing since gravity holds the condensate at this dome. In satellite applications, restoring forces will depend on the low-level gravitational forces

induced by satellite movements, the surface tension characteristics of water, and the wetability characteristics of the inner cell wall. The situation of a single plate pack with a cold dome, without a wall wick, has been described in reference 7. This situation can be addressed using the vapor pressure relationships appearing in that reference and also in reference 16 (NASA Reference Publication 1314). Although the resolution of the chart in reference 7 is not good enough to permit accurate answers to the questions in the following examples, it does suffice to indicate the methods used in approaching these questions. Figure 10 depicts the single plate pack situation. The initial conditions follow. There is a solution of potassium hydroxide in the plate pack at an overall temperature T_1. The solution is not in equilibrium with pure water in the cold dome of the cell. The bottom of the plate pack is radiatively looking at the cold plate such that its temperature is T_2. The general approach to this problem proceeds as follows. Find the point on the concentration temperature curve (Figure 11) that describes the conditions of the plate pack at T_1 (point A). Find the point on the pure water line that corresponds to the colder temperature T_2 (point B). First, determine whether the vapor pressure of the pure water is lower than the vapor pressure of the electrolyte in the plate pack. If it is (yes, in this case), then water vapor from the warmer electrolyte under the driving force of a difference in vapor pressure will be evaporated from the electrolyte and condense onto the wall of the cold, lower dome. On the chart, this is accomplished by finding a point at T_1 that has a vapor pressure equal to the vapor pressure of pure water at T_2 (point C). At the new concentration for the electrolyte, and by knowing that the amount of solute KOH in the plate pack remains the same, the new volume and weight can be calculated. Two examples, starting with 26% KOH and 31% KOH in the plate pack, show the differences (as identified in the reference 7) that 26% KOH solutions are closer to their dew point than 31% KOH solutions. The 26% KOH solutions are thus more susceptible to water condensing at the cold, lower dome. Figure 12 shows the results of the two different starting electrolyte concentrations, for two different plate pack temperatures and various cold finger temperatures. Where the ratios of final volume to initial volume are 1.0, the vapor pressure of water corresponding to the dome temperature is still above the vapor pressure of the electrolyte in the stack, and there would be no driving force to condense water vapor at the cooler portion of the cell.

Depending on the volume tolerance characteristics of the particular cell design, a lower limit to the value of V/V_o would help in suggesting a lower limit to the cold finger temperature of the cold cell dome. The volume tolerance characteristics of any cell design are not only a function of the reservoir properties of the cell design, but it depend on the initial electrolyte volume, the expansion characteristics of the nickel electrode, and possibly other factors. Because of all these factors, the thermal gradients within a cell, and the selection of the electrolyte concentration and the method of heat removal from the cells, are very important. The use of thermal skirts, as opposed to centrally located thermal flanges, results in larger temperature differences between the top and bottom of the cell. When the bottom dome of the cell in is good radiative view of the cold plate, the situation can become exacerbated.

Single Plate Pack with a Cold Dome - with Wall Wick. This situation is similar to the one described in the preceding section, but now the capillary forces of the cell components act as a restoring force to return the water to the plate pack. The separators must, however, be in contact with the wetted cell wall and yet not act to block the free movement of gases within the cell. Several manufacturers offer cells that have a wetable layer of zirconia sprayed onto the interior wall of the cell case. This wall wick, as it is usually called, is also available with catalyzed strips to enable oxygen to recombine on the cell wall. Cell designs based on the Air Force or Man Tech designs employ wall wicks.

Two Or More Plate Packs at Different Temperatures - Without Wall Wick - Without Shunt Currents. - In this situation, one plate pack is at one temperature and another is at a different temperature. Communication of the water vapor, but not of the electrolyte, is allowed between the two plate packs (Figure 13). This communication can exist in a split stack IPV cell (cells built for HST) or a two-cell

or multicell CPV battery. In these cases, the amount of dissolved KOH in each stack remains constant, while the amount of water adjusts itself until the two units at the different temperatures have the same vapor pressure. At the start of the reequilibration process, solution 1, the warmer plate pack (point A on Figure 14), and solution 2, the cooler plate pack (point B), will be at the same concentration but at different temperatures (different vapor pressures). The final concentrations will drift towards the condition where the warmer stack will become more concentrated and the cooler solution will become more dilute as water vapor is transported from the warmer to the cooler portion of the cell or battery. Note that any horizontal line (e.g., 1, 2, or 3 in Figure 14) will designate two solutions that are in equilibrium over this temperature difference. However, the weight of KOH in each of the two stacks (no electrolyte communication) remains constant. Also, the sum of the two water amounts must be equal to the initial conditions following the establishment of isopiestic conditions. There will therefore be a unique solution to the problem of calculating the final concentration and volume of each part of the cell. Table 1 shows typical results of some sample calculations.

Two Or More Plate Packs at Different Temperatures - with Wall Wick - Without Shunt Currents. - This situation is similar to the preceding one, except that wall wicks or other devices permit electrolyte communication between the two stacks. However, there is no voltage difference between the two stacks. A split stack IPV cell with a wall wick (catalyzed or noncatalyzed) would be described by this situation. The solution for this situation (Figure 15) does not exist in closed form, but can be solved iteratively if the pore size distributions of the components are known. As in the preceding situation, it can be seen that, given a temperature gradient, water will be evaporated from the warmer stack and condense into the cooler stack. The concentration gradient that is established will attempt to equilibrate, and KOH will begin to move from the warmer to the cooler stack. Further, as depicted in Figure 15, the gravitational forces will tend to favor movement from the upper to the lower stack. The pore size character of the components will be the only restoring force in this situation, but can be significant in terms of being able to maintain an ample electrolyte quantity in the upper stack.

Consequences of Shunt Currents

There is a situation when two or more plate packs are at different temperatures, with electrolyte path and shunt currents. This situation is coupled with the requirement to maintain isopiestic conditions. The situation can arise in two-cell or multicell CPV batteries that are subject to small shunt currents caused by electrolyte film bridging from one cell to another.

This phenomenon was seen during a fuel cell development effort carried out at NASA LeRC. The program was with Pratt and Whitney Aircraft (now International Fuel Cells). The fuel cell stack was to be assembled from stack elements that had six cells placed side by side that were electrically connected in series (Figure 16a). The six cells were separated by elastomeric seals to preclude the communication of the electrolyte from one cell to the next. There was a common gas flow field across the back side of these six-cell plaques. This flow field permitted the equilibration of the vapor pressure of the electrolytes contained in the individual cells. The electrical connection from one cell to the next was accomplished by the screen used to support the anode catalyst of one cell and the cathode catalyst of the next (Figure 16b). In less than 1000 hr, it became evident that there was a problem with the performance of these six-cell units. Diagnostic evaluation was performed, based on the volume tolerance characteristics of the cells. It was deduced that one of the end cells was gradually being depleted of electrolyte and the cell at the opposite end was gaining in electrolyte volume. This can be understood in terms of the cumulative effects of a low-level shunt current, where the current is being carried partially by the potassium ions and partially by the hydroxide ions. The fraction being carried by each kind of ion is a function of the transference number of the two ion types. If we assume that the transference number for potassium ion is 0.2, then the Hittorf-type diagram in Figure 17 would suggest that the cell at the positive end of the

stack would tend to increase in concentration relative to the cell at the most negative end of the stack. Since the common gas plenum behind all six cells permitted the free movement of water vapor, the cell gaining in hydroxide tended to gain electrolyte volume as water was evaporated from the cell with the lower concentration and condensed into the one with the higher concentration (Figure 16a). Since the cells were all at the same temperature, the final concentration within each of the cells was constant. Only the volume changed as a consequence of the movement of water vapor. In this type of problem, it is not the magnitude of the shunt path that is important, but the cumulative effect of the passage of ionic species when the transference numbers are not 0.50.

There are two examples of contemporary nickel hydrogen devices that may be subject to this type of problem: the two-cell CPV and the multicell CPV. Multicell CPV designers are fully aware of this problem, and use plastic encasements fitted with hydrophobic plugs to preclude the establishment of shunt paths between adjacent cells. In two-cell CPV batteries, different schemes are used to isolate the electrolyte from electrolyte communication between the two series-connected cells. Potassium hydroxide films are very difficult to completely eliminate. For this situation, it is assumed that there is a connecting film 0.5 cm wide, 3 cm long, and 0.01 cm thick between the two stacks of a two-cell CPV battery. Figure 18 shows the results of this calculation when 0.2 is the transference number for potassium ion, 2.5 ohm-cm is the resistivity for potassium hydroxide, and 1000 hr is the time allotted.

Other Situations

It can be seen that a number of other situations could be mentioned. The same general approach used in the previous situations described could be used to investigate the volume tolerance aspects of those particular cell and battery designs. These other situations would be combinations of those already described, and their solutions are left to the reader. From the material presented here, it is seen that the following features of any cell and battery design must be understood before a cell design can be considered appropriate for the application for which it is being designed.

1. The pore size characteristics of each component and how they change over the cycle life of the application.

2. The physical dimensions of each component and how they change over the cycle life of the application.

3. The temperature profile within the cell over the range of performance of the battery.

4. The volume tolerance characteristics of the plate pack, cell, or battery.

SUMMARY

A mechanism for degradation in nickel cadmium and nickel hydrogen cells has been identified that involves the depletion of potassium hydroxide electrolyte in the separator and negative electrodes during high rate discharge. This mechanism, which has been simulated in a nickel hydrogen cell model, is initiated by the uptake of potassium by the nickel electrode when large amounts of γ-phase formation occur in the active material. Guidelines for choosing electrolyte volume and concentration combinations to avoid this problem were presented. These battery and cell performance problems are accentuated by extended overcharge, low temperature operation, extended cycling at low to moderate DOD, thermal gradients, extended open-circuit stand, and cell designs that limit KOH volume or transport below critical

levels. However, regular reconditioning provides an effective means to prevent these processes from causing permanent degradation to the cell components in both nickel cadmium and nickel hydrogen cells.

Other related phenomena, which were already known in principle, were examined as they pertain to volume tolerance considerations. The movement of water vapor and KOH under the influences of temperature gradients and shunt currents was examined for selected situations. The principles involved will permit the reader to explore other, more complicated, situations.

CONCLUSIONS

Several factors that affect electrolyte volume, concentration, distribution, and transport properties in alkaline cells have been reviewed. Reasonable estimates of what changes can take place as a consequence of these factors, and the importance of incorporating these considerations into modern cell and battery designs, have been established. In most cases, battery and cell designers have these general principles and concepts in mind, but lack an accurate way of factoring all of them into their designs. The resulting trial-and-error approach is both time consuming and expensive. However, a different approach, using mathematical cell models developed from first principles, represents an attractive alternative. The models, however, must be validated by real cell data and must be able to replicate a growing number of signatures from cells that have experienced life cycling difficulties due to inappropriate cell designs. At The Aerospace Corporation, cell and battery modeling studies are being carried out under the direction of Dr. Zimmerman to examine how these considerations impact modern power system designs. The modeling studies have already been able to explain cell and battery signatures that, at the time they first appeared, were not fully or logically explainable. As the results from these cell modeling studies become more accepted through validation, they could be used to predict the performance of existing cell designs under a variety of cycling and thermal situations. More important, cell and battery designers may be able to take advantage of the predictive nature of the studies. Thus, some of the extensive performance and life cycle testing could be eliminated that is currently required to validate an existing design under a new set of mission requirements or to suggest a new design for and upcoming mission.

REFERENCES

1. K. M. Abbey and L. H. Thaller, "Pore Size Engineering Applied to Starved Electrochemical Cells and Batteries," 17th IECEC, August 8-13, 1982, pp. 757-764.

2. J. J. Smithrick, M. A. Manzo, and O. Gonzalez-Sanabria, "Advanced Designs for IPV Nickel-Hydrogen Cells," 19th IECEC, August 19-24, 1994, pp. 631-637.

3. L. H. Thaller, M. A. Manzo, and J. J. Smithrick, "Design Principles for Nickel-Hydrogen Cells and Batteries," 20th IECEC, August 18-23, 1985, Vol. 1, pp. 145-150.

4. R. Barnard, C. F. Randell, and F. L. Tye, J. Appl. Electrochem. **10**, 109 (1980).

5. H. Bode, K. Dehmelt, and J. Witte, Electrochim. Acta **11**, 1079 (1966).

6. A. H. Zimmerman and P. K. Effa, Extended Abstracts of the Fall 1985 Meeting of the Electrochemical Society, Vol. 85-2, 43-44 (1985).

7. M. Earl, T. Burk, and A. Dunnet, "Method for Rejuvinating Nickel Hydrogen Battery Cells," 1992 IECEC, Vol. 1, pp. 127-132.

8. J. R. Wheeler, "High Specific Energy, High Capacity Nickel Hydrogen Cell Design," 28th IECEC, August 8-13, 1993, Vol. 1, pp. 89-94.

9. L. M. Handley, A. P. Meyer, and W. F. Bell, Pratt and Whitney Aircraft, "Development of Advanced Fuel Cell System," Phases 2 and 3, NASA -CRs-134818(1975) and 134721(1973).

10. K. H. Fuhr, "Failure Analysis of a 3.5 Inch, 50 Ampere-Hour Nickel-Hydrogen Cell," 1986 NASA Goddard Space Flight Center Battery Workshop, pp. 209-214.

11. A. H. Zimmerman, Proc. of the Symposium on Nickel Hydroxide Electrodes, D. A. Corrigan and A. H. Zimmerman (eds.), Vol. 90-4, The Electrochemical Soc. Inc., Pennington, N.J., 1990, p. 311.

12. A. H. Zimmerman, Proc. of the 1993 NASA Aerospace Battery Workshop, NASA Conf. Pub. 3254, 1993, p. 295.

13. A. H. Zimmerman, Proc. of the 29th IECEC, Amer. Inst. of Aeronautics and Astronautics, ISBN 1-56347-091-8, 1994, pp. 63-69.

14. A. H. Zimmerman, Proc. of the 1994 NASA Aerospace Battery Workshop, "Progress Towards Computer Simulation of NiH_2 Battery Performance Over Life" (to be published).

15. H. S. Lim and S. A. Verzwyvelt, J. Power Sources **22**, 213 (1988).

16. J. Dunlap, G. Rao, and T. Yi, NASA Handbook for Nickel-Hydrogen Batteries, NASA Reference Publication 1314, September 1993, p. I-19.

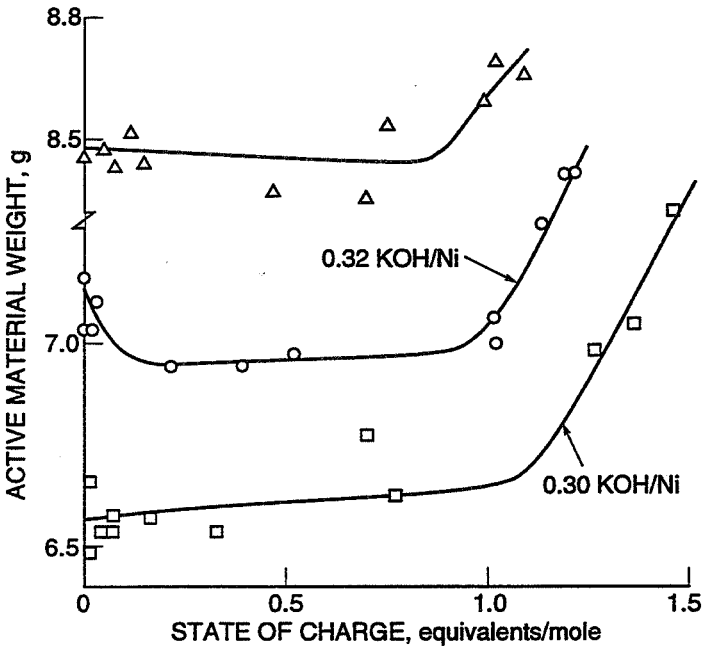

Figure 1. Weight of active material in a nickel electrode as a function of state of charge.

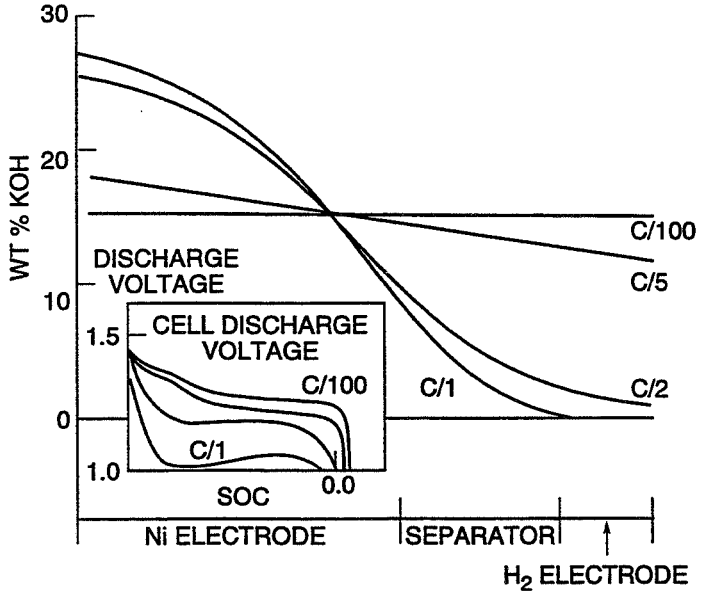

Figure 2. Concentration profiles across a nickel hydrogen cell during discharge at different rates.

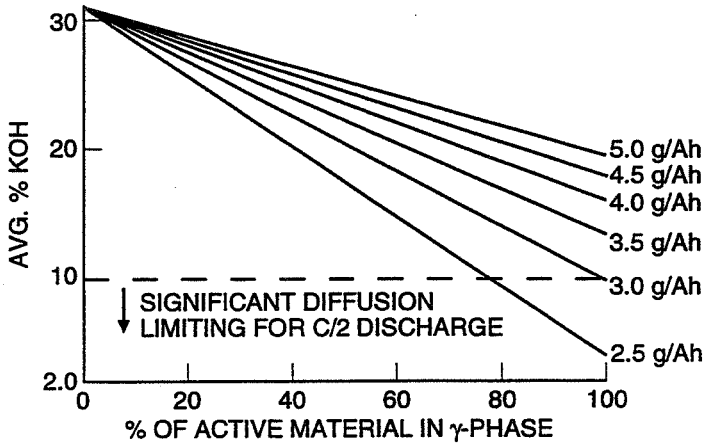

Figure 3. Effects of potassium uptake on average potassium hydroxide concentration.

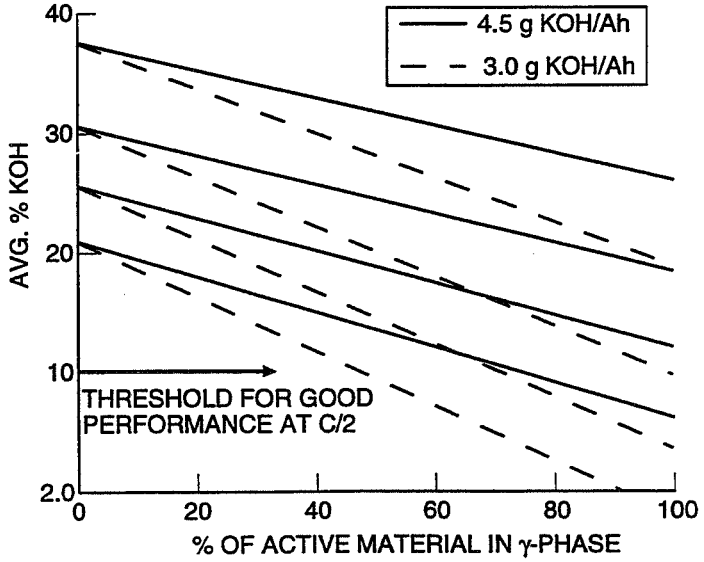

Figure 4. Effect of initial KOH concentration on average electrolyte concentration after potassium uptake occurs.

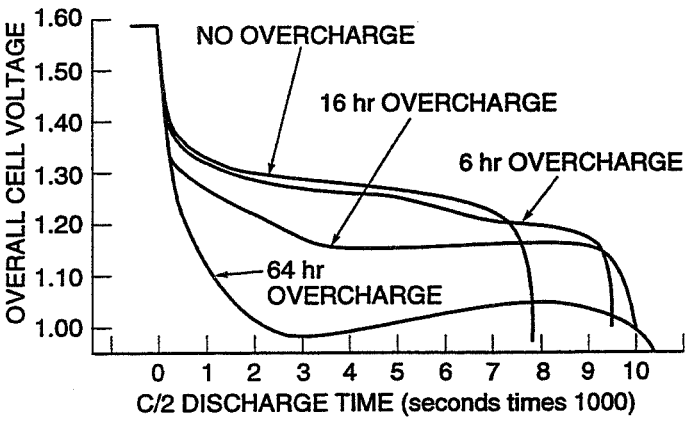

Figure 5. Effect of extended overcharge on C/2 discharge of nickel hydrogen cell containing 3.0 g/Ah of 31% KOH after various periods of C/10 overcharge.

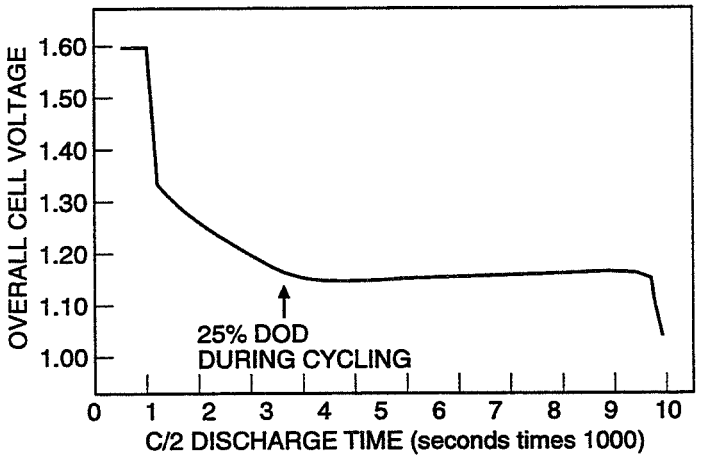

Figure 6. C2 discharge voltage after 1500 cycles at 25% DOD in a nickel hydrogen cell with 3.0 g/Ah of 31% KOH.

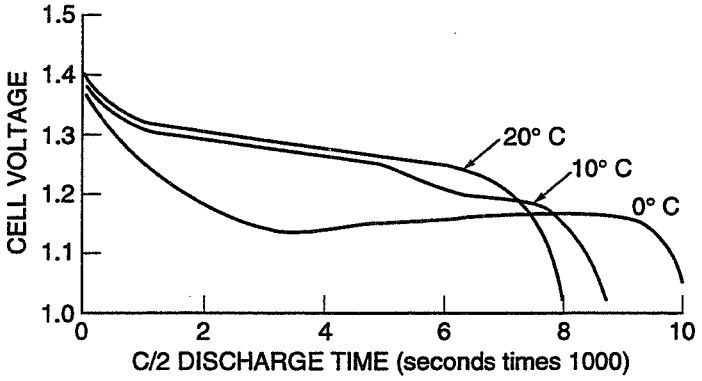

Figure 7. Effect of temperature on discharge voltage after 16 h charge at C/10 for a nickel hydrogen cell containing 3.0 g/Ah of 31% KOH.

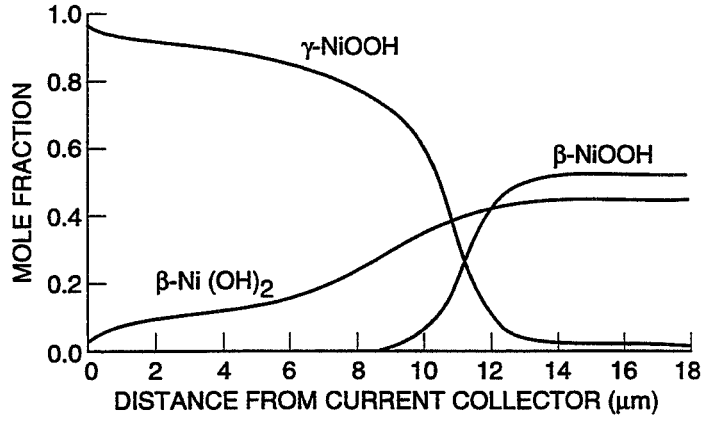

Figure 8. Unusual distribution of phases in nickel electrodes of a nickel hydrogen cell after 72 hours of open-circuit stand in the charged state.

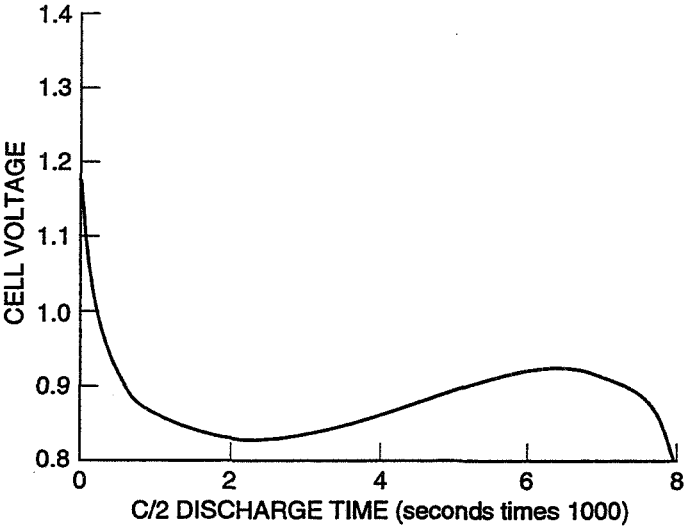

Figure 9. Discharge voltage after 72 hour open circuit stand in the charged state at 10° C in a nickel hydrogen cell with 2.8 g/Ah of 31% KOH.

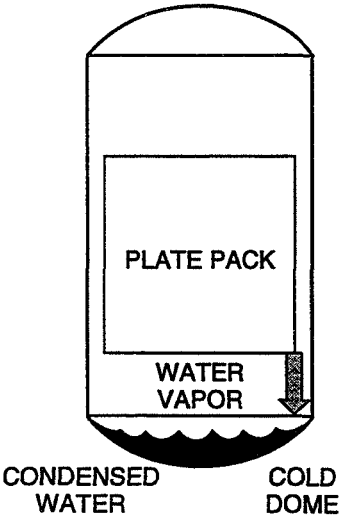

Figure 10. Schematic of a single stack IPV cell with condensing water at the cold lower dome and having no capillary return mechanism.

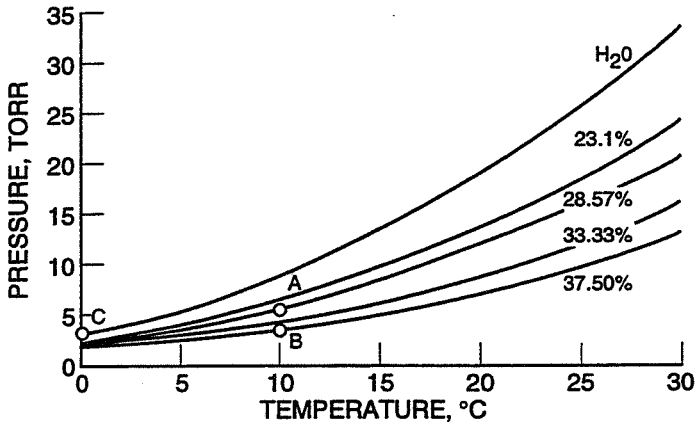

Figure 11. Vapor pressure characteristics of KOH solutions as a function of temperature.

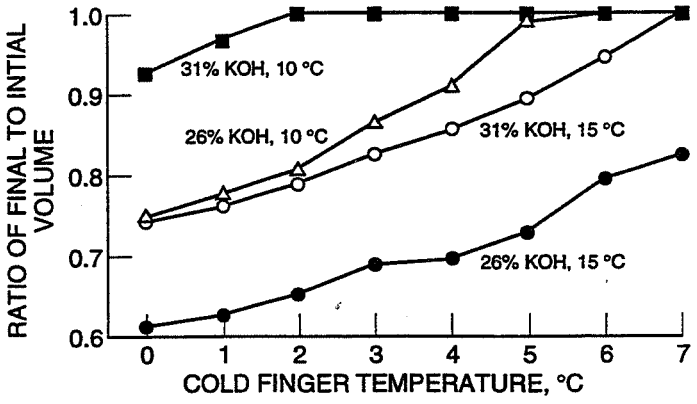

Figure 12. Electrolyte volume changes as a result of water loss as a function of cold finger temperature, temperature diffewrence, and electrolyte concentration.

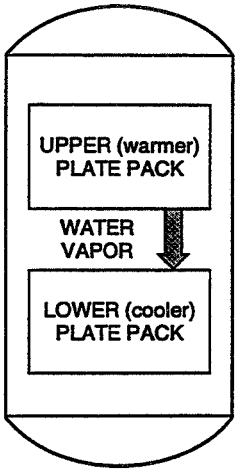

Figure 13. Schematic of a two-stack IPV cell or a two-cell or multi-cell battery subject to movement of water vapor resulting from temperature gradient and having no capillary communication between stacks.

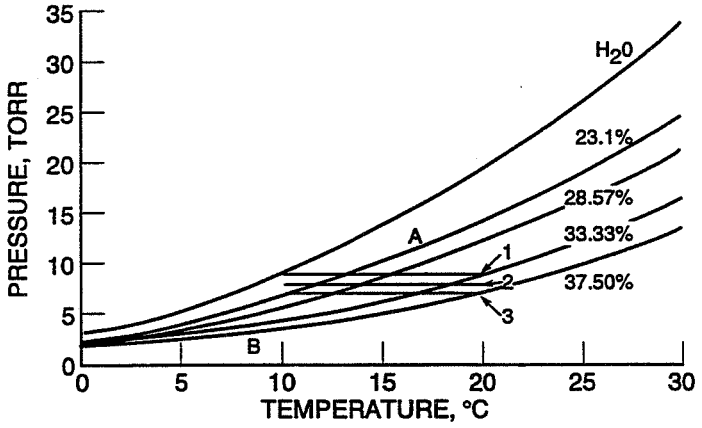

Figure 14. Trial and error solution technique to two-stack water redistribution example.

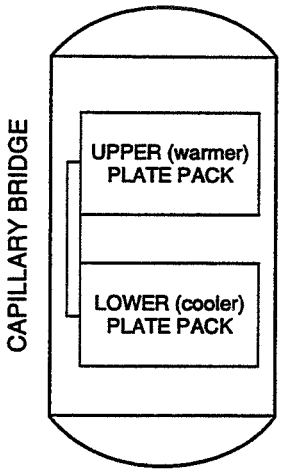

Figure 15. Schematic of a two-stack IPV where capillary communication between stacks is allowed.

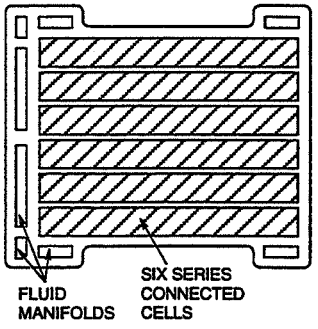

Figure 16.a.

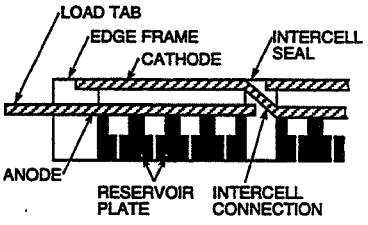

Figure 16.b.

Figure 16. a. Platform of six fuel cells connected in series and having a common gas plenum.
b. Cross section of a single cell.

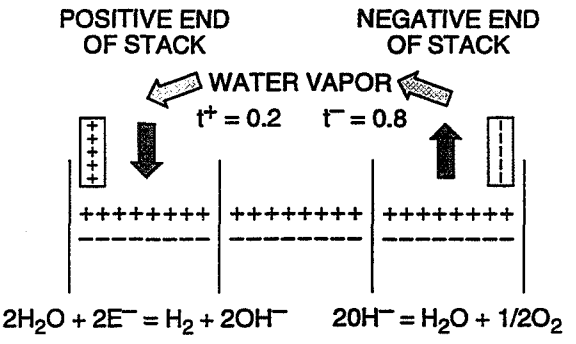

Figure 17. Hittorf-type schematic of shunt current situation resulting in the net movement of solute from one of the strings to the other.

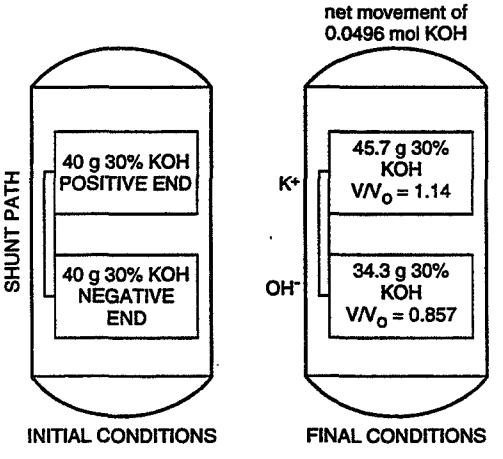
net movement of 0.0496 mol KOH
SHUNT PATH
40 g 30% KOH POSITIVE END
40 g 30% KOH NEGATIVE END
K^+
OH^-
45.7 g 30% KOH $V/V_o = 1.14$
34.3 g 30% KOH $V/V_o = 0.857$
INITIAL CONDITIONS
FINAL CONDITIONS

Figure 18. Estimated redistribution of solvent and solute following 1000 hours given a 1.5 K ohm shunt path between adjacent cells with KOH electrolyte.

Fuel Cells

Page intentionally left blank

57-44
008845

A NOVEL UNITIZED REGENERATIVE PROTON EXCHANGE MEMBRANE FUEL CELL

O.J. Murphy, A.J. Cisar, A. Gonzalez-Martin,
C.E. Salinas, and S.F. Simpson
Lynntech, Inc.
College Station, Texas

256905
18p.

ABSTRACT

A difficulty encountered in designing a unitized regenerative proton exchange membrane (PEM) fuel cell lies in the incompatibility of electrode structures and electrocatalyst materials optimized for either of the two functions (fuel cell or electrolyzer) with the needs of the other function. This difficulty is compounded in previous regenerative fuel cell designs by the fact that water, which is needed for proton conduction in the PEM during both modes of operation, is the reactant supplied to the anode in the electrolyzer mode of operation and the product formed at the cathode in the fuel cell mode. Drawbacks associated with existing regenerative fuel cells have been addressed. In a first innovation, electrodes function either as oxidation electrodes (hydrogen ionization or oxygen evolution) or as reduction electrodes (oxygen reduction or hydrogen evolution) in the fuel cell and electrolyzer modes, respectively. Control of liquid water within the regenerative fuel cell has been brought about by a second innovation. A novel PEM has been developed with internal channels that permit the direct access of water along the length of the membrane. Lateral diffusion of water along the polymer chains of the PEM provides the water needed at electrode/PEM interfaces. Fabrication of the novel single-cell unitized regenerative fuel cell and results obtained on testing it are presented.

INTRODUCTION

Starting with the Gemini Project in 1965, auxiliary power for manned U.S. spacecraft missions in earth or lunar orbit has been provided by fuel cells powered by cryogenic hydrogen and oxygen launched from earth[1]. This approach was determined to have lower weight than primary batteries or batteries recharged using solar energy converted to electrical energy via photovoltaic (PV) panels for missions up to several days. Furthermore, on considering the overall requirements of manned spacecraft missions this solution was found to be capable of providing additional benefits, e.g., spacecraft cabin heating/cooling for increased crew comfort (using fuel cell generated waste heat and cryogenic propellants as a cold source) and potable water for the spacecraft crew (derived from fuel cell product water). For long term spacecraft missions, launching of the propellant weight required renders this approach impractical. Because of the considerable improvements in performance and reliability of PV arrays in combination with rechargeable batteries (e.g., Ni-H2) as power sources for satellites, fuel cells using cryogenic propellants launched from earth will only be lighter than PV arrays/rechargeable batteries for manned spacecraft missions of the order of a few days.

For long-term manned space missions where sufficient solar intensity occurs the most effective power system capable of providing the necessary power during eclipse periods (in planetary orbit, planetary or lunar surface) must involve a secondary energy storage system that combines PV arrays with a high energy density storage system[2]. The PV arrays would provide all system power during periods of sunlight as well as providing power to recharge the high energy density storage system that can be subsequently used to provide power during eclipse periods. For such an application, low mass (and preferably low volume) with very high reliability and long cycle lifetime are required. Because of the paramount importance of reliability, no secondary

energy storage system can be considered which uses extensive mechanical circulation of fluids. For long-range manned space exploration missions, e.g., a lunar base or a Mars landing, the most effective high energy density storage system is likely to involve a regenerative fuel cell (RFC)[3,4].

RFCs may be of two types H_2-O_2 and H_2-X_2, where X_2 is a halogen[5,6]. Because of the more advanced nature of H_2-O_2 RFCs together with anticipated higher energy densities and greater reliability, these systems are preferred at present. In a H_2-O_2 RFC energy storage system water is electrolyzed on charge producing hydrogen gas at the negative electrode and oxygen gas at the positive electrode. The gases produced may be stored in separate pressure vessels, or in a single, suitably divided, pressure vessel. The reactions are reversed on discharge where hydrogen and oxygen gases are fed to the negative and positive electrodes respectively yielding water on being electrochemically combined. In principle, the same electrochemical cell stack module can be used for both charge and discharge processes in a RFC[3]. However, since the physical and chemical requirements differ at the oxygen positive in the charge and discharge modes[7] the tendency up to now has been to separate the functions of charge and discharge by using two distinct electrochemical cell stack modules.

The power requirements of unmanned satellites, e.g., for communications and surveillance applications, are continuing to increase as large sensors, antennas or other massive subsystems are included in satellite packages[8]. In addition, enhanced satellite capabilities, such as on board computer processing as found in the DOD Milstar satellite, greatly increase power needs. An advantage of H_2-O_2 RFCs, compared to rechargeable batteries, for supplying the high power levels of advanced satellites, is that they possess excellent peak power capabilities and, hence, could satisfy periods of extreme power demands, for example during intervals requiring power pulses[2]. They can provide at least 10 times the average or base power output. Another attractive feature of RFCs compared to rechargeable batteries is elimination of the problem of self-discharge, which in the case of the preferred battery for satellite applications, Ni-H_2, can be as high as 10% per day.

REGENERATIVE H_2-O_2 FUEL CELLS

Hydrogen-oxygen RFCs have been identified as an enabling technology for many long-term space applications, particularly those requiring large amounts of energy storage[9]. They are extremely advantageous for applications where high power, low weight, and very long cycle life are important. They can be made in a wide range of sizes, from a fraction of a kW to multi-megawatt, with a system efficiency which is generally largely independent of size. In the design of a regenerative H_2-O_2 fuel cell, two approaches may be followed[10]: (i) fuel cell and electrolyzer modules are separate entities (monofunctional system), and (ii) one module functions as both fuel cell and electrolyzer (unitized regenerative system). The use of the same electrochemical cell stack module for charge and discharge, that is, as an electrolyzer and as a fuel cell simplifies the system, considerably reduces the weight (and volume) of the overall energy storage system and greatly aids reliability[11].

As with primary fuel cells, RFC systems are classified by the electrolyte used in them. For space power applications the most attractive electrolytes would include alkaline, proton exchange membrane (PEM) and solid oxide. Of these systems it is now well established that PEM fuel cells using H_2-O_2 as reactants and PEM water electrolyzers can have very long operating lifetimes[5,11]. At present only alkaline and PEM fuel cells are capable of high energy conversion efficiencies and high power densities. Of these two systems, the PEM based RFC is the most attractive electrochemical power source for long-term space applications. This arises because of a number of attractive features that it possesses compared with the alkaline RFC system. These include: (i) low operating temperature; (ii) rapid cold start-up capability; (iii) no electrolyte volume

management; (iv) infinite life on standby open circuit condition; (v) very high reliability; (vi) capability of tolerating high reactant gas pressure differentials across the PEM electrolyte layer, and (vii) readily facilitates thermal and fluid management. Although the performance of PEM fuel cells is somewhat lower than that of the corresponding alkaline cells, giving slightly less efficiency, this is compensated for by increased reliability, particularly from the viewpoint of fluid management. Furthermore, PEM water electrolyzers are a few percent more efficient than similar alkaline electrolyzers.

Over the past few decades, a number of attempts have been made to produce a high efficiency, high power density unitized regenerative fuel cell (URFC), that is, where a stack of electrochemical cells could operate alternatively as an electrolyzer and as a fuel cell[12-17]. In all of these systems, one electrode in each cell was used for the oxygen reaction (oxygen evolution in the electrolysis mode and oxygen reduction in the fuel cell mode), while the other electrode functioned as the corresponding hydrogen electrode (hydrogen evolution in the electrolysis mode and hydrogen oxidation in the fuel cell mode). Electrodes capable of functioning in this manner are identified as bifunctional electrodes. However, for all these URFCs that have used bifunctional electrodes, reduced performance characteristics (low round trip energy conversion efficiencies at given operating current densities) have been obtained. This, and other drawbacks associated with existing URFCs, can be attributed to a number of problems: (i) incompatibility of electrode structures used for gaseous reactants (hydrogen and oxygen gases) in the fuel cell mode and liquid reactant (water) in the electrolysis mode; (ii) poor electrode kinetics associated with bifunctional oxygen electrodes; (iii) poor thermal and water management, and (iv) low cycle life.

The goal of the work described in this paper was to provide innovative solutions to these problems associated with previous URFC designs. To simplify the URFC stack design, fabrication and management, a polymeric perfluorosulfonic acid proton exchange membrane (PEM) was selected for use as the electrolyte. Primary fuel cells and water electrolyzers using PEMs as electrolyte have demonstrated efficiencies, voltage stabilities and lifetimes[5,11] desired in an advanced URFC energy storage system for long-term space applications.

PEM-BASED ADVANCED URFC DESIGN

Optimal Electrode Configuration and Preferred Electrocatalysts

Platinum, which is necessary for oxygen reduction (fuel cell mode) in acidic media, is a poor catalyst for oxygen evolution (electrolyzer mode). In order to overcome the limitations associated with bifunctional oxygen electrodes used previously, a new concept of bifunctional electrodes was explored[18,19]. In this concept, oxidation and reduction reactions were made to occur at electrodes, independent of whether an electrochemical cell was operating in the fuel cell mode or in the electrolysis mode. Thus, oxygen evolution (electrolysis mode) and hydrogen oxidation (fuel cell mode) took place alternatively at one electrode, the oxidation electrode. Correspondingly, hydrogen evolution (electrolysis mode) and oxygen reduction (fuel cell mode) occurred at the other electrode, the reduction electrode. With this new concept of bifunctional electrodes[18,19], it is much easier to select potential electrocatalyst materials for both electrodes. In addition, since electrodes are only used for either oxidation or reduction reactions in both modes of operation, the URFC should have an extended cycle life.

Since platinum, either as platinum black or as carbon-supported, high surface area, platinum particles, is the superior electrocatalyst material for hydrogen evolution[20] and for oxygen reduction[21], it was used as the electrocatalyst material for the reduction electrode. The actual electrode material used consisted of carbon-supported platinum (40 wt% platinum on carbon, 2 mg of platinum per cm^2) on a hydrophobic carbon cloth based gas diffusion electrode (ELAT, purchased from E-TEK, Inc.). An electrocatalyst for the oxidation electrode was selected on the basis of high electrocatalytic activity and long-term stability for: (i) oxygen evolution, and (ii)

hydrogen oxidation. Various noble metals and their mixed oxides, give the best stable performance for oxygen evolution from acidic media[18,22-24]. These include metals, such as iridium and platinum-iridium alloys, and mixed oxides of ruthenium-iridium and rhodium-ruthenium. Platinum has long been recognized as the most active electrocatalyst for the hydrogen oxidation reaction. Thus, the electrocatalyst for the oxidation electrode consisted of a mixture of fuel cell grade platinum black (~30 $m^2 g^{-1}$) and iridium black (~45 $m^2 g^{-1}$). They were used at a platinum to iridium weight ratio of 60:40, to furnish roughly equal surface areas for each metal. The metal blacks were combined with a Teflon suspension and coated on a wet-proofed, conductive carbon paper support (Toray purchased from E-TEK, Inc.). The entire assembly was dried and heated to 325°C in an inert atmosphere (argon) to sinter the Teflon and bond the catalytic metal particles to the support. The amount of Teflon in the finished oxidation electrocatalyst layer was approximately 15 wt% and the oxidation electrocatalyst loading was 2 mg of noble metals per cm^2.

Compatibility of Electrode Structures With Liquid and Gaseous Reactants

To avoid mass transport limitations when operating in the fuel cell mode at high power densities, highly hydrophobic gas diffusion electrode structures are required. These electrode structures are incompatible with water electrolysis, where liquid water is used as reactant. In the case of a conventional PEM water electrolyzer, liquid water is passed over a porous hydrophilic anodic electrode structure, thus, supplying the reactant needed for oxygen evolution and a means of removing heat generated from electrolyzer multi-cell stacks. Anodic electrode structures in PEM water electrolyzers typically consist of noble metal oxide catalyzed porous titanium substrates where the substrates provide flow fields for reactant supply and product removal, as well as current collection from the electrocatalyst/electrolyte interface[25]. Alternatively, Teflon-bonded platinum black, or noble metal oxides, are pressed onto the PEM and placed in contact with a series of titanium or niobium metal screens[26].

To facilitate the use of hydrophobic gas diffusion electrodes in the fuel cell and the electrolyzer modes of operation of the URFC, an alternative means of introducing liquid water into the URFC was developed. This involved incorporating channels within PEM membrane structures, so that water could be supplied directly lengthwise to the membrane electrolyte and, hence, by lateral diffusion, to membrane/electrode interfaces[27]. These novel PEMs were produced by a simple straightforward process which is illustrated in Figure 1. A sheet of PEM was placed on either side of a set of parallel channel forming elements [cf., Fig. 1(a)]. The entire assembly was then placed on the lower platen of a hot press [cf., Fig. 1(b)] and pressed under conditions that bonded the two membranes firmly and permanently together [cf., Fig. 1(c)]. In some cases (as discussed later), after removing the membrane structure from the hot press, the channel forming elements were physically removed from the pressed assembly, leaving a set of continuous channels through the length of the membrane [cf., Fig. 1(d)]. Appropriate internal manifolding in the URFC components was devised to: (i) accommodate the introduction of reactants; (ii) edge supply of liquid water to the channels within the PEM, and (iii) for product removal from the URFC.

Internal Humidification of Proton Exchange Membranes

Proton exchange membranes will only support ionic conduction adequately if they are wet or in a moist state[28]. Without sufficient humidification, partial drying of a PEM gives rise to an increased ohmic drop across the membrane and, hence, to a less than optimum performance. In conventional PEM water electrolyzers, reactant liquid water passed over the anode electrode surface, also provides the necessary humidification for the PEM membrane. For conventional monofunctional PEM fuel cells, satisfactory performance at high power densities is obtained only if the hydrogen anode gas is humidified to a water vapor pressure level, corresponding to that of pure water at, or slightly above, the operating temperature of the fuel cell[29]. Apparatus for humidification of the hydrogen gas (either internally or externally of the fuel cell stack) adds weight and volume to the fuel cell power source. For the present generation of PEMs, this humidification

is sufficient to give adequate proton conductivity. During operation of a PEM fuel cell, proton migration leads to the transport of one, or more, water molecules through the membrane from the anode to the cathode side, but water formed at the cathode side by reduction of oxygen gas back-diffuses down any concentration gradient across the membrane[28].

It is not necessary to humidify the cathode oxygen gas stream[29]. However, if the anode gas stream is not initially humidified, the PEM at the anode entry will rapidly lose water and, therefore, will lose performance, resulting in a propagation phenomenon throughout the cell from anode entry to anode exit. Humidification of the fuel gas at the anode entry is, therefore, required in conventional PEM fuel cells. Humidification of the PEM in the fuel cell mode of operation of the URFC was accomplished by the introduction of liquid water into channels formed within the perfluorosulfonic acid polymer membrane electrolyte layer, followed by lateral diffusion of water along the polymer chains in the membrane (cf., Fig. 1). Reactant water required for electrolysis in the electrolyzer mode of operation was also supplied by means of these channels to the active electrode/membrane electrolyte interfaces.

Thermal and Water Management of Advanced URFC

An aspect of PEM fuel cells, either monofunctional or unitized regenerative in configuration, that has been difficult to solve is thermal and water management within the cell stack[30]. For multi-cell stacks having large active cell areas (of the order of 500 cm^2), water management has been found to be a considerable problem. In some cases, the PEM within individual cells is subject to drying-out effects (lack of sufficient humidification) or flooding of gas diffusion electrodes (excess humidification). In the advanced URFC, water management is greatly simplified, due to the use of new PEM materials having channels for water flow incorporated within the membrane structures (cf., Fig. 2). Thus, the URFC stack will control itself internally with regard to water requirements.

For instance, in the fuel cell operating mode, water that is electroosmotically transported to the cathode and lost to evaporation will be quickly replaced as the PEM absorbs additional water from the bulk water supply within the channels. Similarly, in the electrolyzer mode, as water is consumed by electrochemical reactions, it will be quickly replaced as additional water is absorbed into the membrane from the channels. While operating in either the fuel cell mode or the electrolyzer mode, water that exits the stack in the gas streams can be phase-separated and/or condensed out and reclaimed for future recycling in the energy storage system, one of the requirements of a regenerative system.

Heat removal in existing monofunctional or unitized regenerative PEM fuel cell designs is accomplished by inserting cooling plates into the cell stacks. The ratio of active cells to cooling plates is determined by the fuel cell power density. For high power density, this ratio can be as high as 2:1 or even 1:1. A nonconducting liquid, high purity water in many cases, is circulated through the cooling plates in series with a heat exchanger. The placement of cooling plates within a fuel cell stack adds additional weight and volume to the stack, thus, lowering the specific power rating. In the advanced URFC design, the need for cooling plates may be eliminated as a result of using new PEM materials having channels for water flow incorporated within membrane structures (cf., Fig. 2). Controlling the flow of water through these channels within each individual fuel cell in a stack could lead to perfect thermal management. This approach to heat removal gives rise to a URFC stack of reduced weight and volume.

RESULTS AND DISCUSSION

Fabrication of Channel-Containing Proton Exchange Membranes

In preliminary work a number of approaches for forming proton exchange membranes with internal channels were devised and tested. Examples of representative approaches that were used to satisfy the goal of maximizing water transport, ionic conductivity and structural integrity of PEMs are illustrated schematically in Figure 3. Because of their commercial availability, Nafion tubes (Perma Pure, Inc.) were initially selected as the preferred channel-forming material. Nafion tubes having a minimum ID of 130 μm and a minimum OD of 250 μm can be obtained commercially. Where hot pressing was used to fabricate channel-containing membranes (cf., Fig. 3, Methods 2 and 3), Nafion tubes were first threaded over small diameter niobium or Teflon wires. In some cases Nafion tubes and sheet were first converted from the as-received proton form of the ionomer to the tetrabutyl ammonium (TBA) form which is pseudo-thermoplastic. This was accomplished using tetrabutyl ammonium hydroxide following a published procedure[31].

An apparatus was designed and constructed to facilitate the fabrication of internally channeled membrane and electrode (M&E) assemblies with stiff channel-forming elements. In this apparatus, shown in Figure 4, individual, small-diameter channel-forming elements were threaded onto the frame through equally spaced holes drilled in Rods A and B. The holes were of a diameter slightly larger than the channel-forming elements which helped to maintain uniform spacing between the elements. The elements were anchored in place with set screws, as shown in the inset of the figure. After all channel-forming elements were in place in the frame, Rod A or B was rotated as shown in the figure to tighten the elements further. In this way, uniform tension was applied to all channel-forming elements simultaneously.

An aluminum block small enough to fit in the space inside the frame was placed on the lower platen of a hot press and covered with a silicone rubber load-levelling pad and a release sheet (PTFE-finished cloth). The lower gas-diffusion electrode and Nafion membrane were placed on the release material, followed by the frame. The upper Nafion membrane and gas-diffusion electrode were then placed on top of the filled frame. The upper gas-diffusion electrode was subsequently covered with a second release sheet, a second levelling pad and a second aluminum block the same size as the first to finish off the package. The press was then closed and the hot press cycle carried out. In some cases plain channel-containing membrane structures were prepared in the absence of gas diffusion electrodes using this procedure.

Although channel-containing membrane structures were successfully produced using Nafion tubes, the resulting membranes were thick since they contained at least one full thickness layer of membrane as well as both walls of the tubes. In an effort to produce a thinner channel-containing membrane, the use of a removable tubulating agent was investigated. In this scheme two sheets of membrane were pressed together with a series of removable wires or tubes between them. For example, small diameter Teflon tubing was wound on a frame following the same pattern as shown in Figure 4. This was loaded in the press between two sheets of Nafion which had been converted to the TBA form. After pressing (170°C for one minute at 5,000 lb) the Teflon tubes were easily removed prior to reconversion of the membrane to the proton form. After reconversion to the proton form the membrane exhibited a slightly reduced water uptake, as defined by Equation (1), where the wet weight was measured after boiling in deionized water and cooling to room temperature and the dry weight was measured after drying in an oven at 110°C. Membranes that originally had a water uptake of 35% had a reduced uptake of 30.5% after reconversion.

$$Uptake_{H_2O} = \frac{\left(Wt_{Wet} - Wt_{Dry}\right)}{Wt_{Dry}} \qquad (1)$$

The fabrication of channel-containing membrane and electrode assemblies where the membranes were originally in the proton form was also perfected using the above procedure. In this case the hot pressing conditions were 200°C for five minutes at 100 lb. followed by one minute at this temperature and 5,000 lb. Channel-containing M&Es used for the measurement of URFC performance characteristics were prepared using membranes that were originally in the proton form.

An optical micrograph of one of these channel-containing PEMs with a fuel cell gas diffusion electrode bonded to either side of it is presented in Figure 5. Several features are apparent from the optical micrograph. The channels produced within the membrane are oval in shape, as would be expected from the hot press compression process. The smooth sides of the channel wall on intersecting the interface between the two Nafion 115 layers is indicative of effective bonding between the two Nafion sheets at the perimeter of the channel. The disappearance of the Nafion layer interface near the center of the gap between channels also indicates that effective bonding occurred in this region. However, separation between the two Nafion 115 layers in other interfacial regions demonstrates that improvement in the fabrication of channel-containing PEMs is needed. The ability to form very small-diameter channels in Nafion membranes was limited due to the breaking of small-diameter wires or tubes (e.g., Nb wires and PTFE tubes) on trying to mechanically remove them from pressed Nafion membrane layers. Difficulty on mechanically removing these channel-forming elements was encountered even when the pressed assembly was allowed to swell on absorbing water.

To reduce the internal resistance to proton transport and the diffusion path for water between the internal channels and the surface of the oxidation electrode electrocatalyst layer where it is needed most, the thickness of the PEM layers needed to fabricate channel-containing membranes were reduced. The 125 μm (5 mils) thick Nafion 115 membranes (equivalent weight of 1100) were replaced with 50 μm (2 mils) thick Nafion membranes, again having an equivalent weight of 1100. The use of lower equivalent-weight thin membranes, e.g., Nafion 105 (equivalent weight of 1000), particularly at the oxidation electrode side, would be even more advantageous. However, the trade-offs involved here are the greater structural integrity of higher equivalent weight membranes and the higher ionic conductivity and water mobility characteristics of the lower equivalent weight materials.

Construction of Single Cell URFC

The design of the single URFC test cell capable of utilizing electrodes having an active area of 25 cm^2 is illustrated in Figure 6. The design features include parallel flow for the water stream inside the PEM and the hydrogen and oxygen gases on the backsides of the gas diffusion electrodes (in the fuel cell mode of operation). The two endplates for this test cell were fabricated from gold-plated titanium. The design for the anode side endplate only is presented in the drawing represented by Figure 6. The cathode endplate has the same flow field and gas port design but lacks the channels to feed water to an internally humidified PEM.

This design accommodates water flow for internally humidified membranes. Water flow within the membrane moves parallel to the lands and grooves of the flow field for the gases in order to eliminate the risk of pinching closed the humidification channels within the PEM. Bipolar plates for the construction of a multi-cell stack will have the same arrangement as shown in Figure 6 for the supply of water for internal humidification and the gas flow fields. As is readily apparent from the figure, the anode and cathode endplates possess a high degree of symmetry. Thus, they can be readily aligned to allow reactant gas co-flow or counter-flow in the fuel cell or electrolysis modes of operation.

The test system for operating the URFC in the fuel cell mode was a model 1000 fuel cell test system (Lynntech, Inc.). On operating the URFC in the electrolyzer mode, a separate power

supply was attached and the test system was used to control exit gas pressures, cell temperature and as a data logger.

Performance Characteristics of Internally Humidified M&E Assemblies

Initial URFC performance characteristics were obtained on using an M&E assembly fabricated with channel-containing Nafion 115 PEMs in a small (25 cm^2 active area) single cell unitized regenerative fuel cell test fixture. Performance characteristics in the fuel cell and electrolyzer modes of operation were recorded. During both modes of operation, water was fed to the channels incorporated in the PEM electrolyte layer. During operation in the fuel cell mode, dry hydrogen and oxygen gases were also fed to the hydrophobic gas diffusion electrodes at the anode and cathode side of the single cell, respectively. On operating the test cell in the electrolysis mode, only water was fed to the channels embedded in the PEM electrolyte material. In this case, the evolved hydrogen and oxygen gas streams were opposite in direction in comparison to those fed to the test cell during the fuel cell mode of operation. The hydrophobic cathode electrocatalyst layer consisted of carbon-supported platinum, having a platinum loading of 2 mg of Pt cm^{-2}, while the hydrophobic anode electrocatalyst layer consisted of a platinum black and iridium black mixture having a loading of 2 mg of noble metals cm^{-2}.

As often observed with conventional monofunctional PEM fuel cells, the performance characteristics were poorest at start-up, and improved with time. This is clearly illustrated in Figure 7 for one of the initially prepared channel-containing PEMs which involved the use of Nafion 115 membranes. The plots shown in the figure are for a membrane humidified internally with deionized water. Since deionized water has very high electrical resistance, the roughly one-third of the membrane area occupied by the tubes is effectively lost to proton flow. This can be improved by the use of a more conductive humidifying agent. To illustrate this concept the deionized water was replaced with 0.05 M sulfuric acid. This concentration was selected in an effort to achieve a balance between improving conductivity, which increases with the log of the acid concentration, and the drying effect that a concentrated acid has on the membrane. An improvement in the performance characteristics obtained on using 0.05 M sulfuric acid as the humidifying agent can be seen from the data presented in Figure 8.

Another way to enhance fuel cell performance on humidifying with water is to operate at higher temperature. As shown in Figure 9, raising the cell temperature from 50°C to 80°C enhances performance as expected.

When operated in the electrolyzer mode an enhancement in performance from the first run with subsequent runs (which had been observed in the fuel cell mode) was not observed as shown in Figure 10. The cell operated with no difficulties either during operation in the electrolysis mode or during change over from the electrolysis to the fuel cell mode or vice a versa.

Following fabrication of an internally-channeled M&E assembly using Nafion 112 sheets, the M&E assembly was positioned in a test cell configured for the internal flow of water (cf., Fig. 6). Deionized water was circulated through the channel-containing M&E assembly in the cell in a closed flow loop using a small pump. The M&E assembly was conditioned for 12 hours at 400 mA cm^{-2} using hydrogen and oxygen as reactants at 0 psi and at a cell temperature of 50°C prior to data collection. The resulting polarization curve collected from the assembly in the fuel cell mode of operation is shown in Figure 11 along with a polarization curve obtained in a similar manner using an internally-humidified M&E assembly based upon the use of the thicker Nafion 115.

As the data in Figure 11 indicate, the polarization curves are virtually identical in the low current density region. As the current density increases, the performances diverge. Clearly, the use of the thinner Nafion 112 membrane material resulted in improved performance. It should also be noted that the data for the Nafion 112 case were collected using relatively mild pressure and

temperature conditions. Better performance is anticipated with further optimization of materials and experimental parameters.

While the performance characteristics obtained (cf., Figs. 8, 9, 10 and 11) are less than that desired for an advanced URFC, nevertheless, these preliminary results are very encouraging and demonstrate that the approach has considerable merit and great potential for achieving the desired goal. The performance characteristics suffered in most cases because of the substantial resistance of the relatively thick PEM electrolyte layers. A critical issue for success, therefore, is the successful fabrication of thin, highly conducting proton exchange membranes containing channels that allow adequate flow of water for membrane humidification, reactant water for electrolysis and cooling water for heat removal from the URFC stack. Another key issue involves the successful development of a highly active oxidation electrode that will function equally well, both for oxygen evolution from water in the electrolysis mode and oxidation of hydrogen gas in the fuel cell mode.

The data presented in this paper demonstrate the feasibility and advantages of truly internally humidifying a PEM membrane for use in a monofunctional PEM fuel cell, a PEM electrolyzer or in a unitized regenerative fuel cell. While further work is required to optimize the internally humidified, channel-containing PEM structures they clearly offer the potential for a substantial reduction in the weight and size of a URFC stack. Thus, for space applications a URFC power source based on the design outlined in this paper has the potential to offer much higher energy densities than Ni-H_2 batteries with almost infinite cycle lifetimes. Their main drawback is associated with their low round-trip energy conversion efficiencies.

CONCLUSIONS

1. Channel-containing proton exchange membranes were prepared successfully.

2. Water in liquid form was introduced successfully into channels within proton exchange membrane structures.

3. Gas diffusion electrodes bonded to channel-containing proton exchange membranes were used successfully in both the fuel cell mode and electrolysis mode of operation of a URFC.

4. Preliminary fuel cell and electrolyzer performance characteristics obtained from a URFC fabricated using channel-containing proton exchange membranes are encouraging.

5. Channel-containing proton exchange membranes can also be used advantageously in monofunctional PEM fuel cells and in PEM electrolyzers.

6. Internally humidified channel-containing membranes eliminate the need for reactant gas humidifiers (external or internal to fuel cell stacks) leading to a reduction in system size and weight and an increase in power densities (volumetric and gravimetric).

ACKNOWLEDGMENT

The work described in this paper was supported by NASA under an SBIR Phase I project (Contract No.: NAS3-27213). This support is gratefully acknowledged.

REFERENCES

1. M. Warshay and P.R. Prokopius, J. Power Sources, 29 (1990) 193.

2. A.H. Zimmerman and D.M. Speckman, "High Energy Density Rechargeable Batteries for Aerospace Power Requirements," Final Report for Contract No.: FO4701-85-C-0086-P00016, submitted to: Space Division, Air Force Systems Command, Los Angeles, CA, August 1987.

3. A.J. Appleby, *J. Power Sources*, 22 (1988) 377.

4. K. Bolwin, *J. Power Sources*, 45 (1993) 187.

5. J.F. McElroy, "Proc. 24th IECEC" , August 6-11, Washington, D.C., editors, W.D. Jackson and D.A. Hull, IEEE, United Engineering Center, 345 East 47th Street, New York, NY, Vol. 3, pp. 1631-1636.

6. R.S. Yeo, J. McBreen, A.C.C. Tseung and S. Srinivasan, *J. Appl. Electrochem.*, 10 (1980) 393.

7. L.L. Swette, A.B. LaConti and S.A. McCatty, *J. Power Sources*, 47 (1994) 343.

8. T.W. Hannemann, *National Defense*, January 1995, pp. 14 and 15.

9. NASA Conf. Publication 3016, Sept. 12-13, 1988, p. 206.

10. F. Mitlitsky, N. J. Colella, B. Myers and C. J. Anderson, "Regenerative Fuel Cells for High Altitude Long Endurance Solar Powered Aircraft," paper presented at the Intersociety Energy Conversion Engineering Conference, Atlanta, GA, August 8-13, 1993.

11. J.F. McElroy, *J. Power Sources*, 36 (1991) 219.

12. J. S. Bone, S. Gilman, L. W. Niedrach and M. D. Read, in: "Proc. of the Ann. Power Source Conf.," 15 (1961) 47.

13. E. Findl and M. Klein, in: "Proc. of the 20th Ann. Power Source Conf.," PSC Publications Committee, Red Bank (1966), p. 49.

14. A. Leonida, in: "Proc. of the European Space Power Conf.," Madrid (1989), p. 283.

15. H. P. Dhar, *J. Appl. Electrochem.*, 23 (1993) 32.

16. J. F. McElroy and G. G. Patwa, Proc. 72nd AIChE Meeting, Nov. 25-29, 1979.

17. L. Swette, J. A. Kosek, C. C. Cropley and A. B. LaConti, Proc. 28th IECEC, Vol. 1, pp. 1227-1232, Aug. 8-13, 1993.

18. J. Ahn and R. Holze, *J. Appl. Electrochem.*, 22 (1992) 1167.

19. K. Ledjeff, F. Mahlendorf, V. Peinecke and A. Heinzel, *Electrochim. Acta*, 40 (1995) 315.

20. H. Kita, J. *Electrochem. Soc.*, 113 (1966) 1095.

21. J. P. Hoare, "The Electrochemistry of Oxygen," Wiley Interscience, New York (1968).

22. S. Gottesfeld and S. Srinivasan, *J. Electrochem. Soc.*, 125 (1978) 89.

23. R. S. Yeo, J. Orehotsky, W.Visscher and S. Srinivasan, *J. Electrochem. Soc.*, 128 (1981) 1900.

24. R. Kotz and S. Stucki, *Electrochim. Acta*, 29 (1984) 153.

25. H. J. Christen, H. Devantay, C. Schellenberg, G. Scherer and S. Stucki, U.S. Patent #4,619,753, October 28, 1986.

26. A. B. LaConti, A. R. Fragala and J. R. Boyack, in: "Proc. Symp. on Electrode Materials and Processes for Energy Conversion and Storage," eds., J. D. E. McIntyre, S. Srinivasan and F. G. Will, Electrochemical Society, Inc., Pennington, N.J. (1977), Vol. 77-6, p. 354.

27. A.J. Cisar, A. Gonzalez-Martin, G.D. Hitchens and O.J. Murphy, patent pending.

28. T.A. Zawodzinski, J. Davey, J. Valerio and S. Gottesfeld, *Electrochim. Acta*, 40 (1995) 297.

29. O. J. Murphy, G. D. Hitchens and D.J. Manko, *J. Power Sources*, 47 (1994) 353.

30. H.H. Voss, D.P. Wilkinson, P.G. Pickup, M.C. Johnson and V. Basura, *Electrochim. Acta*, 40 (1995) 321.

31. R. Moore et al., *J. Membrane Sci.*, 75 (1992) 7.

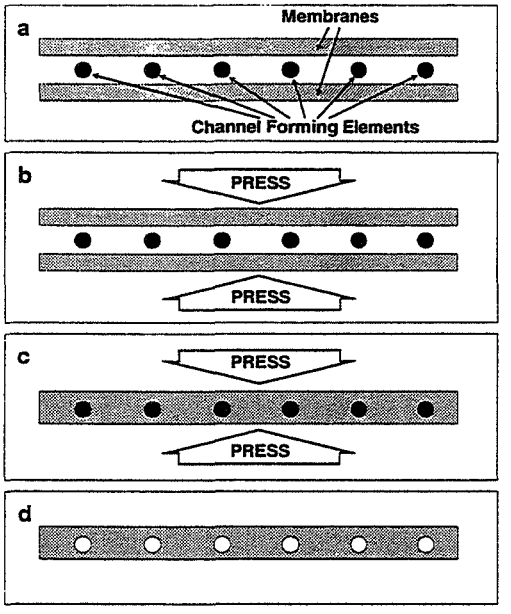

Figure 1. Process for forming proton exchange membranes containing channels.

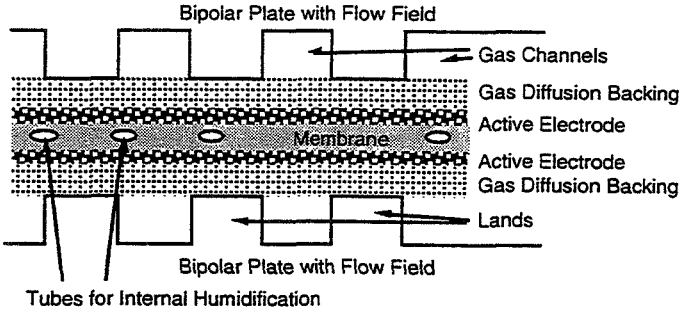

Figure 2. Partial cross section of a single cell assembly fabricated with a tubulated membrane.

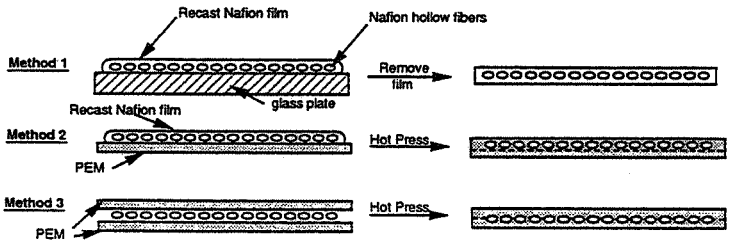

Figure 3. Methods for preparing proton exchange membranes incorporating Nafion tubes.

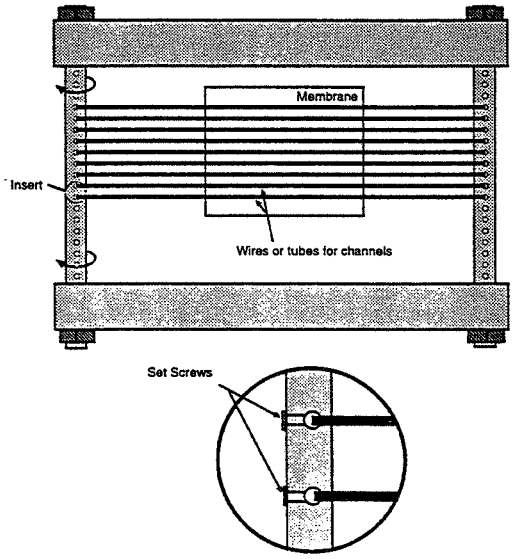

Figure 4. Top view of an apparatus for producing internally-channeled proton exchange membrane and electrode assemblies. The channel-forming element, which can be either wire or tubing, is threaded through holes in the rods and held in place by a set of screws, as shown in the inset. This allows individual tensioning of each of the channel forming elements.

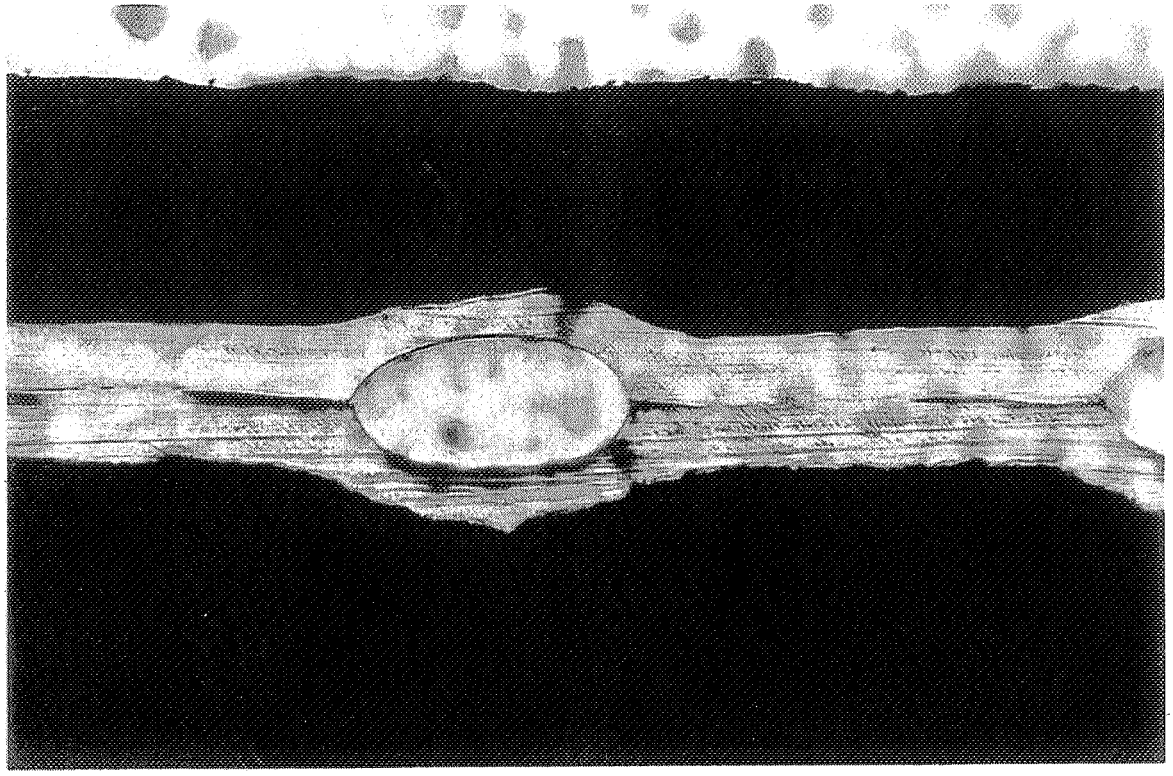

Figure 5. Optical micrograph showing the cross section of a channel-containing proton exchange membrane.

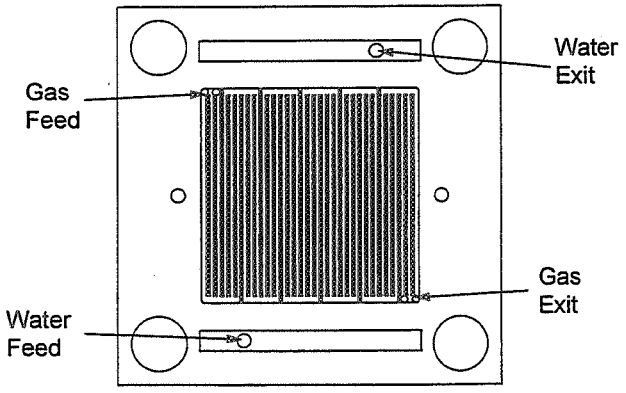

Figure 6. Drawing of the anode endplate for the single cell URFC. This design features channels for use with internally-humidified membranes.

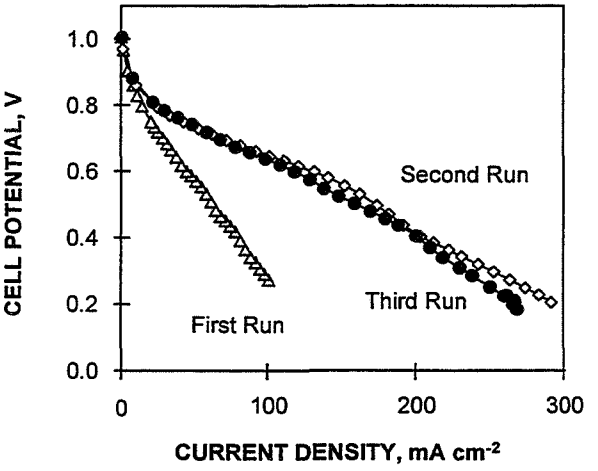

Figure 7. Polarization curves for an internally humidified membrane and electrode assembly through its first three cycles. Operating conditions were 50°C and 40 psig for both gases.

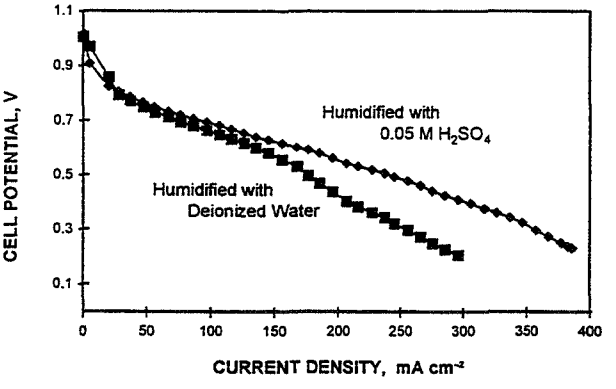

Figure 8. Effect of replacing deionized water with 0.05 M sulfuric acid on the performance characteristics of a single cell URFC. Operating conditions were 50°C and 40 psig for both gases.

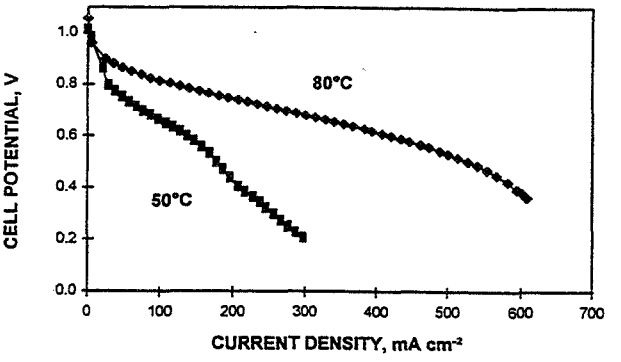

Figure 9. Performance characteristics of a single cell URFC internally humidified with deionized water. Operating conditions were 40 psig for both gases in each case. Cell temperatures were: (◆), 80°C and (■), 50°C.

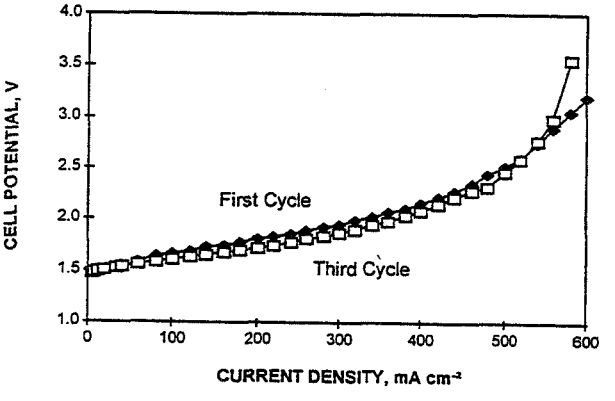

Figure 10. Performance characteristics of an internally humidified single cell URFC functioning in the electrolysis mode. Operating conditions were 50°C and 40 psig.

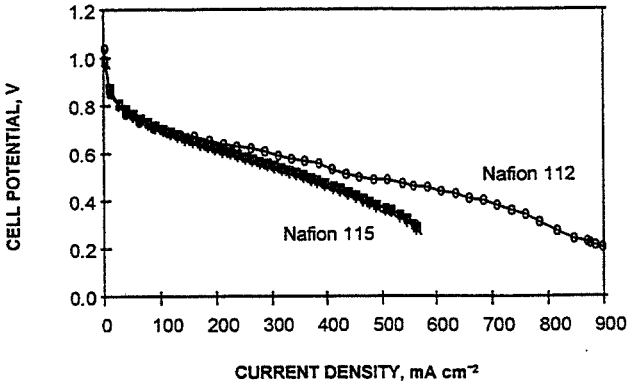

Figure 11. Performance characteristics of M&Es containing internally-humidified membranes fabricated with Nafion 115 and Nafion 112. Operating conditions for the two M&Es were: Nafion 115 cell temperature = 80°C, hydrogen and oxygen pressure = 40 psig; Nafion 112 cell temperature = 50 °C, hydrogen pressure = 0 psig, oxygen pressure = 20 psig.

Page intentionally left blank

58-44
OCB 946

FUEL CELL SYSTEMS FOR FIRST LUNAR OUTPOST—REACTANT STORAGE OPTIONS

P.A. Nelson
Argonne National Laboratory
Argonne, Illinois

256931

8 p.

ABSTRACT

A Lunar Surface Power Working Group was formed to review candidate systems for providing power to the First Lunar Outpost habitat. The working group met for five days in the fall of 1992 and concluded that the most attractive candidate included a photovoltaic unit, a fuel cell, a regenerator to recycle the reactants, and storage of oxygen and hydrogen gases. Most of the volume (97%) and weight (64%) are taken up by the reactants and their storage tanks. The large volume is difficult to accommodate, and therefore, the working group explored ways of reducing the volume. An alternative approach to providing separate high pressure storage tanks is to use two of the descent stage propellant storage tanks, which would have to be wrapped with graphite fibers to increase their pressure capability. This saves 90% of the volume required for storage of fuel cell reactants. Another approach is to use the descent storage propellant tanks for storage of the fuel cell reactants as cryogenic liquids, but this requires a gas liquefaction system, increases the solar array by 40%, and increases the heat rejection rate by 170% compared with storage of reactants as high pressure gases. For a high power system (>20 kW) the larger energy storage requirement would probably favor the cryogenic storage option.

INTRODUCTION

Preliminary planning has been done for the First Lunar Outpost (FLO), a manned mission to send a crew of four on a 45-day stay encompassing two lunar days and one lunar night. This mission requires two flights. The first flight would deliver the habitat for the crew, who would arrive 2 to 6 months later on the second flight. The habitat for the crew, which is 10 m in length and 4.35 m in diameter, is mounted horizontally on the cargo lander, about 7 m above the lunar surface (Fig. 1). The power requirement for the habitat is 10.5 kW during the day and 9.1 kW during the night.

To review the potential power systems for the FLO habitat, Bruce Matthews of the Office of Space, Department of Energy (DOE), appointed the Lunar Surface Power Working Group, which consisted of twelve members from various DOE and NASA laboratories.

The working group met on two occasions, October 20-21, 1992, and November 18-20, 1992, at The Analytical Sciences Corporation (TASC) site in Reston, Virginia. During the October meeting, a facilitator from TASC led discussions to determine the relative importance of evaluation criteria for rating candidate systems for providing power to the FLO habitat. The systems were evaluated according to these criteria during the November meeting. The systems evaluated included photovoltaics with a regenerative fuel cell (PV-RFC); solar heating with dynamic energy conversion; nuclear reactors with dynamic, thermoionic, and thermoelectric conversion systems; and a radioisotope-powered Stirling engine system. The working group gave the highest score, by a small margin, to the PV-RFC unit. The means of deploying the photovoltaic array, the type of fuel cell to be employed, and the specific means of storing the oxygen and hydrogen reactants were discussed. However, the selection of the PV-RFC combination was based on an overall perception of feasibility and characteristics, not on a system having specific components.

ORIGINAL PLANS FOR STORAGE OF REACTANTS

The working group was provided with tables of data for each of the candidate systems for providing power to the FLO Habitat. The parameters for the PV-RFC system are shown in Table 1. In this plan, the fuel cell reactants

would be stored in high pressure tanks, and an empty tank would be provided for receiving the water discharged from the fuel cell. These data indicate a mass of 5000 kg, and a volume of 25 m^3 for the fuel cell and associated reactants and their storage tanks. It was planned that the hydrogen, oxygen, and water tanks be stored below the FLO Habitat module. These tanks were required to fit in the "doughnut hole" provided by the arrangement of the eight descent stage propellant storage tanks (Fig. 1). It is doubtful that there is sufficient room for these tanks in that space. The reactant storage tanks should be spherical for minimum weight and at least be short cylinders with hemispherical ends. They would have a total tank volume of about 24 m^3 at 20 MPa (200 bar) storage pressure, but with the space between tanks they would actually occupy about 40 m^3. At somewhat higher pressures, at least 30 MPa, the reactant tanks might fit the design space, but the operation of the regeneration step at such high pressures would limit the life of the regenerator.

As shown by the weight distribution in Table 2, about 64% of the weight of the entire PV-RFC system comes from the mass of the fuel cell reactants and their storage tanks. These components take up about 97% of the total volume. As noted above, the volume provided in the original plan for the PV-RFC might be inadequate. Therefore, other options for reducing the volume requirements for storage of the fuel cell reactants were reviewed.

OPTIONS FOR STORING FUEL CELL REACTANTS

The following three options were considered for storing the fuel cell reactants:

Option 1. Storage of reactants in high pressure tanks as in the original plan.
Option 2. Storage in two or more of the descent stage propellant storage tanks with reinforcing of the tanks to withstand high pressure.
Option 3. Storage of the reactants as cryogenic liquids.

To evaluate the feasibility of Option 2, data were obtained on these tanks (without additional reinforcement)[1] and are summarized in Table 3. It should be noted that the excess hydrogen provided for contingencies is almost three times that required for fuel cell hydrogen, and the excess oxygen is about 80% of that needed. However, these leftover reactants would quickly evaporate after the lunar landing because the tanks are not designed for low heat loss rates. Although only one of the six oxygen tanks and one of the two hydrogen tanks would be required for storage of the fuel cell reactants, these tanks would have to be reinforced, because as designed for storing the reactants as liquids, the tanks have a pressure capability of only 0.345 MPa (45 psi).

In Table 4, the volumes of the first two storage options are compared. For Option 2, the only additional volumes would be for the product water and the additional materials for reinforcement. This additional tank material would be graphite fiber wrapped around two of the tanks so that the strength of the tanks could withstand the required pressure, which was calculated from the tank volumes and the amount of reactants to be stored. The total volume attributed to storage of fuel cell reactants would be reduced from 23.6 m^3 for Option 1 to only 2.5 m^3 for Option 2.

The masses for Options 1 and 2 are compared in Table 5. One feature of Option 2 is that the reactants would be stored as water during the flight, and oxygen and hydrogen would be generated after landing. This has the advantages of ease of loading before the flight and lower cost, and it provides an opportunity to test the regeneration unit prior to the crew's flight. This approach of storing water instead of the gases should also be considered for Option 1. An obvious conclusion from Table 5 is that little mass is saved by using the descent stage propellant storage tanks for high pressure storage; the weight saved by not providing extra tanks for reactant storage is nearly entirely offset by the weight of the additional material (graphite fibers) to strengthen the propellant tanks. The total masses for the two options, including the balance of the systems, are shown in Table 6. For both options 1 and 2, the masses of the high pressure tanks were calculated by the use of the factor, 5.25 kg/(MPa-m^3), multiplied by the product of the reactant gas pressure and volume.

Scale-up of the power capability is somewhat easier for Option 2 than for Option 1 because of the restriction on volume available for the flight and the much reduced volume requirements for the use of the propellant fuel tanks as fuel cell reactant tanks. The mass required for Option 2 as a function of power is shown in Fig. 2. In the longer term, the mass factor for the weight of the tanks might be reduced from the selected value for the near term of 5.25 kg/(MPa-m^3) to 3.00 kg/(MPa-m^3). This would require improvement in the strength of the wrapping fibers and improvement in the wrapping techniques and the mechanical analysis.

The third option is to store the fuel cell reactants in the propellant tanks under cryogenic conditions. This option has the advantages of requiring no additional storage tank mass or volume, except for the water tank, which has only 5% of the mass and 10% of the volume of the separate hydrogen and oxygen storage tanks. The disadvantage of Option 3 is that it requires a gas liquification system. The weight of this system is expected to be less than that of storage tanks, but it would require development and testing to prove its reliability. Also, additional solar power of 13 kW (40% increase) world be required to operate the liquefaction system, and the heat rejection rate would have to be increased by 15 kW (170% increase). For a high power system (> 20 kW), the amounts of reactants to be stored would probably favor the cryogenic storage option. Any propellants remaining from the lunar descent stage would be available for use. If the availability of extra reactants coincided with temporary malfunctioning of the photovoltaic system, the provision for the use of these extra reactants would be an advantage for Option 3.

CONCLUSIONS

Providing the volume needed for the fuel cell reactants and their storage tanks beneath the FLO habitat, as called for in the original plan, may be difficult to achieve. An alternative that requires much less volume is the use of two of the eight descent stage propellant storage tanks for storing hydrogen and oxygen under pressure. These two tanks would have to be reinforced. Little weight would be saved by this approach, but in the original plan the weight of the reactant storage does not appear to be a problem. Another option which should be considered for a high power system (greater than 20 kW) is the use of the descent stage propellant storage tanks for cryogenic storage of the reactants. This would require additional solar power to operate the liquefaction system and additional heat rejection capability.

ACKNOWLEDGMENT

Work supported by the U. S. Department of Energy, Office of Space, under Contract W-31-109-Eng-38.

REFERENCE

1. James Masciacelli, private communication, Johnson Space Center, Houston, Texas, 1992.

Table 1. Solar Photovoltaic with Regenerative Fuel Cell Energy Storage for First Lunar Outpost Reactants Stored in Separate High Pressure Tanks

SYSTEM PERFORMANCE		SOLAR ARRAY	
Rated Power Outpost	10.5 kW_e	Power	32kW_e
Night Power Outpost	9.1 kW_e	Efficiency	15%
Volume	25 m^3	Solar Array Area	168 m^2
Total Mass	6240 kg	Mass	280 kg
Specific Mass	594 kg/kW_e	Specific Mass	8.8 kg/kW_e
REGENERATIVE FUEL CELL		**THERMAL MANAGEMENT**	
Energy Stored	3540 kW_e	Heat Rejection	8.9 kW_t
Rated Power	9.1 kW_e	Rejection Temperature	350 K
Fuel Cell Efficiency	51%	Mass	450 kg
Round-Trip Efficiency	42%	Specific Mass	56 kg/kW_t
Heat Rejection	8.7 kW_e	**POWER MANAGEMENT AND DISTRIBUTION**	
Mass	5000 kg	Rated Power	10.5 kW_e
Specific Mass (Energy)	1.41 kg/kWh	Efficiency	98%
		Heat Rejection	0.2 kW_t
		Mass	510 kg
		Specific Mass	49 kg/kW_e

Table 2. Mass Distribution for Solar-Fuel Cell System

Daytime Power: 10 kWh; Nighttime Power: 9.1 kW; Energy Storage: 3540 kWh		
	Mass, kg	**% of Total**
Fuel Cell System	1050	17
Reactant Storage		
Reactants	1720	28
Storage Tanks	2230	36
Solar Array	280	4
Power Management and Distribution	510	8
Thermal Management	450	7
Total System	6240	100

Table 3. Cryogenic Storage Tanks for Propellants on FLO Lunar Descent Stage

Item	Hydrogen	Oxygen
Propellant Mass, kg		
Calculated Requirement	6563	39,380
Excess for Contingencies	543	1223
TOTAL	**7,106**	**40,603**
Number of Storage Tanks	6	2
Total Mass of Empty Tanks, kg	2358	1227
Tank Capacity		
Capacity per Tank, m^3	16.045	17.92
Total, m^3	96.3	35.8
Tank Material	Aluminum	Aluminum
Pressure Rating, MPa	0.345	0.345

Table 4. Comparison of Storage Volumes for Fuel Cell Reactants for Use of Separate Storage Tanks Versus Use of Reinforced Descent Stage Propellant Storage Tanks

Item	Containers for Reactant Storage	
	Separate Storage Tanks	Descent Propellant Tanks
Hydrogen Storage		
Pressure, MPa	20	17.2
Volume, m^3	13.8	0 (16)*
Oxygen Storage		
Pressure, MPa	20	7.8
Volume, m^3	7	0 (18)*
Water Tank Capacity, m^3	1.9	1.9
Volume of Tank Materials, m^3	0.9	0.6
Total Storage Volume, m^3	23.6	2.5

*No additional volume for RFC reactants; values in parentheses are propellant tank volumes (using 1 of 6 hydrogen tanks and 1 of 2 oxygen tanks).

Table 5. Comparison of Mass Required for Fuel Cell Reactant Storage for Use of Separate Storage Tanks Versus Use of Reinforced Descent Propellant Storage Tanks

Item	Mass Required, kg	
	Separate Storage Tanks	Descent Propellant Tanks
Fuel Cell Reactants	1720	0
Product Water	0	1720
Reactant Storage Tanks	2180	0
Propellant Tanks		
Mass Added to Withstand Pressure	0	1940
Total Mass of Tanks	(2230)	(3390)
Water Tank	50	50
Total Storage Mass	**3950**	**3710**

Table 6. Comparison of Total System Mass for Use of Separate Storage Tanks Versus Use of Reinforced Descent Stage Propellant Storage Tanks for Storage of Fuel Cell Reactants

Item	Mass Required, kg	
	Separate Storage Tanks	Descent Propellant Tanks
RFC Conversion System	1050	1050
RFC Energy Storage	3950	3710
Solar Array	280	280
Power Management & Distribution	510	510
Thermal Management	450	450
Total System Mass	**6240**	**6000**

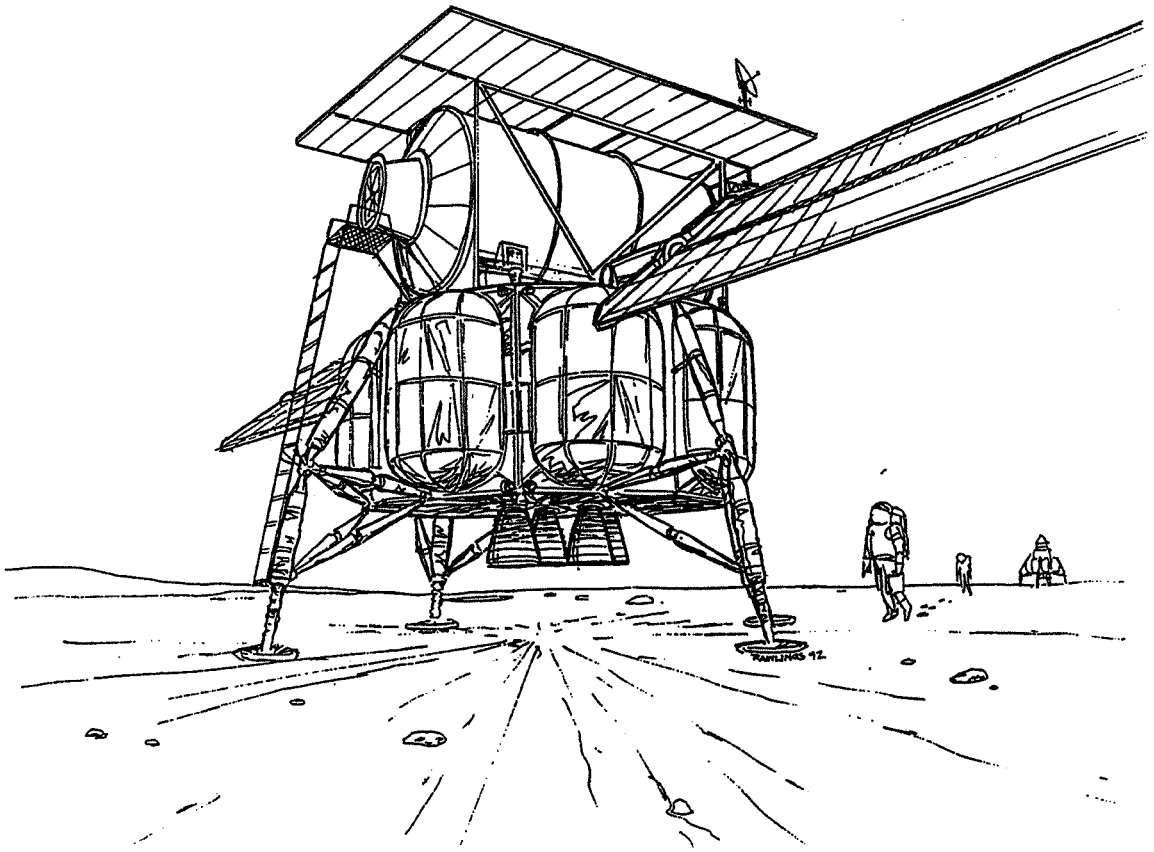

Fig. 1. Habitat for First Lunar Outpost

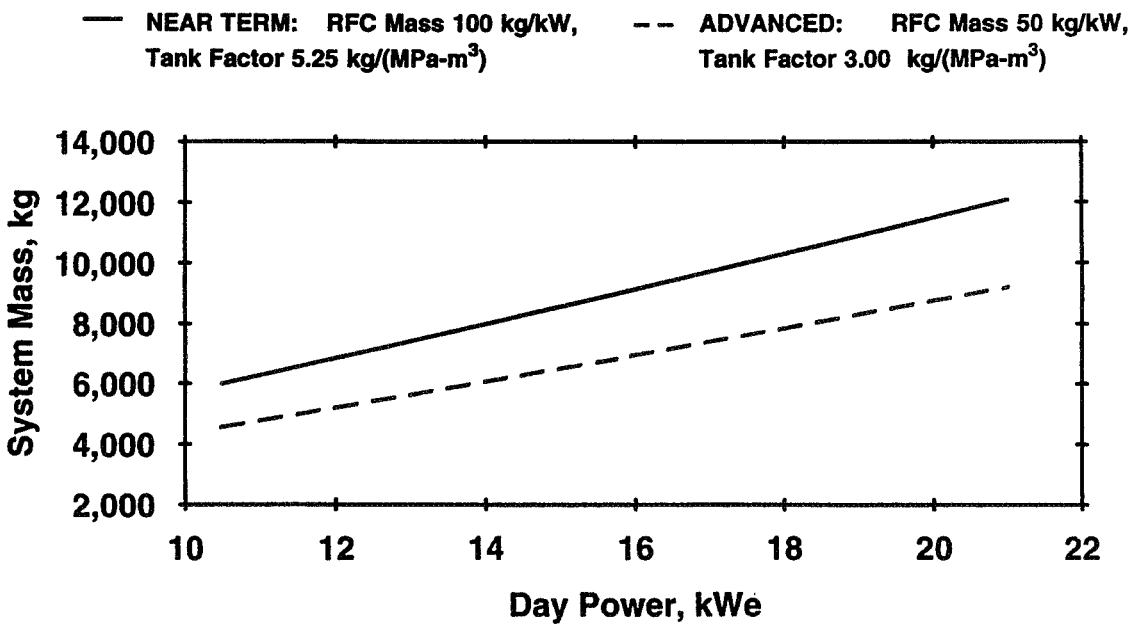

Fig. 2. Mass of Solar-Regenerative Fuel Cell System as a Function of Rated Power. The fuel cell reactants are stored in reinforced descent stage propellant storage tanks.

Page intentionally left blank

59-44
008547
056935
10 p.

THE TMI REGENERABLE SOLID OXIDE FUEL CELL

Thomas L. Cable, Robert C. Ruhl, and Michael Petrik
Technology Management, Inc.
Cleveland, Ohio

ABSTRACT

Energy storage and production in space requires rugged, reliable hardware which minimizes weight, volume, and maintenance while maximizing power output and usable energy storage. Systems generally consist of photovoltaic solar arrays which operate (during sunlight cycles) to provide system power and regenerate fuel (hydrogen) via water electrolysis and (during dark cycles) fuel cells convert hydrogen into electricity. Common configurations use two separate systems (fuel cell and electrolyzer) in conjunction with photovoltaic cells. Reliability, power-to-weight and power-to-volume ratios could be greatly improved if both power production (fuel cell) and power storage (electrolysis) functions can be integrated into a single unit.

The Technology Management, Inc. (TMI), solid oxide fuel cell (SOFC)-based system design integrates fuel cell and electrolyzer functions and potentially simplifies system requirements. The integrated fuel cell/electrolyzer design also utilizes innovative gas storage concepts and operates like a rechargeable "hydrogen-oxygen battery."

Preliminary research has been completed on improved H_2/H_2O electrode (SOFC anode/electrolyzer cathode) materials for regenerative fuel cells. Tests have showen improved cell performance in both fuel cell and electrolysis modes in reversible cell tests. Regenerative fuel cell efficiencies (ratio of power out [fuel cell mode] to power in [electrolyzer mode]) improved from 50% (using conventional electrode materials) to over 80%. The new materials will allow a single SOFC system to operate as both the electrolyzer and fuel cell..

Preliminary system designs have also been developed to show the technical feasibility of using the design for space applications requiring high energy storage efficiencies and high specific energy. Small space systems also have potential for dual-use, terrestrial applications.

INTRODUCTION

To provide a practical focus for design, NASA-Lewis has selected an example case to consider: a Low Earth Orbit (LEO) system. LEO applications require rapid cycle times, good efficiencies, low mass, and low volume. All requirements are critical. An integrated system for both electrolysis and fuel cell operation could reduce stack mass and volume by half and greatly decrease the size and complexity of auxiliary systems. A regenerative fuel cell (RFC) has been identified as having the highest potential for meeting the surface power storage required by this application [1]. Use of a single RFC unit would reduce volume and weight substantially and improve reliability. Past efforts to develop a single unit RFC using proton-exchange membrane (PEM) or alkaline systems has been hindered by the inability to develop a bifunctional oxygen electrode [2]. Current alkaline and PEM RFC systems require a pair of units -- one optimized for the fuel cell mode and the other for electrolysis.

This paper presents preliminary research on improved H_2/H_2O (SOFC anode/electrolyzer cathode) electrode materials. The ultimate goal of the program is to show the feasibility of a reversible SOFC/Electrolyzer system suitable for non-terrestrial energy storage applications with increased power density, lifetime, and extended reliability. Demonstration of these design goals will also provide benefits to dual use (civilian) energy storage and power generation applications, such as cogeneration and transportation.

Solid Oxide Regenerative Fuel Cell Technology

The SOFC, developed primarily for terrestrial power generation applications, provides an alternative type of RFC system. SOFCs utilize a solid electrolyte operating at high temperature (about 1000°C) to electrochemically convert hydrogen and oxygen to electricity. As a group, SOFCs are potentially very reliable and compact. They can produce a high grade heat byproduct, and have high system efficiencies. Unlike PEM and alkaline fuel cells, SOFCs do not require electrolyte management (solid electrolyte), and have very fast electrode kinetics.

The electrolytic counterpart is a solid oxide electrolyzer (SOE), which operates in reverse. A voltage is applied across the solid electrolyte at high temperature to electrolyze steam into hydrogen and oxygen. Because markets for SOE systems are relatively small compared to the SOFC, SOE development is neither as advanced nor as widely pursued as SOFC developments. Similarities in design and operation, however, suggest that an advance in one should benefit the other.

Most SOFC technologies face problems associated with high operating temperatures: a severe operating environment; the requirement to match thermal expansion between layers of different solid materials; interaction between electrolyte and electrode materials; ensuring reliable and sustainable seals at high temperatures; and maintaining electrolyte conductivities.

TMI Solid Oxide Fuel Cell Design

A latecomer, the TMI SOFC was designed specifically to minimize the problems caused by high temperature operation in other SOFC technologies, particularly thermal expansion matching and minimization of sealing area. In addition, the TMI SOFC was designed for manufacture by conventional manufacturing techniques which could be easily automated to minimize stack costs ($/kW).

Developed primarily for terrestrial stationary power generation applications, the TMI SOFC technology utilizes a unique non-co-fired particulate electrode design which allows new materials to be quickly and easily integrated into the cell or stack without the thermal expansion matching required by every other known SOFC designs. The non-co-fired electrodes along with the planar, radial flow design also provide manufacturing flexibility by allowing the use of available, high volume automated manufacturing technologies. TMI believes the ability to produce the TMI SOFC at low cost is critical to achieving success in dual-use terrestrial markets.

Figure 1 shows an expanded schematic of the TMI SOFC single cell with conventional materials. Each cell is made up of four layers: (1) a porous, nickel-zirconia cermet; (2) a sintered, non-porous, yttria-stabilized zirconia electrolyte; (3) a porous, strontium-doped, lanthanum manganite cathode; and (4) a high-temperature metal alloy separator. The cell, approximately 5 cm (2 inches) in diameter, is full commercial scale.

Figure 2 shows a cross sectional view of the cell. Supplied through the center of the cell, fuel and oxidant, usually air, flow radially outward through porous particulate electrodes where they react along a planar non-porous solid electrolyte. Spent fuel and oxidant mix at the periphery and exit as exhaust.

The self-manifolded cell uses minimal seals. Gases flow radially outward through particulate electrode pathways, eliminating the need for separate inlet manifolds for fuel and oxidant. The plug flow through the particulate bed gives rise to high fuel utilization (90% to 95%) without recycling. Internal manifolding minimizes the seal areas between the fuel and oxidant ports and obviates the need for exhaust manifolds at the circumference of the cells. At the circumference, the remaining fuel and excess oxidant mix and react to virtually complete fuel depletion.

The cell is highly tolerant of dimension changes caused by thermal cycling. Since the cell does not co-fire the layers into a monolithic unit, it can be assembled mechanically. Combined with particulate electrode surfaces

at each of the four interfacial boundaries as shown in Figure 2, the effect of mismatches between coefficients of thermal expansion (CTE) at the boundaries during high temperature operation are minimized. Loose particles in the electrodes allow the separator, seals, and electrolyte to expand at different rates and change position with respect to the electrode without losing electrical contact. A "micro- slip" movement occurs between the particles, separators, and electrolytes.

Without the need to match the CTE between adjacent materials, the TMI can easily incorporate new or improved materials that are not feasible in co-fired designs. Electrode materials with thermal expansion characteristics different from the YSZ electrolyte can be used. Metallic separators, which are less expensive and easier to manufacture than ceramic separators, can also be used. Metal separators also serve to arrest and contain crack propagation in a stack, preventing catastrophic failure due to crack migration, without excessive adverse effects on overall stack performance.

SOFC Regenerable Fuel Cell Design

Figure 3 shows a schematic of the electron and oxygen ion flows in the proposed four-layer regenerable SOFC, which uses the patented TMI SOFC particulate electrode geometry. For convenience, the SOFC anode/SOE cathode, will be referred to as the fuel or H_2/H_2O electrode. The SOFC cathode/SOE anode will be referred to as the oxygen electrode.

The cells are circular, with an outside diameter of 5 cm and a thickness (sum of the 4 layers) of close to 1 mm. The impervious components are: (1) yttria-stabilized zirconia (YSZ) solid electrolytes, (2) metallic-alloy separators, and (3) glass seals. The electrodes (H_2/H_2O and oxygen) are made from unsintered particulates. The cells are stacked and manifolded to separate hydrogen-steam and oxygen storage tanks.

During charging mode (Figure 3a), a potential is applied to the cell and steam is electrolyzed into hydrogen and oxygen. Hydrogen flows from the hydrogen-steam storage through the porous H_2/H_2O electrode. Oxygen flows through the under a very slight overpressure (from the electrochemical pumping) through the oxygen electrode into the oxygen storage tank.

During generation mode (Figure 3b), the same cell operates as a fuel cell with oxygen flowing from the tank maintaining a pressure within the porous oxygen electrode and with hydrogen and steam flowing through the H_2/H_2O electrode in directions reversed from charging mode.

Investigation of Improved H_2/H_2O Electrode Materials

The electrocatalytic characteristics of the H_2/H_2O electrode are critical for steam electrolysis. The standard fuel electrode used in SOFCs is a cermet consisting of a mixture of Ni metal and YSZ. The major role of YSZ in the fuel electrode is to aid in dispersion of the Ni metal particles which decreases the rate of sintering of Ni at the high operating temperature of SOFCs. The electrochemically active area at the interface is limited to the three-phase boundary between the electrode, the electrolyte, and H_2 or steam because YSZ conducts mostly oxygen ions and Ni metal conducts only electrons, not oxygen ions. An electrode that incorporates mixed-conducting materials could increase the electrochemically active area and improve cell performance for both SOFC and electrolysis modes of operation.

TMI investigated the effect on the electrochemical performance of the fuel cell, of replacing YSZ in the Ni-YSZ cermet, with mixed ionic- and electronically-conducting (MIECs) or electronically conducting ceramics. The performance of the new Ni-Ceramic cermet compositions as H_2/H_2O electrodes were compared with the standard Ni-YSZ electrode in both power generation and electrolysis mode. Table 1 list five of the electrode compositions investigated. Compoisition A was the standard Ni-YSZ SOFC anode. Two electrodes (B and E)

investigated the use of mixed ionic/electronic conducting (MIECs) ceramics. The remaining two new compositions incorporated electronically conducting ceramics, one a p-type semiconductor and the other an n-type.

EXPERIMENTAL

Reactor Design

The reversible cell test apparatus, shown in Figure 4, is based on the standard TMI reactor for testing fuel cells, modified to allow the cell to be operated in either fuel cell or electrolysis mode. The single cell is placed in a split tube furnace and held between top and bottom feed plates composed of a high temperature metal alloy. The metal feed plates also provide the electrical connections to the fuel cell. In the electrolysis mode steam is fed to the hydrogen electrode, while the oxygen electrode is maintained under conditions of stagnant air. Water is fed through a 0.16 cm OD metal tube (1/16 in.) into the hot zone of the furnace where it is converted to steam. A power supply is used to apply a potential and decompose the steam to hydrogen. The hydrogen is allowed to escape into the furnace (no edge seals were used in this phase of the research). Oxygen ions are transported through the YSZ to the oxygen electrode where molecular oxygen is produced and allowed to escape into the furnace.

Ceramic Powder and Electrode Materials Fabrication

Standard ceramic fabrication techniques were used in making the ceramic materials used in formulating the electrodes. The procedure for fabricating powders involved mixing appropriate amounts of starting materials. Oxides, acetates or carbonates were used as starting materials, anhydrous chemicals were used whenever possible. The starting mixture was well mixed by ball milling in an organic solvent overnight with zirconia grinding media. The powders were sieved and then loosely packed in an alumina container for calcination. The calcination temperatures ranged from 950 to 1500°C, depending on the material. The ceramic powders were then passed through a 40 mesh (425 micron) screen.

The ceramic powders were mixed with NiO and fabricated into electrodes using standard tape casting techniques. Electrodes were produced by cutting 5 cm OD (2 in.) discs from the "green" anode and cathode tapes. The resulting "green" H_2/H_2O electrodes were approximately 0.5 mm thick. A suspension of the anode and cathode materials, in an organic solvent, was painted on either side of a dense YSZ disc which is 5 cm OD and 0.2 mm thick. The painted suspension is allowed to dry, resulting in a thin coating of very fine particles. This pre-coating improves the contact at the electrode/electrolyte interface and decreases the interfacial resistance. The green electrode discs are then stacked with a dense YSZ disc to form a single cell is placed in the furnace between the metal contact plates. The cell is heated slowly to 1000°C, allowing the organic binders and pore-formers to burn out of the electrode tapes, resulting in a porous electrode structure.

Single Cell Regenerable Fuel Cell Tests

The single cell tests of the H_2/H_2O electrodes were conducted by first testing the materials in the standard fuel cell mode. Hydrogen is fed to the anode at a rate of 100 cc/min and air is fed to the standard LSM_2 cathode at 500 cc/min. The cell is operated in this mode for 24 hours at a constant current density of 200 mA/cm^2. The cell is then operated in the reverse mode by feeding water and applying a voltage to electrolyze the water. The LSM electrode is maintained under stagnant conditions, no air is fed. Water is fed at an equivalent steam feed rate of 100 cc/min. The cell voltage was increased until the current density of the electrolysis cell reached 200 mA/cm^2. The electrolysis cells reached a steady state voltage after 2 to 3 hours. The cells were tested in the electrolysis mode for 24 hours; no change in the cell performance was observed once steady state was obtained.

RESULTS AND DISCUSSION

The data in Table 2 shows the steady state voltages and cell efficiencies obtained for the various electrode materials in fuel cell and electrolysis modes of operation. The efficiency is defined as the ratio of power out (fuel cell) divided by power in (electrolysis). Since the cells were operated at constant current the efficiency is equivalent to the ratio of the voltages in the forward and reverse modes as shown in equation (1).

$$E = P_o/P_i = (V_oI_o)/(V_iI_i) = V_o/V_i \text{ (at constant current)} \qquad \text{Eq. (1)}$$

Electrode A shows the baseline performance for a standard Ni-YSZ cermet electrode. The cell operated at 0.806 V in fuel cell mode at a current density of 200 mA/cm^2. When the NC1 cell was reversed and operated in the electrolysis mode the steady state voltage required for the cell to operate at 200 mA/cm^2 was 1.61 V. The ratio of power out to power in was 0.5 or 50% efficiency. This result is the benchmark for comparing the other electrode materials.

Two electrode compositions, B and E, demonstrated performance improvements over the standard SOFC Ni-YSZ electrode (A). Both the B and E compositions were formulated by replacing YSZ in the standard Ni-YSZ electrode with a mixed ionic/electronic conducting ceramic. The benefit of incorporating a MIEC ceramic in the electrode is evident, improving performance in both fuel cell and electrolysis modes of operation. At the standard test conditions, the cell efficiency improved to 73% for composition B and to 84% for composition E.

Composition C, which contained an n-type conductor, did not perform as well as the standard Ni-YSZ electrode in fuel cell mode, and showed no improvement in electrolysis. Composition D, which incorporated a p-type conductor, showed a definite adverse effect on cell performance for both fuel cell and electrolysis modes. Replacing YSZ in the fuel electrode with pure electronically conducting ceramic materials did not increase the number of electrochemically active sites at the electrode/electrolyte interface, and thus did not improve cell performance. However, incorporation of mixed conducting ceramics is effective in improving the electrochemical performance as predicted by theory. The results demonstrate that the MIEC electrode compositions are truly bifunctional and that the TMI cell design is feasible for reversible fuel cell applications.

14 KW LEO CONCEPTUAL DESIGN

An innovative electric energy storage system for space (and also dual-use) applications is proposed using the TMI solid oxide fuel cell stacks, modified so the same high-temperature stacks can alternately perform steam electrolysis (charging mode) followed by hydrogen-oxygen fuel cell operation (discharging mode). The concept integrates gas storage with stacks and the system acts like a "rechargeable hydrogen-oxygen battery." Table 3 indicates the example system requirement. Estimated overall energy storage efficiency is expected to approach 80%. Based on preliminary design efforts, the approximate complete system specific energy per mass and per volume for the 14 KWh system ius projected to be:

Total mass: 90 kg (specific energy mass = 156 Wh/kg)
Total volume: 270 l (specific energy volume = 52 Wh/l)

CONCLUSIONS

Technical feasibility of a regenerative solid oxide fuel cell has been demonstrated experimentally. Electrode materials, with improved electrochemical efficiency, have been identified and demonstrated in reversible cell tests. The technical potential of using the TMI SOFC technology for space (and other dual-use) applications has also been identified in an innovative "rechargeable hydrogen-oxygen battery". The following conclusions can be made from this study:

1. A solid oxide fuel cell can be operated efficiently as a truly reversible or regenerative cell, eliminating the need to optimize two separate cells.

2. The chemical composition of the H_2/H_2O electrode has a strong influence on the electrochemical efficiency of a regenerative SOFC.

3. Replacing YSZ in the standard Ni-YSZ cermet electrode with a mixed conductive material improves the cell performance in both fuel cell and electrolysis modes of operation.

4. Replacing YSZ in the standard Ni-YSZ cermet electrode with a pure electronically conductive ceramic material (either n- or p-type) was not effective in improving cell performance.

ACKNOWLEDGMENT

This work performed under NASA Contract Number NAS3-27227.

References

1. Warshay, M. and Prokopius, P.R., "The Fuel Cell in Space: Yesterday, Today and Tomorrow," Journal of Power Sources, 29 (1990) 193-200.

2. Baldwin, R.S., Fielder, W.L., Loyselle, P.L., and Singer, J., "Oxygen Electrode Bifunctional Electrocatalyst Candidates for Rechargeable Fuel Cell Systems", 1992 Fuel Cell Seminar Abstracts, Nov. 29-Dec. 2, 1992, Tuscon, AZ, p. 140.

Table 1. Ni-Ceramic Electrode Compositions

Electrode	Ceramic Material
A	YSZ
B	MIEC
C	n-type semiconductor
D	p-type semiconductor
E	MIEC

Table 2. Reversible Fuel Cell Results

Electrode	Voltage FC Mode (@200mA/cm^2)	Voltage EL Mode (@200mA/cm^2)	Efficiency (P_{out}/P_{in})
A	0.806	1.61	0.50
B	0.859	1.17	0.73
C	0.747	1.57	0.48
D	< 0.08	1.86	<0.04
E	0.887	1.06	0.84

Table 3. Example System Requirements

Application:	Low Earth Orbit
Storage Capacity:	14 KWh (14,000 Wh) usable
Rated Discharge Power:	14 kW
Normal Discharge Time:	35 min at 14 kW
Reserve Additional Discharge Time:	92 min at 4 kW
Normal Charge Time:	57 min at 10.75 kW
Minimum Life:	30,000 deep cycles and 5 yrs
Minimum Watthour Cycle Efficiency:	80% (excluding power conditioning losses)

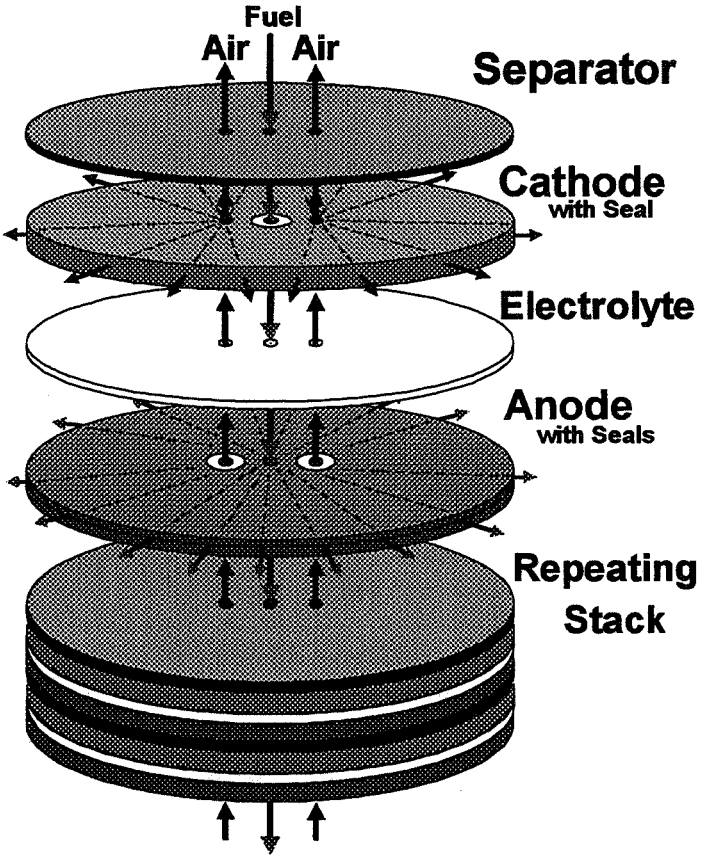

Figure 1. TMI Cell Schematic (Exploded)

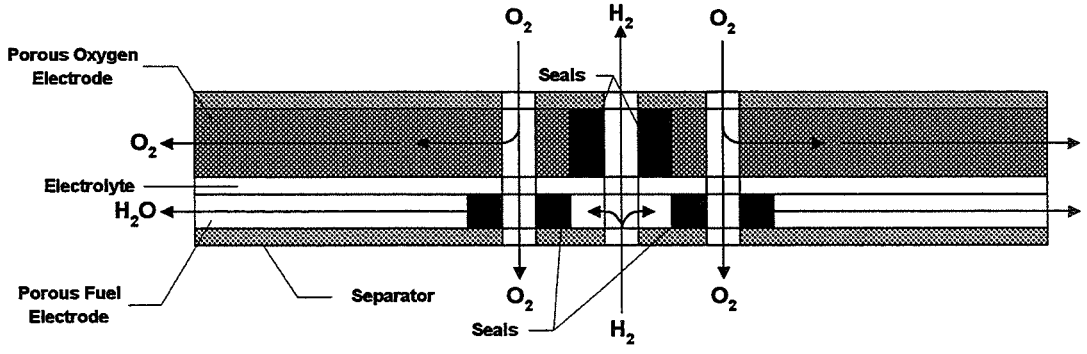

Figure 2. TMI Cell Schematic (Cross Section)

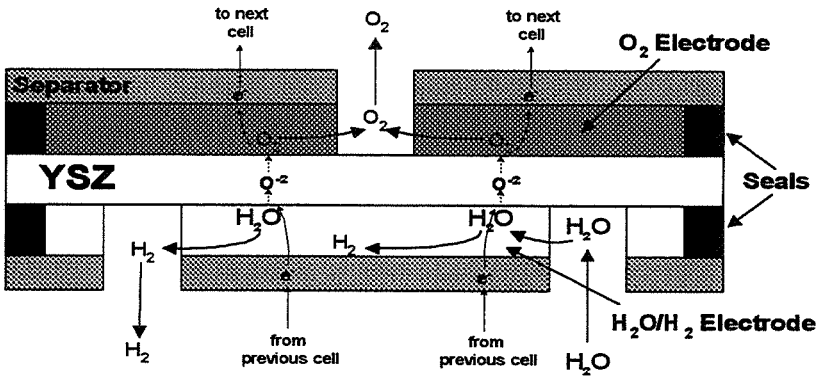

(a) Electrolysis Mode

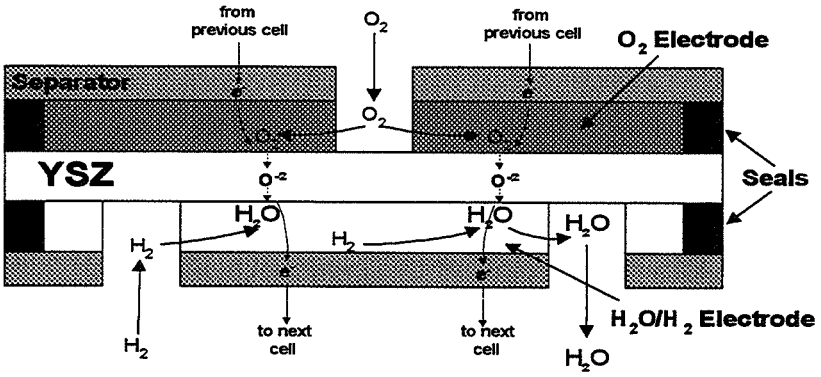

(b) Fuel Cell Mode

Figure 3. RFC Cross Sectional Diagram

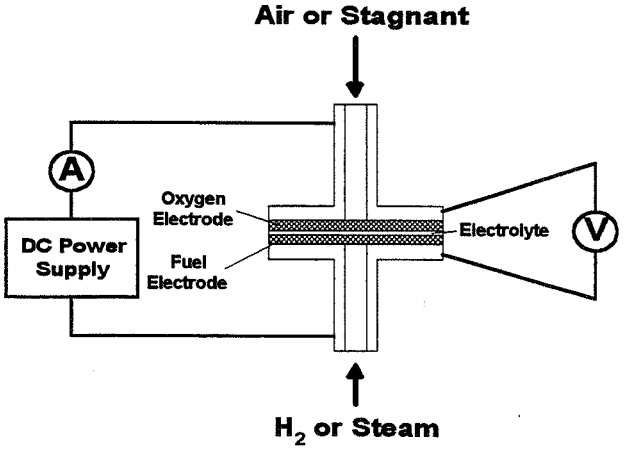

Figure 4. Reversible Single Cell Test Apparatus Schematic

Page intentionally left blank

S10-44
008848

ENGINEERING DEVELOPMENT PROGRAM OF A CLOSED ALUMINUM-OXYGEN SEMI-CELL SYSTEM FOR AN UNMANNED UNDERWATER VEHICLE—AN UPDATE

Dane W. Gregg and Susan E. Hall
Loral Defense Systems—Akron
Akron, Ohio

N95-25694
N/A

ABSTRACT

Most emerging unmanned undersea vehicle (UUV) missions require significantly longer range and endurance than is achievable with existing battery technology. The Aluminum-Oxygen (Al-O_2) semi-cell is a candidate technology capable of providing a significant improvement in endurance compared to the silver-zinc battery technology currently used in UUVs and compares favorably to other proposed UUV power systems not only in performance, but also in safety and logistics. An Al-O_2 semi-cell system is under development by Loral Defense Systems-Akron (Loral) for the ARPA/Navy 44" diameter UUV test vehicle. The power plant consists of a cell stack, gas management, oxygen storage, electrolyte management, coolant and controller subsystems, designed to replace the existing silver-zinc battery and meeting existing weight, volume, electrical and thermal requirements, therefore minimizing modifications to the UUV. A detailed system design is complete. A component and material endurance test to evaluate compatibility and reliability of various material and components is complete. Sub-scale (Short stack) system testing is complete. A full-scale demonstration unit is now under construction for testing in the second half of 1995. The full scale demonstration test will simulate environmental conditions of the operational system. This paper summarizes the results of the extensive short stack and endurance test programs, describes the plan for full-scale testing, and concludes with a brief discussions of future directions for this technology. This program is sponsored by ARPA Maritime Systems Technology Office under NASA contract NAS3-26715.

BACKGROUND

In 1991 Loral Defense Systems - Akron, in response to a competitive solicitation [1], won a contract to design, fabricate and test an aluminum-oxygen fuel cell power system (FCPS) for ARPA's 44" diameter test bed UUV. The FCPS, which is designed to replace the UUV's existing silver-zinc batteries, is electrically transparent to the UUV, meeting the same voltage and power requirements as the current silver-zinc batteries. The initial system design used cryogenic oxygen for oxygen storage. This has been changed to sodium chlorate generated oxygen to significantly increase storage life and handling safety of the FCPS. Although the change in oxygen storage reduced the energy density and specific energy of the fuel cell, the system still possesses an energy density of 450 Wh/liter and a specific energy of 400 Wh/kg, which is at least three times the specific energy of silver-zinc batteries.

ALUMINUM-OXYGEN FUEL CELL CHEMISTRY

As with all electrochemical reactions, the aluminum fuel cell reaction can be broken into its two component half-cell reactions. Electrons are provided to the load by the anodic dissolution of aluminum through reaction with an electrolyte, typically 4M potassium hydroxide circulated through the cell stack and electrolyte subsystem with a pump:

$$Al + 4OH^- + K^+ \Rightarrow KAl(OH)_4 + 3e^- \quad (1)$$

At the cathode, oxygen combines with water and electrons and reduces to a hydroxide species:

$$3/4O_2 + 3/2H_2O + 3e^- \Rightarrow 3OH^- \quad (2)$$

The overall cell reaction, which is maintained at 50°C via a cooling loop to obtain optimum useful energy, consumes aluminum, potassium hydroxide, oxygen, and water, and produces a soluble form of aluminum oxide (potassium aluminate):

$$Al + KOH + 3/4O_2 + 3/2H_2O \Rightarrow KAl(OH)_4 \quad (3)$$

When a crystallization reaction is induced in the system, the dissolved potassium aluminate is precipitated out in the form of hydrargillite, and the KOH required by the cell reaction is regenerated for re-use. The hydrargillite is not soluble and can be removed from the electrolyte as a dense crystalline solid. This process, which occurs in the electrolyte subsystem, is essential to achieving the volume and weight efficiency required for the UUV application:

$$KAl(OH)_4 \Rightarrow KOH + 1/2(Al_2O_3 \bullet 3H_2O)\downarrow \quad (4)$$

As water is consumed from the electrolyte solution to support the cell reaction, make-up water is supplied to keep the electrolyte concentration within optimum limits. The net power reaction requires only aluminum, oxygen, and water:

$$Al + 3/4O_2 + 3/2H_2O \Rightarrow 1/2(Al_2O_3 \bullet 3H_2O)\downarrow \quad (5)$$

ALUMINUM-OXYGEN FUEL CELL POWER SYSTEM DESIGN

Figure 1 shows the inboard layout of the 44" diameter FCPS for the ARPA UUV. The design includes two fully redundant power plants, each capable of providing 7.5 kW of net power. Each plant contains its own cell stack subsystem, electrolyte management subsystem, gas management subsystem, coolant subsystem and controller. Each plant functions independently, sharing only the common oxygen storage subsystem. In addition to providing increased reliability and redundancy, the design provides for minimal CG shift, allowing the design to easily meet UUV constraints.

The 44" diameter power plant is designed to allow either extended missions, using the entire energy supply, or multiple missions where only a fraction of the energy is used on each mission. The power system can be shut down and restarted, with no loss of energy between runs. Figure 2 shows a block diagram of the aluminum-oxygen fuel cell power system with electrolyte management.

Cell Stack Subsystem - The cell stack contains the aluminum fuel and gas diffusion cathodes, and is the primary chemical to electrical energy converter. Oxygen, electrolyte and coolant fluids are circulated to the stack. The cell reaction consists of oxygen reduction at the cathode and aluminum oxidation at the anodes. The solid aluminum anodes are dissolved into the electrolyte as an aluminum hydroxide species.

Electrolyte Management Subsystem - The electrolyte management subsystem circulates electrolyte through the cell stack and removes cell reaction byproducts. The cell byproducts are an aluminum species (dissolved in solution) and hydrogen gas from the parasitic anode reaction. The filter/crystallizer located in the electrolyte tank provides a controlled crystallization site for efficient removal of the dissolved aluminum. The dissolved aluminum is precipitated and stored in the electrolyte tank as a dense hydrargillite slurry. This process regenerates the

electrolyte for return to the cell stack. Water stored in a separate bladder in the electrolyte tank is added to the electrolyte to replace the water consumed in the process reaction. This water addition function maintains molarity. The water bladder collapses as water is consumed, providing additional volume in the electrolyte tank for hydrargillite storage.

The electrolyte management subsystem removes any gases that accumulate in the electrolyte. This is done by a two stage gas separation process. The first stage is a column liquid/gas separator. The second stage removes any small entrained gas bubbles that settle out in the electrolyte tank and sends them back to the column separator. The gas collected at the top of the liquid/gas separator is carried to the gas management subsystem for recombination.

Gas Management Subsystem- The gas management subsystem circulates oxygen to the cell stack and the hydrogen recombination assembly (HRA). The hydrogen recombination assembly receives the hydrogen from the electrolyte management subsystem and catalytically recombines the hydrogen and oxygen at low temperature into water vapor for efficient hydrogen removal. Circulation of the oxygen gas removes any water vapor that transpires through the cathode or is generated within the hydrogen recombination assembly. The water which is removed is returned to the electrolyte management subsystem. The gas management subsystem also regulates the pressure within the closed system by utilizing a pair of accumulators to balance the flow pressure of the electrolyte and coolant. This minimizes pressure differential across the cathode.

Coolant Subsystem - The coolant subsystem circulates the water coolant to the cell stack and the hull heat exchangers. The coolant removes the excess heat generated by the exothermic cell reaction and regulates the temperature of the stack. The temperature of the water fed to cell stack is regulated by a bypass diverter mixing valve. The mixing of hot and cold flows maintains a consistent coolant inlet temperature to the cell stack, further ensuring the stable voltage regulation of the stack over a wide range of power and heat generation.

Oxygen Storage Subsystem - The oxygen storage subsystem uses the same sodium chlorate candle technology used by the Navy and the airlines for emergency oxygen breathing supplies. Sodium chlorate decomposes into gaseous oxygen and sodium chloride under conditions of sufficient heat. The heat is provided by an electrical igniter at one end of the candle. The release of oxygen, and therefore pressure build-up within the oxygen storage vessel, is controlled by using multiple candles. When the pressure in the vessel drops below a pressure threshold another candle is ignited. Oxygen delivery is accomplished by regulating the pressure in the vessel down to the operating pressure of the fuel cell.

Power and Controls Subsystem - The power and controls subsystems condition electrical power from the stack and provide plant operating power. The plant controller automatically monitors and controls the operation of the power plant, detects and takes action to mitigate abnormal conditions, and supplies status information to the primary UUV controller.

SHORT STACK TEST BACKGROUND AND OBJECTIVES

A short stack test program [2] was conducted to evaluate the performance of the full size aluminum-oxygen cell and key critical subsystems. The test program was designed to use an inexpensive, flexible test bed which provided a full range of operating conditions and loads while minimizing resources consumed. The primary goal of the test program was to operate and measure electrical performance of the aluminum-oxygen cell throughout cell and power system operating life using realistic environmental conditions. Test configurations and operational modes were selected to permit cell and power system characterization over a wide range of operating conditions. Each test built confidence and knowledge of performance and operation of the FCPS. Single-cell, 3-cell, and 9-cell stacks were run. The cells were run at high rate, low rate, and duty cycle discharge profiles similar to those

required by UUV operation. Included in the testing were periodic load scans and rising and falling load transients. Transient load evaluations were run from near open circuit to the maximum expected operational load current.

The secondary goal of the test program was to evaluate the integrated operation of the remainder of the power subsystems. Scaled versions of the electrolyte management, coolant, gas management and controller subsystems were included in the test platform. These subsystems were included to observe scale-up factors such as volume, filter area, flow rates, thermal response and control delay parameters. Environmental conditions were maintained by control laws derived from digital simulations. The simulations used models based on subsystem characteristics obtained from individual component tests and detailed thermodynamic analysis. Control laws were flexible enough to allow modification to maintain expected operational conditions.

SHORT STACK TEST RESULTS

Loral successfully completed eighteen major short stack tests. A test summary is shown in Table 1. The first two tests were initial checks of system flow and control. The next five tests were used to identify test setup problems and modify the test setup where necessary to improve controllability. The following three tests identified needed improvements in the anode and cathode assemblies.

Tests KOH-9 and KOH-10 demonstrated feasibility of the cell design and system operation at high and low discharge rates. Test KOH-11 verified the feasibility of repeated shut-down and start-up of the cell. Test KOH-12 was the first successful 9-cell test. Test KOH-13 modified the quality of the oxygen flow distribution within the cell stack, and included the hydrogen recombiner assembly. This allowed closed-loop testing of all subsystems. Test KOH-14 examined the effect of increasing the electrolyte flow rate on cell operation and effects on the filter/crystallizer. Results indicated improved hydrargillite removal from the cell and the flow lines, which improved the cell voltage near the end of cell discharge. Test KOH-15 minimized and balanced the pressure differentials between the three flow streams to create positive oxygen pressure (greater than the pressure in the electrolyte flow) over the entire cathode surface.

Test KOH-16 was a repeat of KOH-15 with sodium chlorate oxygen generators used as an oxygen supply. This test showed no change in cell operation as a result of using sodium chlorate oxygen generators rather than bottled oxygen. The coolant loop was modified to minimize fluctuations of the coolant inlet temperature. This stabilized stack operating temperature over the wide range of heat output and corresponding load currents.

Typical voltage response versus current density during a load scan is shown in Fig. 3. The load scans were run from near open circuit to 150 percent of operational current. The electrolyte conductivity has reached steady state value. Figure 4 shows a typical transient response of the nine cell stack. The current load is changed rapidly from 3 amps to 74 amps. The corresponding cell stack voltage response drops from 15 volts to 11.5 volts. The current load response delay and overshoot is a function of the load bank rather than a characteristic of the aluminum-oxygen fuel cell.

SHORT STACK TEST CONCLUSIONS

The short stack test program successfully met the program and testing goals. The testing program identified problems early and allowed for timely and cost effective modifications. The electrical performance of the aluminum-oxygen fuel cell was characterized. The short stack power system demonstrated consistent voltage-current response over the fuel load life. The cell stack has demonstrated good transient response characteristics far in excess of the requirements of the operational UUV. The integrated system test was also successful. The filter/crystallizer and electrolyte management subsystem demonstrated dense storage of the hydrargillite byproduct. The test using sodium chlorate generators as the oxygen source showed no degradation of electrical performance of the cell stack or any degradation of the HRA performance. The coolant system provided adequate temperature stabilization and control of the cell stack at all load conditions.

ENDURANCE TEST BACKGROUND AND OBJECTIVES

The FCPS system specification [3] contains several operational endurance requirements which drive material selection:

- Routine operation => 150 hours per month
- Operation and maintenance => 5 days per week, one shift only
- Extended test runs => 3 weeks, continuous operation

Furthermore, the system is required to have a five year design life, with no major refurbishment in less than 2 ½ years. Quantitative reliability and availability requirements are imposed on the system.
Additional requirements are derived from these. For example, to support one-shift per day operation, the system is designed to be shutdown and restarted, with no loss of energy between runs. This means that thermal cycling will occur as the system heats up and cools down on a daily basis. The vehicle itself has limited weight and volume available for the energy section. Since a primary goal of the program is to increase energy density, minimizing the weight and volume of the fuel cell material infrastructure is necessary to maximize the quantity of power producing reactants. Also, despite the best design practices, subsystems which are not intended to be exposed to the caustic environment during routine operation (such as the coolant / water addition subsystem), could be subjected to this harsher environment in the event of a component failure. The conclusion, based upon system performance requirements and operational environments: materials and components selected for FCPS use must be chemically compatible, lightweight, small, and have sufficient endurance to support UUV operations.

The fact that a basic design philosophy of the FCPS program is to emphasize rapid development and minimum cost by utilizing standard commercial practices presents a dilemma: on one hand, since this is the first time a large-scale aluminum fuel cell system has been built for this application, there is no design history to guide the selection of ancillary components and materials. On the other hand, rapid prototyping precludes extensive (time-consuming and costly) statistical reliability testing. How to obtain confidence in material selection prior to building and testing the full system?

The compromise solution was to build an endurance test platform early in the program to test preliminary material and component selections by continuously operating them over a long period of time. Goals of the endurance test program included:

- Exercising materials / components in an operational environment similar to that of the UUV.
- Accumulating large number of operating hours for each item relative to its FCPS operational design life requirement.
- Evaluating compatibility of materials and joint sealing methods with electrolyte / precipitate.
- Monitoring degree of wear, and wear pattern development.
- Observing failure mode types and frequency.
- Factoring results into FCPS part selection, reliability analyses, and maintenance requirements.
- Implementing the test with minimal cost and personnel support.

ENDURANCE TEST RESULTS

The endurance test was conducted over a period of approximately one year. During this time, the components and materials were exposed to various periods of operation and rest, as shown in Fig. 5. Failures were not considered "bad" things. On the contrary, identifying the cause of failure through failure analysis typically yielded very useful information. Failed items were removed from test and replaced by alternate candidates. Time on test was recorded for each item.

The accumulation of operational time varied depending upon the type of item. Most of the active components with estimated FCPS duty cycles below 100% were tested well beyond their estimated FCPS design life - as much as 400% in some cases. Materials, sensors, and components (such as pumps) with an estimated 100% duty cycle were tested to approximately 30% of their design life.

Lessons learned from the endurance testing have been incorporated into the FCPS aluminum fuel cell system design. Among the more surprising results are those that were obtained from simple observation - ease of assembly, noise, vibration, discolorations, locations of leaks. Together with data from hard failures, this information has formed the foundation for full-scale FCPS material and component selection. Confirmation of endurance test results under full-scale system operation and controls will occur when full-scale testing begins.

ENDURANCE TEST CONCLUSIONS

By starting the an endurance test early in the design phase, it is possible to accumulate a large number of operating hours, substitute new materials for ones that are not working, and incorporate lessons learned into the design. Endurance testing is a cost-effective method for obtaining information about material compatibility, system design, and durability, prior to building and testing a full-size system.

FULL SCALE TEST BACKGROUND AND OBJECTIVES

The short stack test program conducted by Loral was an excellent test bed for mechanical and electrochemical subsystems. It provided an opportunity to develop basic control algorithms, determine an appropriate system configuration, and improve anode and cathode performance. The Powerplant Demonstration Unit (PPDU) test program will build on this experience, using a full scale (1 plant) system to demonstrate several key technical issues involved with using aluminum-oxygen fuel cells in UUV applications:

- Energy density and specific energy
- Cell voltage and performance
- Electrolyte packing factor
- Oxygen purity over time
- Startup / Shutdown / Controls
- Hydrogen handling
- Preservation of hull ambient atmosphere (no leaks)
- Safety and reliability

To demonstrate the suitability of aluminum-oxygen fuel cells for UUV applications, the following test objectives have been established for the PPDU test program:

A. Develop and demonstrate autonomous operation of the PPDU system.
   - identify key operational issues

B. Develop and demonstrate reliable, safe operation of the PPDU system.
   - show that system faults (if or when they occur) are detectable and solvable
   - achieve reliable and repeatable operation

C. Evaluate system performance using the FCPS specification as a guide.
   - demonstrate chemical to energy conversion
   - validate performance models
   - verify energy density and specific energy predictions (by test & analysis)

PPDU TEST APPROACH

The high-level PPDU test program has been designed to support each of these objectives as shown in Table 2. There are four tests, each requiring one plant-load of fuel. Test conditions have been selected to permit system characterization and evaluation over a wide range of operating conditions. During testing, the PPDU will operate in a lab environment, using the procedures and controls defined in the FCPS Operational Modes Report [4]. Test parameters will be varied sufficiently to identify and resolve full scale operational issues. All three elements of the fuel cell system - people, products, and processes - will be tested. Each test will build confidence and knowledge of the performance and operation of the PPDU, providing valuable "lessons learned" for future aluminum-oxygen fuel cell development efforts. It is anticipated that some development (refinement, optimization) of system operation will occur throughout PPDU testing. However, more emphasis will be placed on development in Tests 1 and 2, with more emphasis on demonstration / evaluation in Tests 3 and 4.

CONCLUDING REMARKS - FUTURE DIRECTIONS

The development of high energy density air-independent power sources for UUVs is critical in the applications of mine reconnaissance and minefield mapping. The high energy density provided by aluminum fuel cell power systems, along with their inherent safety, simple and quick refueling, and low environmental impact, provide a number of important benefits for mine countermeasure UUVs:

- Increased range and endurance
- More room for UUV payload
- Protection of high value launch platform
- Fewer launches and recoveries

An initial design for a 21" fuel cell for a mine countermeasure UUV is shown in Fig. 6. The design is based on the technology proven in the ARPA FCPS program, refined and miniaturized for a 21" system. This system can provide sufficient energy for the UUV to run for 28 hours at 6 knots while powering 1 kW of on-board equipment, such as sonars. The three major components, the cell stack, electrolyte tank, and oxygen storage tank, are arranged to eliminate dynamic longitudinal CG shift. Other small components, wiring, and piping are located around and between these major components.

Another application for the aluminum-oxygen fuel cell system is as a power source for remote, land-based applications such as field communications, surveillance, backup power, and battery rechargers for soldier training or missions. Compared to existing battery technology, aluminum fuel cells are especially suitable for portable, lightweight systems deployed in an air-breathing environment. For soldier applications requiring missions greater than several days, there is a weight and volume advantage to providing power using an aluminum fuel cell battery recharger with rechargeable batteries such as NICAD or Zn-Air, as compared to using primary batteries such as $LiSO_2$. Furthermore, the aluminum system has fewer disposal problems. Other advantages:

- A wide range of discharge rates means that aluminum fuel cells can be used in a wide range of applications
- Greater endurance and longer lifetime allow greater flexibility in mission planning and logistics
- Safety facilitates operation and disposal

REFERENCES

[1] ARPA Request for Proposal MDA972-91-R-0002, Issued 13 December 1990.
[2] "UUV Short Stack Test Plan", FCPS Report No. 041, November, 1992.
[3] Fuel Cell Power System Specification, Revision 2, dated 5 March 1992.
[4] "FCPS Operational Modes", FCPS Report No. 031, October, 1994.

TABLES

TABLE 1

Short Stack Test Summary

Test ID	# Cells	HRA	Load Type	Test Duration		Set Points			Flow Rates			Comments
				Hrs	Amp-hrs	Cell °F	Tank °F	O_2 psia	O_2 cc/min	KOH gpm	H_2O gpm	
1	1	N	High Rate	3.0	32.4	100	120	14.0	0.017	.018	.017	Initial cell and system test
Di-1	1	N	Flow Test	3.7	0.0	105	120	15.0	1.25-3 Stoich	.018	.018	Flow path check
Di-2	1	N	Flow Test	5.0	0.0	118	140	14.6	1.25-3 Stoich	.026	.052	Start of second cell test
2	1	N	High Rate	1.6	0.0	75	140	14.3	1.25-3 Stoich	.026	.052	Test stopped during fill
3	1	N	High Rate	1.8	0.0	100	140	14.4	1.25-3 Stoich	.026	.052	Leak occurred in manifold
4	1	N	High Rate	7.8	236.3	120	135	15.0	1.25-3 Stoich	.026	.026	Manifolds glued to stop leaks
5	1	N	High Rate	5.7	132.1	125	140	14.6	1.25-3 Stoich	.026	.026	Problems controlling system
6	1	N	High Rate	71.0	3769.0	135	140	15.5	1.25-3 Stoich	.026	.022	H_2 venturi eliminated Cathode non-uniformity established
7	1	N	High Rate	45.6	2751.0	125	135	15.5	1.25-3 Stoich	.026	.022	Mapped cathode prior to test
8	1	N	High Rate	28.8	822.3	122	122	15.6	1.25-3 Stoich	.026	.026	Vexar separator tried unsuccessfully
9	1	N	High Rate	44.9	1120.6	124	124	15.9	1.25-3 Stoich	.026	.026	Improved cathodes used
10	3	N	Low Rate	168.8	2943.0	124	140	15.8	1.25-3 Stoich	.078	.078	Cathode burn holes experienced Anode boot improvement used
11	1	N	Start-up / Shut-down	72.6	4300.0	90-140	90-140	16.0	1.25-3 Stoich	.026	.026	Increased cell gap to .075" Increased density of spacers
12	9	N	High Rate	53.4	3128.0	130	130	15.6	1.25-3 Stoich	.233	.233	First 9-cell test
13	9	Y	High Rate	91.2	3766.4	130	124	16.5	3531.0	.233	.200	O_2 recirc rate set at 1.75X stoich Fixed cathode cracks with epoxy O_2 restrictive orifice moved to inlet
14	1	Y	High Rate	63.1	4108.0	126	118	16.5	463.6	.018	.052	KOH flow rate increased by 3X
15	9	Y	Duty Cycle	122.5	3600.0	124	118	17.0	4242.0	.133	.466	Balanced KOH and H_2O flows
16	9	Y	Duty Cycle	131.0	4049.0	124	118	17.0	4242.0	.133	.456	$NaClO_3$ as O_2 source Regulated H_2O inlet temperature

TABLE 2

PPDU Tests

Test	Type	Test Features	Load Profile	O_2 Source	Fuel
1	Checkout tests	Fine-tune operation & controls Finalize SHM thresholds for fault indications	Duty cycling High rate period Low rate period	Bottled	90 cells
2	Checkout tests	Let system run Perform overnight shutdown Evaluate cold start capability Perform roll & pitch	Duty cycling	Bottled	90 cells
3	In-hull tests	Start test with hulls open Integrate chlorate candles Perform roll & pitch Optimize controls & SHM for in-hull op	Duty cycling High rate period Low rate period	Bottled / Candles	90 cells
4	In-hull tests	Run test in closed hulls Evaluate endurance & performance	Duty cycling	Candles	90 cells

FIGURES

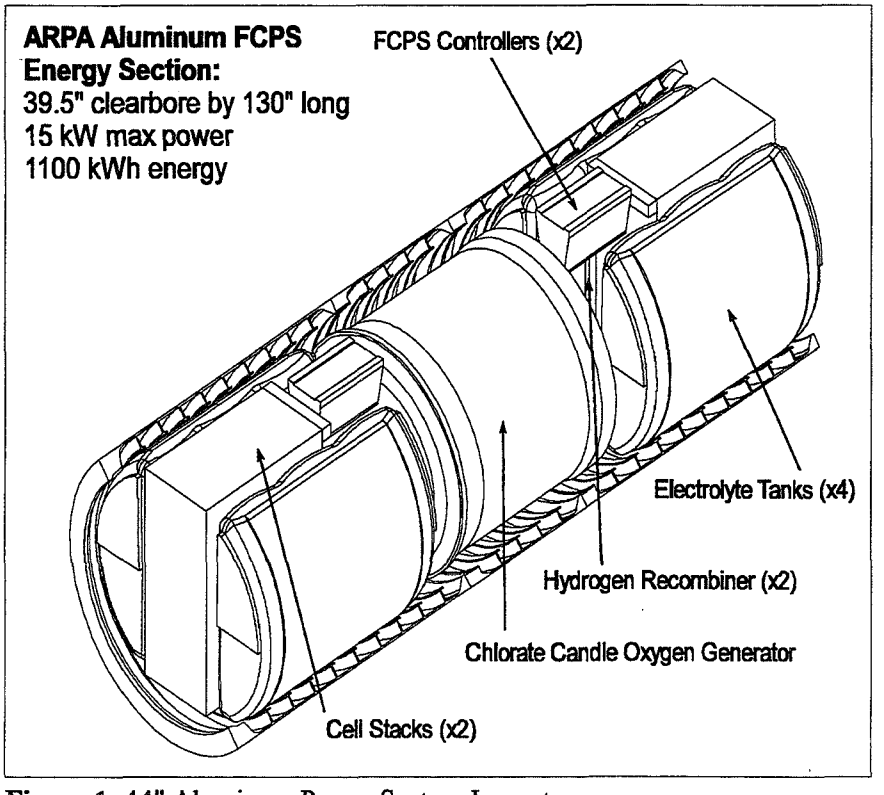

Figure 1: 44" Aluminum Power System Layout

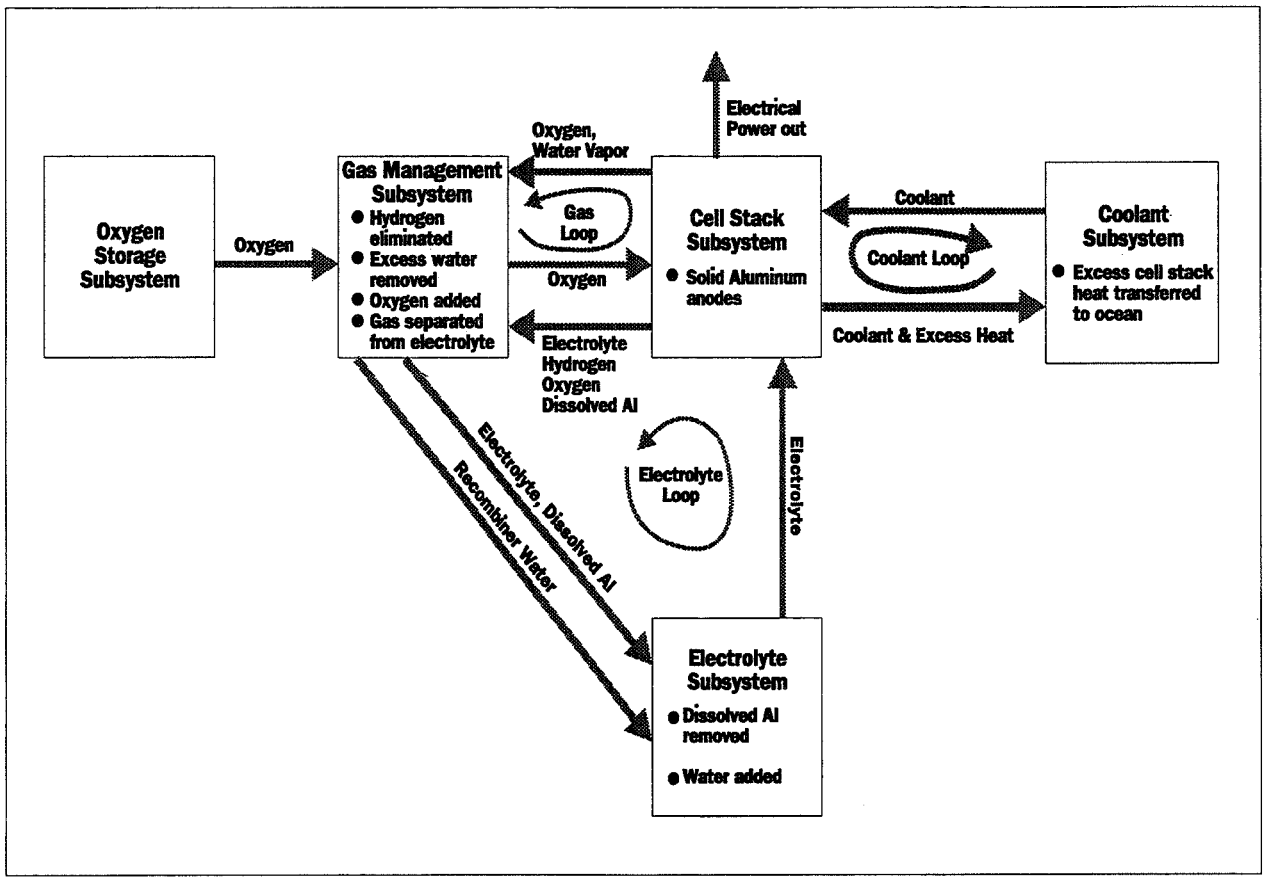

Figure 2: Basic Block Diagram of Aluminum Fuel Cell Power System with Electrolyte Management

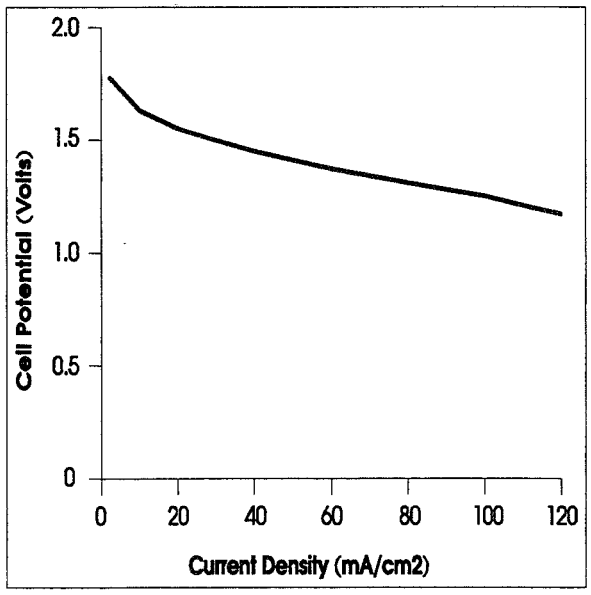

Figure 3: Cell Voltage vs Current Density

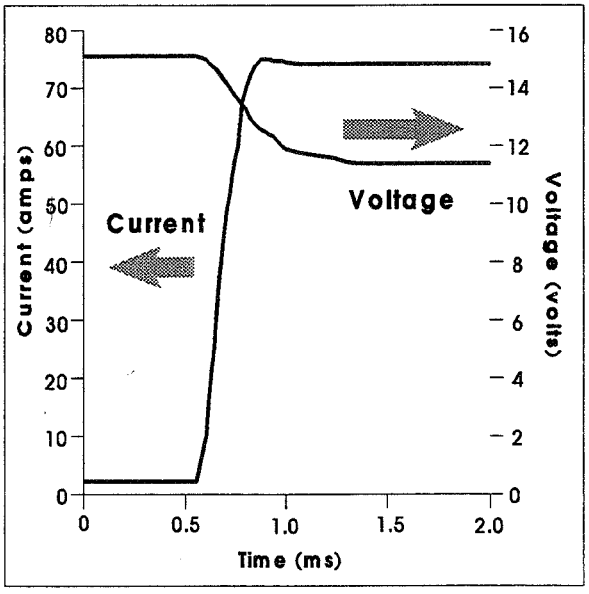

Figure 4: Transient Response of 9-cell Stack

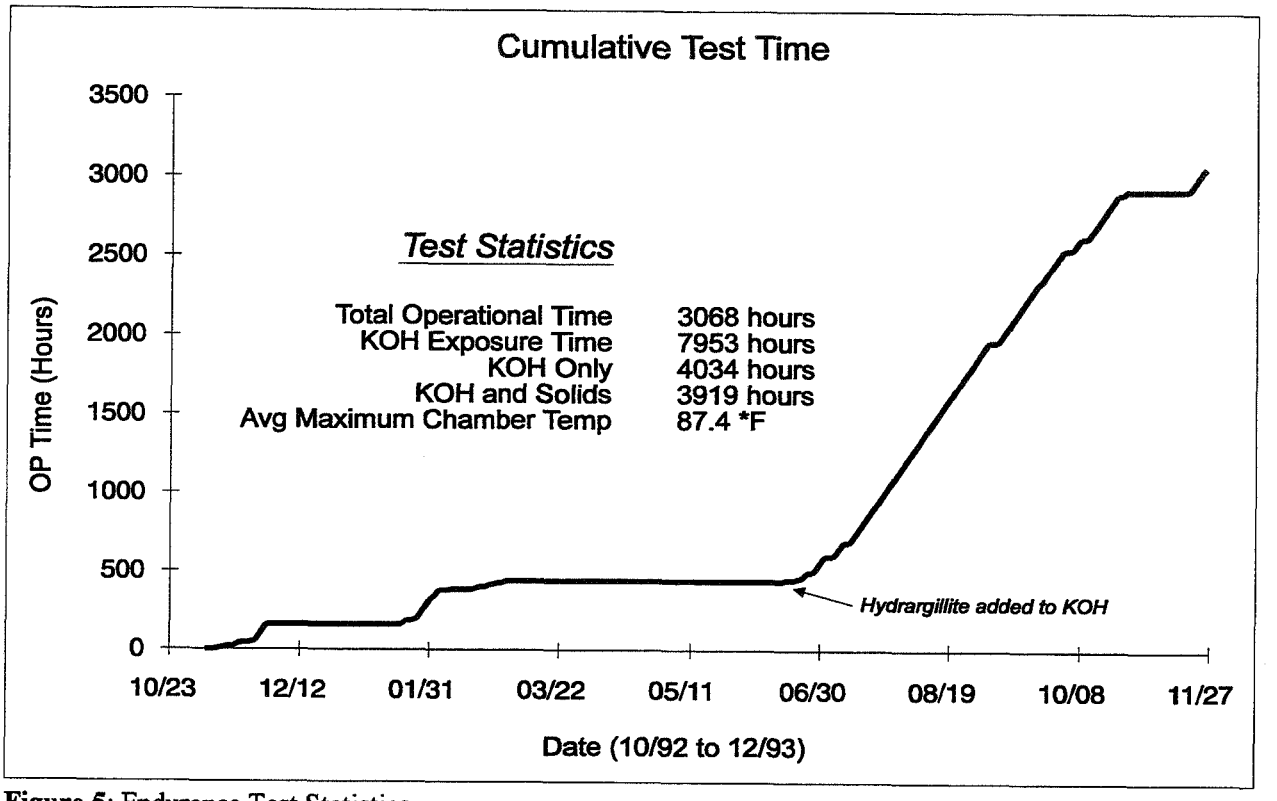

Figure 5: Endurance Test Statistics

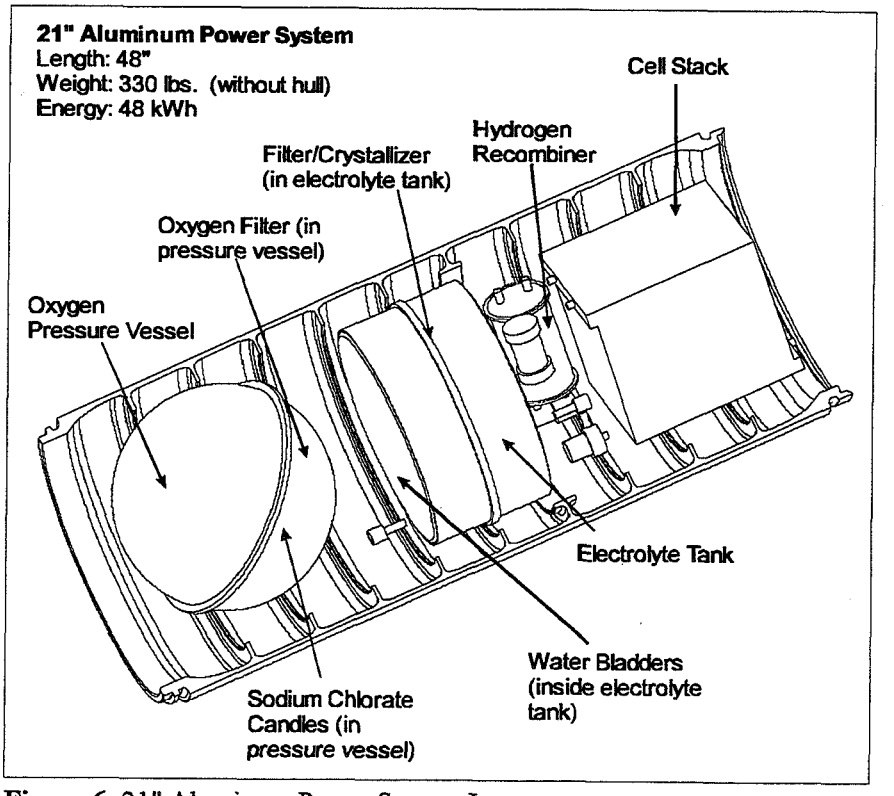

Figure 6: 21" Aluminum Power System Layout

Page intentionally left blank

Advanced Concepts

Page intentionally left blank

SN-54
008 849
14 p.
25694

SPE OBOGS: ON-BOARD OXYGEN GENERATING SYSTEM

James F. McElroy and William F. Smith
United Technologies Corporation
Windsor Locks, Connecticut

SUMMARY

In-Flight Service Evaluation (ISE) of the SPE-OBOGS (United Technologies Corporation) is in the planning stage. This ISE will be conducted on a revenue service commercial aircraft. The 1997 successful completion of the ISE will qualify the SPE-OBOGS for general commercial aircraft use.

INTRODUCTION

Regulations require oxygen usage by commercial airline flight crews during check out and during certain aircraft configurations. This oxygen is drawn from a high pressure on-board cylinder storage system. In a typical aircraft, oxygen cylinder removal for oxygen ground servicing is conducted every 4 to 6 weeks.

In the early 1990's it was recognized that an on-board oxygen generating system could provide an economic advantage for the airlines. In 1992 the decision was made to develop an on-board oxygen generating system for commercial aircraft.

TECHNICAL APPROACH

In specifying the appropriate technology, near term deployment and oxygen safety led to selecting the Proton Exchange Membrane (PEM) technology. The molecular sieve technology combined with an oxygen compressor, although near term, was considered to have oxygen safety questions in compressing oxygen from near ambient pressure to the required 1850 psia. The solid oxide electrochemical oxygen concentrator technology eliminated safety concerns with oxygen generated at pressure without a compressor. However, the solid oxide technology was considered to be several years away from deployment. The PEM technology was considered both near term and oxygen safe without a compressor. Table 1 provides the OBOGS system comparison among the optional technologies.

Any of several approaches could have been used to produce high pressure oxygen using the PEM technology including:

- SPE anode water feed electrolysis (Figure 1)
- SPE cathode water feed electrolysis (Figure 2)
- SPE anode water feed oxygen concentration (Figure 3)
- SPE cathode water feed oxygen concentration (Figure 4)

  Note: All SPE products contain a PEM electrolyte

The SPE cathode water feed electrolysis approach was selected for a variety of reasons as displayed on Table 2.

STACK DEVELOPMENT

The development of the cathode water feed SPE OBOGS built on the cumulative experiences starting with the Gemini SPE Fuel Cell up through current nuclear submarine SPE oxygen generators. In the preparation for advanced nuclear submarine oxygen generation requirements and NASA on-orbit hydrogen and oxygen propulsion requirements, advanced cell structures were developed. These advanced cell structures permitted differential pressures across the membrane electrolyte of several thousands of psi.

The development of the SPE OBOGS stack required the additional solution of sustaining several thousand psi internal pressure without a pressure dome. One demonstrated solution has been the use of a metal laminate configuration where the hoop stress of the high pressure SPE OGOGS is accommodated by metal frames as opposed to traditional plastic frames. Figure 5 shows the laminates of the multiple laminate cell structure.

Although the cathode water feed electrolysis has many advantages for the SPE OBOGS, it does limit the current density that the stack can sustain. This is because the ambient pressure water supply must diffuse through the operating cell membrane in opposition to the proton flux and hydraulic influences before it reaches the anode where the electrolysis process begins. Figure 6 displays the water management within the cathode water feed cell. Using commercially available membranes it was unknown as to the level of current density that could be sustained over the 60,000 aircraft flight hours.

An experimental test program was initiated to determine the appropriate current density. Several dozen single cells were operated at 1850 psi oxygen and ambient pressure hydrogen/water. Figure 7 shows several SPE units undergoing test evaluation. Operating temperatures, electrolyte membranes, catalyst configurations and support structures were all varied in an attempt to establish the sustainable current densities compatible with the aircraft regulations. The selected operating range of 150 to 200 amperes per square foot was established with a

configuration that includes Nafion 117, porous metal membrane supports, and laminated metal cell structures. The duty cycle of the SPE OBOGS is to operate during flight in a "trickle charge" mode to replenish the consumed oxygen at pressures up to 1850 psi. A survey of twelve of the world's airlines, including data on more than 1150 aircraft, revealed that an oxygen rate of 60 liters per day would satisfy 97% of the aircraft surveyed. Figure 8 is a plot of oxygen usage rates for 1182 aircraft of various makes and models. As a result of the survey a generation rate of 0.5 liters per minute was established. Sizing the SPE OBOGS at 0.5 liters per minute output requires the unit to operate about 10 percent of the 60,000 aircraft flight hours. However, in the course of accumulating 60,000 aircraft flight hours the SPE OBOGS must cycle on and off hundreds of times. At each off cycle the oxygen pressure within the SPE OBOGS is vented to ambient pressure.

To simulate the on-off cycles and accumulate the required 6000 hours (i.e.10 percent of 60,000 hours) selected cell configurations were cycled through a 4 hour on-1 hour off cycle for over 6000 hours of accumulated on time. During the on cycle the oxygen pressure built up from ambient pressure to 1850 psi over several minutes. Upon reaching 1850 psi a back pressure regulator vented oxygen while maintaining the 1850 psi generation pressure. After 4 hours of producing 1850 psi oxygen the off cycle was initiated by discontinuing electric current flow and venting the oxygen side of the cell to ambient. With static cooling of the stack over the one hour in the off mode the stack was ready for generation. Figure 9 shows a typical cycle/life test result.

Another aspect of the SPE OBOGS is the requirement that it must be capable of freeze-thaw without damage. This requirement comes from the fact that a commercial aircraft will occasionally be parked overnight on the tarmac in an unpowered mode. If freezing temperatures are possible, the airplane water systems are drained. Although the bulk of the free water in the SPE OBOGS can be drained, the water in the electrolyte membranes and some free water in the cell flow field cavities will remain.

To imitate the potential for the SPE OBOGS being subjected to multiple freeze-thaw cycles, single cells were operated during the normal workday and at the end of the workday these cells were turned off, gravity drained, removed from the test rigs, and placed in a freezer overnight and over weekends at below zero°F. At the beginning of the normal workday these cells were removed from the freezer, installed on the test rigs, and allowed to warm at room condition for about one hour. At this point room temperature process water was circulated throughout the cells and oxygen generation initiated. The cells showed no detectable degradation from these multiple freeze-thaw cycles. Figure 10 provides the results of this freeze-thaw cycle testing.

The SPE-OBOGS stack, sized to produce 0.5 liters of oxygen per minute, will require 10 cells at the selected active area of 0.075 FT^2 each. The small cell size is preferred due to a lower overall stack weight and enhanced power supply efficiency (i.e. higher voltage - lower current). To demonstrate the stackability of the chosen design, a three cell stack was assembled and testing for 900 hours in the production of 1850 psi oxygen gas. Figures 11 and 12 display a photograph and a performance chart of the three cell stack respectively.

IN-FLIGHT SERVICE EVALUATION PLAN

An in-flight service evaluation (ISE) test program has been agreed to in principle involving Hamilton Standard, a major aircraft manufacturer and a commercial airline. This includes a program at Hamilton Standard to develop the flightworthy 0.5 LPM OBOGS topping-off system. Following this, the system will be installed and flight tested on a commercial aircraft in revenue service. Because the ISE system will be the production design, a successful ISE can be followed by the completion of qualification (i.e., endurance testing) after which SPE OBOGS will be production ready. The production design concept is depicted on Figure 13.

FUTURE SPACE PROGRAM BENEFIT

Although the SPE-OBOGS has been specifically developed for use in commercial aircraft, a modified version may find use in future manned space operations.

Currently all space suit oxygen cylinders are filled with oxygen prior to launch. In the space station multiple space walks will be required from each space suit system and therefore refilling the oxygen cylinders on orbit will be mandatory. Currently it is planned to fill the cylinders from liquid oxygen boil off at about 900 psi. A modified SPE-OBOGS could refill two space suit oxygen cylinder systems in about 12 hours from surplus water and power and reduce or eliminate the liquid oxygen logistics requirement.

The modified SPE-OBOGS would use the same cell stack as the commercial aircraft. The gravity phase separator would be replaced with a microgravity membrane phase separator and bellows accumulator. A proposal has been submitted to NASA to develop these modifications.

TABLE 1

OBOGS System Comparison

	SPE OBOGS	Mole Sieve	Ceramic membrane
Oxygen purity	>99.9%	80-90%	>99.5%
Oxygen compressor required	No	Yes	No
Compressed air required	No	Yes	No
Potable water required	Yes	No	No
Reliability and life	Excellent	Good	Unknown
Weight	Low	Moderate	Moderate
Size	Compact	Moderate	Moderate
Development status	Mature	Mature	New technology

TABLE 2

SPE System Options

	SPE Anode Feed Electrolysis	SPE Cathode Feed Electrolysis	SPE Anode Feed O_2 Concentrator	SPE Cathode Feed O_2 Concentrator
Number of Major Components	15	12	18	14
Number of High Pressure Components	9	3	9	3
Number of Rotating Components	3	2	4	3
Relative Humidity of Product Oxygen	~100%	~50%	~100%	~50%

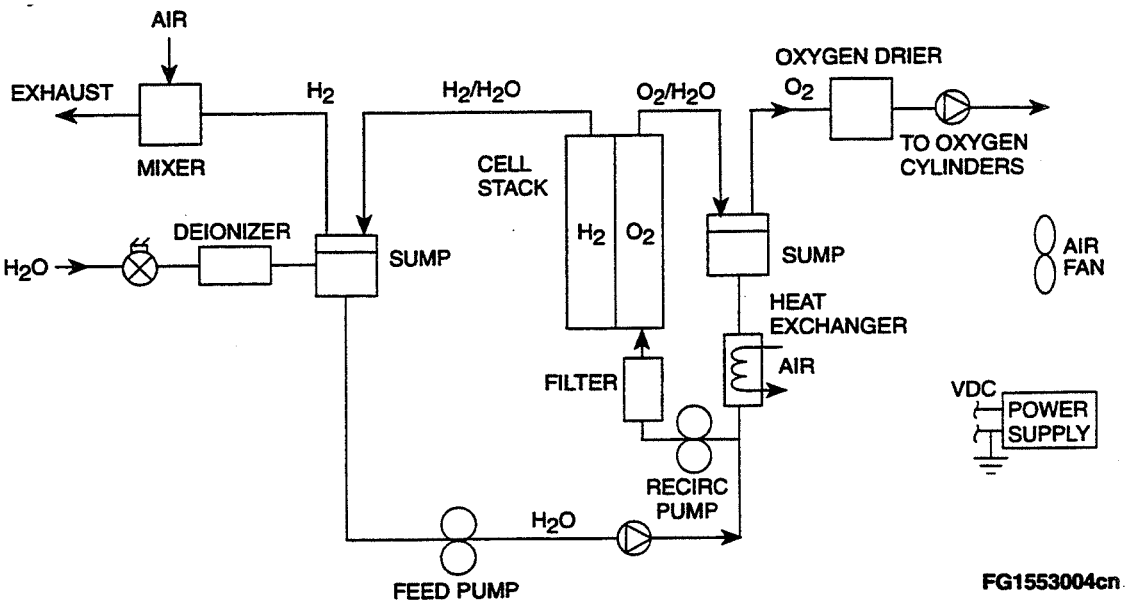

Fig. 1.- SPE Anode Water Feed Electrolysis

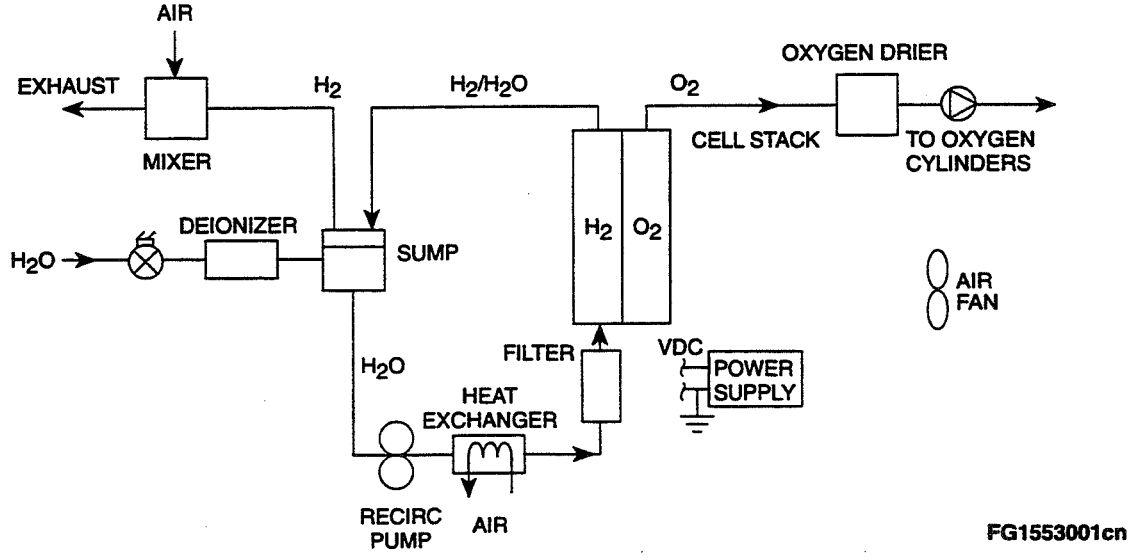

Fig. 2. - SPE Cathode Water Feed Electrolysis

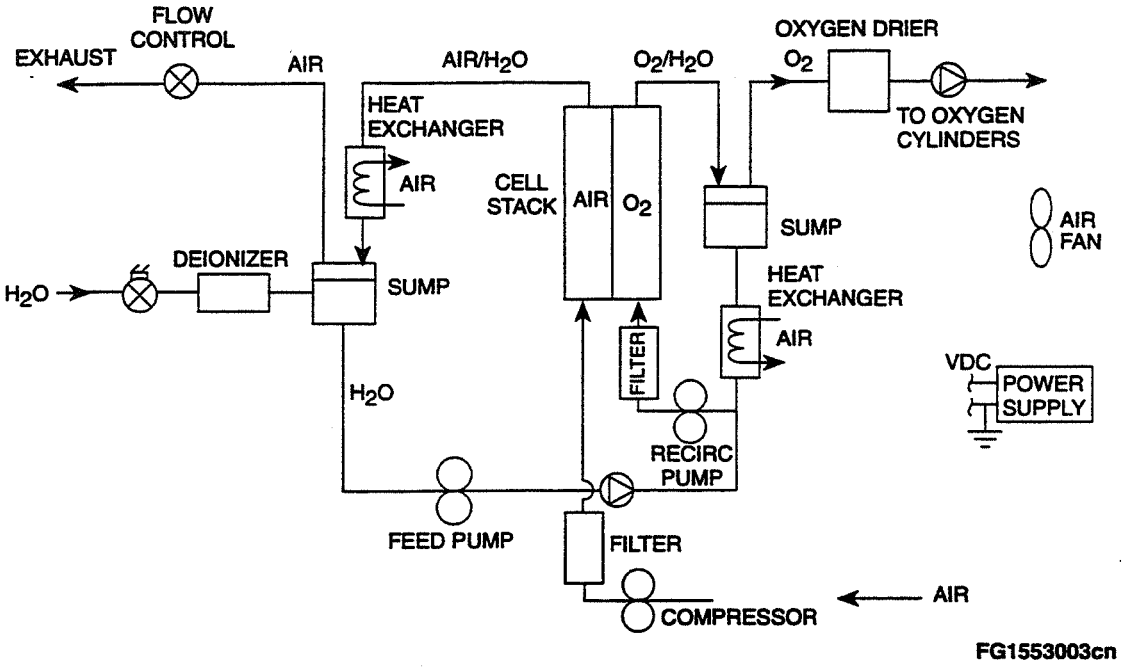

Fig. 3. - SPE Anode Water Feed Oxygen Concentration

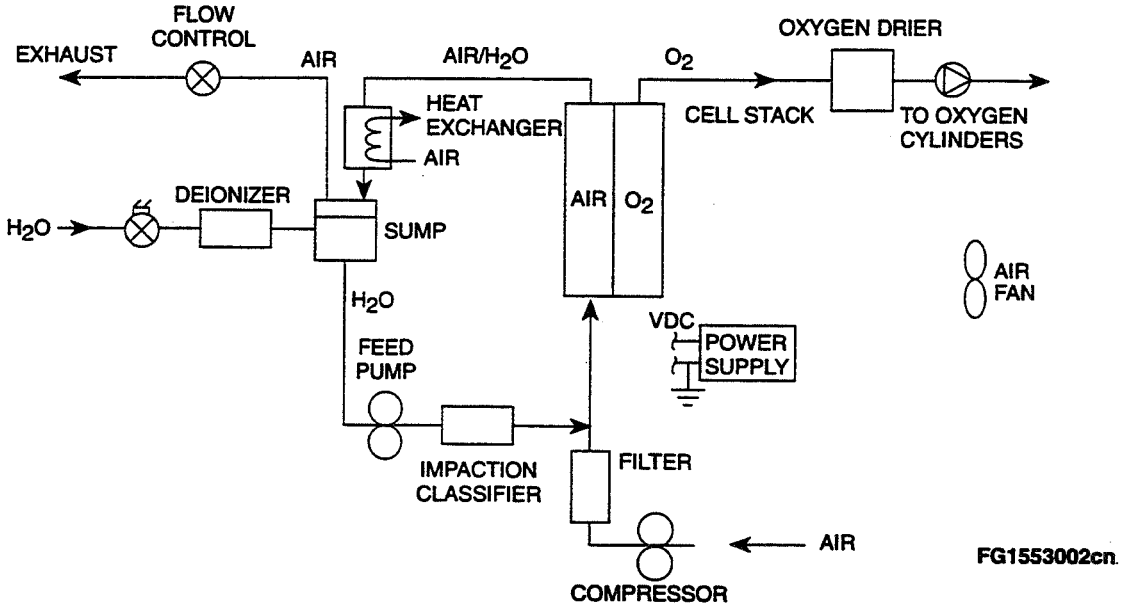

Fig. 4. - SPE Cathode Water Feed Oxygen Concentration

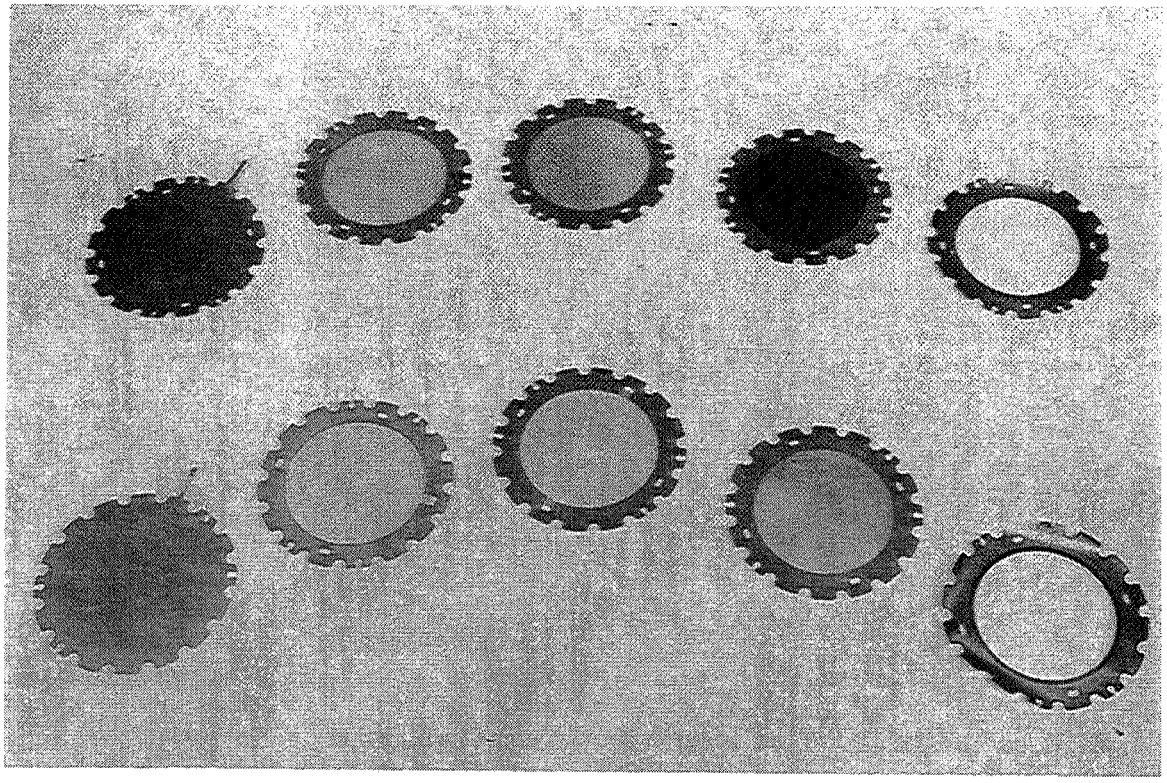

Fig. 5. - Metal Laminates of the New Cell Structure

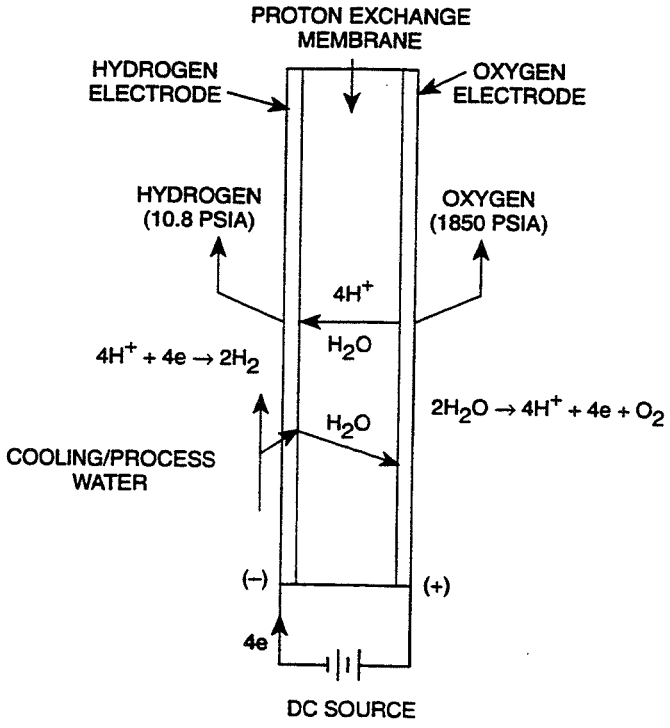

Fig. 6. - SPE Cathode Water Feed Cell Schematic FG1553006cn

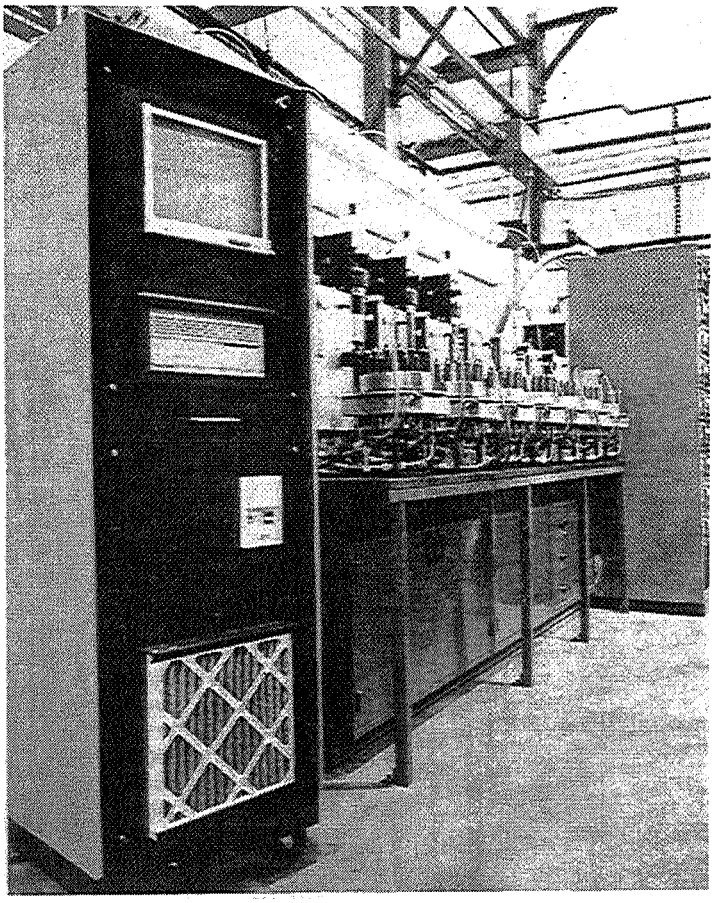

Fig. 7. - SPE OBOGS Test Units

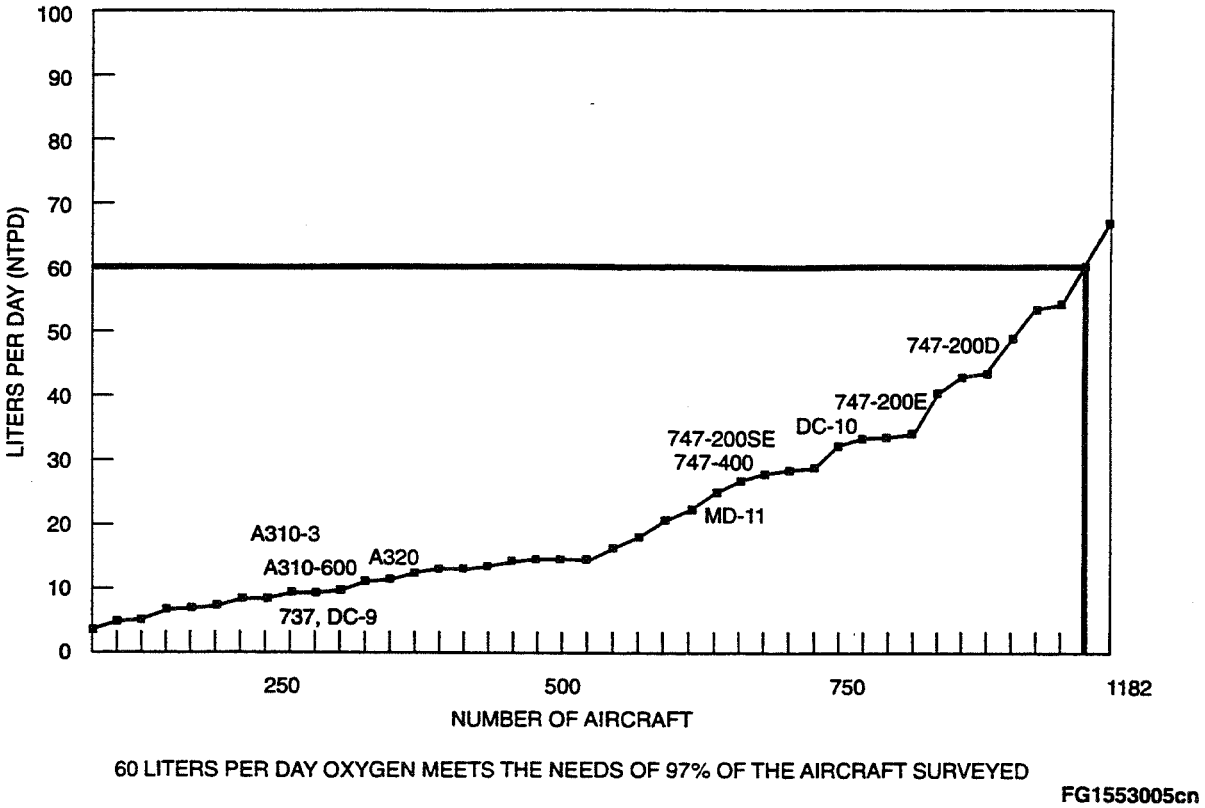

Fig. 8. - Oxygen Usage Summary

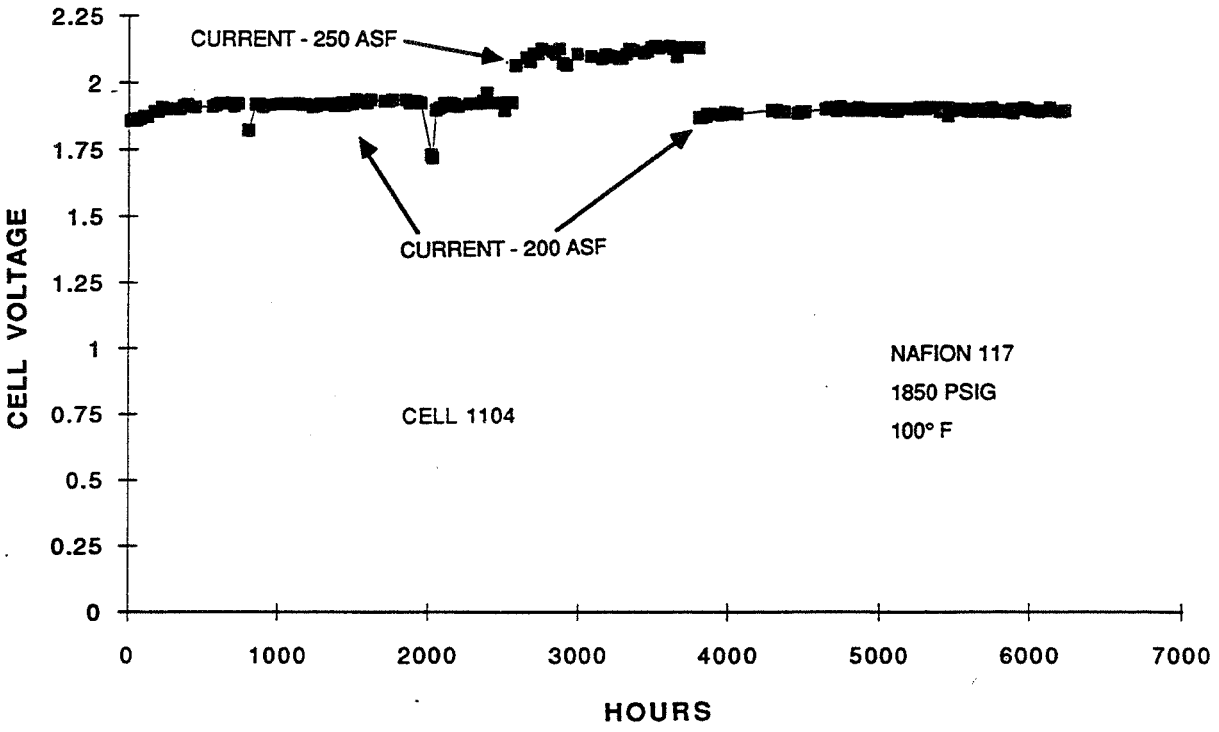

Fig. 9. - SPE OBOGS Single Cell Cycle/Life Test

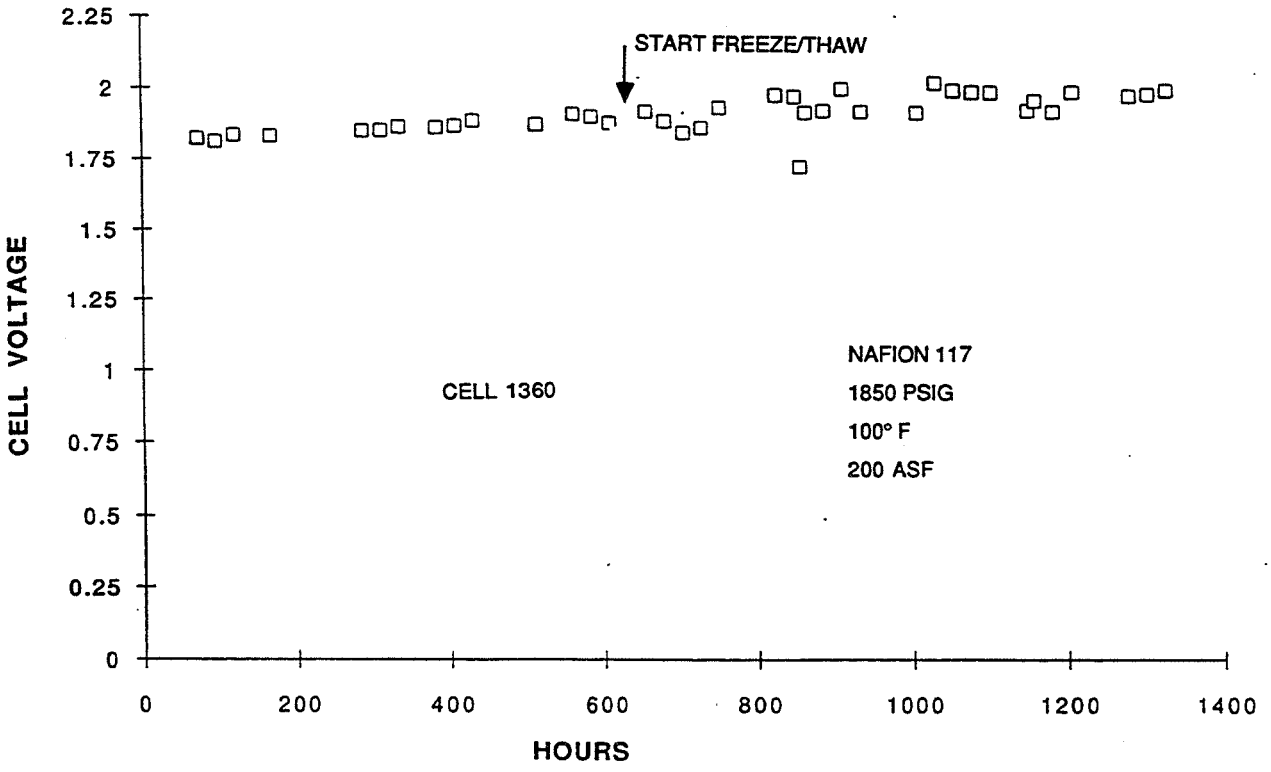

Fig. 10. - SPE OBOGS Freeze-Thaw Testing

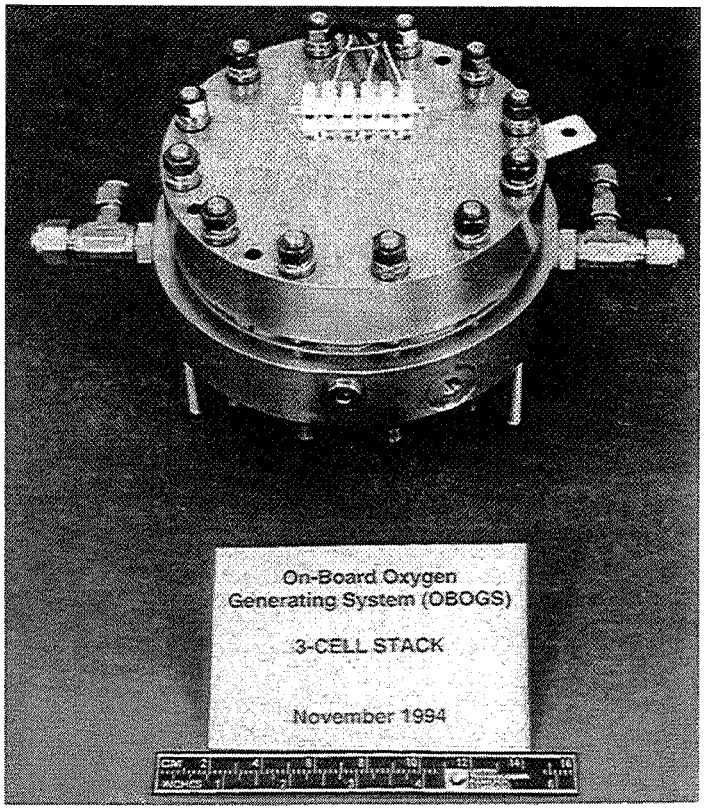

Fig. 11. - SPE OBOGS Three Cell Stack

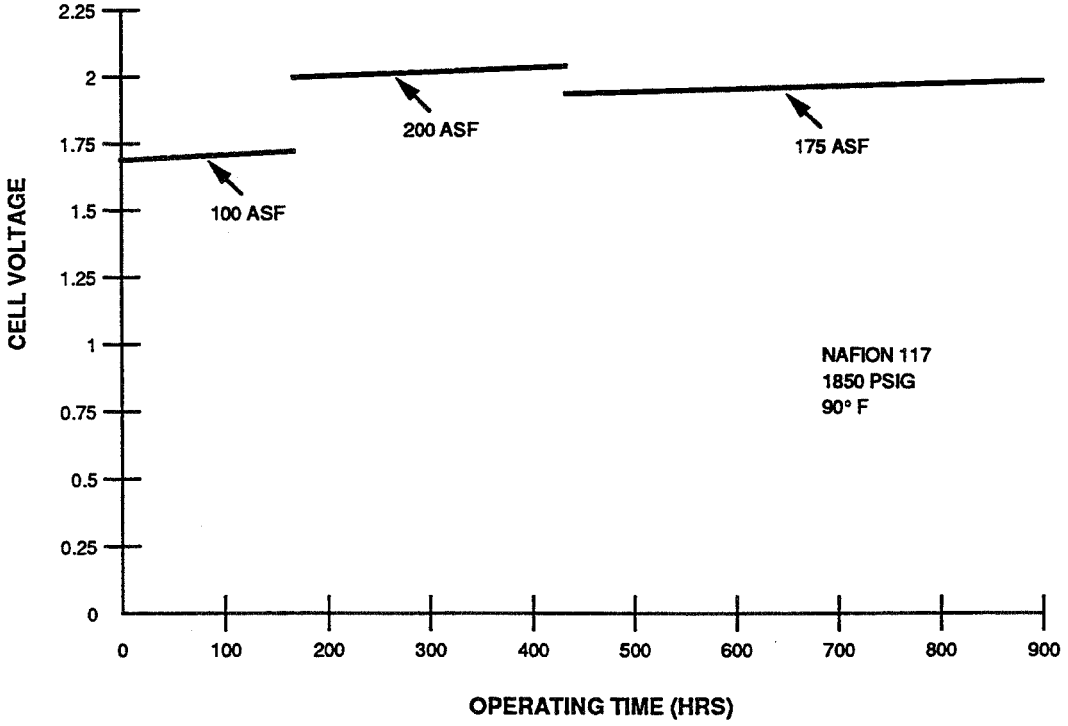

Fig. 12. - SPE OBOGS Three Cell Stack Performance

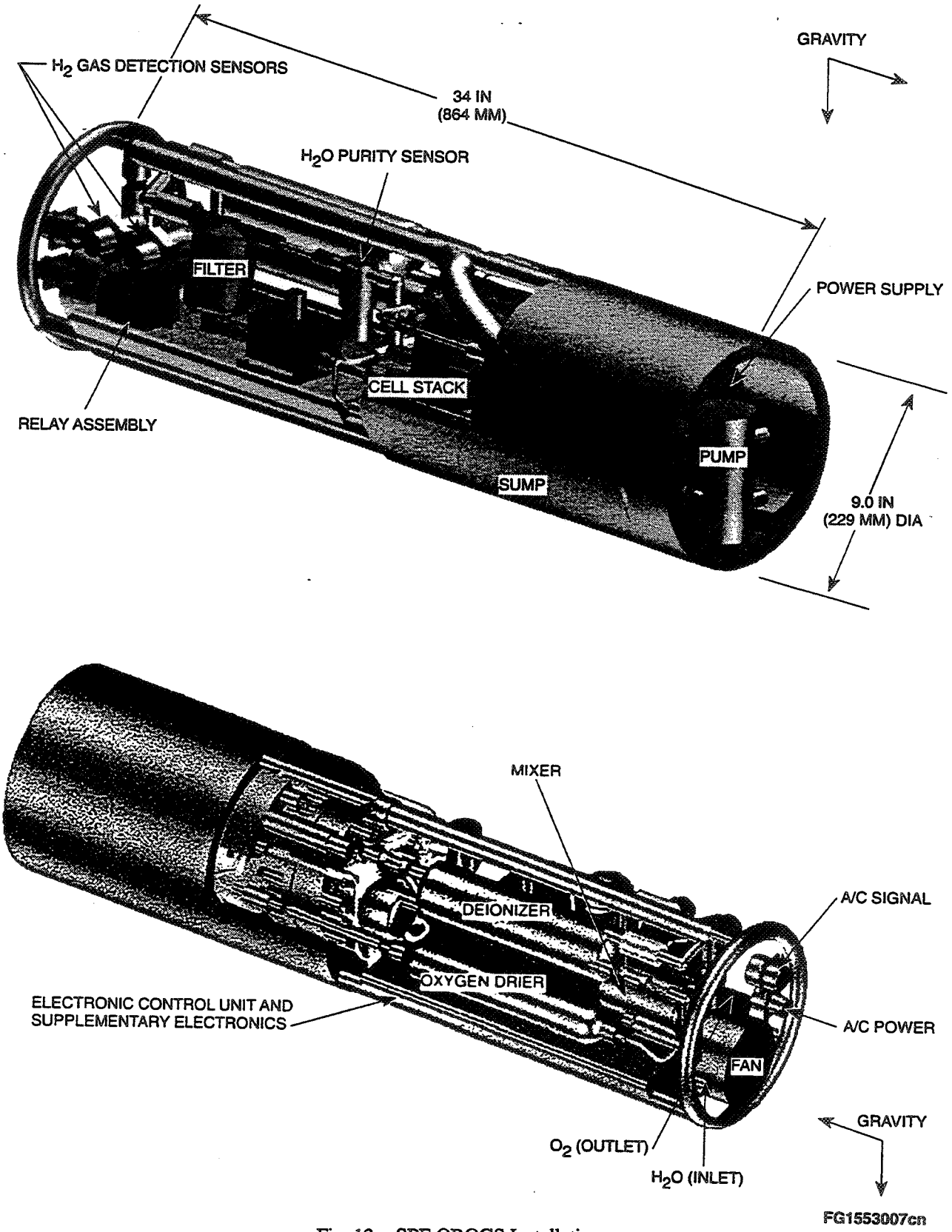

Fig. 13. - SPE OBOGS Installation

5L2-33
008950
16P.
2569/6

HERMETICALLY SEALED ALUMINUM ELECTROLYTIC CAPACITOR

Robert S. Alwitt and Yanming Liu
Boundary Technologies, Inc.
Buffalo Grove, Illinois

and

William Elias
BACE Technologies
Pickens, South Carolina

ABSTRACT

Aluminum electrolytic capacitors are presently not allowed on NASA missions because they outgas water and organic vapors, as well as H_2. As a consequence, for some applications much larger and heavier packages of tantalum capacitors must be used. A hermetically sealed aluminum capacitor has been developed under NASA-MSFC contracts. This contains a nongassing electrolyte that was developed for this application so internal pressure would remain low. Capacitors rated from 250 V to 540 V have been operated under full load for thousands of hours at 85° and 105°C with good electrical performance and absence of gas generation. Electrolyte chemistry and seal engineering will be discussed, as well as the extension of this design concept to lower voltage ratings.

INTRODUCTION

NASA plans to use higher voltage electric power for certain space missions. For example, International Space Station Alpha will have a 120 V power distribution bus. Substitution of electric actuators for hydraulic launch and thrust controls is under study, and this will require high voltage AC motors and inverters. Aluminum electrolytic capacitors are the capacitors of choice for conventional high voltage power electronics applications, but NASA will not use them on space missions. These capacitors are electrochemical devices; they contain an organic electrolyte, and some hydrogen is generated during usual operation. This gas, as well as water and organic vapor from the electrolyte, outgas through the polymer seal. Outgassing is not acceptable for NASA missions, because the vapors can coat optical components, and deposition on other external surfaces may impair radiative heat transfer properties.

The best available present technology to achieve high capacitance and high voltage is to use an array of tantalum

capacitors connected in series/parallel arrangement. These have poor volumeteric efficiency and are heavy. For example, a 1000 μF 270 WV tantalum package used by the military has a volume of 420 cm^3 and weighs 1.4 Kg.

We have developed a family of hermetically sealed aluminum electrolytic capacitors that can be used in new high voltage power electronics applications, and can replace arrays of Ta capacitors. The capacitor contains a cylindrical winding of aluminum foils and spacer sheets, impregnated with organic electrolyte. One hermetically sealed aluminum electrolytic has a rating of 1800 μF at 250 V and has a volume of 180 cm^3 and weighs 0.22 Kg. The volume/μF and weight/μF are reduced by factors of four and ten times, respectively, in comparison with the tantalum package described above. The capacitors are rated for use at 250 V to 540 V at 105°C, and will operate at temperatures as low as -55°C.

This improvement required two advances: (1) a stable, high voltage, nongassing electrolyte; (2) a new package design incorporating a hermetic seal. These developments are described in the following sections.

CAPACITOR ELECTROLYTE

General Characteristics

Fig. 1 shows a sketch of the materials in a capacitor wound element, and defines the function of each. The electrolyte must have certain attributes:

- A wide liquid range to match the operating temperature range of the capacitor.
- A low resistivity, in order to minimize capacitor DF.
- A near neutral pH and absence of aggressive species that might attack metal or oxide.
- Little degradation at elevated temperature.
- Support efficient oxide formation.
- Promote low leakage current.
- Have low toxicity and low flammability.

For this NASA application another electrolyte requirement is no electrochemical gas generation. The capacitor leakage current is the primary source of gas generation. It has both transient and steady components. The transient current is due to dielectric polarization and does not contribute to gas generation. The steady leakage current (SLC) that remains after decay of the transient is an electrochemical current, and generates reaction product at anode and cathode at a rate that is proportional to SLC. The SLC presumably passes at localized defects and impurities in the dielectric. Capacitor electrolytes generally contain a few percent water, and the major source of

gas is hydrogen generated by electrochemical reduction of water at the cathode.

Electrolyte Composition

Some principles and guidelines for formulating capacitor electrolytes are outlined here. Detailed discussions can be found in contract reports [1,2].

The main solvent component is γ-butyrolactone (GBL), which has wide liquid range (-44 to 204°C), high dielectric constant (ϵ=39), low viscosity, low vapor pressure at maximum operating temperature (35mm Hg @105°C), and good chemical stability. GBL is a basic solvent. The electrolyte must have a near neutral pH. Addition of some ethylene glycol (EG), a protic solvent, allows use of a larger amount of the basic solute component, which reduces resisitivity. A ratio of about 9:1 GBL:EG reduced electrolyte resistivity by about 60% compared with GBL as sole solvent (1).

Some water is needed to support formation of the anodic aluminum oxide dielectric, after capacitor assembly, at localized sites of exposed Al metal on the anode foil (e.g., edges and terminations). This oxide growth is achieved during "ageing" of the capacitor at rated voltage. The solvent contains 1-3% water for this purpose. Less water than this results in poor efficiency for oxide growth.

Capacitor electrolyte solutes are usually borates and/or carboxylates. The solute is critical for breakdown voltage, resistivity, and thermal stability. For this high voltage application we used an amine salt of a dicarboxylic acid (DCA). The breakdown voltage (V_b) increases with DCA chain length. Acid solubility decreases with increasing chain length. Balancing these effects, we obtained best results with DCA chain length of 9 to 12.

Medium size tertiary amines (e.g., triethyl-, tripropyl-, tributylamine) were added as the basic component to produce the corresponding DCA salt *in situ*. Larger amines are weak bases and do not react readily with DCA to form salts. Attempts to synthesize quarternary ammonium salts of DCA failed because the reaction product is not stable at room temperature.

Nongassing Characteristic

To prevent H_2 evolution, substances known as depolarizers are added to the electrolyte. Depolarizers are reduced more easily than water and the reaction products are nongaseous. Nitroaromatic compounds, such as 2-nitrophenol, are the most commonly used depolarizers because of their ease of reduction and generation of products that are not harmful to electrolyte

performance. The reduction of nitroaromatic compounds produces amino compounds via nitroso and hydroxylamine compounds as the short-lived intermediates [3]. The general reaction scheme is shown below. The overall reduction consumes six electrons per nitro group.

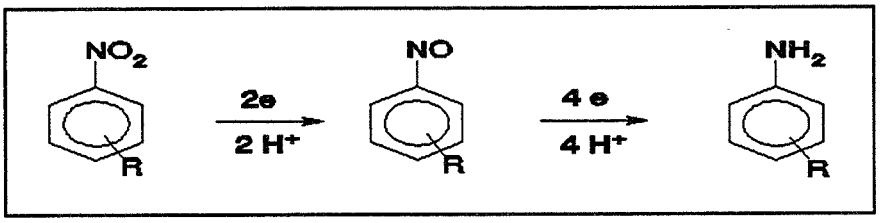

Fig. 2 shows the rate of H_2 generation in laboratory cells for several electrolytes. The same reduction occurs in the EG electrolyte, a glycol-borate composition, as in water. Even in the absence of a nitroaromatic, H_2 generation is reduced in the GBL electrolyte. The current efficiency for H_2 evolution in the GBL electrolyte is about 40% [2]. This is due to parallel reduction of GBL, but details of the reaction scheme are not known. The presence of as little as 0.1% of nitroaromatic (NAN) suppresses gas generation. After its concentration drops to 300 ppm (at 300 hr) gas generation initiates, but at a reduced rate that suggests mixed reduction of remaining depolarizer and GBL.

The amount of nitroaromatic needed in the capacitor depends upon the cumulative charge from leakage current expected over the capacitor lifetime, and the mix of reduction products that are produced. Analysis of electrolyte from capacitors after long term operation showed the presence of only the 6e amino reduction product. Based on the observed operational leakage currents, we estimate that 1-2% concentration is sufficient for the present application to provide 20 year life at 50% voltage derating.

Electrolyte Degradation

These capacitors are expected to operate satisfactorily for thousands of hours at 105°C. Several reactions can occur at high temperature that degrade capacitor performance by increasing electrolyte resistivity and/or decreasing breakdown voltage. It would be very difficult to prevent these chemical reactions. Instead, we try to arrive at electrolyte formulations that result in acceptable parameter change over the required lifetime of the capacitor (2000 hr at 105°C).

GC-MS analyses were performed on electrolyte samples taken from capacitors after more than 1000 hr operation at 105°C. Based on the identified reaction products, three chemical reactions are proposed that can qualitatively account for the observed changes in electrolyte properties. These are acid-glycol esterification,

amide formation, and ring cleavage of GBL.

Acid-EG esterification. - This reaction is well known to occur in capacitor electrolytes. The general reaction scheme is shown on the next page. Because it consumes the acid solute component, this reaction causes an increase in electrolyte resistivity and hence an increase in capacitor equivalent series resistance (ESR). It does not decrease V_b. Fig. 3 gives an indication of the effect from this reaction. With 5% EG the resistivity is unchanged by heating at 105°C. With 10% EG there is a 22% increase, and larger increases occur with higher EG concentration. Because EG reduces the initial resistivity, the final values are little different for EG content of 10% and greater. This was an important factor in selection of 9:1 GBL:EG as the solvent composition for these electrolytes.

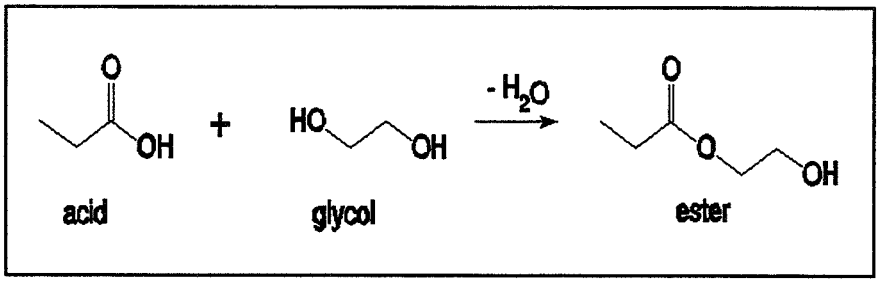

Amide formation. - The amine salts of carboxylic acids can be pyrolyzed to form amides, as shown here. This reaction also consumes solute and has an effect similar to esterification, but it occurs to much less extent.

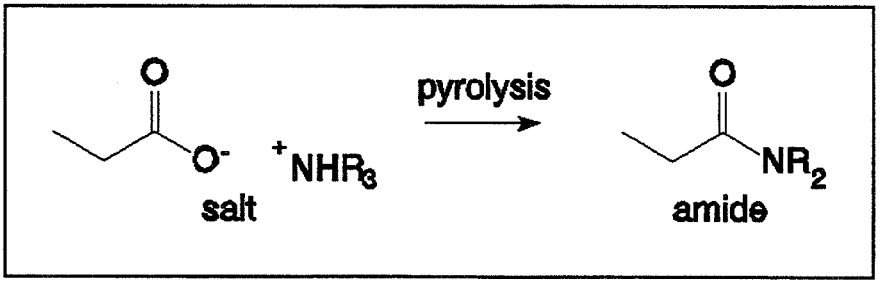

Acid Formation by Ring-cleavage of GBL. - In the presence of nucleophiles such as amines, GBL can undergo ring cleavage to generate γ-substituted butyric acids. These small acids reduce the maximum voltage of the electrolyte. Using amines having low nucleophilicity minimizes this reaction. This is illustrated in Fig. 4; for those examples, nucleophilicity decreases in the order DMEA > DMEAA > TEA > TPA.

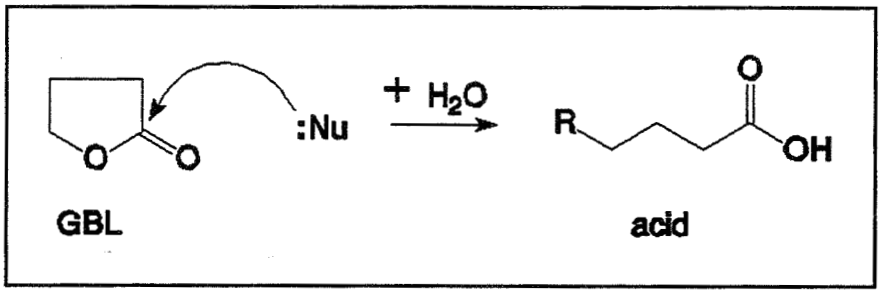

Based on all these considerations, a family of electrolytes was developed for use in 250, 450, and 540 V ratings at 105°C. These formulations are described in a recent U.S. patent application (4).

CAPACITOR SEAL

General

A hermetic seal with electrical feedthrough consist of a glass bushing or disc with a central metal ferrule and peripheral metal ring. The ferrule and ring are bonded to the glass. The ring is welded to the supporting metal structure and the feed-through wire is passed through the ferrule, which is then sealed by welding or soldering. The glass composition is selected so that glass and metal elements of the seal have matched coefficient of thermal expansion (CTE). It is easy to match steel, Kovar, or tantalum with a suitable glass, but aluminum has a CTE that is several times larger than for these metals. Glasses with large CTE have been developed, but no electrical hermetic feedthrough made with these glasses is commercially available.

We elected to use a conventional glass/stainless steel hermetic feedthrough, which raised two problems. First, make a good weld between stainless steel and aluminum. Second, avoid corrosion across this galvanic couple. Both problems were solved by using a double seal configuration, consisting of a hermetic seal enclosing a conventional polymer seal.

A relatively large capacitor, shown in Fig. 5, was selected for this development effort. Its dimensions are 51 mm (2 in) diam and 66 mm high, excluding the seal. The package components are the aluminum can, aluminum cover with a central opening to accept the hermetic enclosure, and the hermetic enclosure assembly. The enclosure is 19 mm diam (0.75 in) and 13 mm (0.5 in) high. The internal electrical connections make the can negative and the lead from the hermetic seal is positive.

Seal Design

Fig. 6 shows a cutaway view of the hermetic enclosure assembly. A stainless steel cylinder holds the glass seal. That cylinder is welded to an aluminum cup. A proprietary electron-beam welding process (5) was found to make a reliable bond between the steel and the aluminum. The capacitor cover is welded to the cup using a conventional GTAW process. The larger of the two openings in the cup bottom holds a rubber grommet and aluminum feedthrough rivet. The smaller opening is an electrolyte fill hole that is plugged after impregnation. The glass seal is put in place as the last step in the assembly process.

Assembly Steps

The assembly procedure for a conventional capacitor of this size is to attach the terminations of the wound element to the cover terminals, impregnate the wound element with electrolyte, then place it in the can, and seal the can. For the hermetic capacitor, the cover is to be welded to the can and surfaces must be clean and dry or the weld may have pinholes. We changed the sequence so that after welding the terminations from the wound element to the cover bottom (negative) and feedthrough rivet (positive), the element is placed in the can and the cover is welded to the can using the GTAW process. Air is evacuated from the can and element, and the element is then impregnated with electrolyte that enters through the fill hole upon removal of vacuum. The capacitor elements are "aged" using a suitable voltage/temperature/time protocol in order to form oxide dielectric on foil edges and at termination connections.

The remaining assembly steps are specific to the hermetic enclosure and verification of hermeticity:

1. Excess electrolyte is drained, the can is back-filled with helium, and a rubber plug is inserted in the fill hole.

2. An epoxy cap is poured over the rubber seals in the bottom of the cup, and the epoxy is cured.

3. Helium leak test #1 is done to test the welds (acceptance limit $< 1 \times 10^{-8}$ std cc/sec).

4. The enclosure is filled with molecular sieve (see below).

5. The glass disc is slipped onto the lead wire and bonded to the steel cylinder.

6. Back fill enclosure with helium and bond wire lead to ferrule.

7. Helium leak test #2 to test seal joints.

Corrosion Prevention

Electrolyte vapor will permeate through the rubber grommet/epoxy into the hermetic seal enclosure, which is a relatively small volume. The capacitor must operate for a long time at elevated temperature, so depending upon the permeation rate and vapor composition, it is possible that condensation could occur in the inner seal volume upon a drop in temperature. The seal is constructed of aluminum and stainless steel, and a conducting electrolyte film bridging these regions could lead to galvanic corrosion of the aluminum. To decide on the best course of action to prevent this, data were obtained for vapor permeation rate at several temperatures, and the composition of the permeating vapor was determined.

It was found that GBL is the main component that permeates, with water vapor and EG essentially blocked. It was calculated that, after several days at 105°C, a condensate film could form if the temperature dropped. Trace impurities on the seal surface that were soluble in GBL could produce a conductive film to support corrosion. We wanted a seal design to assure reliability, so condensation had to be prevented under all circumstances.

Molecular sieves are available that selectively absorb particular vapors. A mixture of two sieve materials, one to absorb GBL vapor and the other to absorb trace moisture, fills the hermetic enclosure cavity. The capacity of the molecular sieve for GBL is high enough to absorb an amount of GBL equivalent to permeation for 6 years at 105°C.

Another consideration was the possibility of a small shunt current passing over the surface of the glass disc due to surface conduction arising from an adsorbed vapor layer. Both GBL and water are polar molecules, and glass has a polar surface, so there is a mutual attraction. To prevent this from occurring, the glass is treated with a silane to render it hydrophobic.

These treatments appear to be successful. After 1300 hr operation at 105°C, capacitor leakage current was measured at room temperature before and after cycling to -55°C. The low temperature exposure was to promote vapor condensation and enhance surface conduction. Leakage currents were normal. No leakage currents were measured that could be assigned to conductive paths across the glass seal. Seal interiors have been examined and there is no evidence of corrosion.

HERMETIC CAPACITOR PERFORMANCE

Hermetic capacitors were constructed with voltage ratings of 250 V, 450 V, and 540 V at 105°C, and these are being tested to Mil specification C-39018. No rating has yet completed the full battery of tests. The results presented here are selected from these tests: dc load at 85°C, dc with ac ripple at 105°C, shelf stability at 105°C, and low temperature properties. It can be noted that failures were encountered during some earlier tests and certain design and procedural changes were made in response. The results presented here represent current best practice.

Table 1 shows results of the 85°C load tests. The range in each test group of electrical parameters is very narrow so we just show here the minimum and maximum values. The capacitors show remarkable stability: After 2,000 hr there is almost no change in electrical characteristics. At least part of this stability is due to the absence of drying out of the wound section that arises from loss of electrolyte solvent and water in a conventional capacitor.

The test conditions with ac ripple for these capacitor ratings are calculated to give a core temperature rise of 3°C over rated temperature (T_{core}=108°C). For the 250 V rating this occurs with 6 Arms using 60 Hz power and a 105°C ambient. The dc voltage was reduced to 245 V so that the instantaneous sum of dc+ac did not exceed 250 V. Table 2 shows the change in parameters after 2,000 hr for the 450 V capacitors (n=16). All parameters are very stable. The dc current measured during test at 105°C is also given in the table, and this increased by only a small amount during the test. Some of these capacitors were opened after test and no corrosion was seen within the winding or at the termination connections.

Table 3 shows the change in parameters after high temperature exposure on open circuit (shelf test). The capacitance and ESR are very stable, and the increase in leakage current is modest for this exposure. The time to charge to voltage was measured for the 450 V units; after the 500 hr exposure it was only 20% longer than the initial charge time, indicating that little degradation of the dielectric has occurred.

Electrolytic capacitors exhibit a characteristic drop in capacitance at low temperature that is related to the increase in electrolyte resistivity. The military specification calls for a change of less than -30% at -55°C. This is met by the 250 V rating, which decreases by no more than 20%. The 450 V units suffer a decrease of as much as 45% at -55°C, but only have a 20% loss at -45°C, which may be adequate for most applications.

Capacitors are randomly tested for hermeticity after completing 2000 hr electrical tests. So far, all seals have retained hermeticity. There have been no signs of high internal gas pressure, such as bulging can bottoms or covers during test, and when capacitors are opened for inspection after test there is no rush of escaping gas. A current of about 100 μA is typical during the 2,000 hr load tests. If this had generated H_2, the pressure within the free volume in the capacitor would have risen by about 4.6 atm (68 psi). Clearly, no gas is being generated. At this current level, about 27% of the nitroaromatic has been reduced after 2,000 hr.

DISCUSSION

Nominal operating conditions are 50% voltage derating and a temperature of 65°C. The leakage current (LC) at 105°C is about 8 times that at 65°C, and the LC at rated voltage is at least a magnitude larger than at 50% derating (see Fig. 22 in ref. 1). We estimate that the nongassing behavior of the electrolyte will be retained for substantially longer than 20 years.

Based on the ac test results, ripple current capability at 120 Hz and 85°C ambient was calculated, and found to exceed that specified for commercial aluminum electrolytic capacitors of similar rating. This attribute, in combination with the stable high temperature performance and long life, makes these capacitors attractive for commercial use in a non-hermetic package.

Vibration tolerance was not designed in at this stage of development since we mostly wanted to establish electrical performance. Vibration proof behavior can be added using the same type spacers and retainers as in present military designs. This gives protection to about 20 G; new designs must be considered if higher acceleration levels are needed.

This work focussed on high voltage applications, where the smaller size and reduced weight of a single aluminum compared with a tantalum package is clearly established. The highest voltage rating for solid Ta capacitors is 50 V 85°C and for wet Ta capacitors it is 125 V 85°C. The aluminum advantage extends to these lower voltages as well, if a need for high capacitance requires use of several parallel connected tantalum capacitors. Aluminum electrolytics <u>always</u> have a substantial weight advantage, even at lower capacitance and voltage ratings where the discrete components have comparable dimensions.

The hermetic design can be modified to be used with smaller case sizes, perhaps down to 6 mm diameter. If successful, this would not only put aluminum in direct competition with tantalum for voltages of 125 V and below, but would also provide new

ratings above 125 V.

CONCLUSIONS

A practical hermetically sealed aluminum electrolytic capacitor has been designed. The present configuration is for large capacitors intended to handle substantial power, but the same principles can be extended to smaller sizes.

A hermetic capacitor for space applications is feasible because it can be used with newly developed nongassing electrolytes with a wide operating temperature range and excellent stability. Even the present first generation designs are estimated to have lifetimes that exceed 20 years under usual operating conditions. The electrolytes are likely to find commercial use for high voltage, high ripple applications.

ACKNOWLEDGEMENT

The authors thank James Lusk for his assistance in constructing the capacitors and supervising the capacitor test program, and Randall Suddeth for running the test program. This work was carried out for Marshall Space Flight Center, under contracts NAS 8-38899 and NAS 8-39371.

REFERENCES

1. Final Report, Contract NAS 8-38899, Boundary Technologies to MSFC, July 1991.

2. Quarterly Reports, Contract NAS 8-39371, Boundary Technologies to MSFC, Dec. 1992 to Dec. 1994.

3. M. Heyrovsky and S. Vavricka, J. Electroanal. Chem., **28** (1970), 409.

4. Y. Liu, U.S. patent appl. 08/360,463, filed Dec. 21, 1994.

5. Trision Welding Process™, Applied Fusion Inc., San Leandro CA 94577.

TABLE 1

Summary of 2,000 hr 85°C load test data

Rating (μF)	(V)	number tested		Capacitance (μF) initial	final	ESR (mohm) initial	final	LC (μA,5min) initial	final
1800	250	42	min	1999	1986	39	38	30	22
			max	2102	2121	49	46	40	50
880	450	38	min	870	874	115	112	41	29
			max	925	932	147	141	50	70
350	540	44	min	322	328	266	246	29	30
			max	369	375	314	284	50	30

TABLE 2

Summary of parameter changes: 2,000 hr 105°C dc+ac ripple test, 250 V capacitors

	% Change		Leakage Current (μA) 5 min (25°C)		at 105°C	
	Capacitance	ESR	initial	final	initial	final
max	1.7	3.9	258	35	83	119
avg	1.2	1.0	52	32	77	105
min	0.9	-2.0	26	29	72	89

TABLE 3

High temperature exposure test: 500 hr at 105°C, no load

Rating	n	Δcap (%)	ΔESR (%)	LC (μA) initial	final
1800 μF 250 V	8	-0.6	-4.1	30	320
880 μF 450 V	7	-1.6	-5.9	41	250

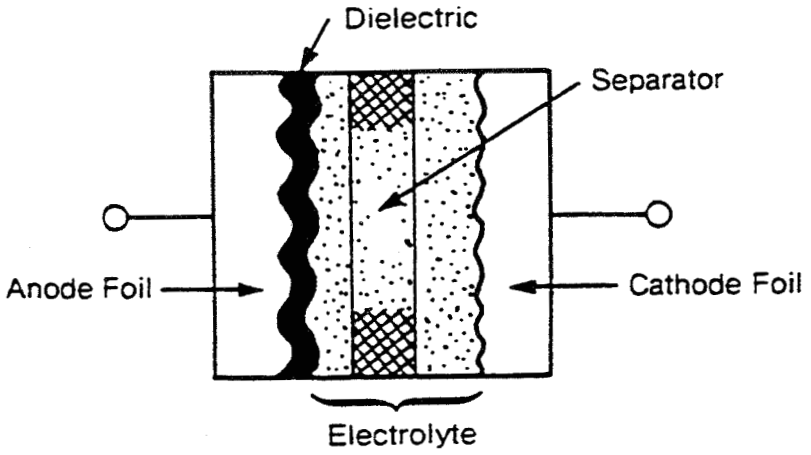

Fig. 1. – Basic elements of an electrolytic capacitor.

· Anode (positive) - Etched Al foil that has been electrochemically coated with an aluminum oxide dielectric layer.

· Cathode (negative) - Etched Al foil current collector.

· Spacer - A thin separator between anode and cathode that prevents shorts and serves as a reservoir for the electrolyte.

· Electrolyte - Provides electrical continuity between anode and cathode, and supports oxide growth when needed.

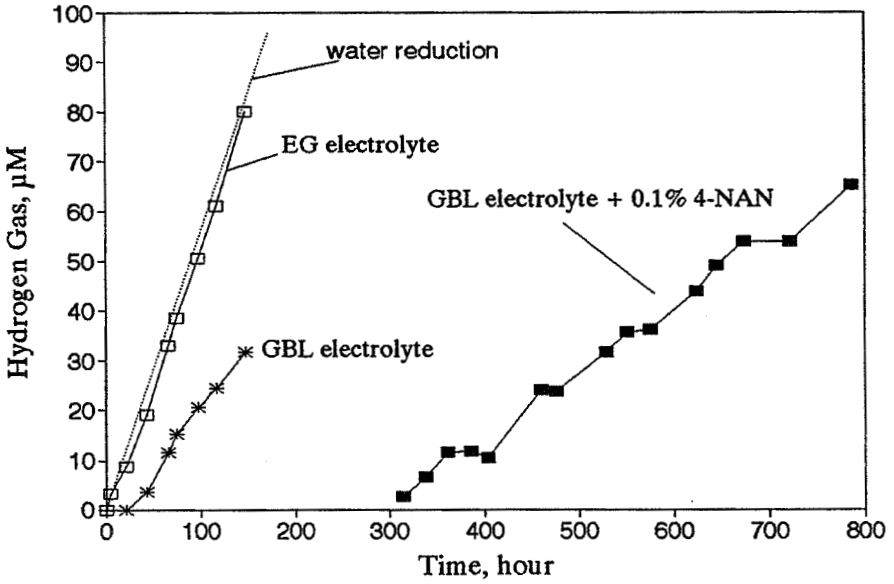

Fig. 2. - H_2 generation in several capacitor electrolytes. Etched Al cathode foil, ~0.1 μAcm^{-2}, room temperature. NAN = nitroanisole.

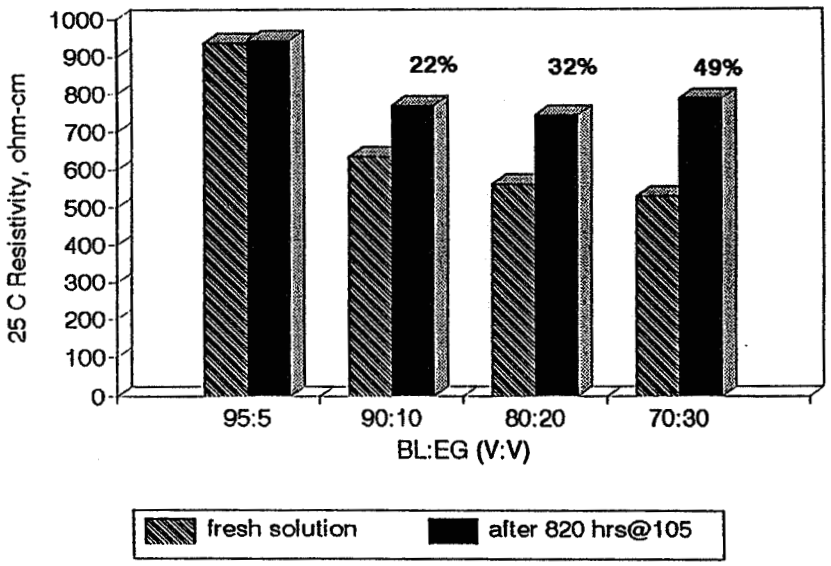

Fig. 3. - Effect of heating at 105°C on electrolyte resistivity. Tertiary amine-DCA solute, BL:EG solvent composition varied as shown.

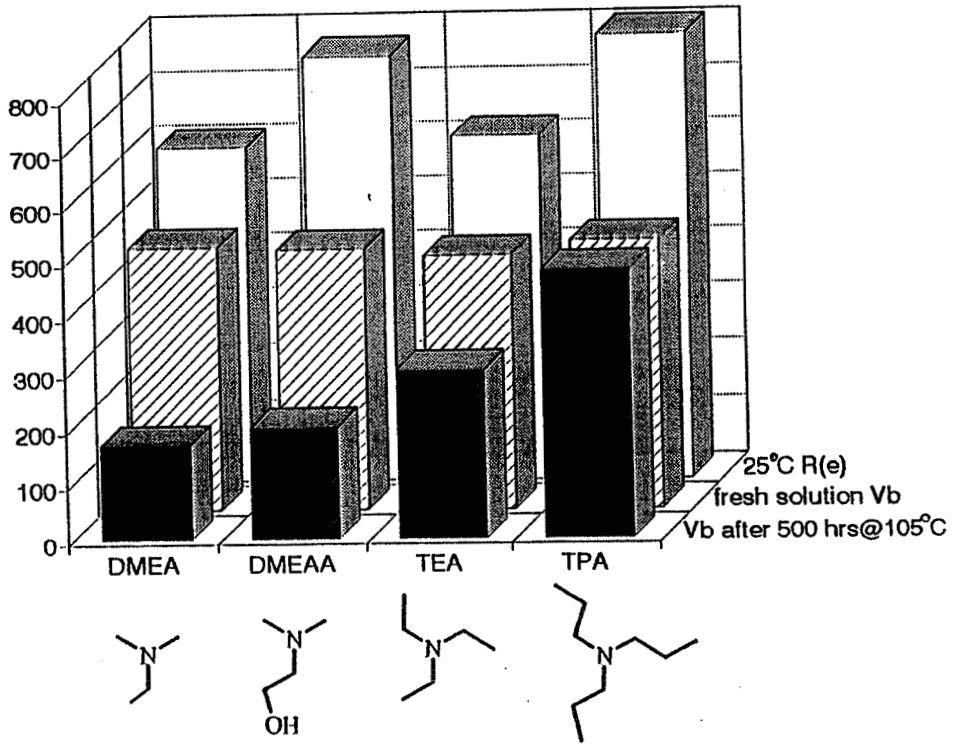

Fig. 4. - Dependence of thermal stability of breakdown voltage on amine structure. BL:EG = 8:2, 0.26 M sebacic acid and 0.39 M amine.

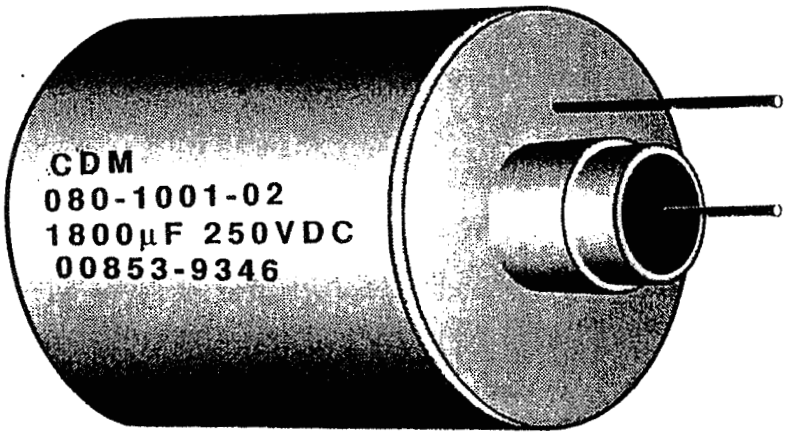

Fig. 5. - Hermetically sealed aluminum electrolytic capacitor. See text for dimensions.

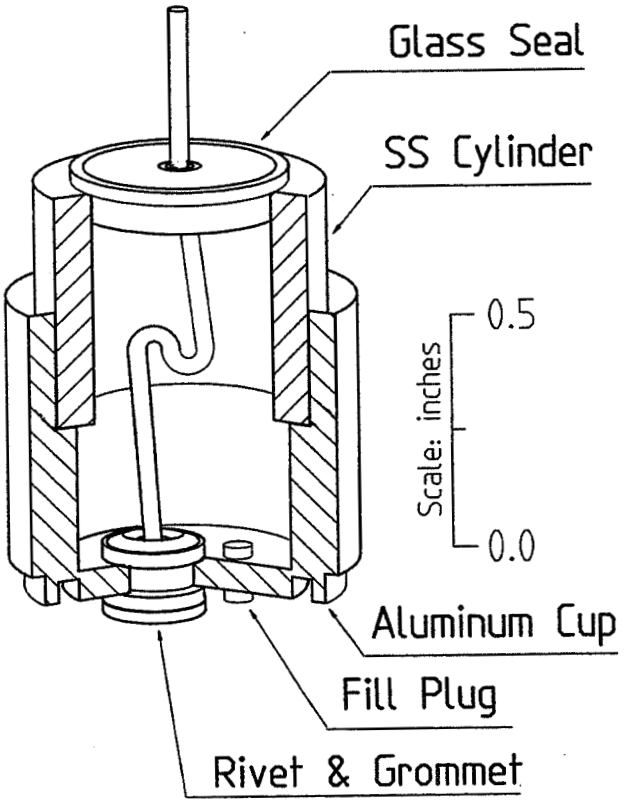

Fig. 6. - Cutaway sketch of hermetic enclosure assembly.

Page intentionally left blank

513-44
008851

SOL-GEL TECHNOLOGY AND ADVANCED ELECTROCHEMICAL ENERGY STORAGE MATERIALS

Chung-tse Chu and Haixing Zheng
Chemat Technology, Inc.
Northridge, California

16 P.
252948

ABSTRACT

Advanced materials play an important role in the development of electrochemical energy devices such as batteries, fuel cells, and electrochemical capacitors. Sol-gel process is a versatile solution technique used in the fabrication of ceramic materials with tailored stoichiometry, microstructure, and properties. This processing technique is particularly useful in producing porous materials with high surface area and low density, which are two of the most desirable characteristics for electrode materials. In addition, the porous surface of gels can be modified chemically to create tailored surface properties, and inorganic/organic microcomposites can be prepared for improved material performance and device fabrications. Applications of several sol-gel derived electrode materials in different energy storage devices are illustrated in this paper. V_2O_5 gels are shown to be a promising cathode material for solid state lithium batteries. Carbon aerogels, amorphous RuO_2 gels, and sol-gel derived hafnium compounds have been studied as electrode materials for high energy density and high power density electrochemical capacitors.

INTRODUCTION

The mission of research and development for space power is toward lighter weight, lower volume, higher efficiency, longer lifetime, and greater reliability. Photovoltaic, solar dynamic, and nuclear systems are common power sources for the spacecrafts, while energy storage options include advanced secondary batteries (Ni/Cd, Ni/H_2, Ni/MH, Na/S, zebra cells, Li/polymer), fuel cells, electrochemical capacitors and flywheels. Development of advanced materials for these energy storage systems play a key role in meeting the goals of future space power requirements.

Sol-gel process is a versatile materials synthesis technique with which material composition, microstructure, and surface chemistry can be tailored to produce desirable properties. In general, the process starts with metal organic compounds, such as metal alkoxides; hydrolysis and polymerization reactions of the precursors lead to gels, which can then be converted into porous or dense materials upon drying and sintering. With this technique, materials can be fabricated into various forms, such as powders, fibers, thin film coatings, and monolithics. Although the sol-gel process is being applied mostly in the preparation of oxide materials, non-oxides such as metal nitrides, carbides, carbonitrides, sulfides and halides can also be synthesized. This technology has been widely investigated and applied in many applications. In this paper, applying of sol-gel technology for advanced electrochemical energy storage materials will be explored. Examples of utilizing sol-gel derived electrode materials in secondary lithium batteries and electrochemical capacitors will be discussed.

THE SOL-GEL PROCESS

The sol-gel technique offers a low-temperature method for synthesizing ceramic materials which are either totally inorganic in nature or composed of inorganic and organic. The process is based on chemical reaction of metal organic compounds in organic solutions. Many inorganic materials which possess special properties are unattainable by conventional ceramic methods, but can be made by the sol-gel process. In addition, the sol-gel process can be used in making porous or dense films or coatings,

highly porous aerogels (porosity up to 98%) and porous xerogels (60% porosity), ultrafine uniform powders and ceramic fibers (Fig. 1). Materials obtained from the sol-gel technique present many unique features and have been explored in wide variety of applications [1].

Chemistry of the Sol-Gel Process

Metal oxides. - Both inorganic or metal organic precursors have been widely used in the sol-gel process for the preparation of oxide ceramics. The most commonly used organic precursors are metal alkoxides ($M(OR)_z$), where R stands for an alkyl group (C_xH_{2x+1}). Normally, the alkoxide is dissolved in alcohol and hydrolyzed by the addition of water under acidic, neutral or basic conditions. The hydrolysis reaction replaces alkoxide ligands with hydroxyl ligands. For example:

$$Si(OR)_4 + H_2O \text{ ----------> } Si(OR)_3(OH) + ROH \quad (1)$$

With hydroxyl ligands, condensation reactions occur among the alkoxides (hydrolyzed and/or un-hydrolyzed) to produce polymers with M-O-M bonds, with water or alcohol as by-products, as shown below for the condensation of silicates:

$$Si(OR)_3OH + Si(OR)_4 \text{ ----------> } (RO)_3Si\text{-}O\text{-}Si(OR)_3 + ROH \quad (2)$$

$$2Si(OR)_3OH \text{ ----------> } (RO)_3Si\text{-}O\text{-}Si(OR)_3 + H_2O \quad (3)$$

Further reactions lead to the formation of silicon oxide polymers. The reactivity of metal alkoxides is usually related to the size of the alkyl group in the alkoxides, such that the rate of hydrolysis decreases with the increasing size of the alkyl group.

Organically modified metal oxides. - Metal alkoxides can react with organic polymers such as polydimethysilane (PDMS) to form organically modified metal oxides. The chemistry of processing is shown in the following reactions:

Condensation between hydrolyzed TEOS and PDMS:

$$2Si(OR)_3(OH) + HO\text{-}[\text{-}Si(CH_3)_2\text{-}O\text{-}]_x\text{-}Si(CH_3)_2\text{-}OH \text{ ---------> } (RO)_3Si\text{-}O\text{-}[\text{-}Si(CH_3)_2\text{-}O\text{-}]_x\text{-}Si(CH_3)_2\text{-}O\text{-}Si(OR)_3 \quad (4)$$

Polymerization:

$$(RO)_3Si\text{-}O\text{-}[\text{-}Si(CH_3)_2\text{-}O\text{-}Si(CH_3)_2\text{-}O\text{-}]_X\text{-}Si(CH_3)_2\text{-}O\text{-}Si(OR)_3 + y\ Si(OH)_4 \text{ ------->}$$

$$\text{-}O\text{-}Si(O)_2\text{-}O\text{-}Si(O)_2\text{-}O\text{-}[\text{-}Si(CH_3)_2\text{-}O\text{-}Si(CH_3)_2\text{-}O\text{-}]_x\text{-}Si(CH_3)_2\text{-}O\text{-}Si(O)_2\text{-}O\text{-}Si(O)_2\text{-}O\text{-}Si\text{-} \quad (5)$$

Besides PDMS, other reactive organics such as conducting polymers and silanes (e.g. $CH_2{=}CHSi(OCH_3)_3$, $H_2NCH_2CH_2Si(OC_2H_5)_3$) will also react with metal alkoxides to form organically modified ceramic materials.

Non-oxide ceramics. - Metal nitrides, carbides, carbonitrides, and sulfides have also been prepared from the sol-gel process. Typical precursors for metal nitrides or carbonitrides are metal dialkylamides, $M(NR_2)_n$, while those for sulfide materials are the metal thiolates, $M(SR)_n$. The chemistry for preparing these two families of materials is similar to those for metal oxides, as shown in Fig. 2.

Control of Microstructure of Sol-Gel Derived Materials

As described above, the hydrolysis and polycondensation reactions of metal alkoxides in an organic solvent result in a colloidal suspension ("sol"). When the electrostatic force on colloidal particles in a sol is de-stabilized, the sol will turn into a wet gel. A wet gel consists of a very porous, 3 dimensional network of colloidal particles, where the pore space are filled with water and solvents. When the fluid evaporates during the normal drying process, the gel shrinks due to capillary pressure. This dried gel is called a xerogel. Subsequent heat treatment of xerogels slowly decreases their porosity and converts them into fully dense ceramics. Ceramics with various porosity can be made by controlling the processing parameters.

Depending on solution conditions, e.g., pH, water concentration, and solvent composition, the polymer may grow into different structures, ranging from linear or randomly branched chains to discrete porous clusters to fully dense colloidal particles (Fig. 3). In general, gels obtained from an acid catalyst has a narrow distribution of pore sizes, while those obtained from a base catalyst exhibit a broad distribution of pore sizes. The microstructure of sol-gel derived materials can also be controlled through aging process and heat treatment (Fig. 4).

Ultra-low-density aerogels are produced by supercritical drying of wet gels. When the liquid phase in a wet gel is dried under supercritical conditions, there is no interface between the liquid and vapor. As a result, the solid skeleton will not be subjected to capillary pressure, and little change in the volume occurs. The supercritically dried aerogels possess exceptionally high porosity, in the range of 90% to 99%, constituting some of the lowest-density solids known. The microstructure can be further modified by heating and/or etching. Heating initially densifies the skeleton and ultimately causes viscous sintering and complete densification. Both xerogel and aerogel exhibit high porosity and high surface area which make them attractive to many applications such as catalysts, catalyst supports, electrodes, filters, insulation materials, etc. Table 1 lists the surface area and pore structure of several xerogels and aerogels [1].

Pekela et al. extended the concept of processing inorganic aerogels to organic aerogels through organic reactions that proceeded through a sol-gel transition [19]. The aqueous polycondensation of (1) resorcinol with formaldehyde (RF) and (2) melamine with formaldehyde (MF) leads to the formation of organic aerogels. The reaction pathway, ultrastructure, and properties of these new materials are analogous to their inorganic counterparts.

Tailoring of the Surface Chemistry

The intrinsically high surface areas of gels permit access of gases to a substantial portion of the solid phase. For example, in a silica gel with a BET surface area of 850 m^2/g, 65% of the silicon atoms are on the surface [1]. The accessibility of the surface makes gas- or liquid-phase reactions a viable means of "bulk" compositional modification. Tailoring the surface chemistry of the pores has been demonstrated in several materials systems.

Nitridation of the pore surface of metal oxides leads to the formation of a metal nitride layer on the surface and subsequent sintering yields metal oxynitride materials which have better

properties. The normal nitridation of metal oxides takes place at high temperature (>1,000°C). However, nitridation of the pore surface of sol-gel derived materials occurs at much lower temperatures (900°C), as shown in the following:

$$-Si_s\text{-}O + NH_3 \text{ ------> } Si_s\text{-}NH_2 + H_2O \quad (6)$$

$$= Si_s - N \begin{matrix} H \\ H \end{matrix} \xrightarrow{\Delta} \begin{matrix} Si \\ Si \end{matrix} N - H \xrightarrow{\Delta} \begin{matrix} Si \\ Si \end{matrix} N - Si \quad (7)$$

Another way to modify the surface of metal oxides is through silylation reactions. Silylation is the displacement of an active hydrogen (usually in a hydroxyl group at the oxide surface) by an organosilyl group which gives organic nature to inorganic surface. The compounds used in this reactions are usually in the form of MX_m, where M is a metal and X is halide, alkoxide, alkyl, allyl, carbonyl, etc. The modification is shown in the following reaction:

$$3Si_sOH + X_3SiR \text{ ------> } -(Si_s\text{-}O)_3\text{-}SiR + 3HX \quad (8)$$

The organic functional group, R, can be vinyl, chloropropyl, epoxy, methacrylate, primary amine, diamine, methyl, cationic styryl, or phenyl. Therefore, the surface of an inorganic material can be modified with a wide variety of organic functional groups.

Modification of the pore surface with other metal compounds has also been widely explored. The simplest scheme to anchor metals on the oxide surface is by reaction with the surface hydroxyls:

$$n\text{Si-OH} + MX_m \text{ ------> } (SiO)_n\text{-}MX_{m-n} + n\text{HX} \quad (9)$$

Organometallics, metal alkoxides, metal halogenides, salts of organic acids, etc. can be attached to oxide surfaces according to this reaction. Thus, a wide range of surface chemistries are possible. These classes of reactions represent potential routes for composite (diphasic) structures, optical and electronic materials, and sensors. The following two reactions illustrate the modification of silicon oxide surface with aluminum compounds, leading to Si-O-Al bonding:

$$Si_sOH + AlR_3 \text{ ------> } Si_sOAlR_2 + RH \quad (10)$$

$$2Si_sOH + AlCl_3 \text{ ------> } (Si_sO)_2AlCl + 2HCl \quad (11)$$

VANADIUM OXIDE GELS FOR LITHIUM BATTERIES

Vanadium oxides, in both the crystalline and amorphous forms, have been studied extensively as reversible cathode materials for lithium batteries [5]. Because of their high redox potential reference to lithium, V_2O_5, LiV_3O_8, and V_6O_{13} have the potential to offer stoichiometric energy density as high as 850 Wh/Kg [6]. However, only part of this energy density has been realized in laboratory studies. This is mainly caused by limitations in the structure and properties of the electrode materials. For example, up to 8 Li^+ ions can be inserted into V_6O_{13} by butyllithium, but only up to 6 lithium can be inserted reversibly. Practical charge densities are even lower since the conductivity of V_6O_{13} decreases when it is lithiated [5]. The versatility of sol-gel processes, on the other hand, provides opportunities for new electrode materials to be synthesized and studied for battery technologies.

The sol-gel chemistry of vanadium oxides has been well studied in the past decade. The chemistry, structure, and properties of vanadium pentoxide gels have been reviewed by Livage [7]. Vanadium pentoxide gels can be synthesized by many different methods, but the most reliable are those based on the hydrolysis and polycondensation of molecular precursors, such as vanadates and vanadium alkoxides. For example, vanadium oxoalkoxides ($VO(OR)_3$) are readily hydrolyzed to form V_2O_5 sol:

$$2\ VO(OR)_3 + 3H_2O \text{ --------> } V_2O_5 + 6\ ROH \qquad (12)$$

Xerogels obtained from sols have a composition of $V_2O_5.nH_2O$, where n usually equals to 1.8 when gels are dried under ambient conditions. Electron microscopy studies indicated that V_2O_5 xerogels had a fibrous microstructure, with the fibers made of ribbon-like particles about 100 Å wide and over 1 μm long [7].

Using vanadium xerogels as cathode materials for rechargeable lithium cells has been the subject of many investigations [6-9]. Baddour et al. performed a detailed investigation of lithium intercalation into the xerogel $V_2O_5.1.6H_2O$ in a propylene carbonate electrolyte solution [8]. They concluded that the lithium intercalation into the gel was a reversible process, and that the vanadium xerogel constituted a promising cathode material. West et al. studied the lithium intercalation of a V_2O_5 xerogel in a lithium cell with a polymer electrolyte ($LiCF_3SO_3$ dissolved in poly(ethylene oxide), PEO) [6]. The cell showed good cycling efficiency of 99.7% during the first 46 cycles and an energy density of 420 Wh/Kg for insertion of 1.1 Li/V_2O_5. In a more recent report, they have demonstrated solid-state thin film batteries base on the V_2O_5 xerogels [10].

In the efforts to improve the performance of solid state lithium batteries, Minett and Owen explored new composite cathode materials with the sol-gel technique [9]. They pointed out that, for solid state lithium cells with polymer electrolytes, the ideal structure for an insertion oxide electrode material would be a composite structure in which the oxide was microdispersed in, and in intimate contact with, an ionically and electronically conducting medium. Composite electrodes were prepared using the sol-gel method to incorporate ionically and electronically conducting polymers, $PEO/LiCF_3SO_3$ and polypyrrole, respectively, into the vanadium oxide gel matrix. Results from the microstructure study suggested that the desired uniform microcomposite structure had been achieved. However, because the loading of the electron conducting polymer to the gel matrix was relatively low, the finely dispersed polymer particles did not form interconnected pathway for the electrons. Therefore, both electric conductivity and cycling efficiency were lower than expected. Nevertheless, this study did demonstrate that the sol-gel process provided opportunity for novel electrode materials to be synthesized.

For an intercalation electrode material to be more efficient, it is generally conceivable that this material should have an open structure, high surface area, and low density, so that the electrode surface can be easily accessed by lithium ions and intercalation will occur rapidly in short dimensions. As described in the previous section, the characteristics of aerogel materials match these features perfectly. As such, V_2O_5 aerogels have been prepared, and their structure and properties have been studied recently [11,12]. The structure of V_2O_5 aerogels were similar to those of xerogels, but had much lower densities (less than 0.1 g/cm^3 vs. 2.0 g/cm^3 for V_2O_5 xerogels). Surface areas as high as 400 m^2/g have been achieved [12]. The electrochemical properties of V_2O_5 aerogels have also been investigated. Initial results indicated that lithium can be intercalated reversibly into the structure [12].

HIGH SURFACE AREA ELECTRODE MATERIALS FOR CAPACITIVE ENERGY STORAGE

Electrochemical Capacitors

Electrochemical capacitors are capacitive energy storage devices based on double-layer capacitance or pseudocapacitance. In comparison with rechargeable batteries, electrochemical capacitors features higher power density and longer cycle life. However, the energy density of electrochemical capacitors is about two orders of magnitude lower than that of secondary batteries. These characteristics allow them to be used as alternatives to batteries for specific applications in which high power rate and long cycle life are important (Table 2).

The double layer capacitance is based on the electrochemical principle that an array of charged particles and oriented dipoles exist at every solid/liquid interface. Energy can be stored at the a solid/electrolyte interface through the charging process at the electric double layer. Typical capacitance obtained from double layer is in the range of 20 ~ 40 $\mu F/cm^2$. Activated carbon represents the best example of double-layer capacitance. Pseudocapacitance arise from highly reversible reactions, such as redox reactions, which occurs at or near the electrode surfaces. Because these reactions involve discrete charge transfer processes, much larger quantities of energy can be stored per volt of charge/discharge than those obtained from the double layer. Pseudocapacitance is generally in the range of 150 ~ 200 $\mu F/cm^2$, and has been found to exist at the solid/electrolyte interface of certain transition metal oxides, such as RuO_2 [14]. Since double-layer capacitance and pseudocapacitance are both surface related processes, surface area and surface chemistry of the electrode materials will greatly affect its capacitance (Table 3).

With its extremely high specific surface area (1000 ~ 2000 m^2/g), activated carbon clearly should have very high energy storage capability. The calculated energy density of activated carbon is around 625 Wh/Kg, when an non-aqueous electrolyte is used[13]. In the real systems, however, the packed energy density of activated carbon based electrochemical capacitors is much less than that value. Most of the capacitors tested have energy density lower than 5 Wh/Kg [16]. The main reason for this low energy density is due to the fact that the electrolyte solution is not able to access the electrode surface present in the micropores of the activated carbon. This lack of electrolyte accessibility also contribute to the internal resistance of the capacitor.

Ruthenium oxide is a material with typical pseudocapacitance. It has been widely studied as an electrode material for electrochemical capacitors [17]. Although the capacitance per unit surface area for RuO_2 is about one order of magnitude higher than that of activated carbon, the surface area of RuO_2 electrodes made by conventional methods has been limited to 100 m^2/g, much lower than that of the activated carbon. Recently, a few non-oxide transition metal compounds have been identified to exhibit capacitance comparable to that of RuO_2 [18]. Since these transition metal compounds cost much less than RuO_2, they can be potential electrode materials for high energy density electrochemical capacitors.

It is clear that the energy density of RuO_2 and the transition metal compounds can be much higher if the surface area can be increased. The sol-gel process is a unique method in making materials of extremely high surface areas. It is, therefore, an ideal process for preparing electrode material for high energy density electrochemical capacitors.

Electrode Materials Prepared by Sol-Gel Technique

Carbon aerogels. - A carbon aerogel material was developed at Lawrence Livermore National Laboratory (LLNL), and has been tested as an electrode material for electrochemical capacitors (Aerocapacitor) [19,20]. The carbon aerogel material is derived from organic aerogels which are produced from base catalyzed, aqueous polycondensation reactions of resorcinol (1,3 dihydorxy benzene) with formaldehyde, as shown in Fig. 5 [21]. Wet gels (aquagels) obtained from the reaction are solvent exchanged with acetone first, and then with liquid CO_2. The organic aerogels are then obtained by drying the wet gels at the supercritical conditions of CO_2. Organic aerogels are further pyrolyzed in inert atmosphere to form vitreous carbon aerogels.

The BET surface areas of the carbon aerogel material range from 500 to 850 m^2/g, with bulk densities of 0.3 - 1.0 g/cm^3 [20]. Two types of pores were observed to exist in the carbon aerogels. Mesopores (20 - 500 Å) were formed by the interconnected particle chains, while micropores (<20 Å) resided primarily within the individual particles. The double layer is formed mainly at the surface of the individual particles in the mesopore region. Capacitance measurement performed at unit cells fabricated by two identical carbon aerogel electrodes indicated that specific capacitance as high as 43 F/g (equivalent to single electrode capacitance of 172 F/g) has been achieved. Due to the unique interconnected structure of aerogels, they allow lower internal resistance and permit stored energy to be released more rapidly. Power density of 7.5 KW/Kg has been obtained [20].

Amorphous Ruthenium Oxide. - Recently, Jow and Zheng have studied the electrochemical properties of an amorphous ruthenium oxide ($RuO_2.xH_2O$) prepared by the sol-gel technique [22,23]. They found that while the charge can only be stored at the surface of crystalline RuO_2, the charge storage in $RuO_2.xH_2O$ extends beyond that of the surface and into the bulk. A specific capacitance of 760 F/g was observed from the amorphous ruthenium oxide material, which corresponds to an energy density of 26 Wh/Kg. These values are about two time higher than the reported values for RuO_2.

Transition Metal Compounds. - We have studied several transition metal compounds for their potential applications as electrode materials for electrochemical capacitors. A few hafnium compounds have shown double layer capacitance in the range of 100 ~ 200 $\mu F/cm^2$, which are comparable to that of RuO_2 [17]. A modified sol-gel method has been used to fabricate the hafnium compounds. The BET surface area of the synthesized Hf compounds was measured with a Micromeritics FlowSorb II 2300 surface area analyzer. Surface areas as high as 180 m^2/g have been obtained. Unit cell capacitors were constructed using coatings of hafnium compounds on titanium substrate(Fig. 6). A cyclic voltammogram of the unit cell is shown in Fig. 7. The calculated specific capacitance for the hafnium compound was 197 F/g.

Efforts are also being carried out to modify the pore surface of activated carbon powder with the hafnium compound. The as-received activated carbon (Aldrich Chemical) has a surface area of 980 m^2/g, with a measured specific capacitance of 100 F/g. Preliminary results on the modified carbon powder indicated that the surface area had reduced slightly to around 900 m^2/g, while the specific capacitance had improved more than 50 % to 162 F/g. A cyclic voltammogram of the modified activated carbon is shown in Fig. 8. Unit cells using the modified carbon powder and 30 w/o H_2SO_4 electrolyte have been constructed. A prototype bipolar 3-cell stack electrochemical capacitor has also been fabricated to further characterize the performance of the modified activated carbon, as shown in Fig. 9. Fig. 10 shows the charge-discharge curve of the capacitor at a fixed current of 17.5 mA/cm^2 after 8,000 cycles. With an electrode area of 2.85 cm^2, the capacitance of the capacitor is calculated as 1 F, and the energy density is 4.6 Wh/Kg of active material.

CONCLUDING REMARK

For aerospace applications, energy storage devices need to be light, small, reliable, long life, and with high energy and power densities. Advanced materials play an important role in developing new energy storage systems to meet these requirements. Sol-gel process is a versatile and powerful technique for fabrication of a wide variety of ceramic materials with tailored microstructure and properties. It offers opportunities for new energy storage materials to be synthesized and studied for secondary batteries, fuel cells, and electrochemical capacitors. In this paper, porous high surface area materials and organic/inorganic micro-composites derived from sol-gel process have been demonstrated as potential electrode materials for high energy density and high power density energy storage devices for future spcae power applications.

ACKNOWLEDGMENTS

Work on transition metal compounds for electrochemical capacitors is supported by NASA and US Department of Energy.

REFERENCES

1. C.J.Brinker and G.W.Scherer, Sol-Gel Science, Academic Press, Inc. San Diego, 1990.
2. C.J. Brinker and G.W. Scherer, J. Non-Cryst. Solids, 70 (1985) 301.
3. C.J. Brinker and G.W. Scherer in Ultrastructure Processing of Ceramics, Glass, and Composites, eds. L.L. Hench and D.R. Ulrich, Wiley, N.Y., 1984, p.43.
4. B.E. Yoldas, Am. Ceram. Soc. Bull., 54 (1975) 286.
5. J. Desilvestro and O. Haas, J. Electrochem. Soc., 137 (1990) 5C.
6. K. West, B. Zachau-Christiansen, M.J.L. Ostergard, and T. Jacobsen, J. Power Sources, 20 (1987) 165.
7. J. Livage, Chem. Mater., 3 (1991) 578.
8. R. Baddour, J.P. Pereira-Ramos, R. Messina, and J. Perichon, J. Electroanal. Chem., 314 (1991) 81.
9. M.G. Minnett and J.R.Owen, J. Power Sources, 28 (1989) 397.
10. K. West, B. Zachau-Christiansen, T. Jacobsen, and S. Skaarup, Electrochim. Acta, 38 (1993) 1215.
11. K. Sudoh and H. Hirashima, J. Non-Cryst. Solids, 147&148 (1992) 386.
12. F. Chaput, B. Dunn, P. Fuqua, and K. Salloux, J. Non-Cryst. Solids, in print.
13. S.P. Wolsky and R.S. Wissoker, The International Technology and Market Study for Electrochemical Capacitors, Florida Educational Seminars, Inc., Boca Raton, FL., Feb. 1994.
14. B.E. Conway, in New Sealed Rechargeable Batteries and Supercapacitors, eds. B.M. Barnett et al., The Electrochem. Soc., N.J., 1993, Vol. 93-23, p. 15.
15. J.C. Currie, D.L. Boos, V.F. Gaylor and P.D. Bennett, in The Chemistry and Physics of Composite Media, eds. M. Tomkiewicz and P.N. Sen, The Electrochem. Soc., N.J., Vol. 85-8, p.169.
16. T. Murphy and W. Kummar, Proc. 4th Intl. Seminar of Double Layer Capacitors and Similar Energy Storage Devices, ed. S.P. Wolsky and N. Marincic, Deerfield Beach, FL, Dec. 1994.
17. I.D. Raistrick and R.J. Sherman, Electrode Materials and Processes for Energy Conversion and Storage, ed. S. Srinivasan et al., The Electrochem. Soc., N.J., 1987, Vol. 87-12, pp. 582.
18. Chemat Tech. Inc., unpublished results.
19. R.W. Pekala and F.M. Kong, Polymer Prpts., 30 (1989) 221.
20. S.T. Mayer, R.W. Pekala, and J.L. Kaschmitter, J. Electrochem. Soc., 140 (1993) 446.
21. J.D. LeMay, R.W. Hopper, L.W. Hrubesh, and R.W. Pekala, MRS Bulletin, 15(12) (1990) 19.
22. T.R. Jow and J.P. Zheng, Proc. 4th Intl. Seminar on Double Layer Capacitors and Similar Energy Storage Devices, ed. S.P. Wolsky and N. Marincic, Deerfield Beach, FL, Dec. 1994.
23. J.P. Zheng and T.R. Jow, J. Electrochem. Soc., 142 (1995) L6.

TABLE 1

Surface area and porosity of different silicate xerogels and aerogels. (from ref. [1])

Silica Sample	Surface Area (m^2/g)	Pore Diameter (Å)	Bulk Density (g/cm^3)	Pore Volume (%)
Two-step acid catalyzed xerogel	740	18	1.54	0.54
Two-step acid-base catalyzed xerogel	910	46	0.99	0.67
Particulate (one-step base-catalyzed xerogel)	515	125	0.60	0.70
Two-step acid-catalyzed aerogel	858	186	0.30	0.82

TABLE 2

Applications for electrochemical capacitors. (from ref. [13])

Capacitor Category	Typical Discharge Time	Typical Applications
Pulse Power	Milliseconds or Less	SDI
Bridge Power	< 5 Seconds	Automotive Subsystems Smart Weapons
Load Leveling	< 2 Minutes	Automotive Subsystems
Standby Power	Hours at Low Rate	Memory Protection

TABLE 3

Capacitance Values of Carbon Materials Obtained from Different Starting Materials. (from ref. [15])

Carbon Source	Surface Area (m^2/g)	Capacitance ($\mu F/cm^2$)
Coconut Shell (A)	1219	21
Coal (A)	1072	13
Petroleum	1143	13
Coal (B)	1282	10
Wood (B)	2121	4
Coconut Shell	929	15
Peat	958	15
Petroleum	1147	9
Wood (A)	1524	1
Synthetic	155	30

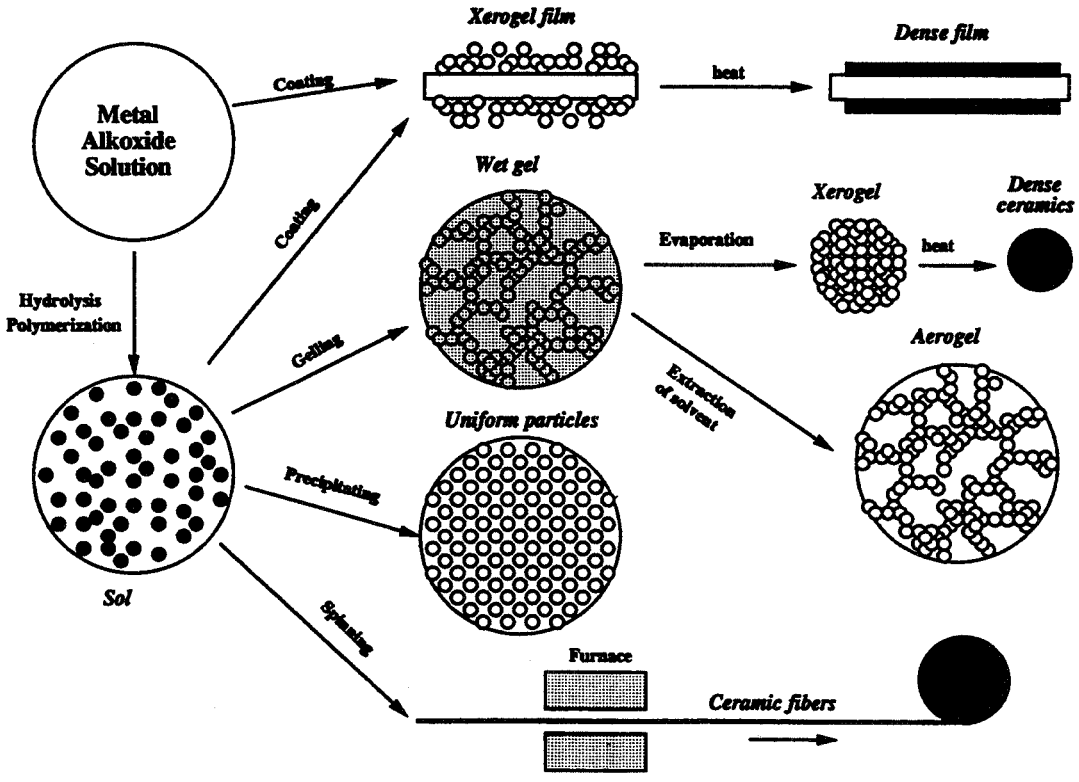

Fig. 1. - Sol-gel processes and their products.

The Sol-Gel Processing of Metal Sulfides, Nitrides and Carbonitrides

Sulfide	Metal Nitride and Carbonitride
$M(SR)_n$	$M(NR_2)_n$
Thiolysis:	**Aminolysis:**
$M(SR)_n + HSH \longrightarrow (SR)_{n-1}M(SH) + RSH$	$M(NR_2)_n + RNH_2 \longrightarrow (NR_2)_{n-1}M(NRH) + R_2NH$
Polymerization:	**Polymerization:**
$(SR)_{n-1}M(SH) + (RS)M'(SR)_{m-1} \longrightarrow (SR)_{n-1}M\text{-}S\text{-}M'(SR)_{m-1} + RSH$	$(NR_2)_{n-1}M(NRH) + (NR2)M'(NR_2)_{n-1} \longrightarrow (NR_2)_{n-1}M\text{-}N(R)\text{-}M'(NR_2)_{n-1} + R_2NH$
$\longrightarrow$ -M(S)(S)-S-M'-S-M(S)(S)-S-M'-S-	$\longrightarrow$ M(NR)(NR)-M'(NR)(NR)-M(NR)(NR)-M'(NR)(NR)
	$\xrightarrow{\Delta}$ M(C,N)
Example: ZnS, As_2S_3, SnS, CuS, In_2S_3	Example: TiN, Ti(C,N), ZrN, Zr(C,N)

Fig. 2. -Sol-gel processing of non-oxide ceramics.

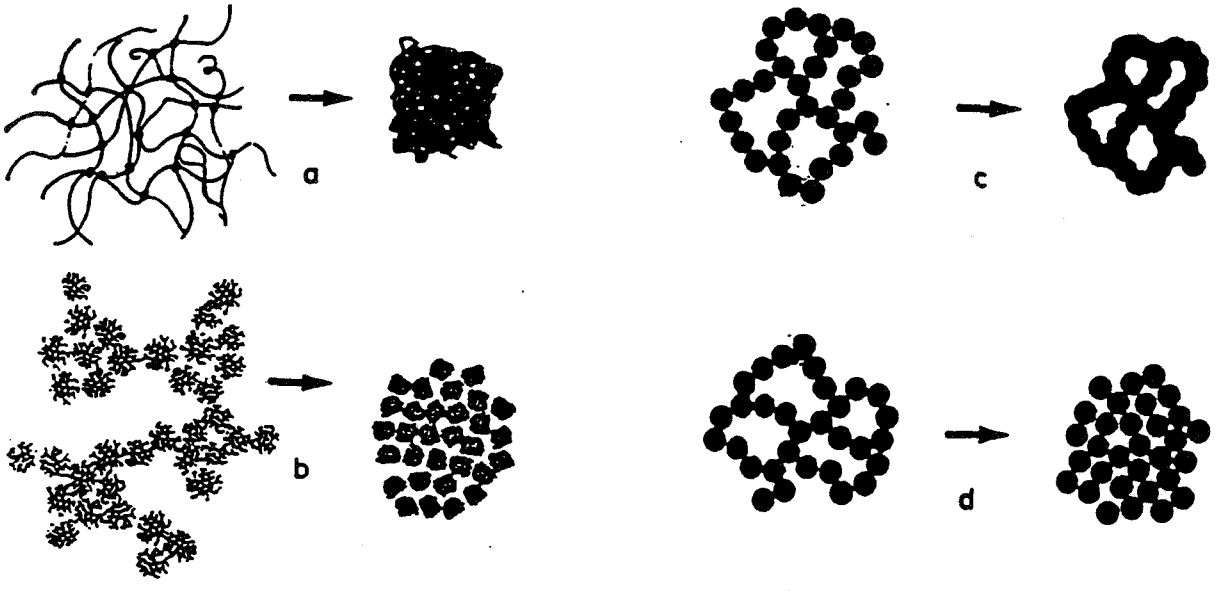

Fig. 3. -Schematic of gel structure derived under different conditions: a) acid-catalyzed gels, b) base-catalyzed gels, c) colloidal gel aged under conditions of high silica solubility, d) colloidal gel composed of weakly bonded particles (from ref. [2]).

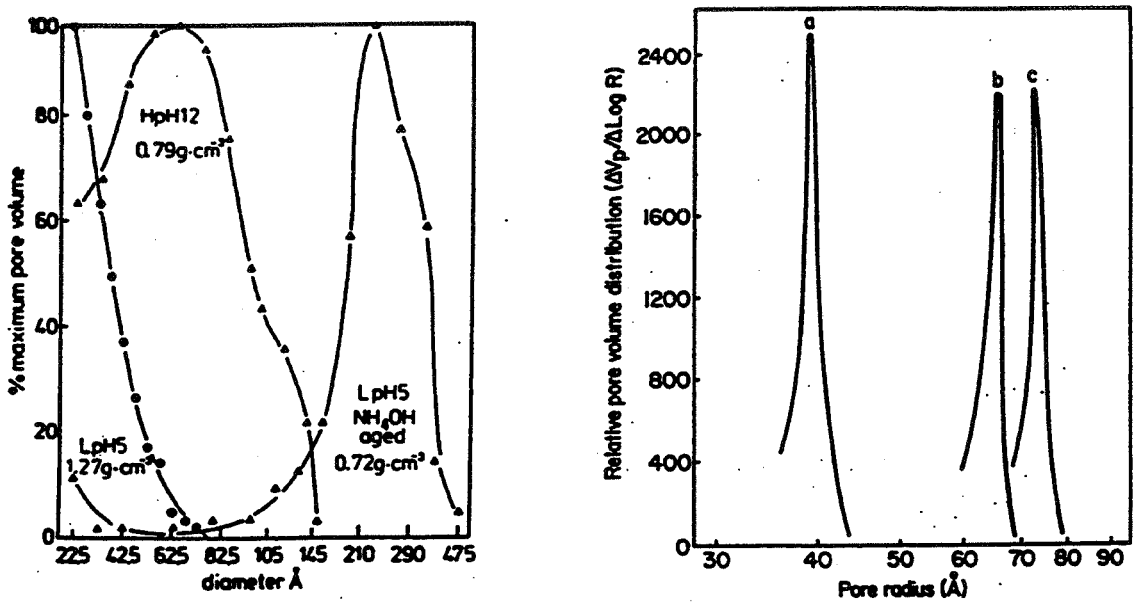

Fig. 4. -(a) The effects of aging on pore structure of xerogels, LpH5 made at pH 2.5 with 5 moles water/mole TEOS, HpH12 made at pH 9.2 with 12 moles water/mole TEOS, and LpH5 aged one week at 50°C in 3 M NH_4OH prior to drying. (from ref. [3]); (b) the effects of heat treatment on pore structure of sol-gel derived materials, 24 hours at a) 500oC, b) 900oC, c) 1000oC (from ref. [4]).

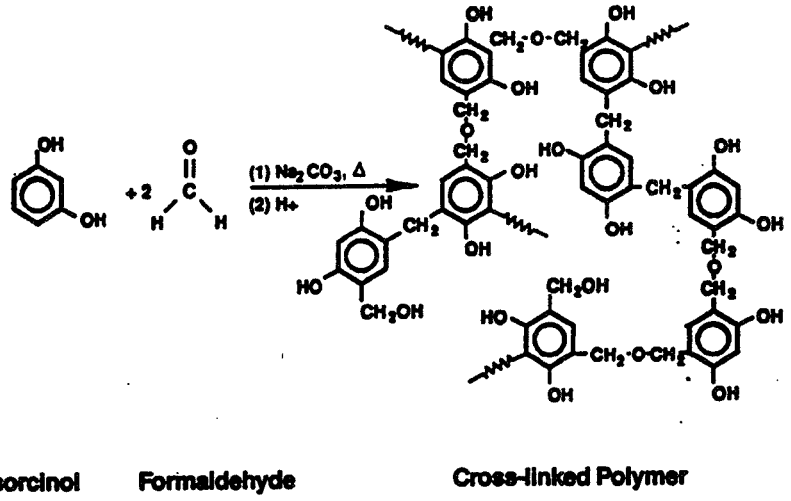

Fig. 5. - Schematic diagram of the sol-gel polymerization of resorcinol with formaldehyde. (from ref. [20])

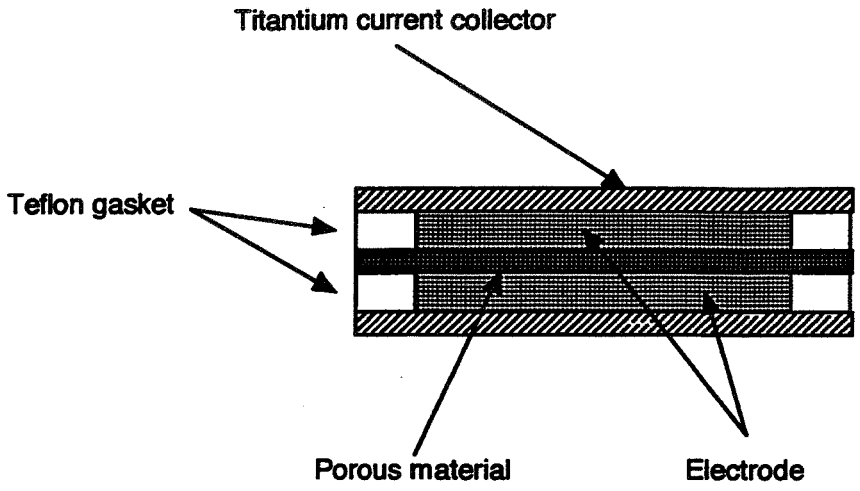

Fig. 6. - Schematic of an electrochemical capacitor unit cell with hafnium compound as the electrode material.

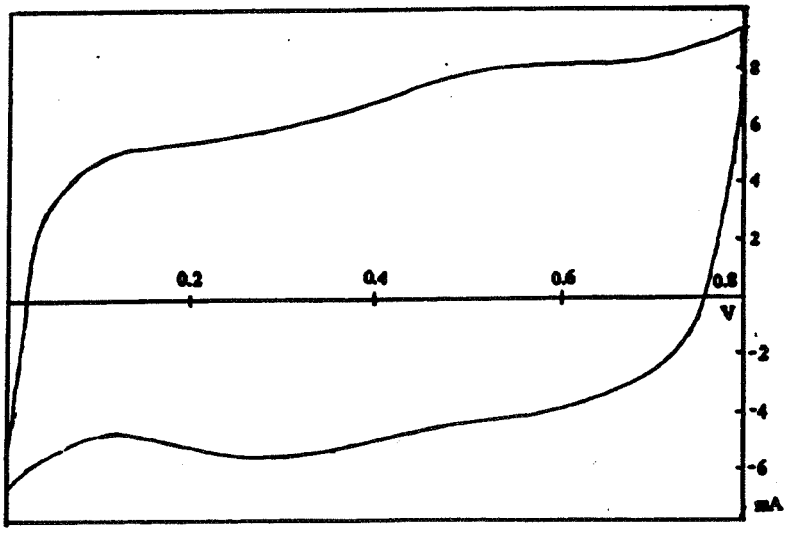

Fig. 7. - Cyclic voltammogram of the hafnium compounds based electrochemical capacitor unit cell, the electrolyte was 10% H_2SO_4 and the scan rate was 50 mV/s.

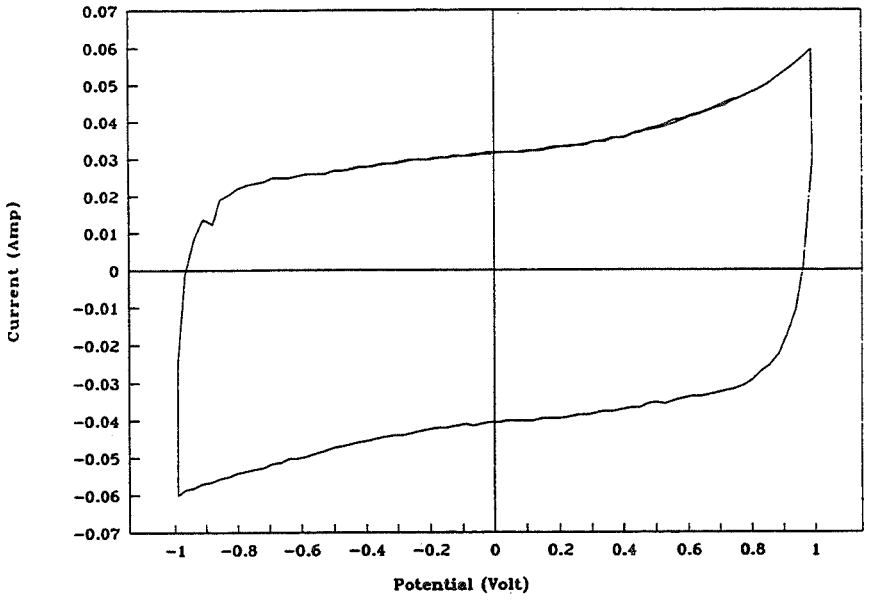

Fig. 8. - Cyclic voltammogram of a hafnium compound modified activated carbon sample, 10% H_2SO_4, 50 mV/s.

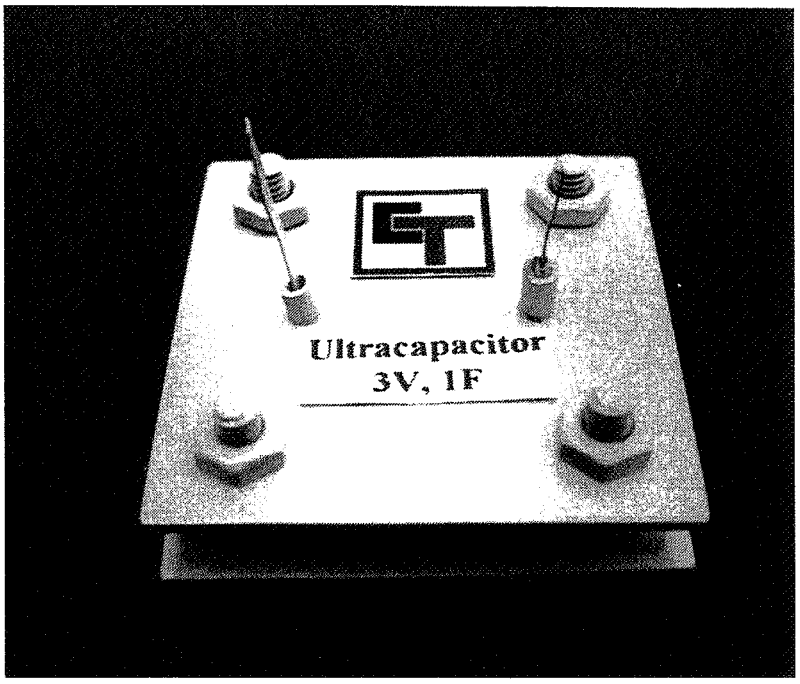

Fig. 9. - Prototype bipolar 3-cell stack electrochemical capacitor. The capacitor uses hafnium compound modified activated carbon as the active electrode materials with a electrode surface of 2.85 cm^2. The electrolyte is 30 w/o H_2SO_4.

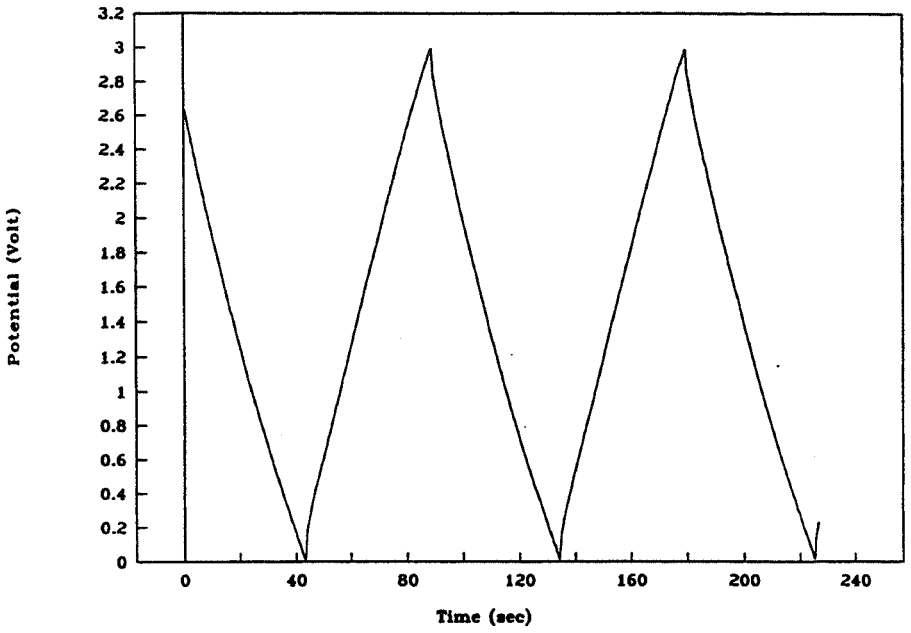

Fig. 10. - Constant current (17.5 mA/cm^2) charge/discharge curve of the prototype 3-cell stack electrochemical capacitor after 8,000 cycles.

Page intentionally left blank

54-33
068852

DEVELOPMENT OF ELECTROCHEMICAL SUPERCAPACITORS FOR EMA APPLICATIONS

John A. Kosek, Thomas Dunning,
and Anthony B. LaConti
Giner, Inc.
Waltham, Massachussetts

056919

10P.

ABSTRACT

A limitation of the typical electrochemical capacitor is the maximum available power and energy density, and an improvement in capacitance per unit weight and volume is needed. Giner, Inc. has developed a solid-ionomer electrochemical capacitor having a unit cell capacitance greater than 2 F/cm^2 and a repeating element thickness of 6 mils. This capacitor could provide high-current pulses for electromechanical actuation (EMA). Primary project objectives were to develop high-capacitance particulates, to increase capacitor gravimetric and volumetric energy densities above baseline, and to fabricate a 10-V capacitor with a repeating element thickness of 6 mils or less. Specific EMA applications were identified and capacitor weight and volume projections made.

INTRODUCTION

In a NASA SBIR Phase I program (Contract No. NAS8-40119), Giner, Inc. evaluated the feasibility of fabricating an all-solid-ionomer multicell electrochemical capacitor having a unit cell capacitance greater than 2 F/cm^2 and a repeating element thickness of 6 mils. This capacitor can possibly be used by NASA as a high-rate energy source for electromechanical actuator (EMA) activation for advanced space missions. The high unit cell capacitance and low repeating element thickness will allow for the fabrication of a low-volume, low-weight device, favorable characteristics for space applications. These same characteristics also make the capacitor attractive for terrestrial applications, such as load-leveling batteries or fuel cells in electric vehicle applications.

Although the projected energy densities for electrochemical capacitors are about two orders of magnitude lower than that of batteries, the high-power-density characteristics of these devices render them as potentially viable candidates for meeting pulse or peak electrical power requirements for some anticipated aerospace mission scenarios, especially those with discharge times on the millisecond to second time scale. On a volumetric or gravimetric basis, the advantages of utilizing electrochemical capacitors rather than batteries for meeting the peak power demands associated with a specific mission scenario will largely depend upon the total and pulse durations of the power peaks.

The all-solid Giner, Inc. electrochemical capacitor, fabricated from high-surface-area RuO_x bonded to a proton-exchange membrane, derives its high capacitance from a combination of double-layer processes and surface-redox type processes (pseudocapacitance). A number of papers have been published, describing the basic Giner, Inc. supercapacitor technology. First-generation capacitor stacks (25 cm^2 active area, 5 V and 35 V, respectively) have been fabricated and tested intermittently over the past 5 years, with absolutely no maintenance performed on these stacks. Life plots of the 5-cell and 35-cell stacks are shown in Figures 1 and 2, respectively. Performance of both stacks has remained highly invariant over their lifetimes. During this test period, the stacks have been loaned to potential customers for evaluation, and have undergone extensive testing for a variety of burst power applications; this testing was conducted at the customer's facilities and was not under the supervision of Giner, Inc. When returned to Giner, Inc., the stacks were parametrically tested to verify life and performance characteristics.

The first-generation capacitors used low-surface-area (60 m^2/g) RuO_x as an active material; this material had a capacitance on the order of 1 F/cm^2 for a 10 mg/cm^2 loading. More recent work, using an advanced preparation method, has resulted in a high-surface-area (160 to 200 m^2/g) RuO_x with a capacitance approaching 2 F/cm^2 for a 10 mg/cm^2 loading. In the recently completed NASA SBIR Phase I program, studies were conducted on the effect of RuO_x preparation conditions and membrane on capacitor performance. This

work is described below. Brief discussions are also included on a current program aimed at introducing low-cost components into the capacitor.

EXPERIMENTAL

Noble Metal Oxide

An advanced noble metal oxide preparation method was recently developed at Giner, Inc. which resulted in a substantial increase in noble metal oxide surface area and capacitance and decrease particle size, as compared to the standard method. The advanced method preparation conditions were systematically varied to determine the effect on both particulate surface area and unit cell capacitance; the effect of batch size was also investigated.

To evaluate the capacitance of the particulates prepared above, they were bonded to both sides of a Nafion 117 membrane to form a membrane-electrode assembly (MEA). Particulate loadings in all cases were 10 mg/cm^2. The capacitor active area was 6.45 cm^2. To evaluate the effect of membrane on total capacitor response, a large batch of RuO_x was prepared. Then, RuO_x from this batch was used in conjunction with 5 separate membranes (Nafion 105, 112 and 117; Dow XUS 13204.10; and W.R. Grace Daramic). Loadings of 10 mg/cm^2 RuO_x were used in all cases.

Capacitor Testing

A schematic of the single-cell hardware used in this program is shown in Figure 3. The MEA is compressed between two titanium end plates. These plates are lightly platinum plated where they contact the MEA in order to decrease contact resistance. A gasket is placed around the MEA to prevent the hydrated MEA from drying out. Contact is made to the external circuit via gold-alloy-plated tabs.

Electrical testing.-Discharge of the capacitor through a resistor is used to characterize devices for charge storage, energy storage, and degree of capacitative behavior. Figure 4 shows a typical curve of voltage across the external load versus time. The charge storage is obtained by integration of the voltage-time transient:

$$q = \int \frac{V}{R_L} dt \tag{1}$$

From the charge and initial voltage the integral capacity is calculated:

$$C = \frac{q}{V_o} \tag{2}$$

Capacitance is also calculated by non-linear least squares fitting to the discharge curves. The energy storage is also calculated by integration of the data:

$$E = \int \frac{V^2}{R_L} dt \tag{3}$$

RESULTS AND DISCUSSION

Particulate Studies

Twelve separate batches of RuO_x were prepared, systematically varying preparation conditions; results are summarized in Table 1. The highest surface areas and capacitance were measured for Sample A-1 (baseline conditions; 225 m^2/g, 2.23 F/cm^2) and Sample A-2 (185 m^2/g, 2.47 F/cm^2).

A plot of capacitance vs. surface area (Fig. 5) shows that there is a relatively linear relationship between surface area and capacitance. An additional data point is plotted on Fig. 5. Particulates for this point were obtained by a standard preparation. The standard preparation point falls on the same line as the points obtained from the advanced process, except with a much lower surface area and capacitance.

TEM analysis.-Samples from 2 separate batches of RuO_x particulates were examined by Transmission Electron Microscopy (TEM). Preparation conditions for the samples were the same as in Table 1, Preparations A-1 and A-2. Characterization data, including surface area and measured capacitance, is summarized in Table 2.

The differences in surface area and capacitance for the two materials listed in Table 2 is surprising. Sample 19 prepared using Conditions A-1 had the lowest surface area of the two and of any of the materials summarized previously in Table 1; this sample had two distinct sizes of particulates. One group of particulates had a particle size range from 10 to 45 Å, while the second ranged from 60 to 300 Å in diameter. This material was used in the 10-cell capacitor stack described below.

The primary difference among the samples was the batch size, with Sample 02 using 11 g of starting material, while Sample 19 used 110 g, a tenfold increase in batch size. At the present time we suspect the lower surface area of Sample 19 was due to starting material at the bottom of the reaction vessel, not being able to react completely. This will be investigated further in a Phase II follow on program.

Processes to Increase Capacitor Gravimetric and Volumetric Energy Density

Effect of membrane.-The electrolyte in an all-solid ionomer capacitor is a thin, solid proton-exchange membrane. These materials have a perfluorocarbon backbone with pendent sulfonic acid groups which provide ionic conductivity. In order to function properly, the membranes are boiled in distilled water to set the membrane internal water content. Typically, the higher the membrane water content, the lower the membrane resistance. A high membrane resistance will limit the rate at which charge can be extracted from the capacitor.

All test results summarized in Fig. 5 were obtained using Nafion 117 as the capacitor electrolyte. Previous work at Giner, Inc. has used the Dow XUS 13204.10 membrane as the capacitor electrolyte. With the Dow membrane, capacitances as high as 2.8 F/cm^2 have been recorded primarily due to the higher ionic conductivity (lower resistance) of the Dow membrane. However, due to a change in corporate philosophy, the Dow membrane is extremely difficult to obtain. Therefore, the bulk of our testing in this program to screen the various batches of particulates for performance was performed with Nafion 117. Subsequently, a total of five different membranes were evaluated with two goals in mind: (1) to obtain the highest capacitance and lowest ionic resistance possible and (2) to use the thinnest membrane possible in order to decrease the repeating element thickness in a capacitor stack.

Table 3 summarizes the results of the membrane study. For this testing, a new batch of RuO_x had been prepared, but its surface area was only 90 m^2/g. This RuO_x was then coated with ionomer. Since the particulate batch, particulate loading and ionomer loading were all being kept constant, it was felt that the results of the test would provide a relative indication of the effect of the membrane even though the particulate surface area was lower than desired. The highest capacitance was measured with Nafion 105; this is a new membrane developed by DuPont, which has properties similar to that of the Dow membrane. Performance of a capacitor using a Dow membrane was almost equivalent to that of the Nafion 105 capacitor. These two membranes have a thickness of 5 mils. Daramic, made by W.R. Grace, is a 2-mil thick polyethylene-based material, containing silica and a binder. It was originally developed as a battery separator. Its cost is expected to be significantly below that of the Nafion membranes. Unexpectedly, the lowest performance was observed for the capacitor with Nafion 112, a 2-mil (dry) thick membrane. It is suspected that the Nafion 112 cell may have had some microshorts due to the relatively thin film. Further optimization of the bonding conditions to this film will be conducted in Phase II. Previous proton exchange membrane fuel cell testing at Giner, Inc., which utilizes MEA technology similar to that in the capacitor MEA, has shown comparable performance between fuel cells using Dow XUS 13204.10 membrane and Nafion 112 membrane (LaConti et al., 1992). Based on results of the membrane testing, Nafion 105 was selected to be used in the capacitor stack. Additional

work with Nafion 112 and Daramic is being conducted in a follow-on Phase II program.

Multicell Capacitor Stack Fabrication

A multicell capacitor stack was designed, fabricated and operated as part of this program. The active area was 222 cm^2, almost a 10-fold increase in area from capacitors previously fabricated at Giner, Inc. and over a 30-fold increase in active area from the capacitors used in the particulate screening studies in this Phase I program. The stack used the high performance Nafion 105 as the electrolyte in the MEAs. To reduce the stack weight and increase the gravimetric energy density, the stack used Lexan end plates with a 3-mil-thick current collector; sheets of 1-mil foil (platinized) were used as bipolar elements in the stack. Some of the stack particulars are summarized in Table 4. The end plate dimensions were 20.3 cm x 20.3 cm x 1.3 cm.

The stack was charged to 10 volts (1 V per cell) and then discharged across a 10 Ω resistor. The capacitance was measured after each MEA was installed; no change in average capacitance was noted going from 1 to 10 MEAs. The initial unit cell capacitance was an average of 0.45 F/cm^2. A study was conducted to investigate the effect of contact pressure on capacitor performance. Due to the large scale-up in capacitor active area, it was thought the lower than expected output could be due to poor contact of the bipolar current collector plates to the membrane and electrode assembly, resulting in high resistive losses within the cell. Table 5 summarizes results of this study. As contact pressure increased, unit cell capacitance increased. Recent studies indicate a design contact pressure of 200 to 250 psig should be applied to the capacitor element active cell area. Additional testing will be conducted in a Phase II follow-on program to further investigate the effects of contact pressure on capacitor performance.

The repeating element thickness in the stack was calculated to be 8 mils; this is close to one of the goals originally set for the program. The unit cell capacitance, however, was not as high as previously demonstrated at Giner, Inc. This is due primarily to the increase in particulate batch size for preparation of the particulate needed for the capacitor stack. Testing in this program with small batches of starting material (11 g) resulted in a high surface area (185 m^2/g) and a capacitance of 2.5 F/cm^2. Scale-up of the batch size to 110 g resulted in a decreased surface area (80 m^2/g) and a decrease in capacitance. We suspect that in a preparation involving 110 g of starting material, not all the material reacted properly, resulting in a lower than expected particulate surface area. The effect of scaled-up batch size on particulate surface area and capacitance is being investigated in a Phase II follow-on program.

EMA Applications

A brief study was made to investigate the feasibility of using the Giner, Inc. capacitor as part of an electromechanical actuator electrical power system. Electrical power requirements are:

- Quad-redundant (4 independent power channels)
- 5.5 kWh per channel
- 3.5 kW average power
- 120 kW peak power (400 ms total; 40-80 ms pulses)
- 270 VDC

To meet these power requirements using the capacitor technology described above, a 278-cell stack would be required with an active area of 0.66 ft^2 (610 cm^2). Assuming an 8-mil repeating element thickness, the 278-cell stack, exclusive of end plates, would have a total height of 2.22 inches (current technology). With the projected 6-mil (or less) repeating element thickness, the stack height (exclusive of end plates) would be only 1.67 inches. Adding end plates yields a volume of approximately 0.34 ft^3 (current technology; 8-mil repeating element thickness) or, for the advanced technology (6-mil repeating element), a volume of approximately 0.29 ft^3. The volumetric energy density for a 270 Vdc (120-kW - 400-millisecond) PEM electrochemical capacitor based on a 0.34-ft^2 volume is approximately 1.4 Wh/L or 5.0 J/cm^3. Through the advanced development of the 6-mil repeating element thickness, it should be possible to increase the volumetric energy density to 1.6 Wh/L (5.8 J/cm^3).

Low-Cost Capacitor

Work is being conducted under NSF funding to develop lower-cost materials for use in electrochemical supercapacitors to be potentially used in commercial back-up power and load-levelling applications. A promising material identified for the capacitor positive electrode is MO_2, where M is a low-cost non-noble metal particulate; RuO_x will be used as the negative electrode. Capacitors fabricated with these materials, and using Daramic as the electrolyte, have exhibited a capacitance similar to the baseline cells with RuO_x on both sides integrally bonded to a perfluorocarbon membrane. Several other very-low-cost ionomer membranes have been identified and will be evaluated with the low-cost ionomer-coated, non-noble metal positive electrode. The approach to lowering the cost of the negative electrode is through minimizing the quantity of RuO_x and evaluating select high-surface-area non-noble metal oxides, carbides and nitrides.

CONCLUSIONS

The feasibility of fabricating and operating a 10-cell, all-solid ionomer capacitor stack, with each cell having an active area of 222 cm^2, was demonstrated. A unit cell capacitance of 0.94 F/cm^2 was obtained and a unit cell thickness of 8 mils was demonstrated. Two additional membranes, each having a thickness of 2 mils, were identified as candidates for future research to decrease the stack repeating-element thickness. Some reproducibility concerns were identified when the particulate batch size was increased 10-fold. Research is needed to investigate methods to prepare reproducible batches of high-surface-area particulates. A low-cost particulate was identified for use in the capacitor positive electrode and also several very-low-cost ionomer membranes. Further work is required to reduce the cost of the negative electrode for commercial load-levelling applications.

ACKNOWLEDGEMENT

The work was performed under NASA Contract NAS8-40119 and NSF Grant III-920096.

REFERENCES

LaConti, A.B., S. Sarangapani, J.A. Kosek, and J. Forchione, "Proton Exchange Membrance Electrochemical Capacitors and Fuel Cells for Pulse Power Applications," Paper presented at the 35th International Power Sources Symposium, Cherry Hill, NJ, June 22-25, 1992.

TABLE 1
Characterization data of RuO_x particulates

Preparation No.	Surface Area (m^2/g)	Capacitance (F/cm^2)*
A-1	225	2.23
-2	185	2.47
-3	89.6	1.19
B-1	137	1.41
-2	159	1.50
-3	138	1.42
C-1	164	1.15
-2	140	1.29
-3	138	0.61
D-1	129	1.19
-2	132	1.22
-3	129	1.15

* 10 mg/cm^2 particulate loading; Nafion 117

TABLE 2
Select RuO_x characterization data

Sample Number	Prep. Conditions	Surface Area (m^2/g)	Capacitance (F/cm^2)	Particle Size Range (Å)
02	A-2	185	2.47	15-30
19	A-1	80	0.94	60-300

TABLE 3
Effect of membrane

Membrane	Thickness (Dry) (mil)	Capacitance* (F/cm^2)
Dow	5	1.43
Daramic	2	1.04
Nafion 105	5	1.51
Nafion 117	7	0.88
Nafion 112	2	0.64

* 10 mg/cm^2 particulate loading

TABLE 4
10-Cell capacitor stack particulars

Weight (excluding end plates)	240 g
Height (including end plates)	3.66 cm
Height (excluding end plates)	2.0 mm
Repeating element thickness	0.20 mm
Active area per cell	222 cm^2

TABLE 5
Effect of contact pressure on unit cell capacitance

Contact Pressure (psi)	Unit Cell Capacitance (F/cm^2)
20	0.53
40	0.70
60	0.82
80	0.89
120	0.94

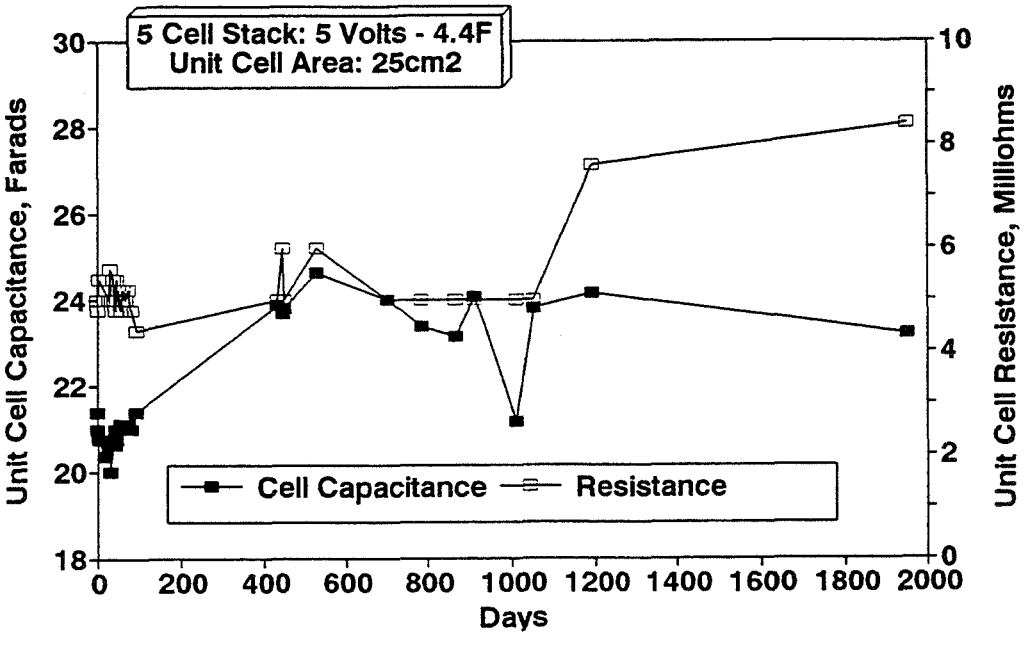

Fig. 1.—5-Cell stack capacitance and resistance life data

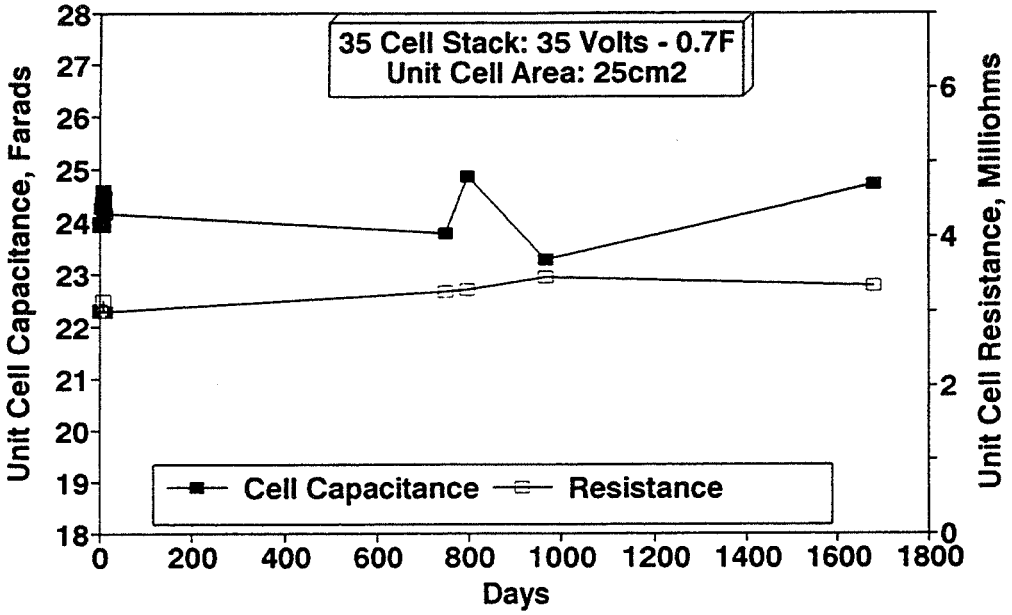

Fig. 2.—35-Cell stack capacitance and resistance life data

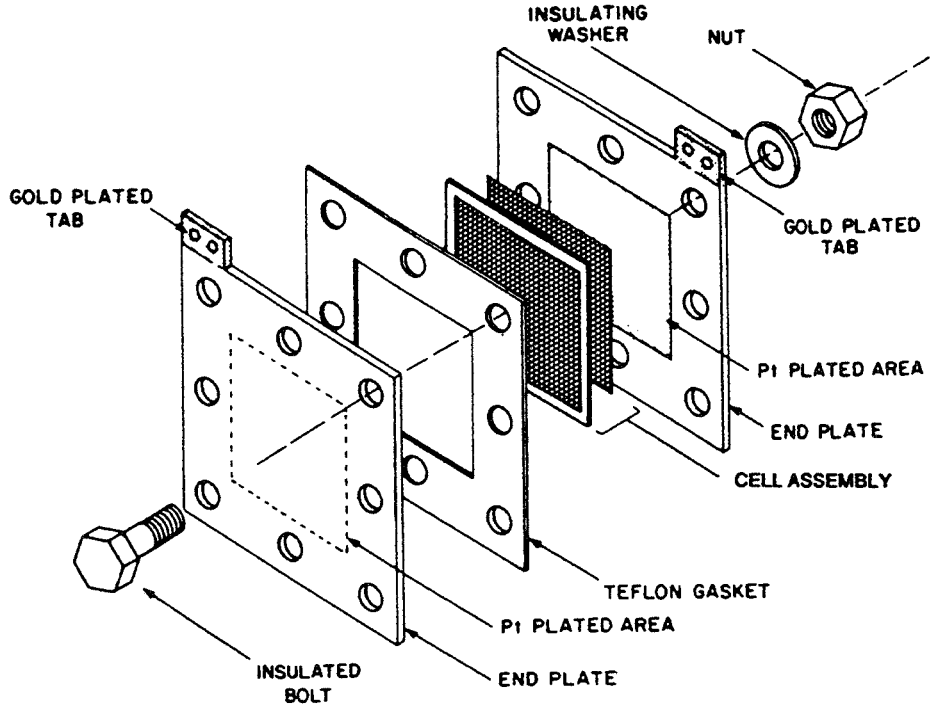

Fig 3.—Capacitor single cell test hardware

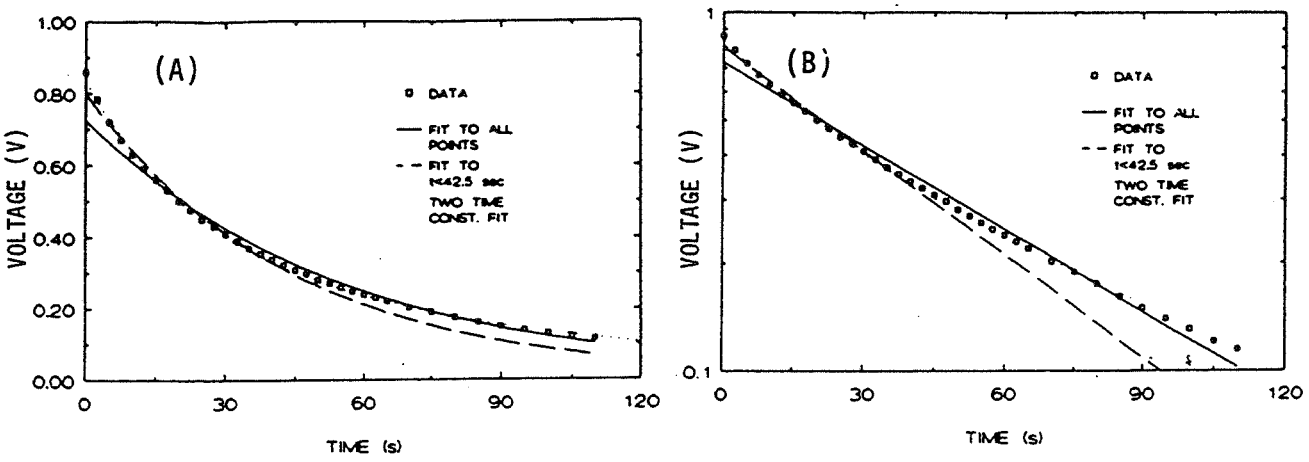

Fig. 4.—Discharge of a single cell across a 100-ohm load
a) voltage vs. time, b) log V vs. time

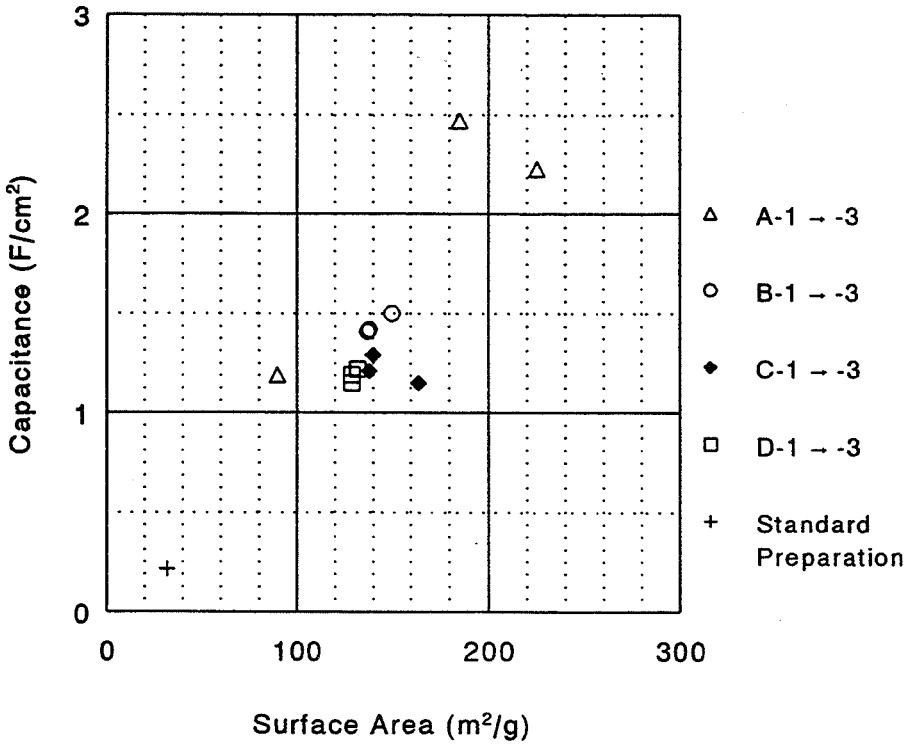

Fig. 5.—Effect of surface area on capacitance

Page intentionally left blank

S/S 33
008 853
Close

HIGH ENERGY DENSITY ELECTROLYTIC CAPACITOR

David A. Evans
Evans Company
East Providence, Rhode Island

ABSTRACT

Recently the Evans Company developed a new type of electrolytic capacitor. This capacitor, the Evans Hybrid, combines an electrolytic capacitor anode with an electrochemical capacitor cathode. The resulting capacitor has four times higher energy density than standard electrolytic capacitors, with comparable electrical performance. The prototype, a 480μF, 200 V device, had an energy density exceeding 4 J/cc. Now, a 680μF, 50 V, MIL-style all tantalum device has been constructed and is undergoing qualification testing. Pending a favorable outcome, work will begin on other ratings.

Potenial for commercially significant development exists in applying this technology to aluminum-based electrolytic capacitors. It is possible to at least double the energy density of aluminum electrolytics, while using existing manufacturing methods, and without adding material expense.

Data presented include electrical characteristics and performance measurements of the 200 V and 50 V Hybrid capacitors and results from ongoing qualification testing of the MIL-style tantalum capacitors.

BACKGROUND

One year ago, a new capacitor technology combining elements of electrochemical and electrolytic capacitors was introduced. The Evans hybrid capacitor (U S Patent 5,369,547) used a sintered tantalum slug anode, aqueous electrolyte, and a RuO_2 ceramic cathode. A four-fold increase in energy density over existing electrolytic capacitors was reported for a 200 volt, 480 μF prismatic single cell capacitor. [1]

Electrochemical capacitors (ECs) using activated carbon electrodes have been available for a number of years. The most important application for these devices has been for power backup for computer memory circuits. Their high capacitance rating (on the order of one farad), small size, high cycle life, and maintenance free operation have made them a good alternative to batteries. Another type of EC uses electrodes made of ruthenium oxide. Usually, a high surface area film of this material is formed on a thin titanium substrate. Two identical electrodes are separated a short distance with electrolyte filling the space between them. Charge is stored by double layer capacitance and by charge injection into the electrode material. Known as a pseudocapacitor, a ruthenium oxide electrode 0.001" thick can have a capacitance on the order of several farads per in^2.

The main disadvantage ECs suffer compared to electrolytic capacitors is that the cell voltage is limited to the breakdown potential of the electrolyte. For aqueous electrolytes, this is about 1 V. To build a capacitor with a higher working voltage, cells must be connected in series. The dynamic performance of these devices deviates greatly from ideal capacitor behavior, and limits their use in ac applications. Figure 1 is a typical plot of reactance vs. resistance for a carbon EC in the frequency range of 0.03Hz to 10Hz. Although electrolytic capacitors also exhibit non-ideal ac response, this is not usually evident except at higher frequencies.

To understand how the Evans hybrid capacitor works, one must first examine the construction and function of electrolytic and electrochemical capacitors. They may be simply modeled by two capacitors, one representing the anode, the other the cathode, and a resistor in series, representing the electrolyte.

In the Evans hybrid capacitor, an electrochemical capacitor electrode is substituted for the cathode in an electrolytic capacitor. This increases the capacitance of the cathode by many orders of magnitude. The anode is unchanged, so

high working voltage is maintained. Energy density is increased by this approach because: $1/C_t = 1/C_a + 1/C_c$, where C_t is the total capacitance, C_a is the anode capacitance and C_c is the cathode capacitance. For the electrolytic capacitor, $C_c \sim C_a$, therefore $C_t \sim \frac{1}{2} C_a$.

For the hybrid capacitor $C_c >> C_a$, so $C_t \sim C_a$. This represents an approximate doubling of the total capacitance without changing the anode. Energy density is increased further because the EC cathode occupies only a small fraction of the volume of a regular electrolytic capacitor cathode.

The first hybrid capacitor had disk-shaped tantalum pellet anodes, ruthenium oxide on titanium foil cathodes, and phosphoric acid electrolyte. The units had a rating of 500 μF. Data show that capacitance for these units was strongly dependent on frequency. The prototype is pictured in Figure 2. Figure 3 is a Nyquist plot showing prototype reactance vs. resistance over the frequency range of 100Hz to 79.4kHz.

DISCUSSION

The performance of this prototype suggested the direction for our next efforts in the development of the Evans hybrid technology. To be efficiently applied in ac circuits, the frequency response of the capacitor needed improvement.

A capacitor with porous electrodes can be thought of as a network of connected resistor-capacitor elements. Each element has an associated time constant. At a given rate of charge or discharge, only elements with a sufficiently small time constant can contribute to the overall performance. For a RC element, the time constant is $\mathbf{T = R \cdot C}$, where R and C are resistance and capacitance. Minimizing R allows C to be maximized for a given T. For a porous metal electrode, most of the resistance is due to the electrolyte, and is proportional to the electrolyte resistivity and to the square of the electrolyte path length. Both factors were investigated to improve device frequency response.

The electrolyte resistivity can be changed by changing electrolyte temperature, concentration, or species. The most highly conductive aqueous electrolyte is sulfuric acid. Changing to sulfuric acid electrolyte presented some materials problems. Although ruthenium oxide coatings are stable in sulfuric acid, the titanium substrates are readily attacked. Electrodes on tantalum and titanium substrates were tested by soaking them in 38% sulfuric acid at a temperature of 85 °C. In less than one week, the titanium substrates were completely dissolved. However, the tantalum substrates were not affected after many months of testing.

Tantalum, however, has a tough surface oxide which degrades the electrical contact with the ruthenium oxide coating. An inexpensive method has been discovered for preparing the tantalum surface, increasing its conductivity and enhancing the bond to the ruthenium oxide. Processing methods now implemented yield electrodes with a tightly bonded, highly conductive interface promoting stable performance. [2]

MIL-type Hybrid Capacitors

Military style hermetic tantalum capacitors (like CLR-81) incorporating the hybrid technology were assembled by North American Capacitor Co. Figure 4 shows the construction in a schematic view. These parts had a nominal rating of 680 μF at 50 V. The rating for the standard part in the same case size (T4) was 680 μF at 25 V. Thus the hybrid had the same capacitance at twice the voltage rating, and thereby increased the stored energy by a factor of four.

In addition to regular electrical measurements, frequency response analysis was done using a Solartron 1250. The frequency response of the hybrid is compared to that of a 680 μF, 25 V CLR810216, as shown in the Nyquist plots in Figure 5. The frequency response of the hybrid is significantly improved over previous hybrid prototypes and is very comparable to the standard device. This improvement was due mainly to the use of high conductivity sulfuric acid electrolyte.

The units are currently undergoing qualification testing according to MIL-C-39006. Testing is aimed at determining whether the capacitor can be specified as a substitute for standard all tantalum capacitors in high-reliability applications. While some tests were completed successfully, others revealed the need for improved control of critical

process parameters. Figure 6 shows capacitance and ESR as a function of time for 85°C life test units. [3]

Aluminum Hybrid Capacitor?

Tantalum wet-slug capacitors are ideal candidates for incorporation of the hybrid technology because of their construction. The anode electrode is in pellet form, and this allows the efficient use of a small geometric area hybrid cathode. For ESR to be minimized, the physical separation between the anode and cathode must also be minimized.

Aluminum electrolytic capacitors enjoy wide popularity due to their high voltage and capacitance ratings, high energy density compared to competing technologies, low mass, and low cost. Aluminum electrolytics are made by winding two ribbons of aluminum foil, serving as anode and cathode, on a central core. The foils are prevented from making electrical contact by thin separators, typically paper, which are interleaved with the foils during winding. The separator allows ionic conduction and serves as an electrolyte reservoir. The foils are etched to increase surface area, then the dielectric Al_2O_3 coating is electrochemically formed on the surface.

Significant potential exists to improve the energy density of aluminum electrolytics by incorporation of the hybrid technology. This would be done by substituting a foil coated with ruthenium oxide for the aluminum foil cathode. Unlike the case for tantalum capacitors, there would be no volume savings by doing this. However, as with the tantalum capacitors, the 100X increase in cathode capacitance would provide an approximate doubling of energy density. Attractive as this doubling would be, considerable materials-related development effort must be performed to realize the potential of the hybrid aluminum capacitor.

CONCLUSION

The Evans hybrid capacitor provides a four-fold increase in energy density over standard MIL-type hermetic tantalum capacitors. The hybrid capacitor and standard capacitor have very similar impedance behavior. This allows the application of hybrid capacitors wherever tantalum wet-slug capacitors are now used. Ongoing work on different hybrid systems, such as the hybrid aluminum, will expand the number of applications benefitted by this technology.

REFERENCES

1. D. A. Evans, "High Energy Density Electrolytic-Electrochemical Hybrid Capacitor" Proc. 14th CARTS, Jupiter, Florida, 3/94.

2. D. A. Evans, "Developments in Hybrid Capacitor Technology", The Fourth Int. Seminar on Double Layer Capacitors and Similar Energy Storage Devices, Deerfield Beach, Florida, 12/94.

3. D. A. Evans, "Performance of MIL-type Hybrid Tantalum Capacitors", Proc. 15th CARTS, San Diego, CA, 3/95.

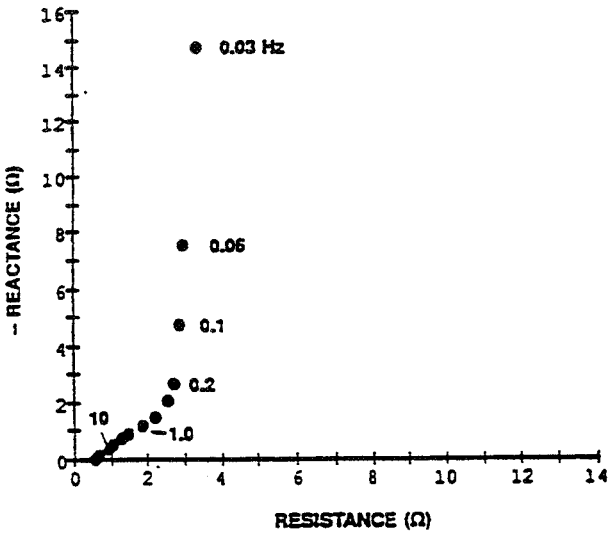

Figure 1. Nyquist plot of a 0.47 F, 11 V Capattery carbon EC.

Figure 2. Hybrid prismatic capacitor construction.

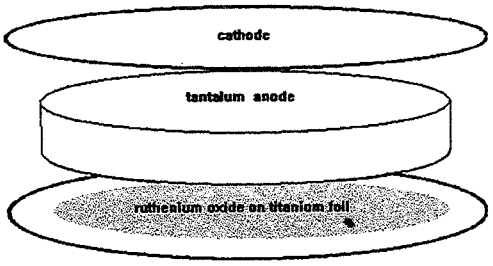

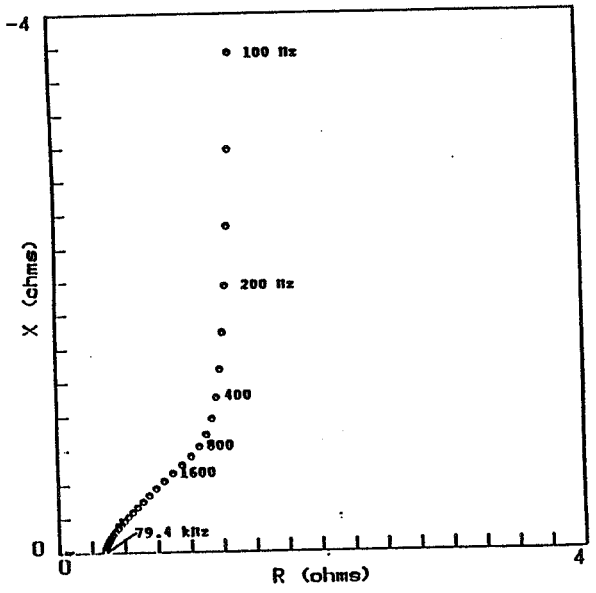

Figure 3. Nyquist plot of the prismatic hybrid capacitor prototype.

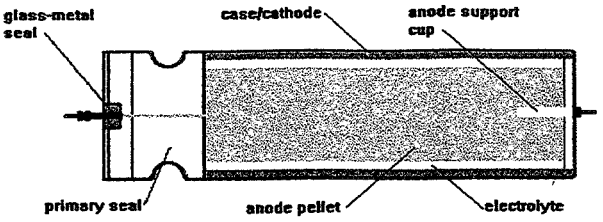

Figure 4. Cross-section view of the MIL-type tantalum hybrid capacitor.

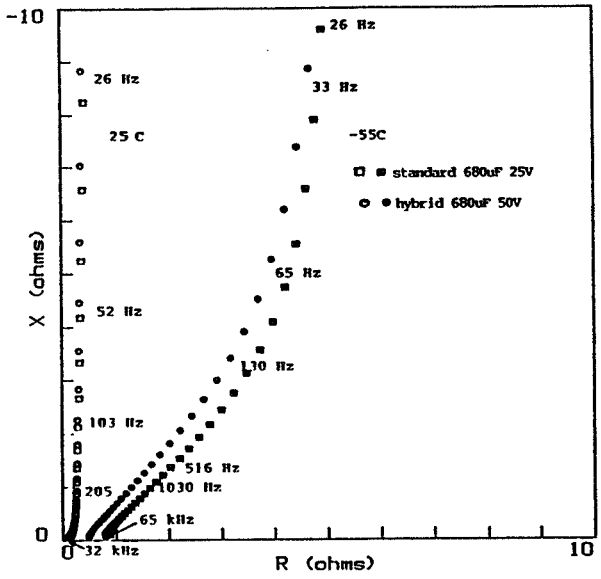

Figure 5. Nyquist plots of standard CLR81 680µF, 25V and hybrid 680µF, 50V capacitors.

Figure 6. Capacitance and ESR for hybrid capacitor life test.

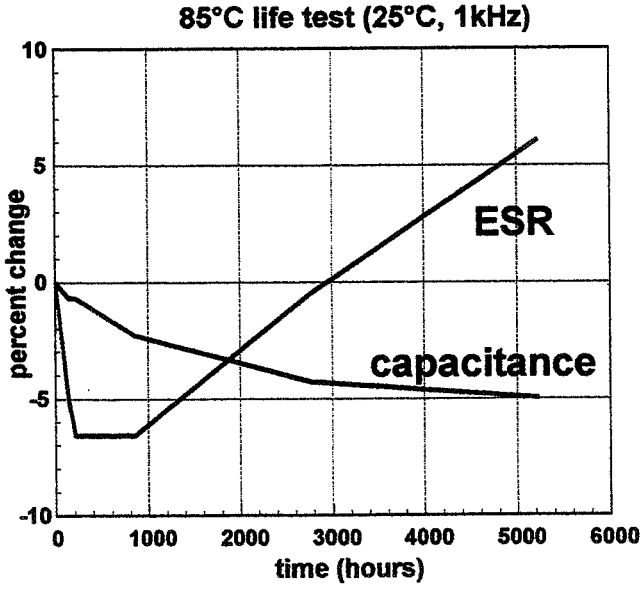

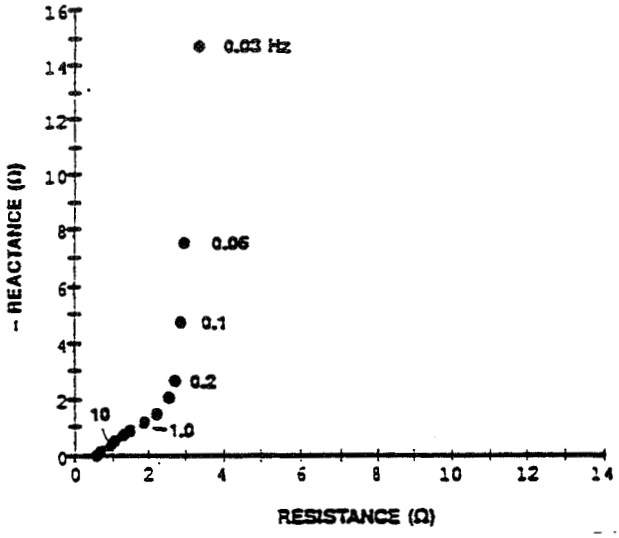

Figure 1. Nyquist plot of a 0.47 F, 11 V Capattery carbon EC.

Figure 2. Hybrid prismatic capacitor construction.

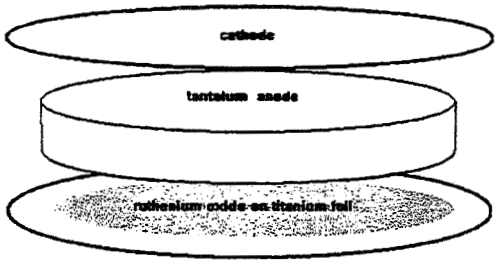

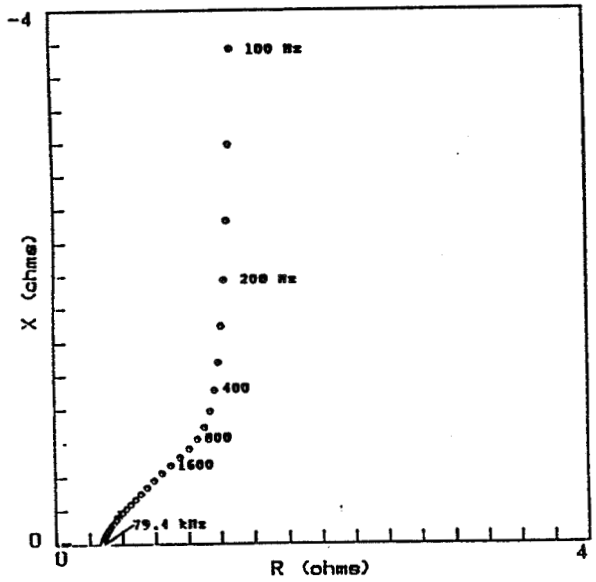

Figure 3. Nyquist plot of the prismatic hybrid capacitor prototype.

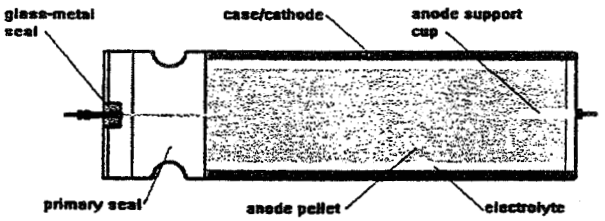

Figure 4. Cross-section view of the MIL-type tantalum hybrid capacitor.

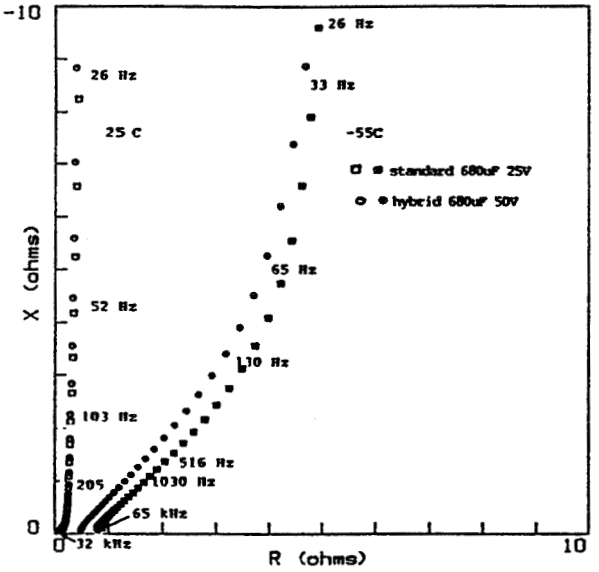

Figure 5. Nyquist plots of standard CLR81 680µF, 25V and hybrid 680µF, 50V capacitors.

Figure 6. Capacitance and ESR for hybrid capacitor life test.

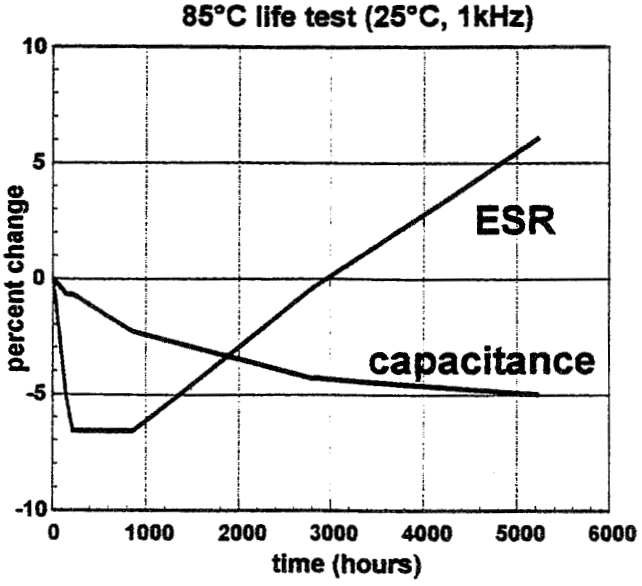

REPORT DOCUMENTATION PAGE

Form Approved
OMB No. 0704-0188

Public reporting burden for this collection of information is estimated to average 1 hour per response, including the time for reviewing instructions, searching existing data sources, gathering and maintaining the data needed, and completing and reviewing the collection of information. Send comments regarding this burden estimate or any other aspect of this collection of information, including suggestions for reducing this burden, to Washington Headquarters Services, Directorate for Information Operations and Reports, 1215 Jefferson Davis Highway, Suite 1204, Arlington, VA 22202-4302, and to the Office of Management and Budget, Paperwork Reduction Project (0704-0188), Washington, DC 20503.

1. AGENCY USE ONLY (*Leave blank*)	2. REPORT DATE	3. REPORT TYPE AND DATES COVERED
	December 1996	Conference Publication

4. TITLE AND SUBTITLE

Space Electrochemical Research and Technology

5. FUNDING NUMBERS

WU-506-41-21

6. AUTHOR(S)

Richard M. Wilson, compiler

7. PERFORMING ORGANIZATION NAME(S) AND ADDRESS(ES)

National Aeronautics and Space Administration
Lewis Research Center
Cleveland, Ohio 44135-3191

8. PERFORMING ORGANIZATION REPORT NUMBER

E-9609-1

9. SPONSORING/MONITORING AGENCY NAME(S) AND ADDRESS(ES)

National Aeronautics and Space Administration
Washington, D.C. 20546-0001

10. SPONSORING/MONITORING AGENCY REPORT NUMBER

NASA CP-3337

11. SUPPLEMENTARY NOTES

Responsible person, Richard M. Wilson, organization code 5420, (216) 433-5916.

12a. DISTRIBUTION/AVAILABILITY STATEMENT

Unclassified - Unlimited
Subject Category 44

This publication is available from the NASA Center for AeroSpace Information, (301) 621-0390.

12b. DISTRIBUTION CODE

13. ABSTRACT (*Maximum 200 words*)

This document contains the proceedings of NASA's fifth Space Electrochemical Research and Technology (SERT) Conference, held at the NASA Lewis Research Center on May 1-3, 1995. The objective of the conference was to assess the present status and general thrust of research and development in those areas of electrochemical technology required to enable NASA missions into the next century. The conference provided a forum for the exchange of ideas and opinions of those actively involved in the field, in order to define new opportunities for the application of electrochemical processes in future NASA missions. Papers were presented in four technical areas: Secondary Batteries, Fuel Cells, Advanced Concepts for Space Power, and Commercialization—Dual Use. This document contains the papers presented.

14. SUBJECT TERMS

Electrochemistry; Batteries; Fuel cells

15. NUMBER OF PAGES

198

16. PRICE CODE

A09

17. SECURITY CLASSIFICATION OF REPORT	18. SECURITY CLASSIFICATION OF THIS PAGE	19. SECURITY CLASSIFICATION OF ABSTRACT	20. LIMITATION OF ABSTRACT
Unclassified	Unclassified	Unclassified	